

Aalborg Universitet



AALBORG UNIVERSITY
DENMARK

Static Behaviour of Bucket Foundations

Thesis submitted for the degree of Doctor of Philosophy

Larsen, Kim André

Publication date:
2008

Document Version
Publisher's PDF, also known as Version of record

[Link to publication from Aalborg University](#)

Citation for published version (APA):

Larsen, K. A. (2008). *Static Behaviour of Bucket Foundations: Thesis submitted for the degree of Doctor of Philosophy*. Department of Civil Engineering, Aalborg University.

General rights

Copyright and moral rights for the publications made accessible in the public portal are retained by the authors and/or other copyright owners and it is a condition of accessing publications that users recognise and abide by the legal requirements associated with these rights.

- Users may download and print one copy of any publication from the public portal for the purpose of private study or research.
- You may not further distribute the material or use it for any profit-making activity or commercial gain
- You may freely distribute the URL identifying the publication in the public portal -

Take down policy

If you believe that this document breaches copyright please contact us at vbn@aub.aau.dk providing details, and we will remove access to the work immediately and investigate your claim.

Aalborg University
Department of Civil Engineering
Division of Water & Soil

DCE Thesis No. 7

STATIC BEHAVIOUR OF BUCKET FOUNDATIONS

Vol.1

PhD Thesis defended public at Aalborg University
(January 11, 2008)

by

KIM ANDRÉ LARSEN

2008

© Aalborg University

Scientific Publications at the Department of Civil Engineering

Technical Reports are published for timely dissemination of research results and scientific work carried out at the Department of Civil Engineering (DCE) at Aalborg University. This medium allows publication of more detailed explanations and results than typically allowed in scientific journals.

Technical Memoranda are produced to enable the preliminary dissemination of scientific work by the personnel of the DCE where such release is deemed to be appropriate. Documents of this kind may be incomplete or temporary versions of papers—or part of continuing work. This should be kept in mind when references are given to publications of this kind.

Contract Reports are produced to report scientific work carried out under contract. Publications of this kind contain confidential matter and are reserved for the sponsors and the DCE. Therefore, Contract Reports are generally not available for public circulation.

Lecture Notes contain material produced by the lecturers at the DCE for educational purposes. This may be scientific notes, lecture books, example problems or manuals for laboratory work, or computer programs developed at the DCE.

Theses are monographs or collections of papers published to report the scientific work carried out at the DCE to obtain a degree as either PhD or Doctor of Technology. The thesis is publicly available after the defence of the degree.

Latest News is published to enable rapid communication of information about scientific work carried out at the DCE. This includes the status of research projects, developments in the laboratories, information about collaborative work and recent research results.

Published 2008 by
Aalborg University
Department of Civil Engineering
Sohngaardsholmsvej 57,
DK-9000 Aalborg, Denmark

Printed in Denmark at Aalborg University

ISSN 1901-7294
DCE Thesis No. 7

Preface

The present thesis "Static behaviour of bucket foundations" has been prepared in connection with a Ph.D. study carried out at the Department of Civil Engineering, Aalborg University, Denmark. The study is carried out under supervision of Prof. Lars-Bo Ibsen, whom I would like to thank for this opportunity.

This thesis consists of 2 parts. Part I is divided into 8 numbered chapters; a list of references is situated after the last chapter. Four chapters associated with the main chapters are placed at the end of Part I. The appendices are numbered with letters. Tables, equations and figures are indicated with consecutive numbers in each individual chapter or appendix. Cited references are marked as e.g. Lundgren & Mortensen (1953), with author specification and year of publication in the text. In Part II the results from the performed experiments on bucket foundations are reported.

During my Ph.D. study I visited the Norwegian University of Science and Technology (NTNU) in Trondheim. I would like to express my appreciation to Professor Lars Grande for this opportunity and to Gudmund Eiksund at SINTEF for his assistance with ABAQUS.

A major part of this thesis has concerned experimental work in the laboratory and at the test site in Frederikshavn. In this connection I would like to thank my colleagues at the laboratory in the section of Water and Soil for their help and good friendship. I moreover appreciate the support from my colleagues, Lars Andersen, Anders H. Augustesen, Morten Liingaard and Carsten S. Sørensen.

Most importantly, I would like to thank Marlene for her patience and love during this work and to our kids Amalie and Nicholai for their essential love.

Aalborg, June 2007

Kim André Larsen

Resumé (Summary in Danish)

Et nyt funderingskoncept i forbindelse med havvindmøller er bøttefundamenter. Konceptet er kendt fra olie og gas industrien hvor belastningssituationen dog er meget anderledes. Bøttefundamentet kan i forbindelse med havvindmøller bruges som både enkeltstående fundamenter og som fundamentskonstruktioner bestående af flere fundamenter. Konceptet er i denne afhandling undersøgt i tilfælde af bøtten som enkeltstående fundament og statiske laster relevante i forbindelse med havvindmøller. Problemstillingen i dette koncept er hovedsageligt rotationsstivheden af fundamentet samt kapaciteten domineret af momenter.

Det eksisterende kendskab til bøttefundamenters opførsel fra kombinerede laster er dokumenteret ved hjælp af et litteraturstudie. Litteraturstudiet er givet i henhold til makro model metoden, hvor bøttefundamentet er modelleret som et makro element.

Den vertikale bæreevne af bøttefundamenter er af stor vigtighed i forbindelse med denne metode. Bæreevnen af bøttefundamenter inklusiv cirkulære overfladefundamenter er undersøgt analytisk, numerisk samt eksperimentielt. Et nyt generelt udtryk der beskriver bæreevnefaktorerne i henhold til den klassiske bæreevne teori er foreslået. Udtrykket gælder både i tilfælde af plan tøjnings- samt aksesymmetrisk spændingstilstand for både glatte og ru fundamenter.

En omfattende eksperimentel undersøgelse af bøttefundamenteres statiske opførsel i tilfælde af kombinerede lastkombinationer er udført i forbindelse med denne afhandling. Dette omhandler både laboratorie og stor skala forsøg. De eksperimentelle resultater er brugt til at evaluere bøttefundamenters opførsel i relation til makro model metoden. I denne forbindelse er der foreslået to kriterier som beskriver den kombinerede kapacitet af bøttefundamenter ved indførelse af bøttefundamentets trækbæreevne.

Numeriske simuleringer af de udførte forsøg er fortaget ved brug af MohrCoulomb materialemodellen og det kommercielle finite element

program ABAQUS. Finite element metoden er, baseret på det pågældende arbejde, konkluderet at være overlegen til estimering af bøttefundamenters opførsel indtil brud samt kapaciteten fra kombinerede laster relateret til havvindmøller.

Numeriske simuleringer af bøttefundamenter er ydermere udført for at undersøge brudmåderne af bøttefundamenter og sammenhængen mellem opførelsen af bøttefundamenter og ækvivalente nedgravede gravitations fundamenter.

Summary in English

One new foundation concept in relation to offshore wind turbines is bucket foundations. The concept is known from the oil and gas industry, though the load conditions here are significantly different. The bucket foundation can be used as monopod or e.g. tripod foundations for offshore wind turbines. The monopod concept is investigated in this thesis, regarding the static behaviour from loads relevant to offshore wind turbines. The main issue in this concept is the rotational stiffness of the foundation and the combined capacity dominated by moments.

The available knowledge regarding the behaviour and combined capacity of bucket foundations is documented by means of a literature study. The literature study is given according to the macro model approach, where the bucket foundation is regarded as a macro element.

The vertical bearing capacity of bucket foundations is of great importance according to this approach. The bearing capacity of bucket foundations including circular surface footings is investigated analytically, numerically and experimentally. A new general expression that describes the bearing capacity factors according to the classical bearing capacity theory is proposed. The proposed expression applies to plane strain as well as axis-symmetric stress conditions for foundations with smooth or rough bases

A thorough experimental investigation of the static behaviour of bucket foundations subjected to combined loading is carried out. Laboratory tests as well as large scale tests on bucket foundations subjected to low vertical load are performed during this work. The experimental results are used to evaluate the behaviour of bucket foundations in accordance with the macro model approach. In relation to this, two combined failure criteria for bucket foundations are proposed in order to involve the tensile capacity of the bucket foundation.

Numerical simulations of the performed tests are carried out using the Mohr Coulomb material model and the commercial finite element code ABAQUS.

The finite element method is based on the present work concluded to be a superior method in estimating the post peak behaviour as well as the combined capacity of bucket foundations in relation to the offshore wind turbine problem.

Numerical simulations of bucket foundations are moreover performed in order to investigate the failure modes of bucket foundations and the resemblance in behaviour of bucket foundations and equivalent embedded solid foundations

Table of content

1. Introduction.....	5
1.1 The concept of bucket foundations.....	9
1.1.1 Installation of bucket foundations.....	10
1.1.2 Performance of the bucket foundation.....	11
1.1.3 Prototype of bucket foundation.....	13
1.2 Research aims.....	16
1.3 Thesis outline.....	19
2. Experimental test setup (Laboratory tests).....	21
2.1 Laboratory tests.....	21
2.1.1 Construction of the test box.....	23
2.2 Aalborg University Sand No.0.....	24
2.3 Design basis- Aalborg University Sand No.0.....	25
2.3.1 General behaviour of the sand.....	25
2.3.2 Evaluation of failure parameters.....	27
2.3.3 Evaluation of dilation angle.....	33
2.3.4 Evaluation of elastic parameters.....	36
2.4 Test procedure.....	38
2.4.1 Preparation of the test box.....	39
2.4.2 Installation of the bucket foundation.....	45
2.4.3 Application of vertical load.....	46
2.4.4 Loading phase.....	47
2.4.5 Measured displacements.....	48
2.4.6 Measured forces.....	49
2.4.7 Test results.....	49
2.5 Summary.....	50
3. Experimental test setup (Large scale test).....	51
3.1 Large scale test.....	51
3.2 Summary.....	58

4. Behaviour of bucket foundations subjected to combined loading.....	59
4.1 Combined bearing capacity (The classical approach).....	59
4.2 Combined behaviour of bucket foundations (The macro model approach).....	64
4.2.1 Elastic behaviour.....	65
4.2.2 Yield surface.....	66
4.2.3 Failure surface.....	77
4.2.4 Hardening law.....	81
4.2.5 Flow rule.....	83
4.3 Influence from installation procedure on the behaviour of bucket foundations.....	90
4.4 Summary.....	91
5. Vertical bearing capacity of bucket foundations.....	93
5.1 Skirt friction.....	94
5.2 Bearing capacity factors for frictional materials.....	97
5.2.1 Plane strain bearing capacity factors.....	98
5.2.2 Axis-symmetric bearing capacity factors.....	101
5.2.3 Comparison of plane strain and axis-symmetric bearing capacity factors.....	104
5.2.4 New general expression for N-factors.....	105
5.3 Vertical bearing capacity of bucket foundations (Experimental observations).....	108
5.3.1 Byrne & Houlsby (1999).....	108
5.3.2 Byrne et al. (2003).....	109
5.3.3 Vertical bearing capacity tests at AAU.....	110
5.4 Summary.....	119
6. Bucket foundation tests subjected to combined loading at AAU.....	121
6.1. Combined peak capacity.....	122
6.1.1 Linear failure criterion at low vertical load.....	122
6.1.2 Complete 3-D failure criteria “Macro model approach”.....	129
6.2 Combined behaviour prior to failure.....	146
6.3 Summary.....	156
7. FE-simulations of bucket foundations	159
7.1 FE-simulations of laboratory tests.....	160
7.1.1 Parameter study.....	166
7.1.2 Comparison of small scale tests and FE-simulations.....	173
7.1.3 Failure modes.....	176
7.1.4 FE-simulations of embedded solid foundations.....	182
7.2 Simulation of large scale loading test.....	187
7.3 Simulation of swipe test.....	195
7.4 Summary.....	196

Table of content

8. Concluding remarks.....	199
8.1 Conclusion-main findings.....	199
8.1.1 Experimental work.....	199
8.1.2 Vertical bearing capacity of bucket foundations.....	200
8.1.3 Combined behaviour of bucket foundations.....	201
8.1.4 Numerical simulations.....	203
8.2 Directions for future work.....	204
References.....	207

List of Appendices

- A.** Method for Predicting Void Ratio and Triaxial Friction Angle from Laboratory CPT at Shallow Depths (Report 0608)
- B.** FE-calculations of N_γ
- C.** Elastic displacements of bucket foundations
- D.** FE-calculations
- E.** Survey of measured capacities

1. Introduction

The energy production from offshore wind turbines are expected to increase significantly in the near future, as offshore wind turbines are expected to be more profitable. The foundations are however a great economical expense in connection with offshore wind turbines. The present situation regarding energy production from wind turbines is in this chapter briefly presented. Various foundation types for offshore wind turbines are introduced with emphasis on the bucket foundations principle, which is investigated in this thesis. Finally the aims of the project and an outline of the thesis are presented.

The market for wind energy has increased tremendously within the past years. The global capacity from wind in 2006 was 74223MW, according to the Global Wind Energy Council (www.gwec.net). This corresponds to an increase in the electrical consumption from wind energy resources equal 32% world wide in 2006. The production of electricity from wind in European countries constitutes as much as 65% of the global production. The countries with the highest total installed capacity in 2006 are Germany (20621MW), Spain (11615MW), the USA (11603MW), India (6270MW) and Denmark (3136MW). The main reason for the increase is due to a global requirement on reducing the amount of CO₂ emitted. A total production of wind turbine generated energy equal 60% of the national electric consumption in Denmark is proposed and regarded as highly plausible, according to a newly published energy plan by the Danish Society of Engineers, Energy Plan 2030 (2006). This corresponds to 6000MW, of which 50% should be offshore. This is an increase of 50% corresponding to the present Danish Government's Plan for Energy, Energy 21 (1996). At the time being several new offshore wind turbine locations have already been pointed in the coastal areas around Europe. A survey of existing and planned offshore wind farms are shown in Figure 1.1, where a green marker indicates wind farms in operation, yellow indicates new planned wind farms and red shows plans which is cancelled. The majority of the operational and planned offshore wind farms are located in the coastal areas around Denmark, UK and Germany shown in Figure 1.2

and Figure 1.3. A list of existing and planned offshore wind farms can be found at www.offshorecenter.dk.

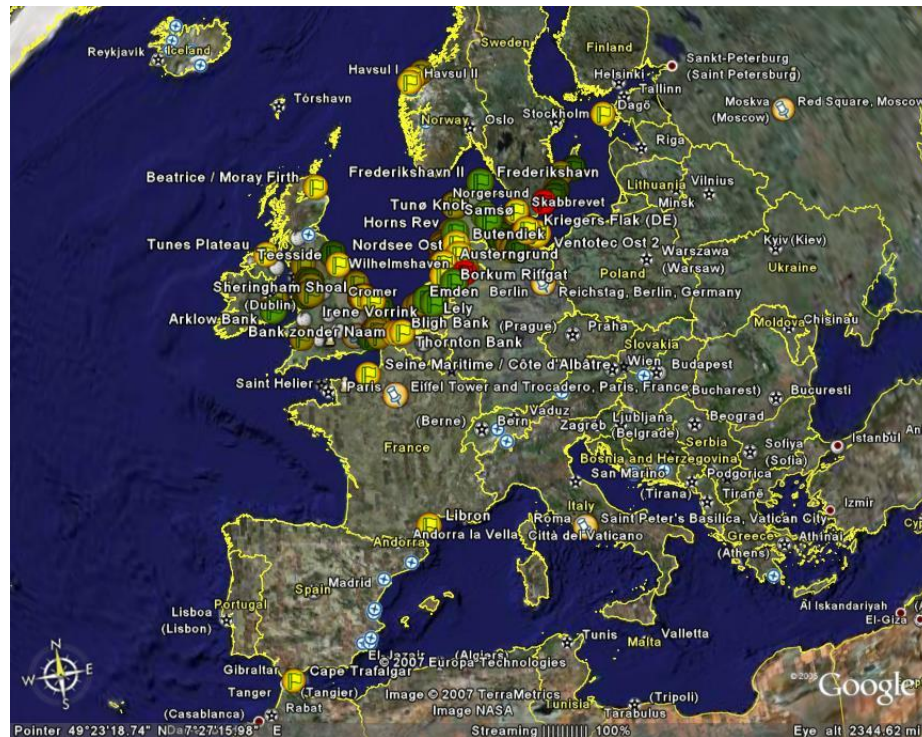


Figure 1.1 Existing and planned offshore wind turbine farms in Europe.
<http://earth.google.com>

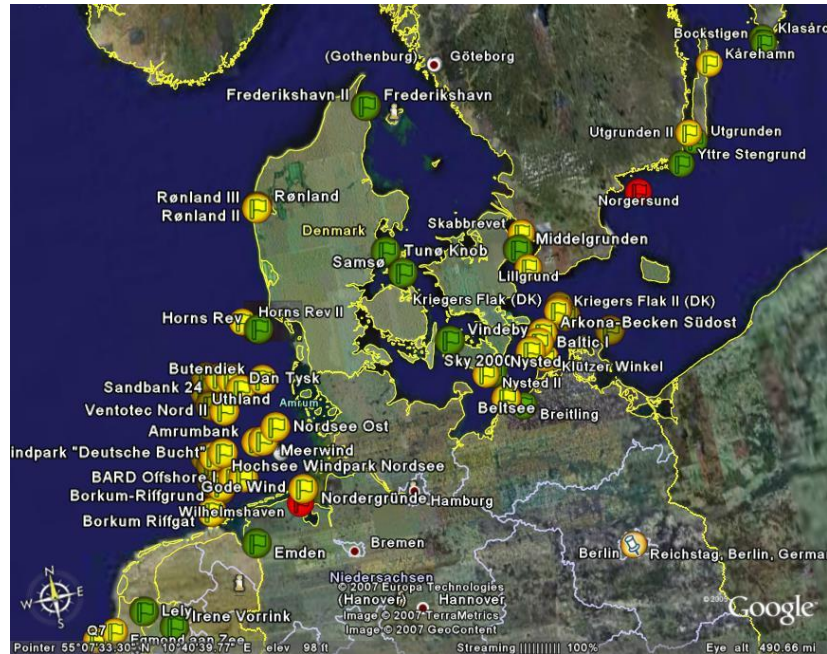


Figure 1.2 Existing and planned offshore wind turbine farms in Denmark. <http://earth.google.com>



Figure 1.3 Existing and planned offshore wind turbine farms in UK and Northwest Germany. <http://earth.google.com>

Denmark has been both a pioneer and is today one of the leading countries in the development of wind energy technology, with manufactures as VESTAS and Siemens Wind Power (Former BONUS). During the recent years the location of new wind turbines has mainly been offshore. Moving the wind turbines offshore has several advantages. The location onshore has shown to breeds large discussions due to the noise and their appearance in the country. Less opposition is seen when the wind turbines is located offshore at some distance from the cost lines. Another obvious benefit of the offshore location is the efficiency of the turbines as offshore wind are usually more constant, Byrne and Houlsby (2002b). The development in wind turbine technology is continuously improving the economics of offshore wind turbines with increasing size and performance. This increase combined with offshore location has however also increased the demands to the foundations as larger forces must be sustained.

Due to foundation cost in connection with offshore wind turbines as high as up to 30% of the total costs, the foundation design is presently undergoing large attention with the increased interest in offshore wind turbines, e.g. Kelly et al. (2003).

Offshore wind turbines structures are traditionally founded on gravity concrete foundations or on mono-piles. Different foundation solutions are sketched in Figure 1.4. A relative new concept for foundation of such structures is the bucket foundation also shown in Figure 1.4. The concept of bucket foundations is known from the offshore oil and gas industry. The load condition in this connection are however very different from offshore wind turbines. The loads from offshore wind turbines are characterized by low vertical weight due to the slender construction combined with large horizontal forces inducing a large overturning moment, whereas loads from constructions in connection with offshore oil production mainly are vertical.

The choice of foundation type depends on several factors as soil conditions, water depth, structure of the wind turbine, environmental conditions, economics and politics etc, Feld (2004). Advantages and disadvantages of the foundation types in relation to the factors presented above are outlined by Liingaard (2006) and Ibsen et al. (2003). Only foundation principles with use of the bucket foundation will be discussed here.

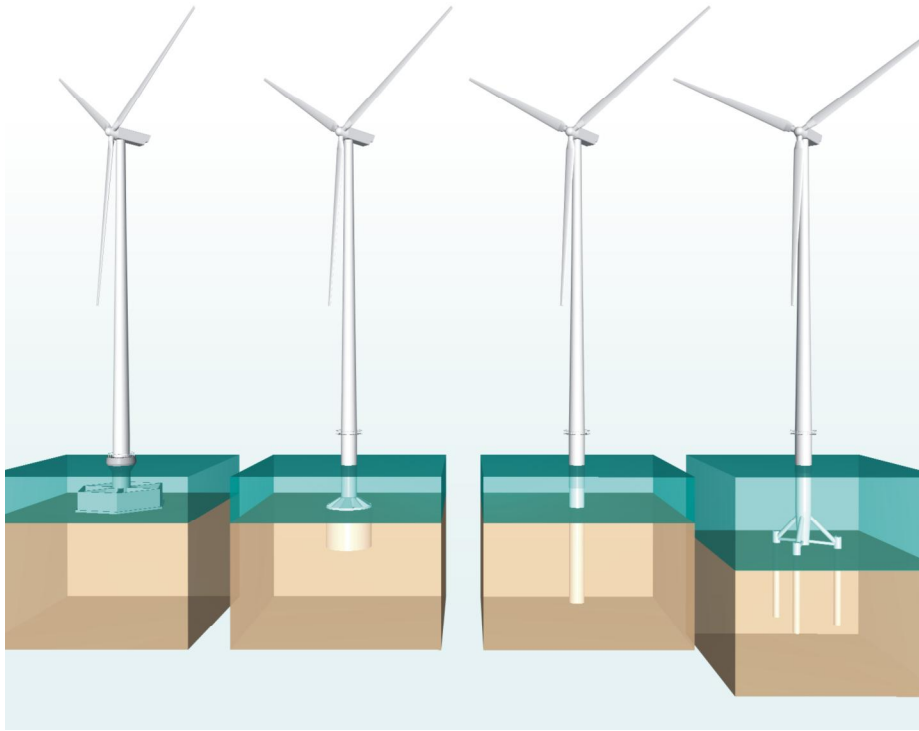


Figure 1.4 Foundation concepts for offshore wind turbines. From left to right: Gravity foundation, bucket foundation, monopile and tripod foundation with piles.

1.1. The concept of bucket foundations

A bucket foundation (also denoted a skirted foundation or suction caisson) is large cylindrical structures that is open at the base and closed at the top, see Figure 1.5. The cylindrical part is denoted “bucket skirt” and upper plate that closes the bucket is denoted “bucket lid” or “top plate”. The bucket foundations considered in this thesis is assumed to be constructed of steel. The skirts are during installation penetrated into the soil until the bucket lid is resting on the seabed. If the installation leaves a gap between soil and bucket lid this void is grouted.

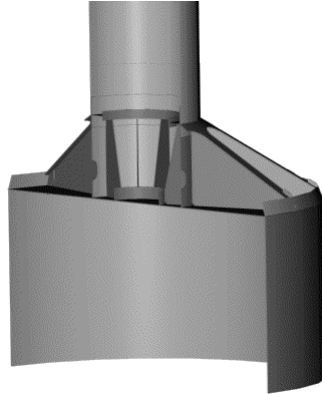


Figure 1.5 Sectional view of bucket foundation including reinforcement of top plate and superstructure for connection of wind turbine tower.

Several indications in the literature show that large savings can be made by using bucket foundations instead of example driven piles, e.g. Ibsen et al. (2003) and Byrne & Houlsby (2003).

1.1.1. Installation of bucket foundation

The bucket foundation is during installation penetrated vertically into the soil by means of suction within the bucket. The penetration of bucket foundations in sand, silt and clay is by method the same but are caused by different effects in the soil. Only bucket foundations located in sand are included in this work, thus the installation in silt and clay will not be explained.

The installation phase can be divided into two parts: 1) Self penetration of the bucket and 2) penetration of bucket by means of suction applied. The skirt is in phase 1 penetrated into the seabed from the self weight of the structure. In phase 2 the penetration is caused by applying suction to the inside of the bucket. The suction creates an upward flow in the soil within the bucket reducing the effective stresses in the sand beneath the skirt tip and a net downward force on the bucket lid, as illustrated in Figure 1.6. This reduction in effective stresses greatly reduces the penetration resistance allowing the skirt to penetrate the soil further from the self weight of the structure and the downward force from the suction between bucket lid and soil surface. The suction applied is limited by the gradient that causes piping channels in the soil within the bucket, i.e. the critical gradient and the water depth at shallow waters. Once piping channels are created the suction can no longer be sustained. If the suction is kept at a minimum not causing piping in the sand, the sand is assumed to regain its strength when pumping is ceased. The time necessary and degree of regeneration is presently investigated from large scale tests at Aalborg University.

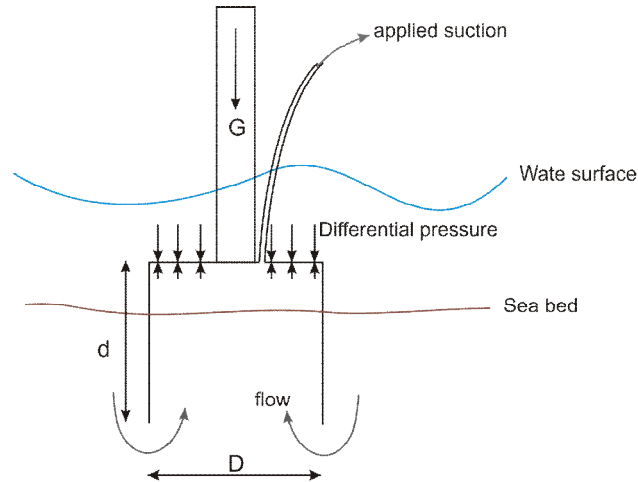


Figure 1.6 Installation of bucket foundations by suction.

In sand the relation between the diameter of the bucket foundation, D and the length of the skirt, d given by the non-dimensional embedment ratio, d/D are limited by the critical gradient. The limit is in sand generally assumed to be given as the ratio d/D equal 1 approximately, e.g. Houlsby & Byrne (2005). Large scale tests on bucket foundations with D equal 2 and 4 meters and $d/D=1$ at Aalborg University has proved that the upper limit is indeed achievable for dense sand, e.g. Ibsen et al. (2005) and Larsen & Ibsen (2005). Besides the limitations in suction also the risk of buckling in the skirt during penetration must be considered during the design of the bucket foundation.

If the critical suction is exceeded, experience from installation tests with large scale buckets have shown, that the situation can be stabilized by adding soil to the seabed in the area of the piping hole outside the bucket foundation. After dissipation of the pore pressure in the soil the installation procedure can be continued. The critical gradient and penetration resistance from suction-installed bucket foundations in sand is investigated by e.g. Houlsby et al. (2005a), Houlsby & Byrne (2005) and Feld (2001).

An environmental issue in connection with offshore location of wind turbines are the remediation of the seabed in connection with decommissioning of the wind turbines. The bucket foundation is easy to remove as the installation procedure is merely reversed.

1.1.2. Performance of the bucket foundation

The bucket foundation can be used as a single foundation (monopod) or as a multiple foundation system (e.g. tripod). For monopods, the key issue is the performance of the foundation subjected to horizontal load and large moment

applied by e.g. the wind and waves on the structure combined with small vertical load. For the multi-footing case the applied moment will mainly be reacted as vertical compression and tension load on the individual foundations.

The bucket foundation as a monopod for offshore wind turbines is investigated in this thesis. One major challenge in this connection is the installation procedure. Strict requirements concerning the horizontal alignment of the foundation upon installation is a great challenge in connection with a monopod bucket foundation. An installation technique has been developed at Aalborg University controlling the level of the bucket foundation during installation, e.g. Larsen & Ibsen (2005). Another challenge is the design of the foundation in the service and ultimate limit states (SLS & ULS). Thus the behaviour of the bucket foundation subjected to combined loading from the wind turbine structure must be investigated.

Combined loading of a rigid bucket foundation can be described by the six degree of freedoms shown in Figure 1.7. The problem of combined loading during extreme environmental conditions from wind, waves and current becomes often unidirectional, Byrne & Houlsby (1999). Thus the problem can be reduced to involve the degrees of freedom shown in Figure 1.8 if only loads in the x_2 : x_3 -plane are regarded. Using the standardized sign conventions in Figure 1.8 the deformations and forces are work conjugated and will be used throughout this thesis, Butterfield et al (1997). Due to consistency of the units in for example a plot or function, moments are often given as the value normalized by the diameter, i.e. M/D . Since the work is calculated by the following formula the corresponding work conjugate rotation in this case will be $D\varphi$:

$$\begin{aligned} dW &= Vdw + Md\varphi + Hdu \\ \text{Equation 1.1} \quad &= Vdw + (M / D)D(d\varphi) + Hdu \end{aligned}$$

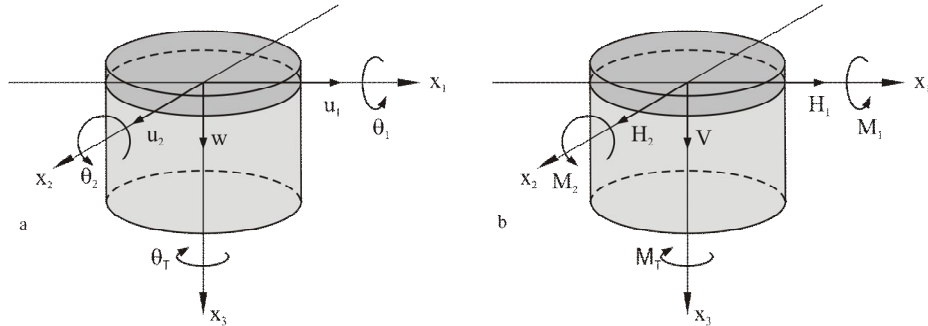


Figure 1.7 Degrees of freedom for a rigid bucket foundation: (a) displacements, and (b) forces and moments.

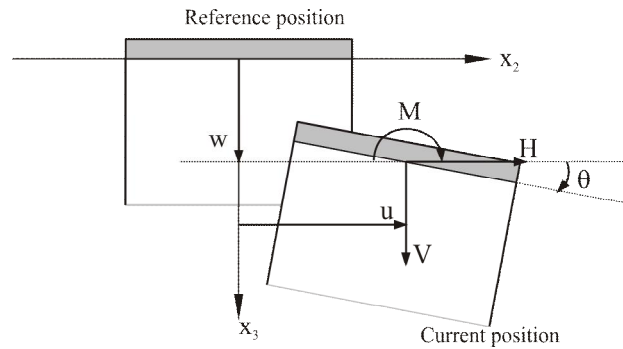


Figure 1.8 Standardized sign convention for plane loading of bucket foundations. Adopted from Butterfield et al (1997).

The behaviour of monopod bucket foundations subjected to true environmental loads is only known from a single reference turbine. This project is described below.

1.1.3. Prototype of bucket foundation

In November 2002 the first and to date only bucket foundation for a fully operational wind turbine was installed at the offshore test facility in Frederikshavn, in the northern part of Jutland, see Figure 1.9. The project is described in Ibsen et al. (2005). The wind turbine is a Vestas V90-3.0MW turbine and was at the time being the largest wind turbine in Denmark with a total height equal 125m. The diameter and the skirt length of the bucket foundation are equal 12m and 6 m respectively, and the total weight of the foundation is 135 tons. The bucket foundation prior to and upon installation is shown in Figure 1.10 and Figure 1.11. The installation of the bucket foundation was carried out by the geotechnical department at Aalborg University.

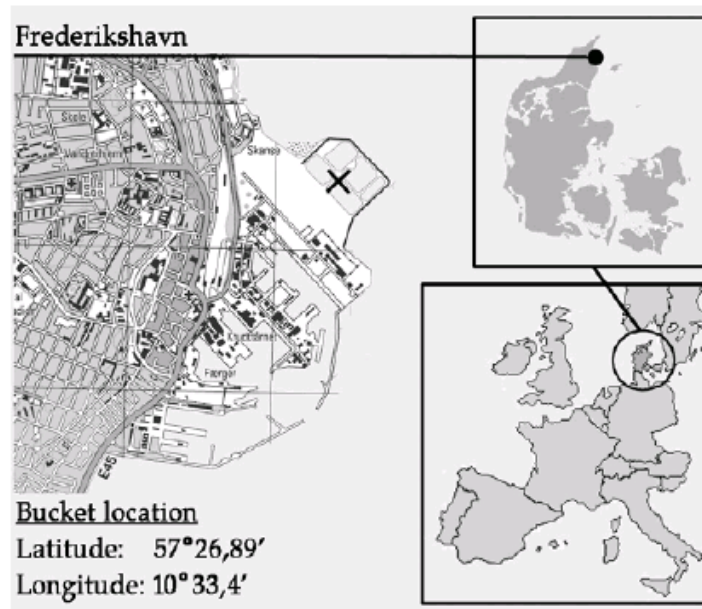


Figure 1.9 Location of Vestas V90-3.0MW wind turbine on bucket foundation.



Figure 1.10 Bucket foundation for Vestas 3MW wind turbine in Frederikshavn.



Figure 1.11 Bucket foundation after installation in Nov. 2002.

The wind turbine is located in area where it was possible to dam the area around the location during installation, see Figure 1.11 and Figure 1.12. After assembling of the tower the area was once again flooded. Prior to the installation a set of experiments on installing a 4 meter bucket foundation with an embedment ratio equal 1 was performed using suction at the same test site during the summer and fall of 2002.



Figure 1.12 Assembling of wind turbine tower after installation of the bucket foundation. The test site is kept dry during assembling by pumping.

1.2. Research aims

Skirted foundations are expected to behave equivalent to a solid embedded foundation because of the trapped soil within the skirts in case of undrained conditions, e.g. Tani & Craig (1995). The behaviour in the drained case is less well understood due to only limited experiments on studying the performance of skirted foundations in drained soils. In case the same assumption is applied for drained soil the weight of this soil can be regarded as a part of the foundation reducing the necessary base area, i.e. diameter of the bucket foundation.

The state of the art methods for estimating the static behaviour of bucket foundations are primarily the macro model approach according to the work hardening plasticity theory and the finite element method. Only limited experience is available on bucket foundations located in sand in relation to the use of these methods.

The purpose of this thesis is to investigate the static behaviour of bucket foundations subjected to combined loading, i.e. combinations of moment, vertical and horizontal loads. The situations considered are relevant for offshore wind turbines located on monopods in dense saturated sand. Only static loads are considered.

A design chart for bucket foundations are proposed by Ibsen et al. (2003), see Figure 1.13. The work within this thesis concerns “Model experiments” and “Simple design models” according to the conceptual design phase and “Geotechnical bucket design” according to the detailed design phase.

The research aims in connection with this study are categorized as:

- Development of a method for estimating the compactness and strength of the tested sand samples from a laboratory CPT-probe.
- Evaluation of the bearing capacity factors according to the classical bearing capacity relevant for bucket foundations in sand.
- Experimental investigation of the vertical bearing capacity of bucket foundations. The results are compared with the evaluated bearing capacity factors.
- Experimental investigation of the static behaviour of bucket foundations subjected to combined loading.
- Calibration of the state of art macro model approach from the experimental results.
- Evaluation of the applicability of the finite element method to predict the observed behaviour from combined loading.
- Analyzing the difference in behaviour and failure mode for bucket and embedded solid foundations using three dimensional finite element calculations.

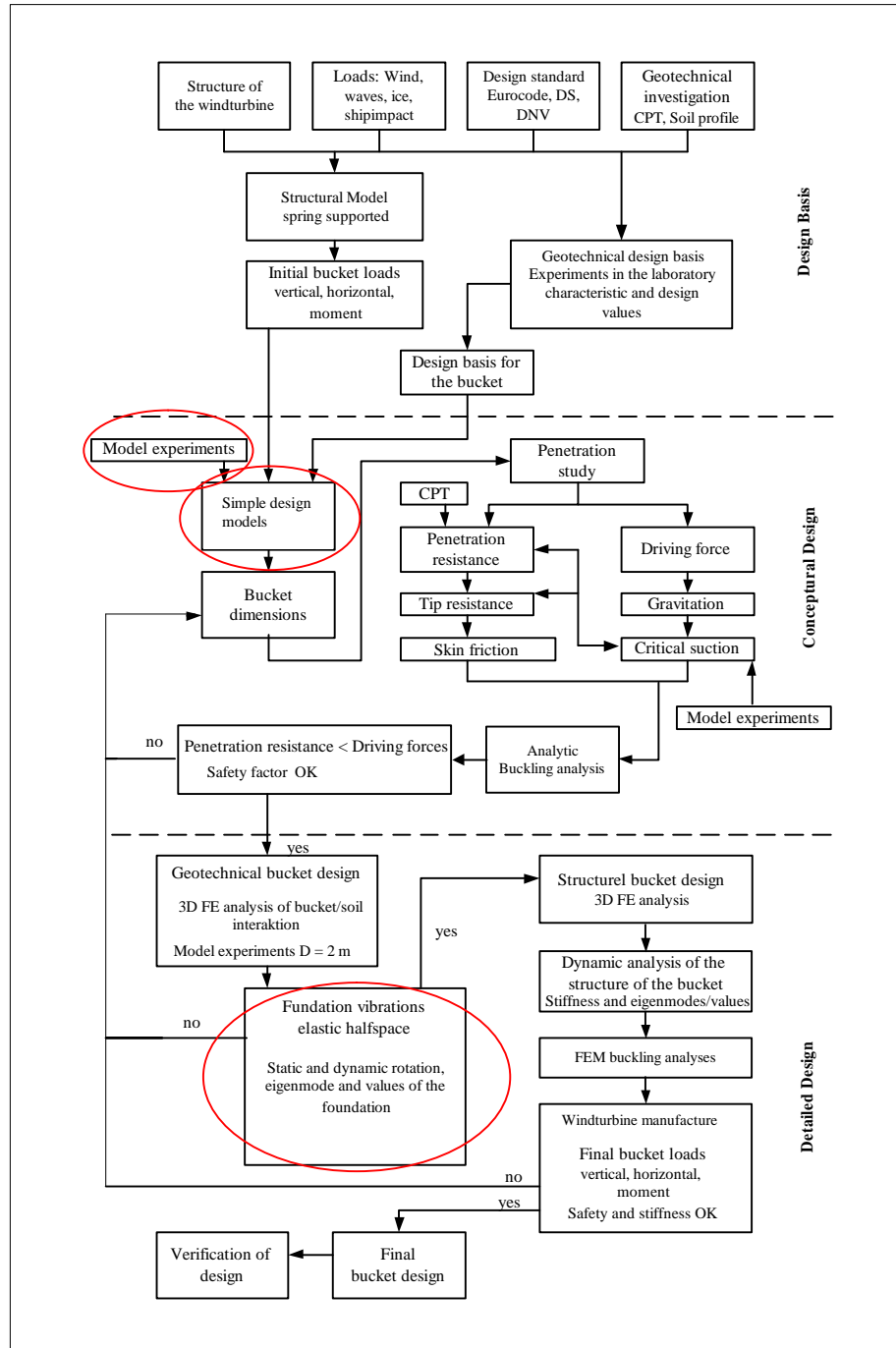


Figure 1.13 Design chart for bucket foundations, after Ibsen et al. (2003).

1.3. Thesis outline

The thesis consists of two volumes. Vol. 1 is the main part containing 8 chapters and five associated appendices, related to the topics described in section 1.2. Vol. 2 contains the reported results from experiments on bucket foundation carried out in the laboratory. A complete survey of forces and displacements measured at failure from laboratory tests available at Aalborg University are given at the end of the volume.

Part I

Chapter 2 contain a description of the test setup and characteristics of the sand used in connection with the experimental work performed on bucket foundations in the geotechnical laboratory at Aalborg University. The characteristics of the sand are evaluated regarding the stress dependency present in sand at low stress levels. An extensively amount of loading tests on bucket foundations are carried out during this work. The test setup used in this study deviates significantly from other studies as the bucket is free to move during loading.

During the period of this work a set of large scale tests similar to the laboratory tests are carried out at a test facility in Frederikshavn. The results from one of these large scale tests are presented in chapter 3.

Chapter 4 contains a literature review concerning the static behaviour of bucket foundations in sand. The description is given within the context of work hardening plasticity theory, also denoted the macro model approach.

Chapter 5 concerns an investigation of the bearing capacity factors of bucket foundation according to the classical bearing capacity formula. The main purpose of this chapter is to investigate whether this method can predict the vertical bearing capacity of bucket foundations in sand as this is used in the macro model approach in chapter 4. Numerical evaluations of the bearing capacity factors relevant for sand are carried out by means of the commercial FE-codes Plaxis and ABQUS. The bearing capacity of bucket foundations are compared to vertical bearing capacity tests carried out in the laboratory.

Chapter 6 contains the summarized results from performed experiments on bucket foundations subjected to combined loading performed at Aalborg University during and prior to this work. The observed behaviour is compared with the information's and models presented in chapter 4. The emphasis of this chapter concerns the capacity of bucket foundations, and behaviour at failure.

Chapter 7 contains numerical simulations of the experiments performed during this work. The simulations are three dimensional and are carried out by the finite elements program ABAQUS. The applicability of the finite element model is analyzed by comparison with the experimental results. The behaviour and failure mechanisms of bucket foundations are compared with embedded solid foundations based on numerical simulations.

Chapter 8 contains the main conclusions of the thesis and directions for future work are given, based on the findings in this thesis.

Appendix A contains the reported work on the method proposed for predicting the density of the tested sand samples by use of a laboratory CPT-probe. The report is included in its full version, including test results.

Appendix B contains the numerical results concerning the evaluation of the bearing capacity factor, N_g for circular- and strip foundations.

Appendix C contains a description of an elastic stiffness tensor used to describe the elastic behaviour of bucket foundations. The relevant stiffness components of this tensor are presented. The elastic behaviour is used to estimate the plastic behaviour of bucket foundations in chapter 6.

Appendix D contains results from various three dimensional FE-calculations of bucket foundations subjected to combined loading. Special features used in connection with the calculations performed during this work and benefits from using these are described.

Appendix E contains a survey of tests results from tests on small scale bucket foundations at failure evaluated within this thesis.

2. Experimental test setup (Laboratory tests)

During the work of this thesis more than 100 small scale tests on bucket foundations subjected to static combined loads are performed in the geotechnical laboratory at Aalborg University. The tests are carried out using water-saturated dense Aalborg University sand No.0 (also denoted Baskarp Sand No. 15). The test-setup used in these tests is presented in this chapter and the results are reported in Volume 2 of this thesis. Besides the tests performed in connection with this work, a corresponding number of small scale tests under different load conditions has previous been carried out in the laboratory. These tests are carried out using the same type of sand. The measured data from these tests have been evaluated by the author during this work and are reported in Larsen and Ibsen (2006a, b). Thus a total of more than 200 loading tests of small scale bucket foundations with a diameter varying from 50mm to 400mm are presently available at Aalborg University. Characteristics of the sand tested in connection with this study are presented based on existing classification tests and several triaxial tests. The characteristics of the sand are used to calibrate the response of the laboratory CPT-probe and to describe the behaviour of the sand in connection with numerical simulations of the performed tests. The description is given according to the Mohr-Coulomb material model.

2.1. Laboratory tests

The following section contains a description of the test setup, including the test box, used for the static load tests carried out in the geotechnical laboratory at Aalborg University.

An example of the bucket foundations tested in the laboratory is shown in Figure 2.1. The diameter, D of the bucket foundations tested in the laboratory is 50, 100, 200, 300 and 400 mm. The diameter of bucket foundations tested during this work is primarily 300mm. The embedment ratio of the bucket foundations, d/D are 0, 0.25, 0.5, 0.75 and 1. In order to compare the results

sand is glued on to the base of surface foundations, i.e. $d=0$ to ensure a rough base.



Figure 2.1 Bucket foundation tested in the laboratory. $D=200\text{mm}$ and $d/D=0; 0.25; 0.5; 0.75$ and 1 are shown.

Two types of loading tests have been performed on bucket foundations with varying diameter and skirt length. This is bucket foundations subjected to 1) pure vertical loading and 2) combined loading, i.e. a combination of moment, horizontal and vertical loads. Tests with bucket foundations subjected to combined loads are carried out with constant vertical load, V and constant ratio of moment to horizontal load, M/H . The ratio of M/H is applied to the foundation by means of a rigid loading tower bolted to the bucket lid, see Figure 2.2. During loading the tower is exposed to a horizontal load, H applied at a given height of impact equal $h=M/H$.

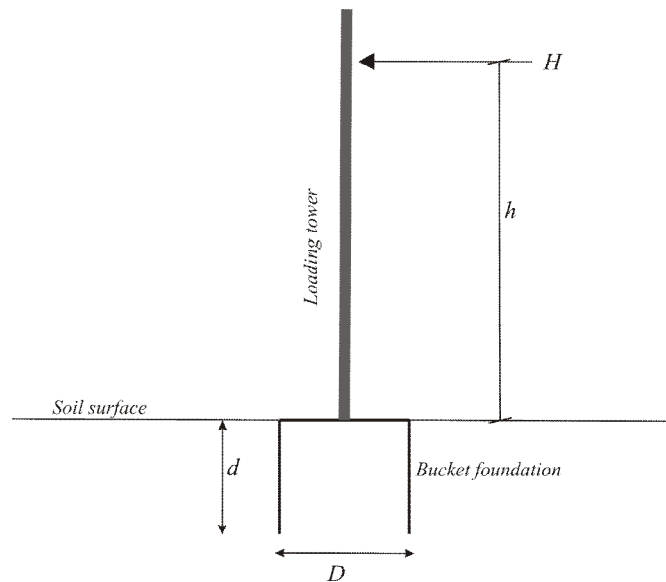


Figure 2.2 Horizontal loading of bucket foundation.

The loading tests are carried out on dense saturated sand in a special designed test box, see Figure 2.3. The construction of the test box is described in the following sections.

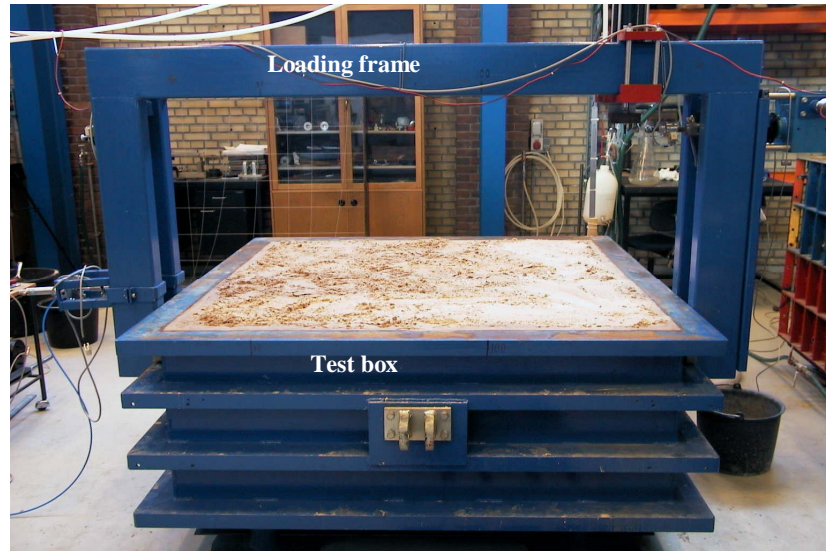


Figure 2.3 Test box used for loading tests on bucket foundations.

2.1.1. Construction of the test box

The test box used to investigate the behaviour of bucket foundations has been improved in connection with this work. The structure of the test box is illustrated in Figure 2.4. By redesigning the drainage system in the bottom of the test box, the depth of the sand sample has increased by approximately 100 mm to 530 mm.

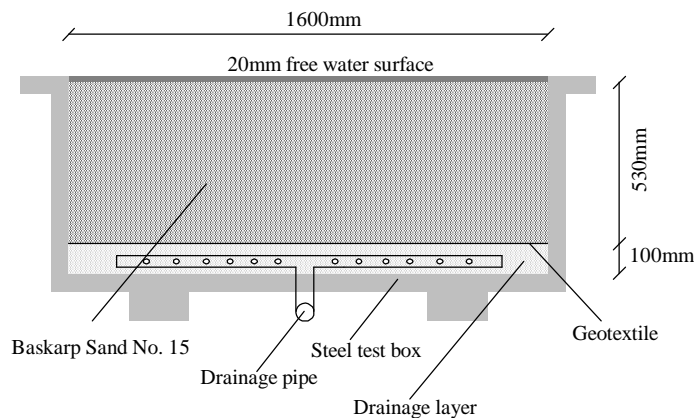


Figure 2.4 Structure of the test box used for the small scale loading tests.

The test box consists of a rigid steel construction with inner horizontal dimensions of 1600 x 1600 millimetres and an inner total depth of 650 millimetres. In the bottom of the test box a drainage system provides the sand with water through a drainage layer. The drainage system consists of a set of perforated pipes, which is used to lead the water in and out of the test box. In the drainage layer the water is, through jets in the pipes, distributed across the entire area of the test box before entering the sand above. The drainage layer consists of stones around the drainage pipes with a diameter from two to five millimetres. Between the sand layer and the drainage layer a sheet of geotextile is placed to prevent the sand in penetrating the drainage layer. The sand used in the test box is Aalborg University Sand No. 0 and is water saturated during the experiments. A description of the sand including deformation and strength properties is given below.

2.2. Aalborg University Sand No.0

Aalborg University Sand No. 0 is a graded sand from Sweden. The shape of the largest grains is round while the small grains have sharp edges. The main part of Aalborg University Sand No. 0 is quartz, but it also contains feldspar and biotite.

The properties of Aalborg Universitet Sand No.0 are well described due to an extensively testing program performed at Aalborg University. Triaxial, true triaxial and other tests have been performed as well as classification tests. All tests are performed in the geotechnical laboratory at Aalborg University. These information's are necessary in order to model the behaviour of the bucket foundations tested in the laboratory. The classification of the sand has been investigated by Borup and Hedegaard (1995), from which the following results are collected.

The distribution of the grains has been investigated by means of sieve tests. The resulting grading curve is shown in Figure 2.5, from which it can be concluded:

- Mean grain size, $d_{50} = 0.14$ mm
- Coefficient of uniformity, $U = d_{60}/d_{10} = 1.78$

in which index 50 represents the % quantile etc.

The grain density, maximum and minimum void ratios are found to be:

- $d_s = 2.64$
- $e_{max} = 0.858$
- $e_{min} = 0.549$

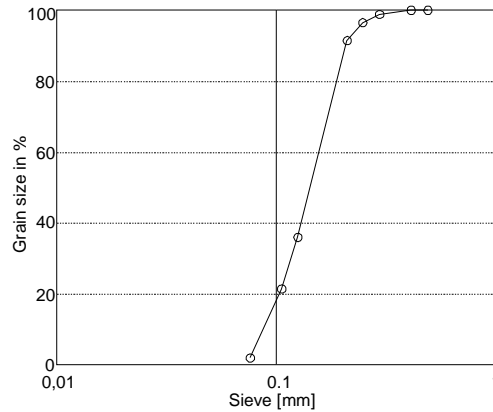


Figure 2.5. Distribution of grains for Aalborg University Sand No. 0.

All the tests have been performed according to the standard procedures used in the laboratory. For further information regarding the standard procedures see DGF-Bulletin (2001)

2.3. Design basis- Aalborg University Sand No.0

The behaviour of Aalborg University Sand No. 0 is in the following section investigated in order to evaluate the design parameters. The investigation is based on an extensive number of performed triaxial tests on the sand with different void ratios and confining pressures. The tests are reported in Ibsen & Bødker (1994), Borup & Hedegaard (1995), Ibsen et al. (1995) and Andersen et al. (1998). All the tests are performed in the Danish triaxial apparatus in the geotechnical laboratory at Aalborg University. The tests are all drained and performed on samples with a height and diameter ratio equal 1 and with lubricated ends according to Danish traditions.

2.3.1. General behaviour of the sand

The behaviour of a given sand is known to be dependent of the density and the stress level. Results from 3 triaxial tests on Aalborg University Sand No.0 are shown in Figure 2.6 and Figure 2.7 in order to illustrate this dependency. In Figure 2.6 the tested specimens is deposited with a void ratio of 0.61, and exposed to two different isotropic stress situations, i.e. confining pressures before shearing the soil samples. In Figure 2.7 the confining pressure is 800 kPa for both tests and the void ratio is changed instead. Failure is in the figure shown as solid dots and the state of which the soil goes from compression to dilation, i.e. the characteristic state is marked with circles. The stresses in the figures are given as the deviatoric stress, q which is defined as the difference between the major and the minor principal stress in the principal stress space.

The deformations in the figures are given as the vertical strain, e_v and the volumetric strain e_v .

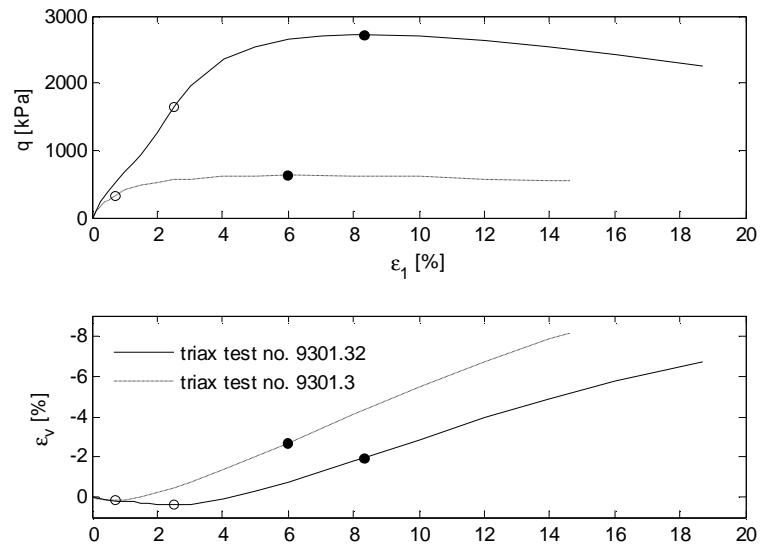


Figure 2.6 Triaxial results from tests on Aalborg University Sand No.0. Test 9301.3: Confining pressure=160kPa and Test 9301.32: Confining pressure=800 kPa. $e = 0.61$

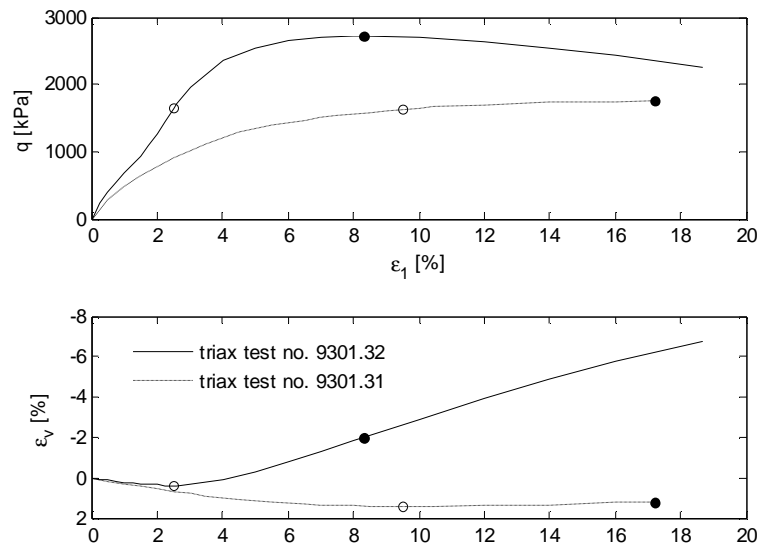


Figure 2.7 Triaxial results from tests on Aalborg University Sand No.0. Test 9301.32: $e = 0.61$ Test 9301.31: $e = 0.85$ Confining pressure is 800 kPa.

From the above figures it can be seen that the specimen exposed to high confining pressure shows more compression before the sand dilates compared to the specimen exposed to a lower confining pressure. The same behaviour is observed for the sample with lower density, i.e. higher void ratio, though almost only compression occurs in this sample. At very low densities the characteristic state actually coincides with the stress situation at failure. The specimen is also seen to dilate more at low confining pressure than at high and for higher densities of the sample.

At the characteristic state the capacity of the sand is governed by an inner friction between the soil grains alone. At stress situations below this state the sand contracts because of sliding between the soil grains. At stress situations higher than the characteristic state the sand starts to dilate because the soil grains need to rearrange so that further deformation can occur. This rearrangement requires extra energy which causes an increase in the soil strength.

The soil parameters that defines the elastic properties of the soil, the failure criterion, the characteristic state and the rate of dilation at failure, is evaluated in the following.

2.3.2. Evaluation of failure parameters

The drained failure of sand is according to the Mohr-Coulomb failure criterion assumed to follow:

$$\text{Equation 2.1} \quad t_f = c' + \sigma' \tan j'$$

where t_f is the maximum possible shear stress and σ' is the corresponding normal effective stress, c' and j' are the effective cohesion and friction angle, respectively. Only drained behaviour is investigated in this thesis, thus the notation used in connection with effective values, i.e. ' is left out in the following.

The use of the Mohr Coulomb failure criterion is often preferred because of its simplicity due to the linearity between the limiting shear stress, t and the corresponding normal stress, s . Unfortunately this linearity is only a rough approximation when dealing with small stress levels, which is often the case in the laboratory. At small stress levels the strength parameters in Equation 2.1 varies with the stress level, which means that the parameters must be defined for a stress level corresponding to the problem investigated. This can be done in different ways as shown in the following.

The results from some of the triaxial tests on Aalborg University sand with a void ratio equal 0.61 is in Figure 2.8 and Figure 2.9 used to illustrate how the

strength parameter according to Equation 2.1 can be derived. The parameters are determined at a stress level of approximately 1200 kPa in the figures.

In Figure 2.8 the Coulomb failure criterion is shown as the tangential line to the stress situation at failure expressed by Mohr's circles. This gives a tangent cohesion of the material equal 65 kPa and a tangent friction angle equal 37.5° . Alternatively, the secant failure line to the Mohr's circles can be used, forcing the failure line through origo, resulting in a secant friction angle equal 39.3° . As seen from the figures the tangent values overestimates the strength of the sand at low stresses whereas the secant value underestimates the strength at this stress level.

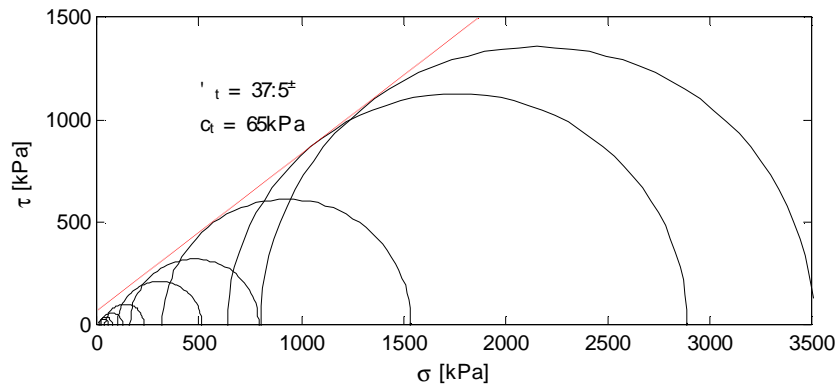


Figure 2.8 Mohr's circle at failure for tests on Aalborg University Sand No. 0 ($e=0.61$). Tangential failure determined at $S = 1200$ kPa is shown as dotted line.

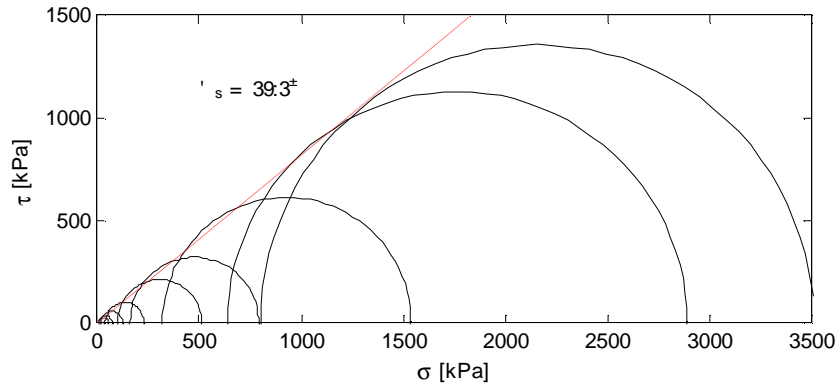


Figure 2.9 Mohr's circle at failure for tests on Aalborg University Sand No. 0 ($e=0.61$). Secant failure determined at $S = 1200$ kPa is shown as dotted line.

From Figure 2.8 and Figure 2.9 it is seen that the true failure envelope is actually not linear but curved. Jacobsen (1970) suggested the following curved failure criterion in order to capture this stress dependency on the strength parameters at low stress levels:

Equation 2.2

$$q = s_1 - s_3 = 2t = \frac{2 \sin(j_a)}{1 - \sin(j_a)} s_3 \left(1 + \frac{c_a \cdot \cot(j_a)}{m \cdot s_3} \right)^m$$

where index a denotes the asymptotic value, i.e. the strength values at high stress levels and m is a parameter that describes the curvature of the failure envelope at low stress levels. s_1 and s_3 is the major and minor principal stress at failure respectively.

In this thesis the Mohr-Coulomb failure criterion is chosen as constitutive model in the numerical simulations of the bucket behaviour. The curved failure envelope in Equation 2.2 is in the following used to derive the Mohr-Coulomb strength parameters at a given stress level.

The secant friction angle, j_s from a triaxial test is easily derived from Mohr's circle, and is given by:

Equation 2.3

$$\sin(j_s) = \frac{s_1 - s_3}{s_1 + s_3}$$

The variation of the triaxial secant friction angle with respect to the minor principal stress, s_3 can be calculated if Equation 2.3 is transcribed into a function of s_3 and the deviatoric stress, q which is known from Equation 2.2:

Equation 2.4

$$\begin{aligned} \sin(j_s) &= \frac{q}{2 \cdot s_3 + q} \\ \text{or} \\ \sin(j'_s) &= \frac{2 \frac{\sin(j_a)}{1 - \sin(j_a)} s_3 \left(1 + \frac{c_{t,a} \cdot \cot(j_a)}{m \cdot s_3} \right)^m}{2 \cdot s_3 + 2 \frac{\sin(j_a)}{1 - \sin(j_a)} s_3 \left(1 + \frac{c_a \cdot \cot(j_a)}{m \cdot s_3} \right)^m} \end{aligned}$$

If the tangential strength parameters are preferred, these can be found with respect to the minor principal stress, s_3 by differentiating Equation 2.2 and solving with a set of matching values of q and s_3 , Hansen and Jakobsen (1995):

$$\sin(j'_t) = \frac{\left(1 + \frac{s_0}{s_3}\right)^m - \frac{s_0 \cdot m}{s_3} \cdot \left(1 + \frac{s_0}{s_3}\right)^{m-1}}{\frac{1 - \sin(j_a)}{\sin(j_a)} + \left(1 + \frac{s_0}{s_3}\right)^m - \frac{s_0 \cdot m}{s_3} \cdot \left(1 + \frac{s_0}{s_3}\right)^{m-1}}$$

Equation 2.5

$$c_t = \tan(j_t) \frac{1 - \sin(j_t)}{2 \cdot \sin(j_t)} \cdot \left(\frac{2 \cdot \sin(j_a)}{1 - \sin(j_a)} \cdot s_3 \cdot \left(1 + \frac{s_0}{s_3}\right)^m \right) - \tan(j_t) \cdot s_3$$

where $s_0 = \frac{c_a}{m} \cdot \cot(j_a)$ and index t denotes the tangential strength.

Based on the available triaxial test results the variation of the secant and tangent strength parameters for Aalborg University Sand No.0 can be determined by means of Equation 2.4 and Equation 2.5. The results from tests on samples with a void ratio equal 0.61 are shown in Figure 2.10. The secant and tangent friction angles are seen to decrease with increasing stresses, whereas the tangent cohesion increases. It is also seen that at a stress level of approximately $s_3 = 1000$ kPa only small changes in the strength parameters are present.

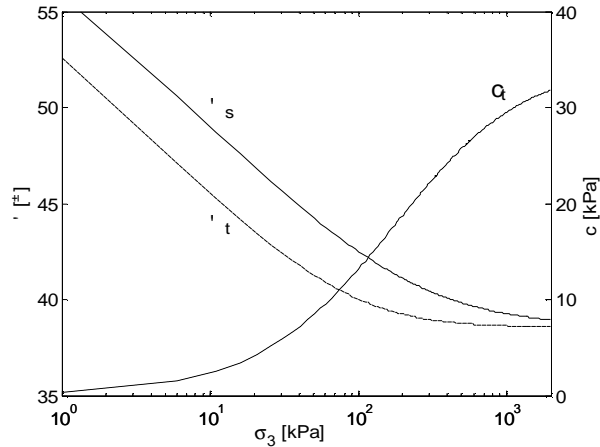


Figure 2.10 Variation of strength parameters according to the curved failure envelope proposed by Jacobsen (1970) for Aalborg University Sand No. 0. $e = 0.61$.

Using the secant or tangential strength parameters from the curved failure envelope by Jacobsen (1970), the failure envelope is plotted in Figure 2.11 using Equation 2.1. As seen the curved failure envelope fits the results from the triaxial tests at all stress levels.

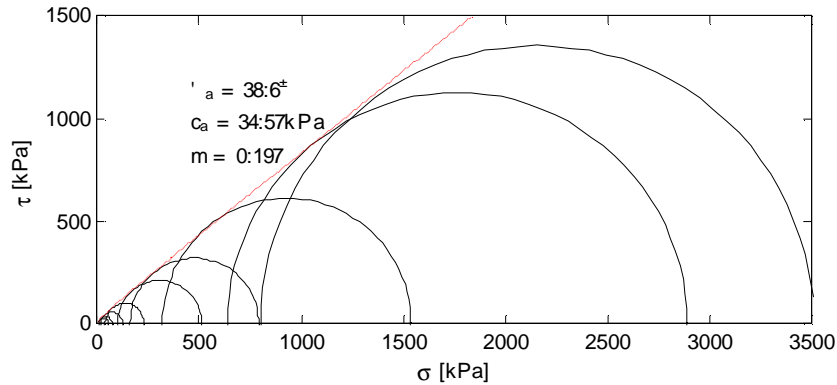


Figure 2.11 Mohr's circle at failure for tests on Aalborg University Sand No. 0, $e=0.61$ Curved failure envelope by Jacobsen (1970) is shown as dotted line.

The previous illustrations of the different strength parameters are all derived based on triaxial tests on soil specimens with an initial void ratio equal 0.61. The available material on Aalborg University Sand No.0 also consists of triaxial tests with other densities of the tested samples. The results from these additional triaxial tests are calibrated to the curved failure envelope given by Equation 2.2. The calibration is performed by Didriksen and Kristensen, (2000) for void ratios of 0.61, 0.7 and 0.85. The parameters are listed in Table 2.1.

Table 2.1 Values of strength parameters according to curved failure criterion by Jacobsen (1970) for Aalborg University Sand No.0.

e	j_a [°]	c_a [kPa]	m
0,55	41,00	19,90	0,350
0,61	38,60	34,57	0,197
0,70	34,21	40,42	0,187
0,85	30,93	7,00	0,451

The friction angles in the previous are based on the results from triaxial tests. The angles used within this thesis is therefore unless specified given as the triaxial friction angle. Sand is generally regarded as a pure friction material which means that the secant friction angle is used as representative for the soil strength instead of the tangential values. Thus the friction angle is unless specified the secant friction angle.

The tests on bucket foundations performed in the laboratory, in connection with this thesis, are all performed at low stress levels, i.e. the curvature of the failure envelope is of great importance. The strength parameters of the tested soil must therefore be given as a function of not only the compactness but as shown, also by the stress level. The curved failure envelope according to

Table 2.1 is shown in Figure 2.12, where the stress situations at failure for the performed triaxial tests on Aalborg University Sand No.0 are plotted as well. The corresponding values of the secant friction angle for different void ratios are shown in Figure 2.13.

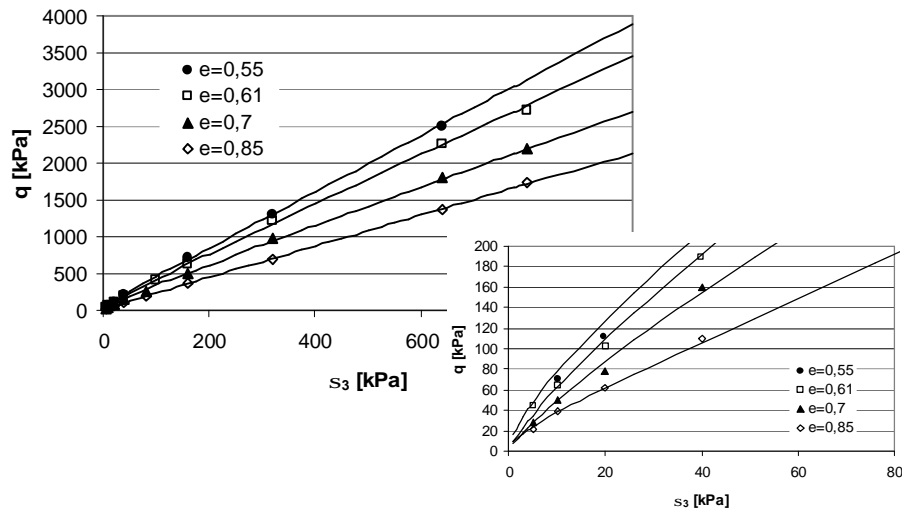


Figure 2.12 Failure envelope from triaxial tests on Aalborg University Sand No.0. The points represent the failure value from triaxial tests.

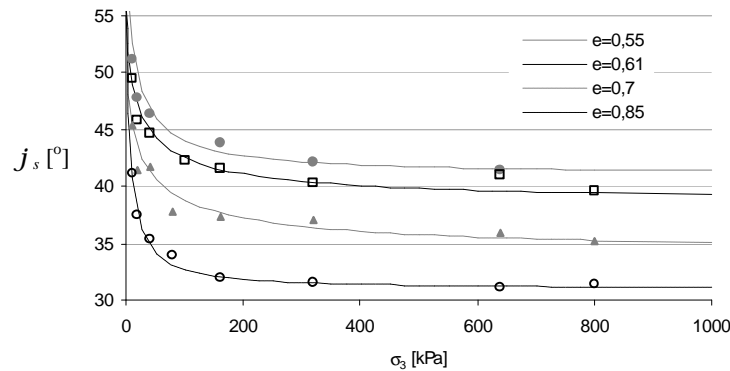


Figure 2.13 Variation of the triaxial secant friction angle for Aalborg University Sand No.0. The results from the triaxial tests are shown as points.

Based on Figure 2.13 the friction angle for Aalborg University Sand No.0 can be determined if the stress level of the problem is known. The value of the friction angle for intermediate values of the void ratio can be estimated by interpolation. Very often the stress level, i.e. the minor principal stress is not known in advance. Moreover, the stress level is also varying within the volume of soil affected by the loading. Thus the friction angle or stress level is difficult to evaluate. In the laboratory the strength parameters can in this

case for instance be determined from plate load tests. When the void ratio and the corresponding friction angle are determined, Figure 2.13 can be used to determine the mean value of the minor principal stress within the soil affected.

2.3.3. Evaluation of dilation angle

The development of the plastic deformations in e.g. ABAQUS and Plaxis are governed by a plastic potential surface. This surface is according to a Mohr Coulomb material model given as a function of the dilation angle, ψ . The rate of dilation at failure is given by the dilation angle which can be determined from Mohr's circle of strain increments in case of plane strain loading. The dilation angle is defined as follows for the triaxial case, Hansen (1958), though the meaning of this is not identical with the plane strain case.

Equation 2.6

$$\sin \psi = \frac{de_v}{de_1 - 2de_v}$$

The dilation angle determined from the triaxial tests at failure is shown in Figure 2.14. The dilation angle varies with both the void ratio and the stress level. Unfortunately no expression that describes the relation between the dilation angle and the stress level is available.

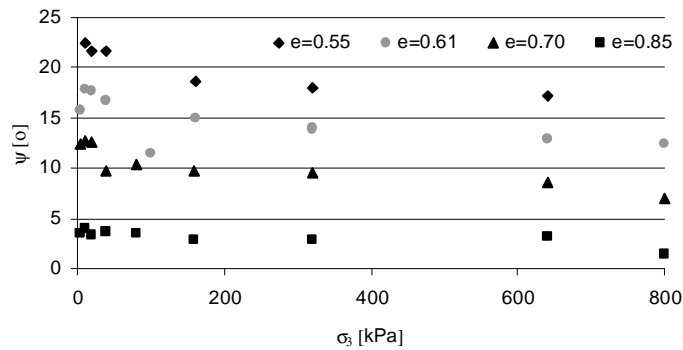


Figure 2.14 Dilation angle determined from triaxial tests on Aalborg University Sand No.0 using Equation 2.6.

Different relations for determining the dilation angle based on the shear strength are suggested in the literature. Bolton (1986) suggests a relation between the shear strength of sand and the corresponding dilation angle as follows:

Equation 2.7

$$j - j_{cs} = 0.8\psi$$

where j_{cs} is the secant angle at the critical state. The critical state is defined as the state under drained conditions where the volume, normal- and shear stresses are constant under continued shearing, Casagrande (1940). The

critical state angle is difficult to determine due to large deformations on reaching this state. The critical state angle can alternatively be determined from triaxial tests on samples with a low density and high confining pressure, where no softening after failure occurs, see Figure 2.7. In Figure 2.13 the friction angle at high stress levels and a void ratio equal 0.85 can be found to approximately 31° . The response from these triaxial tests exhibits a small amount of softening after failure, thus the critical state angle might be overestimated slightly if this angle is adopted.

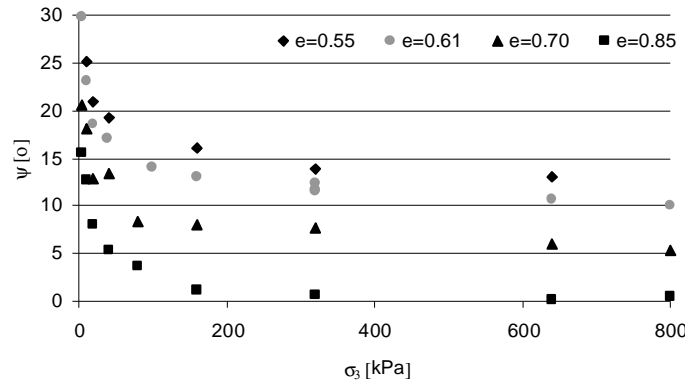


Figure 2.15 Dilation angle determined from triaxial tests on Aalborg University Sand No.0 after Equation 2.7.

From the work during the design of foundations for the East Bridge across the Great Belt between Funen and Sealand in Denmark the use of Equation 2.7 is recommended in describing the strength of sand, Steenfelt (1992). At low stress levels they found that this theory would however under estimate the soil strength if used.

Another relation between the dilation angle and the friction angle is given by use of the characteristic state angle, j_{cl} . The shear strength is proposed by Seed & Lee (1967) to be composed of mainly two components, a frictional component given by the basic friction angle of the sand grains and a dilatancy component depending on pressure and void ratio. However, a third component is present for loose sands or for sands at high pressures. That is the rearrangement and crushing of grains respectively. By ignoring the third component the dilation can be estimated by the following relation:

$$\text{Equation 2.8} \quad j = j_{cl} + \gamma$$

The characteristic state is characterized as the state where the sand goes from contraction to dilation in a triaxial test with constant confining pressure, see Figure 2.6 and Figure 2.7, Luong (1982). The characteristic state can be illustrated by the characteristic state line in a q - p plot as shown in Figure 2.16, where p is the mean effective stress.

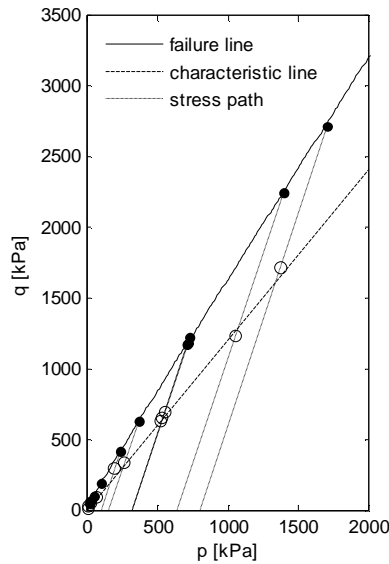


Figure 2.16

Stress paths for triaxial tests on Aalborg University Sand No.0 with samples deposited with a void ratio equal 0.61. Dots and circles indicate failure and characteristic state, respectively.

The parameter that defines the characteristic state is the characteristic state angle, j_{cl} which is determined by Equation 2.3. The characteristic state is found only to dependent of the grains in the tested sand and not the stress level as well as the void ratio, Ibsen and Lade (1998). It is however shown from true triaxial tests on the present sand to be clearly dependent of the stress path at low stress levels, e.g. Larsen and Pedersen (2001). The characteristic state angle determined from the available triaxial tests is shown in Figure 2.17.

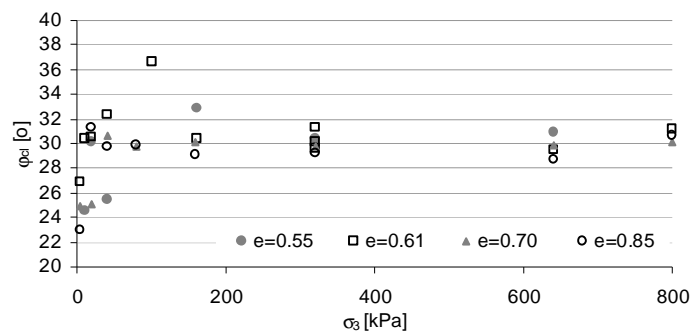


Figure 2.17 Characteristic friction angle determined from triaxial tests on Aalborg University Sand No.0

The characteristic friction angle is seen to yield a constant value equal 30° approximately, though with some scatter at low stress levels. The results from triaxial tests performed at low stress levels are generally regarded as less

reliable due to the degree of accuracy in the test setup regarding the deformations. The characteristic state angle is often assumed to be constant for all sands with a value equal 30° . The use of this value is supported from the results shown in Figure 2.17. The dilation angle evaluated from the friction angle at the characteristic state and failure using Equation 2.8 are shown in Figure 2.18.

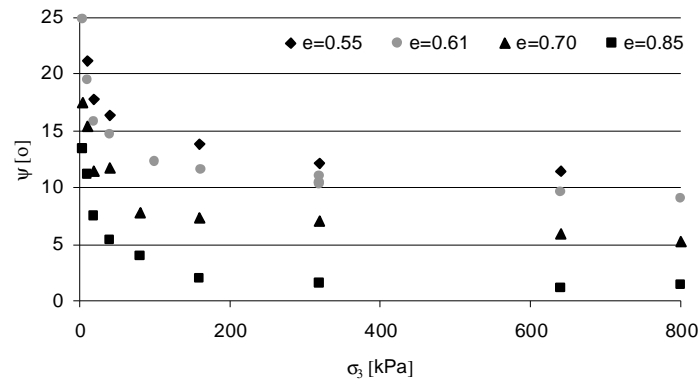


Figure 2.18 Dilation angle determined from triaxial tests on Aalborg University Sand No. 0 after Equation 2.8. $j_{cl} = 30^\circ$

The dilation angle from the two presented strength theories (Equation 2.7 and Equation 2.8) can by comparison be seen to be more stress dependent than found from the definition in Equation 2.6. The dilation angle from these two methods is generally larger than according to Equation 2.6 at low stress levels. The opposite result is seen at high stress levels. Equation 2.7 and Equation 2.8 is moreover found to yield similar results.

In a design situation a simple relation between the measured strength and the dilation angle is useful as the variation of ψ with stress level is not expressed. It is in the following chosen to calculate the dilation angle based on the difference between the friction angle and the characteristic state angle according to Equation 2.8.

2.3.4. Evaluation of elastic parameters

The elastic deformations of the soil can in e.g. a FE-simulation be calculated based on an elastic stiffness tensor containing the elastic parameters E and n , which in the triaxial case is given by:

Equation 2.9
$$E = \frac{ds'_1}{de_1} = \frac{dq'}{de_1} \quad \text{and} \quad n = -\frac{de_3}{de_1}$$

where E is the Young's modulus with dimension of stress and n is the non-dimensional Poissons ratio for an isotropic and homogeneous soil.

Poisson's ratio has been investigated for Aalborg University Sand No.0 for void ratios varying between 0.55 and 0.85. From triaxial compression tests with unloading and reloading cycles Andersen et al. (1998) found a value of Poisson's ratio for Aalborg University Sand No.0 equal 0.25 for the tested void ratios. An investigation of the Poisson's ratio of Eastern Sheldt Sand have shown that it is unaffected of the stress level as well, which is also assumed for Aalborg University Sand No. 0.

Young modulus, E_0 can be determined from triaxial tests as the initial slope of stress strain curve or from the unloading-reloading curve if measured. The stress-strain curve from triaxial test No. 9301-31 is shown in Figure 2.19 illustrating Young modulus.

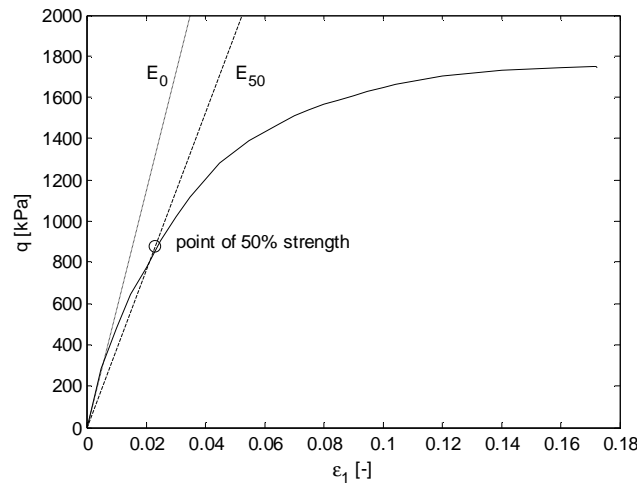


Figure 2.19 Triaxial test No. 9301-31. Young's modulus corresponding to E_0 and E_{50} are shown.

Since soil shows a nonlinear behaviour and the material is modelled as linear elastic and perfect plastic, the secant modulus E_{50} at q equal 50% strength is often used instead. Both modules are illustrated in Figure 2.19.

The elastic stiffness of soils is known to vary with the stress level and density. The stiffness' modules illustrated in Figure 2.19 from triaxial tests on Aalborg University Sand No.0 are shown in Figure 2.20 and Figure 2.21 for different void ratios.

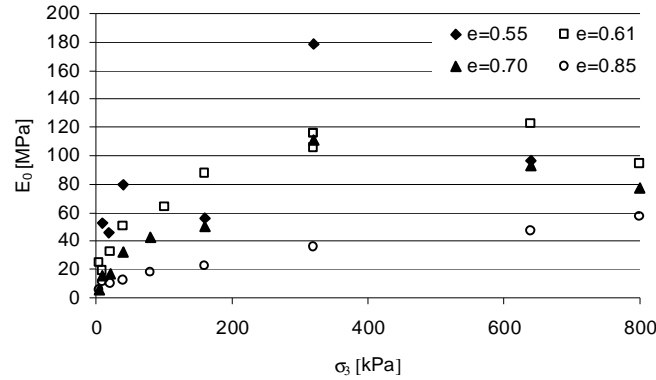


Figure 2.20 Initial stiffness modulus determined from triaxial tests on Aalborg University Sand No.0.

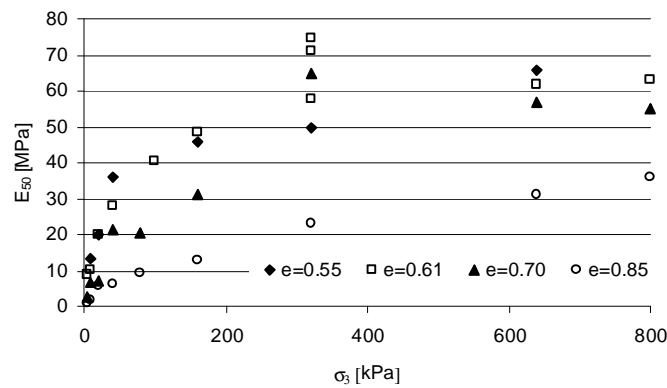


Figure 2.21 Secant stiffness modulus at 50% strength determined from triaxial tests on Aalborg University Sand No.0.

The stiffness of the soil is seen to increase with increasing stress level and compactness until reaching a constant value of σ_3 at approximately 300 kPa. It is also noticed that the stiffness is almost independent of the void ratio for the dense and medium dense samples.

2.4. Test procedure

The test procedure used in the tests on the small scale bucket foundation is described in the following. During the tests on bucket foundations displacements and forces are measured using a Spider 8 sampling device connected to a PC, see Figure 2.22.



Figure 2.22 Spider 8 Sampling device connected to a PC.

2.4.1. Preparation of the test box

The test box is after each set of experiments prepared in a systematic way to ensure homogeneity of the soil. The method used is an optimization of the method used prior to this work, and is found to result in homogenous soil samples. The density is with this optimized procedure found to deviate only minor in-between the test-boxes prepared.

Before each test the soil within the test box is prepared in the following way. The soil surface is raised by applying an extra amount of sand to the test box and a wooden frame is mounted on the top of the test box, see Figure 2.23. The purpose of this frame is to retain the additional sand and increased water level in the test box during the following preparation procedure.

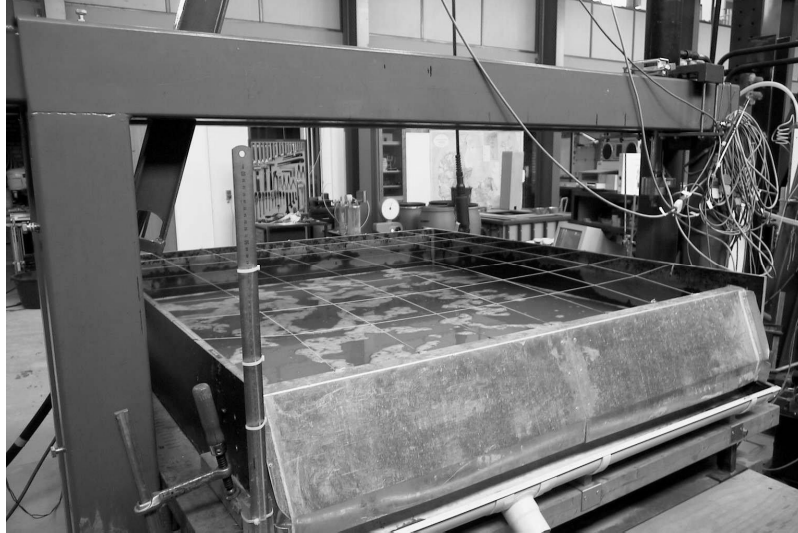


Figure 2.23 The test box ready for preparation.

The soil in the test box is at this state not homogeneous because of the interference from the prior set of experiments performed in the test box. The sand in the test box is brought to a homogenous condition by raising the water level with a vertical water flow that loosens up the sand. The water flow is applied through the perforated pipes in the drainage layer with a pressure level just below the one that causes flow channels in the sand i.e. the critical gradient. The pressure level is obtained from a reservoir located above the test box, and adjusted by a valve on the inlet pipe. The pressure level applied is measured outside the test box with a transparent tube connected to the inlet of the drainage pipes, see Figure 2.24. The water level in the test box is raised 5-10 cm above the present level of the sand surface during this phase. After this procedure the sand is vibrated with a rod vibrator twice in a systematic way, see Figure 2.25.

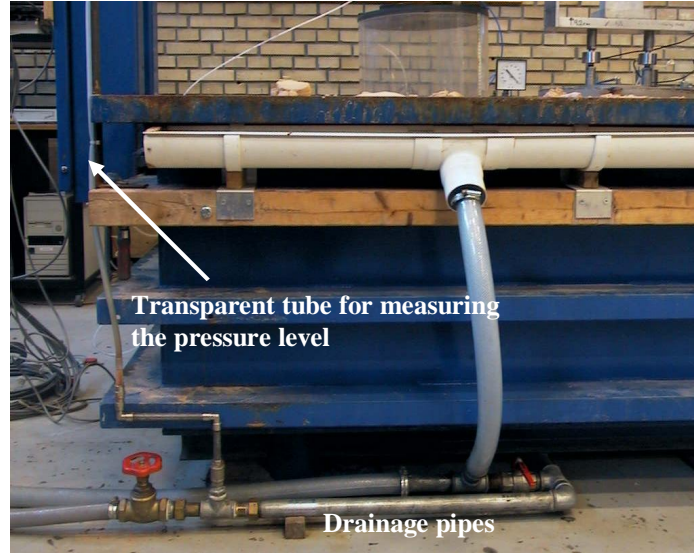


Figure 2.24 Pressure level measure.

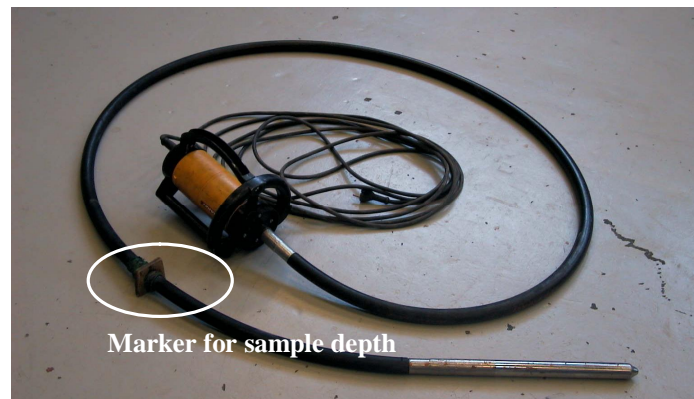


Figure 2.25 Rod vibrator used to compact the sand

The wooden frame on top of the test box is rigged with a set of strings that divide the surface into 64 equal squares, see Figure 2.23. These squares are divided into two sections where every second square forms the first section and the rest the second. All the squares in the first section are vibrated by vertical penetration of the rod vibrator into the sand. A marker is mounted on the rod to identify the boundary between sand and drainage layer during penetration. When pulling back the rod it is important to do it as gentle as possible to ensure that the rod does not leave a volume consisting of loose sand. When all the squares in the first section have been vibrated, the squares in the second section are vibrated in the same manner. The vibration procedure described above is hereafter repeated, after the sand is once again loosened by raising the water level through the drainage system. The method

used to compact the sand by use of a rod vibrator has shown not to cause separation of the grains, Rasmussen (1996).

The water level is lowered after compaction of the soil so that the surface can be adjusted to the final level. The excess water is initially removed through a hole in the wooden frame which lowers the water level corresponding to the top of the test box. The water is hereafter lowered beneath the final surface of the sand through the drainage layer with a minimum pressure level. Thus further compactness is minimized. The water level in the test box must at all time during the described procedures be kept above the drainage layer to prevent air to enter the soil through the drainage layer.

At this state the sand surface is ready to be aligned, see Figure 2.26. When the soil surface has been aligned the water level is once again raised to a level of two centimetres above the sand surface. The water is applied to the test box from above and not through the drainage layer as it is experienced that the upper part of the soil sample is loosened from this. The test box is hereafter ready for a new set of experiments.



Figure 2.26 Alignment of the soil surface after preparation.

After preparation of the test box and prior to the installation of the bucket foundation, Cone-Penetration-Tests are performed in order to estimate the characteristics of the prepared sand sample. The tests are carried out with a laboratory CPT-probe as described in appendix A. A method has been proposed to estimate the relative density, D_r and friction angle, ϕ from the cone resistance of the CPT-probe at the low stress levels present in the laboratory. This method is presented in appendix A. The relative density of each test box is investigated and is shown on the data sheets in Volume 2.

Homogeneity of sand samples

The optimized preparation procedure has shown to generate a compactness of the sand that is homogenous. That is internally and between the samples prepared. In Figure 2.27 and Figure 2.28 the CPT-response and the void ratio of the sand in test box number 0104-05 are shown. The inspections are carried out at various locations in the tests box. Only small variation in the cone resistance, q_c and the void ratio measured is seen within the test box. The void ratio is measured by excavating the sand sample in the test box to several depths. At each depth the void ratio is measured by removal of a known volume of sand which is then dried and weighted. A total of 9 CPT's at different locations are performed in the test box analyzed. The void ratio is measured at 4 different locations and 5 different depths. At each of these locations and depths 4 samples are collected. In Figure 2.28 the mean void ratio at each location and depth are shown.

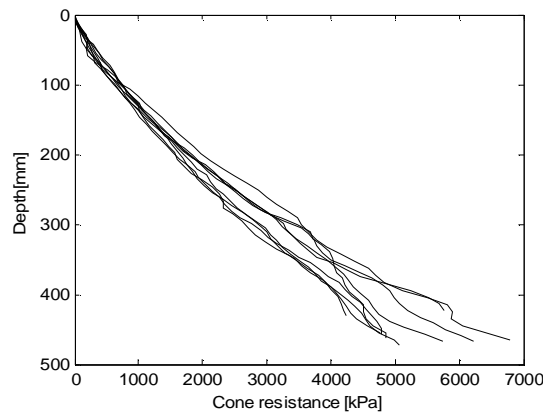


Figure 2.27 CPT-response from test box No. 0104-05

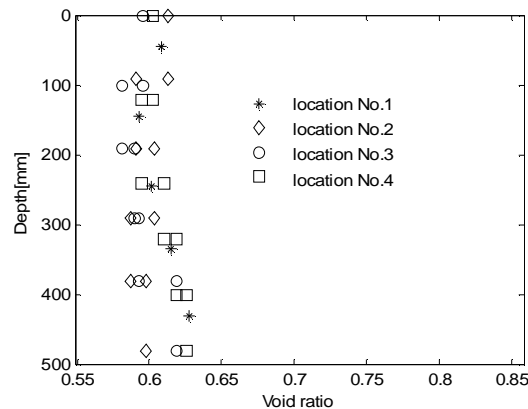


Figure 2.28 Mean void ratio measured by excavation. Test box No.0104-05

The homogeneity between the test-boxes is investigated from vertical bearing capacity tests. The tests are performed on circular surface foundations with a diameter equal 200mm. The measured vertical bearing capacities are shown in Figure 2.29 and Figure 2.30. The sand in the test box was dried out after experiment 0104-3301. In Figure 2.29 the vertical bearing capacity measured from tests in the following prepared samples are shown. The capacity is seen to increase until seven complete preparation procedures have been completed. After seven preparation procedures the measured capacities are seen to become constant equal 7100N. The estimated relative density of the sand samples tested is however not observed to be significantly influenced by the dry-out.

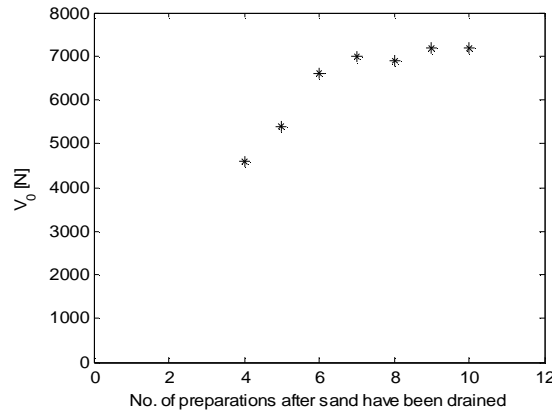


Figure 2.29 Influence of sand dry-out. $D=200\text{mm}$ and $d/D=0$.

The capacities from the performed load tests presented in Figure 2.29 are carried out with different loading velocities, i.e. dw/dt . The influence of the loading velocity is shown in Figure 2.30. Combining the results from this and Figure 2.29 shows that the bearing capacity is not affected by the loading velocity within the range examined. Hence Figure 2.29 is not influenced from this.

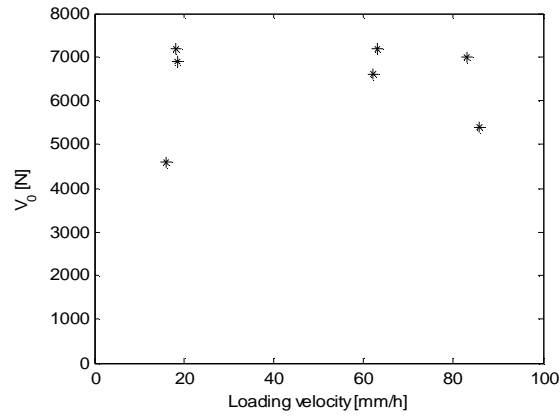


Figure 2.30 Influence of loading velocity $D=200\text{mm}$ and $d/D=0$.

2.4.2. Installation of the bucket foundation

Circular plates ($d=0$)

In the case where the skirt length is zero i.e. a circular surface foundation, the installation is carried out by locating the foundation manually on the soil surface prior to loading.

Bucket foundations ($d \neq 0$)

Bucket foundations are installed by means of an electric motor or hydraulic cylinder attached to the loading frame on test box, see Figure 2.31. An air screw is installed on the bucket lid so that the air and water inside the bucket can escape during installation. The installation velocity is minimized in order to prevent an overpressure inside the bucket. After installation the air screw is closed.



Figure 2.31 Installation of bucket foundation with hydraulic cylinder.

2.4.3. Application of vertical load

A constant vertical load is in case of tests with combined loads applied to the foundations after installation. The load is applied in three different ways depending on the size:

1. Vertical load equal to self weight.
2. Zero vertical load (Unloading of self weight is necessary)
3. Vertical load that exceeds the self weight. (Additional load is necessary)

Tests performed with a vertical load corresponding to the self weight of the bucket foundation, loading tower and the measurement devices does not involve any action in this phase. Tests carried out with zero vertical load are due to the self weight of the system unloaded by a system of pulleys, wires and loads as illustrated in Figure 2.32.

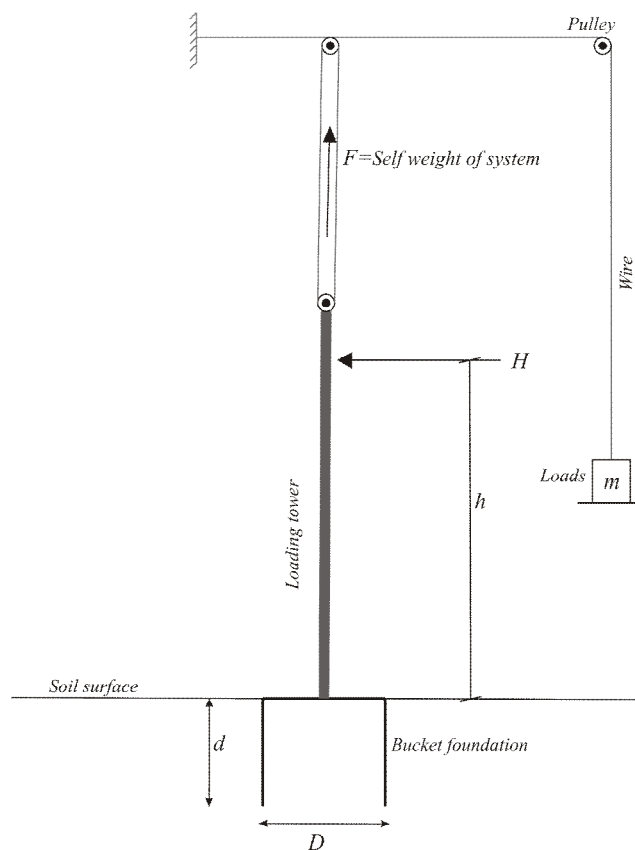


Figure 2.32 Test setup for tests with zero vertical load.

In case of tests with a vertical load that exceeds the self weight of the system, additional load is applied. This is done by applying a dead load to the bucket

without inducing a moment. The excess dead load is applied by use of a loading beam which loads the bucket only vertically, see Figure 2.33.



Figure 2.33 Excess vertical load applied by use of loading beam.

2.4.4. Loading phase.

Vertical loading tests

The vertical load applied to the bucket foundation is applied using the electric motor from the installation phase. Since the loading is displacement controlled the total response of the bucket can be determined, including the post peak response. The penetration velocity is during the loading phase kept at a rate that ensures a drained response of the bucket foundations, cf. section 2.4.1.

Combined loading tests

After application of the vertical dead load a moment and horizontal force is applied to the bucket foundation until failure is achieved. A tower is bolted to the lid of the bucket foundation, which is used to load the bucket with a constant load combination, i.e. ratio of M/H . The loads are induced by applying a horizontal load to the tower at a predefined height with an electro motor attached to the loading frame on the test box. The loading tower and electro motor are connected through a steel wire. Applying the moment and horizontal load in this way, the foundation is free to move as in nature when exposed to e.g. environmental forces from wind, wave and current. The pre as well as the post peak behaviour of the bucket foundation subjected to combined loading is measured due to the deformation controlled loading. The loading velocity is at all time kept at a rate that ensures a drained response.

A small series of experiments are loaded with a given number of cycles using pneumatic cylinders instead of an electro motor. Two pneumatic cylinders are used for some of the experiments in order to load the bucket with a moment that changes in sign, see Figure 2.33. Experiments performed prior to this work are carried out by applying ratios of M/H caused by two horizontal forces applied to the loading tower with different directions and height of impact. These experiments are reported in Larsen & Ibsen (2006a,b)

2.4.5. Measured displacements

The arrangement used to measure the displacement of the bucket foundation when exposed to combined loading is illustrated in Figure 2.34. Two vertical and one horizontal displacement transducers are used to determine the displacement of the bucket foundation according to the sign convention used, cf. chapter 1.

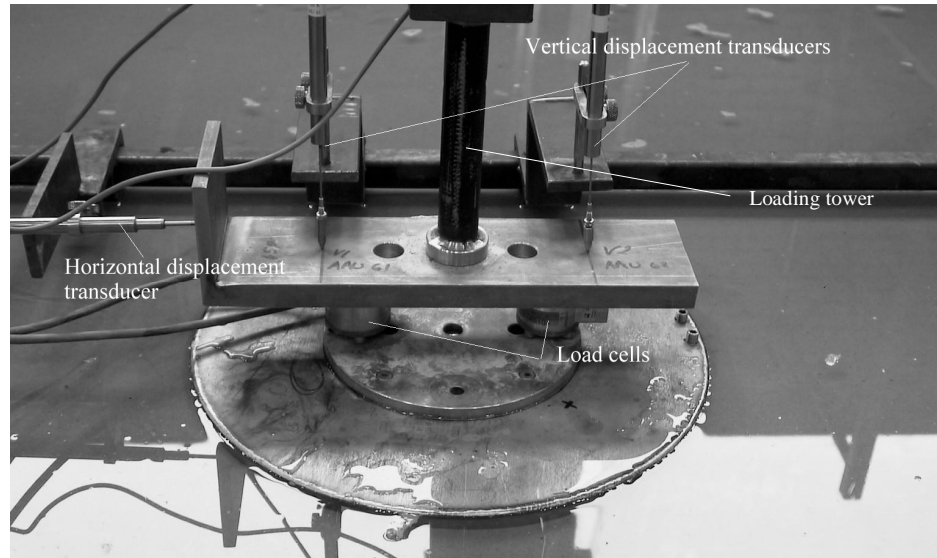


Figure 2.34 Measuring of the deformations and the moment on the foundation.

In case of pure vertical loading only the vertical displacements are measured during the loading phase. The displacement transducers are in this case located directly on bucket lid.

2.4.6. Measured forces

The moment applied to the foundation is measured by two load cells located between the bucket foundation and the loading tower, see Figure 2.34. The applied moment in case of small values of M/H , i.e. low height of impact, are however calculated from the horizontal load and height of impact. This is due to measurement errors when exposing the load cells with large shear forces. The horizontal force is measured during the experiment using a load cell on the horizontal loading device.

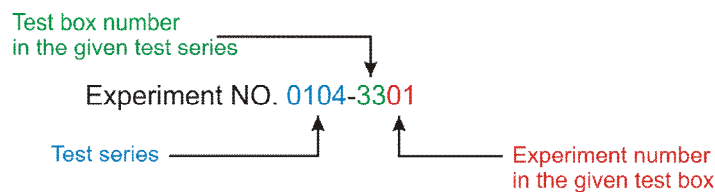
In case of vertical bearing capacity tests only the vertical force is measured during the loading phase. The force is measured using a single load cell located between the bucket lid and the loading device.

2.4.7. Test results

The test results from the loading tests performed during the work of this thesis are presented in Volume 2 of this thesis. Measured data's as well as displacements and forces according to the sign convention adopted are presented in the data sheets. Displacements and forces are tarred at the beginning of the loading phase. The tarred values are given in the data sheets as displacements and forces after the preparation phase. This phase includes

the phases where the vertical load is applied and the tower is bolted to the bucket.

The experiments are numbered consecutively according to the illustration below.



2.5. Summary

The test setup used for small scale loading tests in the laboratory is described. An optimized preparation procedure of the sand sample within the test box is proposed. The procedure has shown to generate samples that are homogenous.

The effect of complete dry out of the sand is investigated. Seven complete preparation procedures have been found necessary to obtain homogeneity between the sand samples after a complete dry out of the sand.

A penetration rate below 80mm/h is from vertical loading tests shown to entail a drained response.

The behaviour of Aalborg University sand No. 0 is investigated in order to determine the characteristics of the sand. This is to be used in connection with FE-modelling of the observed behaviour of bucket foundations. Available test results from drained triaxial tests have been used to determine the stress dependency of the characteristics. The curved failure criterion by Jacobsen (1970) has been used to describe the strength parameters according to the Mohr-Coulomb failure criterion as a function of the minor principal stress.

It is clear from the stress dependency of the characteristics that the stress level is of great importance in modelling the behaviour of bucket foundation tested in the laboratory. The Mohr Coulomb material model doesn't take into account this stress level dependency. A representative mean value corresponding to the modelled problem must therefore be used in a numerical simulation.

3. Experimental test setup (Large scale test)

A total of seven large scale loading tests are during the period of this work performed in connection with a research and development project between Aalborg University and MBD-Offshore-Power A/S. The project is described in Ibsen et al. (2005a). The test results are confidential thus only one of these tests is included in this work. The results from the test are presented in this chapter.

3.1. Large scale test

A tests program on a large scale bucket foundation has been carried out within the period of this work. The test program involves installation tests and combined loading of the bucket foundation upon failure. The test program is unique as no corresponding loading tests have ever been carried out. The large scale bucket foundation is loaded until failure and is located in natural deposited sand.

A test site in Frederikshavn in the northern part of Jutland is established within the period of this project in connection with a research and development project between Aalborg University and MBD Offshore Power A/S¹. The location of the test site is presented in chapter 1. The test site is a dammed area near the sea, see Figure 3.1. Seven large scale loading tests are performed at this test site. The bucket foundation used in the tests is shown in Figure 3.2. The skirt length and diameter of the bucket is 2 meters, i.e. $d/D = 1$ and the thickness of the skirt is 12mm. The tests are carried out with different height of impacts and with a vertical load that is small compared to the vertical bearing capacity of the foundation. These load paths, M/HD and the vertical load ratio V/V_{peak} corresponds to the small scale tests presented in chapter 2. Only results from one test are included in this thesis. The complete experiment including the installation are described and reported in Ibsen et al. (2005) and Larsen and Ibsen (2005).

¹ MBD is a research and development company established in 2001 by: Ørskov Shipyard, Bladt Industries MarCon, ELSAM and Novasion.



Figure 3.1 Test site for large scale experiments.



Figure 3.2 Bucket foundation used in large scale tests.

During installation and loading of the bucket foundation an extensively measurement program is established. The data are collected from a mobile control room using three Spider 8 sampling devices connected to a PC, see Figure 3.3.



Figure 3.3 Sampling devices and PC located in the mobile control room.

The sand at the test site consists of fine post glacial marine sand. The sand is dense naturally deposited undisturbed saturated sand and the shape of the grains is surrounded to round. The characteristics of the sand are investigated from standard classification tests according to the Danish code of practice, cf. DGF-Bulletin (2001)

The characteristics from the classification tests are determined as follows, Hansson et al. (2005).

- Mean grain size, $d_{50} = 0.16$ mm
- Coefficient of uniformity, $U = d_{60}/d_{10} = 1.47$
- Grain density, $d_s = 2.65$
- Maximum void ratio, $e_{max} = 0.962$
- Minimum void ratio, $e_{min} = 0.598$

in which index 50 represents the % quantile etc.

The soil characteristics are seen to be identical to Aalborg University Sand No.0, c.f. chapter 2.

The bucket foundation is prior to each loading test installed by applying suction to the inside of the bucket as described in chapter 1. The equipment used to create the suction inside the bucket is shown in Figure 3.4.



Figure 3.4 Equipment used for installation of the bucket foundation.

After installation a three-legged lattice tower from an old wind turbine is bolted to the bucket lid, see Figure 3.5. Each leg is bolted to the bucket through a load cell, see Figure 3.6.

The bucket foundation is after complete assembling loaded with combined loads in a similar way as for the small scale tests. The moment is induced by applying a horizontal load to the loading tower at a given height of impact. The horizontal load is applied through a steel wire and a hydraulic cylinder. The hydraulic cylinder is attached to a corresponding though stronger tower located on three circular concrete gravity foundations. The height of impact in the present test is $h = 11.6\text{m}$ and the vertical load from the self weight of the bucket foundation, measurement equipment and loading tower are 44.7 kN.

The horizontal force, H applied to the tower is measured by use of a HBM 50 kN load cell located between the loading wire and the hydraulic cylinder. The corresponding moment, M is calculated from the applied horizontal force as $M = hH$. The moment can alternatively be evaluated from the three HBM 500 kN load cells between bucket and tower, see Figure 3.6. During the present experiment problems occurred with one of these. Moreover these load cells are sensitive to shear forces. Thus the moment presented herein is calculated from the applied horizontal force.

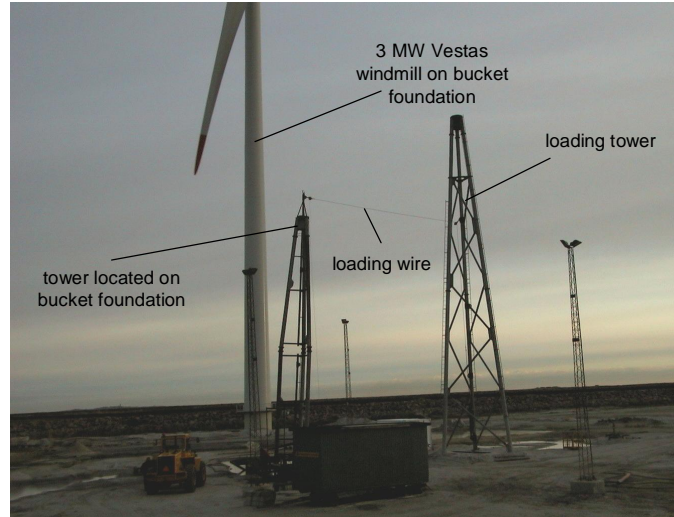


Figure 3.5 Test setup during Loading. VESTAS wind turbine located on a full scale bucket foundation is seen to the left in the picture.



Figure 3.6 Coupling between tower and bucket. Load cell are located between the green steel plates.

The displacements of the bucket are measured during loading by use of four ASM 10 meter wire position sensors. The vertical movement of the bucket is measured at three different locations with an internal angle equal 120° in the horizontal plane, see Figure 3.7. From these the vertical displacement, w and the rotation, q are calculated. The Horizontal movement of the bucket is measured at the backside of the bucket relative to the loading direction on the bucket lid, see Figure 3.7.

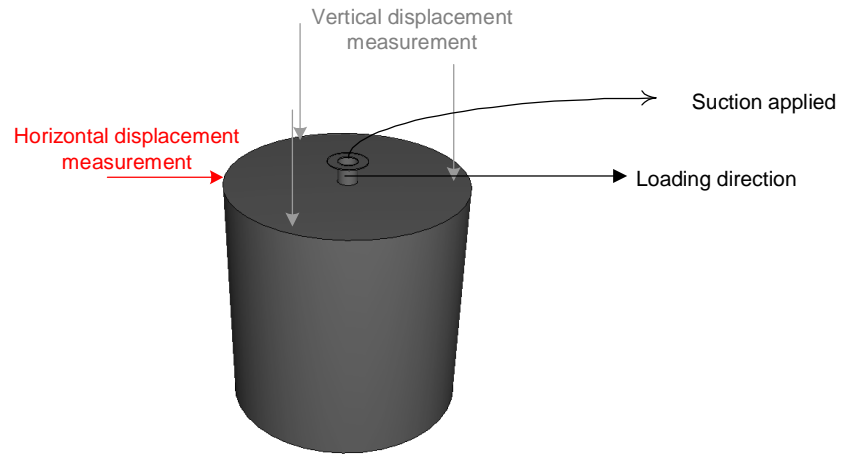


Figure 3.7 Location of displacement transducers during loading.

The measured response from the experiment is shown in Figure 3.8 to Figure 3.10, according to the sign convention used, cf. chapter 1.

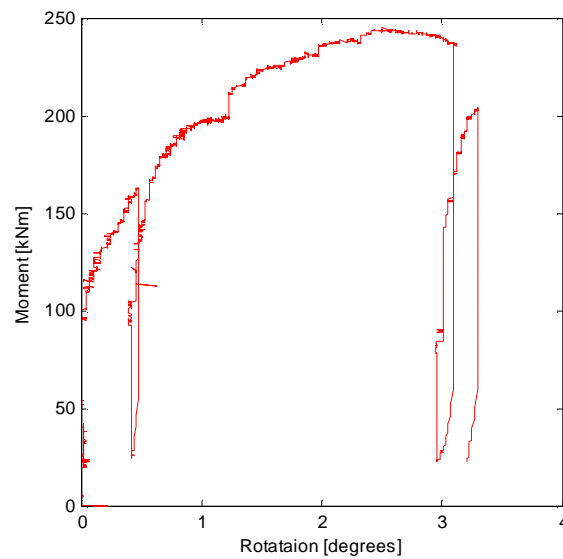


Figure 3.8 Rotation of the bucket vs. the applied moment.

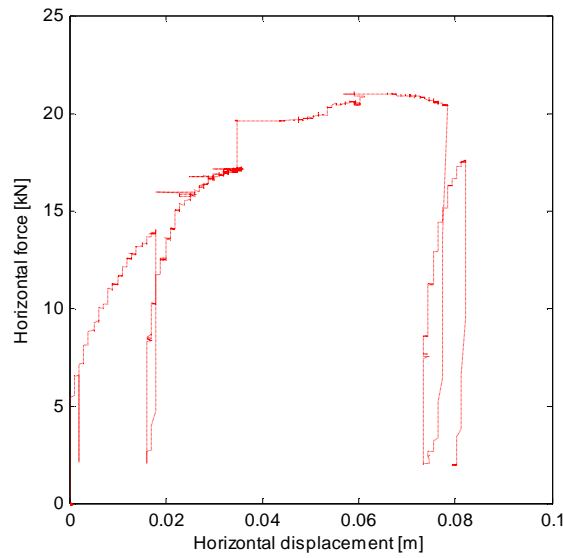


Figure 3.9 Horizontal displacement of the bucket vs. the applied horizontal force.

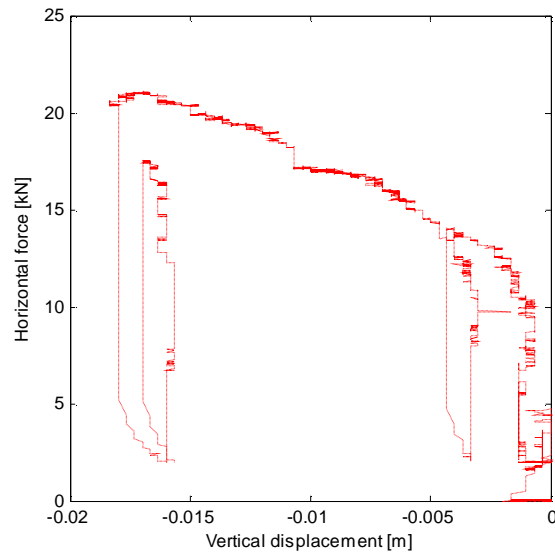


Figure 3.10 Horizontal displacement of the bucket vs. the applied horizontal force.

The rotational velocity of the bucket foundation during loading is illustrated in Figure 3.11. The mean rotational velocity after the bucket begins to move is 1.1 °/h approximately. The pore pressure near the skirt in three different depths is measured during loading of the bucket foundation. No pore pressure build up is observed during loading, thus the response is drained, Larsen & Ibsen (2005).

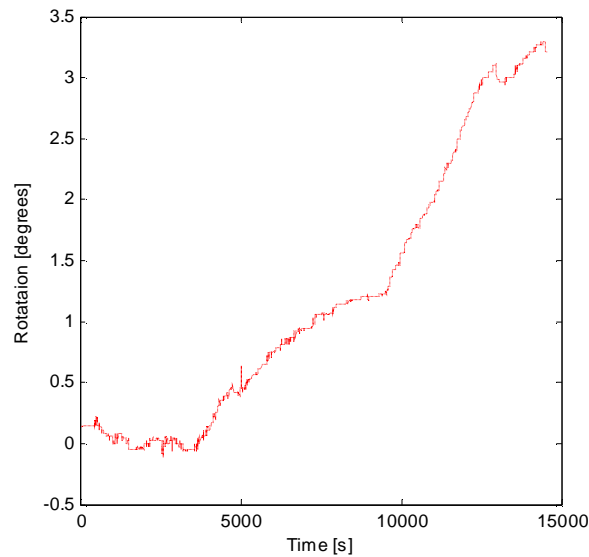


Figure 3.11 Rotational displacement vs. time during the loading phase.

The bucket foundation is after the experiment removed by reversing the installation procedure and reinstalled at another location. The bucket foundation is lifted from the sea bed by pumping in water through a hole in the bucket lid as illustrated in Figure 3.12. An overpressure equal 26 kPa was found to lift the bucket foundation.

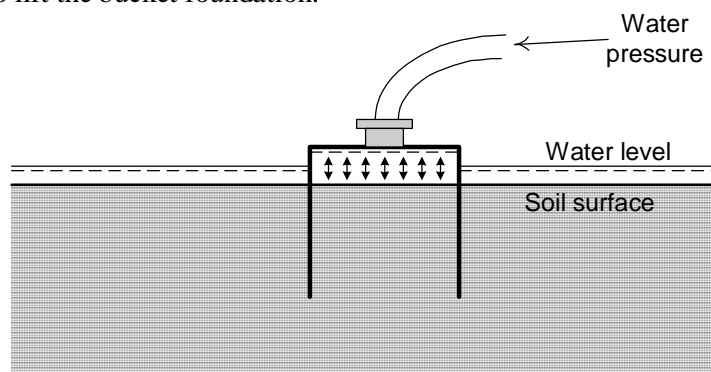


Figure 3.12 Removal procedure.

3.2. Summary

Results from a large scale loading test are presented in this chapter. The sand tested in connection with the large scale test is described from classification tests. The sand and loads applied to the large scale bucket foundation corresponds to the situation in the laboratory described in chapter 2.

4. Behaviour of bucket foundations subjected to combined loading

The behaviour of bucket foundations subjected to combined loads is only to a limited extent investigated in the literature. This chapter contains a literature study of the behaviour of bucket foundations, within the context of work hardening plasticity theory, based on static loading tests. The static and drained behaviour of both bucket foundations as well as surface footings on sand is presented.

Based on experimental investigations, different methods for modelling the behaviour and capacity of foundations subjected to combined loading are proposed in the past. The classical approach to predict the combined bearing capacity is by use of the general bearing capacity formula. In recent time the problem is often pursued by use of e.g. the finite-element-method or a macro model, where the foundation is regarded as a single element within the model. In the following the first and last method will be presented. Since only little experience is available for bucket foundations, the presentation will include relevant models for surface and embedded foundations, which are supposed to behave similar to the bucket foundations. The surface foundation is a special case of the bucket foundation i.e. $d=0$, thus this will also be included.

4.1. Combined bearing capacity “The classical approach”

The classical approach to predict the combined bearing capacity, i.e. capacity from combined loading, of a foundation is by use of Terzaghi's bearing capacity theory. Originally Terzaghi only described the bearing capacity of strip foundations subjected to a vertical and aligned load, Terzaghi (1943). In case of footings subjected to combined loading, the bearing capacity is determined by introducing shape factors, inclination factors in case of horizontal loads and effective area in case of moment loading. This modified bearing capacity is known as the general bearing capacity formula and is still today used worldwide. The general drained bearing capacity, R for cohesion

less soils is given by the following equation ignoring the friction between skirt and soil.

$$\text{Equation 4.1} \quad R = \frac{V}{A'} = \frac{1}{2} D' g' N_g^* i_g + q' N_q^* i_q d_q$$

where i is the inclination factors, d_q is a depth factor and N^* is the axis-symmetric bearing capacity factors. The values of N^* are investigated in chapter 5.

Using the inclination factors and effective area approach from e.g. Hansen (1961) the following capacity interaction solution for a circular surface footing on sand can be found, Byrne & Houlsby (1999):

$$\begin{aligned} \text{Equation 4.2} \quad \frac{H}{V_0} &= \frac{V}{V_0} \left[1 - \left(\frac{V}{V_0} \right)^{0.25} \right] \\ \frac{M}{BV_0} &= \frac{1}{2} \frac{V}{V_0} \left[1 - \left(\frac{V}{V_0} \right)^{0.5} \right] \end{aligned}$$

where V_0 is the bearing capacity under pure vertical load of a surface footing, $i_g = (1 - H/V)^4$. Equation 4.2 has been found to provide a close approximation to the observed combined capacity of circular surface footings in the laboratory, Byrne & Houlsby (1999). The solution becomes more complex in case of an embedment of the foundation or for a bucket foundation due to the overburden pressure, i.e. the N_q -term.

Besides the combined capacity given in Equation 4.2 an upper limit of the capacity is present in the case of horizontal loads given by the following equation:

$$\text{Equation 4.3} \quad H \leq S + \Delta E$$

where S is the frictional sliding resistance between the soil and the foundation base and ΔE is the difference between the passive and active earth pressures on the sides of an embedded- or bucket foundation. The friction resistance, S is quite easily estimated whereas ΔE is more complicated and is depended of the failure mode of the foundation as well as the soil stiffness and the soil strength.

The capacity from pure horizontal load, H_{peak} of a bucket foundation can be determined from the sum of the sliding resistance according to the Coulomb failure criterion and earth pressure difference on the skirt, Byrne (2000):

$$\text{Equation 4.4} \quad H_{peak} = V \tan j + \frac{1}{2} g' h^2 D (K_g^p - K_g^a)$$

where K_g^p , and K_g^a is the passive and active earth pressure coefficients respectively. Equation 4.4 is only valid in case of rupture zones in the soil, i.e. a horizontal sliding of the bucket or a point of rotation of the skirt located beneath the skirt tip in line with the skirt. The values of the earth pressure coefficients in case of plane strain conditions can be determined after the earth pressure theory by Coulomb (1776) or Hansen (1953). The conditions in connection with horizontal loading of a bucket foundation is however a complete three dimensional problem.

It is clear that for large embedment ratios the above method is not sufficient in predicting the combined bearing capacity. The contribution to the moment capacity from the active and passive earth pressures on the skirt is for instance not included.

From tests on skirted rectangular footings on loose sand, Yun & Bransby (2003) found that the sliding failure mechanism of surface footings for purely horizontal load is changed to a rotational mode when skirts are applied. The mechanism in case of pure horizontal loading is however clearly depending of the location of the reference point according to the sign convention used.

Ibsen (2002) suggests a method that involves the earth pressure on the out side of the bucket skirt from the horizontal load as well as the moment assuming a rotational failure mechanism. The earth pressures are calculated from the earth pressure theory by Hansen (1953) and are depended of the location of the point of rotation, O', see Figure 4.1. The method assumes a deformation of the bucket as illustrated in Figure 4.2 to the right.

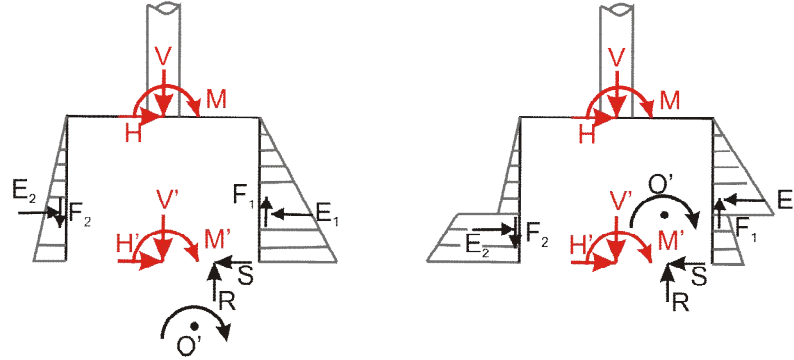


Figure 4.1 Forces acting on the bucket foundation and soil trapped within the bucket, after Ibsen (2002). (V', H', M') is loads at the base of the foundation equivalent to the loads (V, H, M) .

The combined capacity (V, H, M) of the bucket can from Figure 4.1 be evaluated by changing the location of O' until equilibrium within the system is obtained. It is noticed that the forces (V', H', M') from the turbine tower, used in the method are located at a depth corresponding to the skirt length. Thus the combined capacity (V, H, M) must be transposed according to the sign convention in chapter 1. The method assumes plane strain conditions and is modified to a three dimensional capacity by introducing a shape factor.

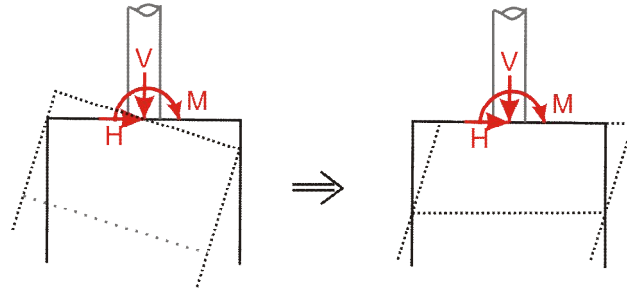


Figure 4.2 Left: True deformation of bucket, Right: Assumed deformation, after Ibsen (2002).

Equation 4.2 combined with Equation 4.3 or Equation 4.4 is seen to give a unique failure criterion for a circular surface footing which can be plotted as a fully three-dimensional failure surface. The idea of a three dimensional failure surface in this connection was originally suggested by Roscoe & Schofield (1956). Butterfield & Ticof (1979) were among the first to investigate the capacity of strip footings on dense sand in this manner. They found that an elliptical cigar shaped failure surface could capture the measured data of a strip footing (both surface and embedded), see Figure 4.3. In order to get a non-dimensional plot Butterfield & Ticof (1979) suggested that the failure values are to be normalized by the vertical bearing capacity, which is also used in Equation 4.2.

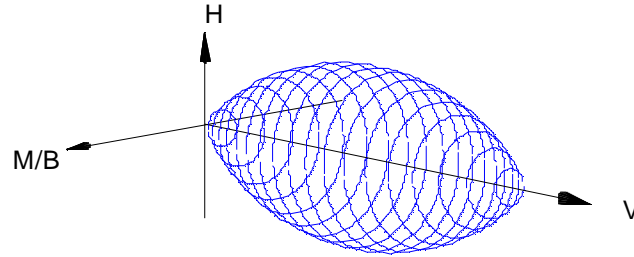


Figure 4.3 Illustration of failure surface, after Butterfield & Ticof (1979).

From experiments they found that the end slopes of the failure surface in the $(H; V)$ -planes are identical for the surface foundations as well as for the embedded. This is illustrated in Figure 4.4 as the angle between the H -axis and the failure surface at intersection, δ° . Further more they found that the end slope at the intersection with the V -axis at pure vertical load, i.e. V_{peak} is $3/2$ the end slope at small vertical load, see Figure 4.4.

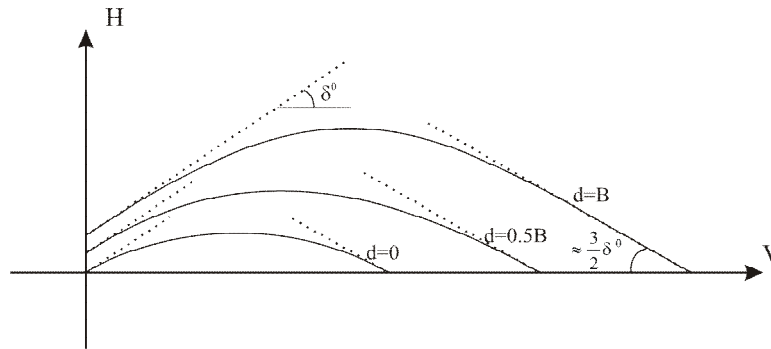


Figure 4.4 Experimental observations from vertical capacity tests with rectangular foundations, after Butterfield & Ticof (1979).

The overall shape of the failure surface in Figure 4.3 is later supported by results from several other experimental investigations on both strip, rectangular and circular foundations as well as spudcans and to some extent bucket foundations in the $(H/V_{peak}; V/V_{peak})$ and $(M/BV_{peak}; V/V_{peak})$ planes. In the $(M/BV_{peak}; H/V_{peak})$ planes the failure surface is found to approximately follow a rotated ellipsoid, e.g. Zaharescu's (1961), Butterfield (1981), Georgiadis & Butterfield (1988), Georgiadis (1993), Gottardi & Butterfield (1993), Byrne & Houlsby (1999), Gottardi et al. (1994), Gottardi et al. (1999), Tan (1990) and Cassidy (1999).

The $(M/B; H/)$ or $(M/BV_{peak}; H/V_{peak})$ planes are often denoted the radial plane, the deviatoric plane or the π -plane. These denominations are randomly used in the literature.

The classical approach is limited to predict the capacity of foundations subjected to combined loads and not the behaviour prior to failure. In the following section a model that is capable of describing the entire behaviour are described. The introduction of a failure surface as shown in Figure 4.3 is however the first step necessary in developing such a model.

4.2. Combined behaviour of bucket foundations

“The macro model approach”

A modern approach to the combined load problem is within the concept of strain hardening plasticity theory, often denoted macro models or force resultant models. The foundation is within this approach regarded as a macro element subjected with force resultants and corresponding deformations according to the sign convention used, cf. chapter 1. From a macro model the displacements and rotation of a foundation can be calculated if the load path is known, i.e. the pre-peak behaviour can be predicted in contrary to the classical approach. Further more the model can be implemented in to a numerical model with any structure attached to the foundation so that the interaction between structure and a single or multiple foundations can be investigated.

A complete Macro model requires the following components when the complete behaviour is desired:

- A yield surface restrained by a failure criteria or surface.
- A hardening law which defines how the yield surface expands or contracts.
- A flow rule which defines the plastic displacements at yield.
- An elastic model which defines the elastic displacements.

From the work by Roscoe & Schofield (1956) and Butterfield & Ticof (1979) the first step in creating a macro model for foundations was born with the investigation of the failure surface presented in section 4.1. Later complete macro models for footings on clay were developed by Martin (1994) and denoted Model A and Model B. These models has since been altered according to the drained behaviour of footings on sand and is known as Model C. Model C is described in details by e.g. Gottardi et al. (1999), Houlsby & Cassidy (2002) and Cassidy et al. (2002). Model C is based on loading tests on a rough rigid flat circular footing resting on dry dense Yellow Leighton-Buzzard sand reported in Gottardi & Houlsby (1995).

For a given combination of V, M and H a current yield surface is created in the corresponding load space. Any changes in these loads inwards the yield surface is assumed only to create elastic displacements, specified by a set of

elastic components. A change in the loads outward or along the yield surface however creates both elastic and irreversible plastic displacements. If the change in load is directed outward from the yield surface, an expansion of the yield surface occurs given by the hardening law. The size of the yield surface during expansion is in Model C assumed to be controlled by the vertical plastic deformation w_p , i.e. the model is of the strain hardening type. The size and ratio of the plastic displacements are given by a flow rule, that in Model C is linked directly to the yield surface i.e. associated flow is assumed.

During loading of the foundation the deformations are continually calculated by the principle of superposition. The total deformations are calculated as the sum of the elastic and plastic components:

$$\text{Equation 4.5} \quad \begin{bmatrix} dw \\ dq \\ du \end{bmatrix} = \begin{bmatrix} dw_e \\ dq_e \\ du_e \end{bmatrix} + \begin{bmatrix} dw_p \\ dq_p \\ du_p \end{bmatrix}$$

where index e and p indicates elastic and plastic.

The following sections contain a literature review of experimental observations leading to information's regarding the individual components within the macro model approach for bucket foundations (including surface footings) on sand. The general behaviour of bucket foundations is found to be similar to flat footings, Byrne (2000). This is consistent with the capacity observations made by Butterfield & Ticof (1979), presented in section 4.1. The Model C is therefore in the literature proposed as a basis model for a macro model for the bucket foundations.

4.2.1. Elastic behaviour

The elastic behaviour of a circular foundation subjected to planar loading can be described by the following general elastic matrix according to the sign convention used, see appendix C.

$$\text{Equation 4.6} \quad \begin{bmatrix} V / GR^2 \\ H / GR^2 \\ M / GR^3 \end{bmatrix} = \begin{bmatrix} K_{VV}^0 & 0 & 0 \\ 0 & K_{HH}^0 & K_{HM}^0 \\ 0 & K_{HM}^0 & K_{MM}^0 \end{bmatrix} \begin{bmatrix} w / R \\ u / R \\ q_M \end{bmatrix}$$

where R is the radius of the foundation, G is the shear modulus of the soil and K_{ij}^0 are the non-dimensional static stiffness components.

The static stiffness components for surface-, embedded- and bucket foundations have been theoretically investigated by e.g. Spence (1968),

Poulos & Davies (1974), Bell (1991), Ngo-Tran (1996), Doherty & Deeks (2003 and 2006), Doherty et al. (2005) and Liingaard (2006). The static stiffness components are found to depend of the poissons ratio, the shear modulus, the embedment ratio, i.e. d/D , stiffness of the foundations relative to the stiffness of the soil and the base roughness. In appendix C the static stiffness components relevant for the bucket foundation tests in connection with this work are presented.

The shear stiffness, G of the soil is stated by Houlsby & Cassidy (2002) to be one of the most difficult parameters to establish for the model. They suggest the following formula (Janbu 1963) to calculate the shear stiffness as a function of the effective vertical stress beneath the foundation.

Equation 4.7

$$\frac{G}{p_a} = g \sqrt{\frac{V}{pR^2 p_a}}$$

where p_a is the atmospheric pressure and g is dimensionless constant which is found to approximately 400 for dense sand and is expected to depend mildly on the relative density. Alternatively G can be determined from tests e.g. triaxial tests, CPT's or loading tests with the foundation.

4.2.2. Yield surface

The shape of the yield surface for different foundation types have been investigated experimentally, especially within the last decade. The tests performed during the investigation of the yield surface for different types of foundations in the literature are mainly of the type “swipe test”. During swipe tests the foundation is loaded with a predefined vertical load before loading in the radial plane. During loading in the radial plane the vertical displacement is kept constant while constraining the foundation along a predefined horizontal and rotational displacement path. The proposed models assume a hardening of the yield surface that is controlled by the vertical plastic settlement of the foundation. It is furthermore assumed that the maximum vertical preload, V_{pre} applied to the foundation is linked directly to the vertical plastic settlement alone. Tan (1990) argues based on this assumption that if the vertical stiffness is large compared to the plastic, the displacement path in this case is close to a track across the yield surface at a given penetration or preload. Since the elastic response is much stiffer than the plastic, the stress path will almost exactly follow the shape of the failure locus, as negligible expansion of the failure locus will be required to balance the small elastic deformations ($w_{total}=0 \Rightarrow dw_e = -dw_p$).

The shape of the yield surfaces presented in the following can be expressed by the following general empirically equation.

Equation 4.8

$$f = \left(\frac{H}{h_0 V_{pre}} \right)^2 + \left(\frac{M}{m_0 D V_{pre}} \right)^2 - 2a \left(\frac{H}{h_0 V_{pre}} \right) \left(\frac{M}{m_0 D V_{pre}} \right) - F(V, V_t, V_{pre}) = 0$$

where f describes a yield surface corresponding to the shape of the failure surface presented in the previous section and V_t is the tension capacity of the bucket foundation. The general shape of the surface is determined by the three parameters h_0 , m_0 and a in the radial-planes. The parameters h_0 and m_0 determines the size of the yield surface at the widest section of the surface along the V-axis by $H_{M=0}/V_{pre}$ and $M_{H=0}/D V_{pre}$ respectively. Where $H_{M=0}$ is the value of H at intersection with the $M=0$ axis and $M_{H=0}$ is the corresponding value for M . $H_{M=0}$ and $M_{H=0}$ is also denoted H_{peak} and M_{peak} respectively. The section that defines the parameters is given as the ratio $v=V/V_{pre}$ at the peak of the parabola along the V-axis. The eccentricity parameter, a determines the rotation of the ellipse in the radial planes. An example of the complete three dimensional shape of a rotated yield surface after Equation 4.8 is shown in Figure 4.5 for a circular surface footing.

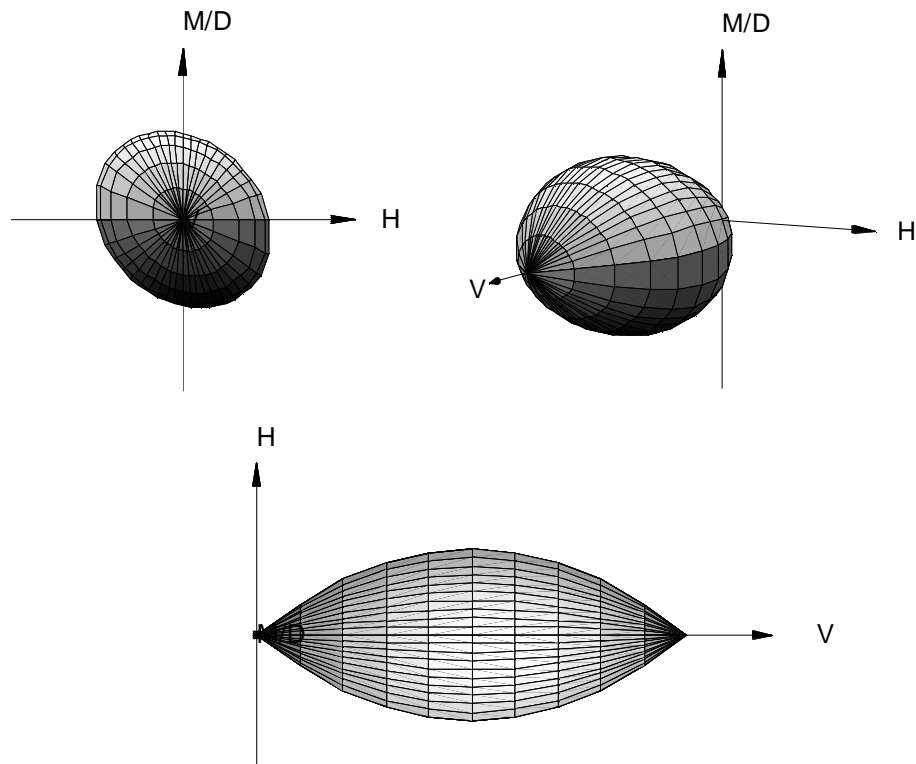


Figure 4.5 Illustration of yield surface for a surface footing shaped as a parabola and rotated ellipse, according to the expression of f from Byrne and Houlsby (1999).

The eccentricity parameter, a is from the experimental results presented in this section found to be negative with the sign notation used in Equation 4.8. The influence from the eccentricity parameter on the shape of the yield surface in the radial plane is illustrated in Figure 4.6 and Figure 4.7. From the figures it can be seen that the parameter not only rotates the ellipse but also stretches the surface in the second and fourth quadrant. It is also noticed that a value equal -1 is a limiting value since the shape changes radically for values below this.

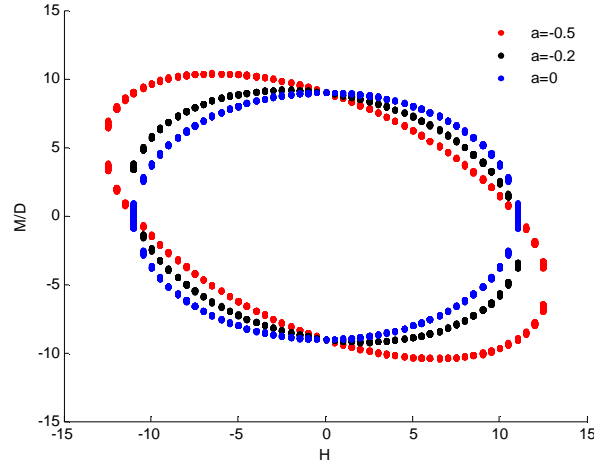


Figure 4.6 Influence of a on the yield surface, in the radial plane. $h_0=0.11$ $m_0=0.09$, $V=0.5V_{pre}$ and $V_{pre}=100$ [F]

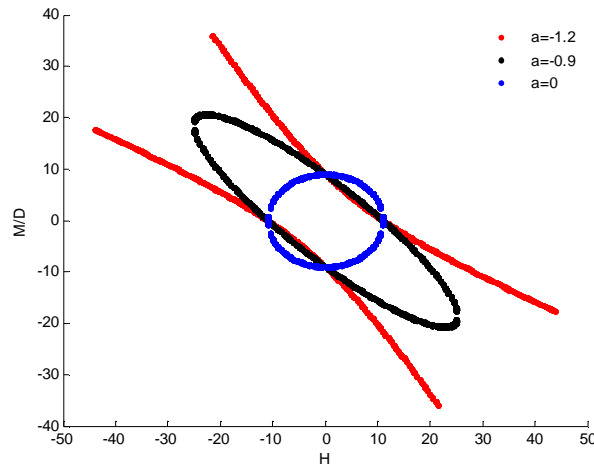


Figure 4.7 Illustration of the limitation on the value of a . $h_0=0.11$ $m_0=0.09$, $V=0.5V_{pre}$ and $V_{pre}=100$ [F]

Gottardi & Houlsby (1995) were among the first to investigate the full behaviour of circular footings on sand in the laboratory under combined loads within the macro model approach. The tests were performed on dense dry sand ($D_r=75\%$). The experiments are interpreted by Gottardi et al. (1997/99) who suggested an expression of $F(V, V_b, V_{pre})$ given in Table 4.1. Cassidy (1999) modified this expression by introducing a set of curvature factors, b_1 and b_2 . The function by Cassidy (1999) is used in the Model C and is adopted from the work by Martin (1994) concerning combined loading of spudcans on soft clay and is shown in Table 4.1 as well. A slight tendency was found from

tests on spudcans in sand that these b -factors varied with the load path given by the ratio HD/M , *Cassidy (1999)*. He though suggested using constant values due to few tests.

A large set of combined loading tests on bucket foundations in very dense sand ($D_r=95\%$) are evaluated by Byrne & Houlsby (1999) and Byrne (2000). They found that the shape of the yield surface in this case, also could be approximated by rotated ellipses in the radial-planes. The rotation of the yield surface as well as the shape was found to change with the embedment ratio. Adopting the yield surface expression suggested by Gottardi et al. (1997/99) this results in a change in parameters with the embedment ratio.

The yield surface functions presented clearly have one draw back, relative to the behaviour of bucket foundations. The apex of the yield surface at low vertical load for bucket foundations is not located at the origo in contrary to surface foundations. The yield surface of a bucket foundation will not intersect the V-axis at zero vertical load, but at a negative value due to the tension capacity. This is also noticed by Villalobos et al. (2004) and Villalobos et al. (2005). They suggested a modified yield function by introduction of a dimensionless constant, t_0 , see Table 4.1. The constant t_0 is proposed to be a function of the skirt thickness, t relative to the diameter of the bucket. The apex of the yield surface at low vertical load is especially of great importance for wind turbine foundations, due to the small self weight of the structure. The yield surface expression by Villalobos et al. (2005) are based on experiments on bucket foundations with a single embedment ratio equal 0.5 on saturated medium dense sand. Villalobos et al. (2004) based their observations from the results of experiments with bucket foundations with two different embedment ratios (0.5 and 1) on loose ($D_r=30\%$) dry sand.

Table 4.1 Yield surface expressions from literature relative to Equation 4.8.

Reference	$F(V, V_t, V_{pre})$	Foundation type tested
Gottardi et al. (1997/99)	$16 \left(\frac{V}{V_{pre}} \right)^2 \left(1 - \frac{V}{V_{pre}} \right)^2$	Circular surface footings.
Martin (1994) adopted by Cassidy (1999) for surface footings and Byrne & Houlsby (1999) for bucket foundations	$b_{12} \left(\frac{V}{V_{pre}} \right)^{2b_1} \left(1 - \frac{V}{V_{pre}} \right)^{2b_2}$ where $b_{12} = \left(\frac{(b_1 + b_2)^{b_1 + b_2}}{b_1^{b_1} b_2^{b_2}} \right)^2$	Circular surface- and bucket foundations with $d/D = [0; 0.16; 0.33;$ $0.66]$ $D = 100\text{mm}$
Villalobos et al. (2005)	$\left(\frac{b_{12}}{(t_0 + 1)^{(b_1 + b_2)}} \right) \left(\frac{V}{V_{pre}} + t_0 \right)^{2b_1} \left(1 - \frac{V}{V_{pre}} \right)^{2b_2}$ $t_0 = 0.064 \text{ for } D/t = 86$ $t_0 = 0.04 \text{ for } D/t = 200$	Bucket foundations $d/D = 0.5,$ $D = [200; 293]\text{mm}$

The curvature factors, b_1 (low stresses) and b_2 (high stresses) in Table 4.1 allow adjustments to the parabolic shape of the yield surface along the V axis in order to fit the experimental data. The choice of b_1 and b_2 determines the value of $v = b_1 / (b_1 + b_2)$, i.e. the location of the peak of the parabola along the v -axis as well as the slope of the ends of the parabola, see Figure 4.8. b_{12} are merely defined so that h_0 and m_0 retain their original meanings. The value of b_1 and b_2 is generally found to be close to but less than 1. Values of b_1 and b_2 less than unity reduces the sharp angles of the yield surface at the intersections with the V -axis, see Figure 4.8. The values of b_i are limited by a value equal 1.0 as the failure surface for larger values becomes concave. For $b_1 = b_2 = 1$ the yield surface is seen to coincide with the expression from Gottardi et al. (1997/99) and the widest section in the radial plane is located at $v = 0.5$. The value of v is in the literature generally found to be between 0.45 and 0.5 for surface footings, i.e. $b_1 < b_2$. This is in contrast to observations from tests, from which the slopes of the yield surface at the apex's indicate that $b_2 < b_1$, e.g. Butterfield & Ticof (1979), Byrne & Houlsby (1999) and Gottardi et al. (1999).

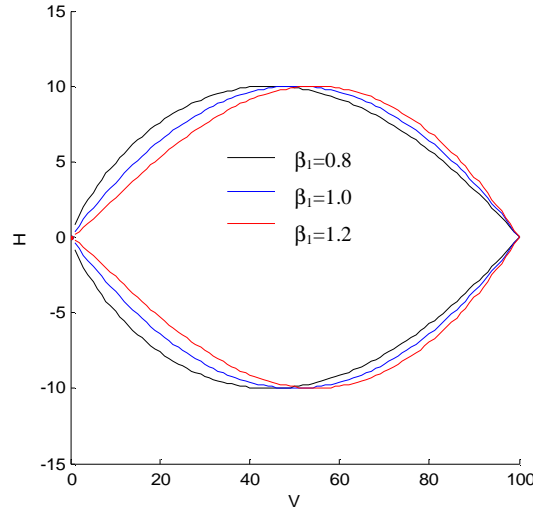


Figure 4.8 Influence of curvature factors on the shape of the yield surface. $b_2=1.0$ and $M=0$ -plane

For surface footings Houslsby and Cassidy (2002) suggests that the expression from Martin (1994) is simplified by choosing $a=0$ and $b_1 = b_2 = 1$ which will corresponds to observations from by Butterfield and Ticof (1979). Also Byrne (2000) comments that the introduction of the b -factors is not appropriate for surface footings, as the slight improvement of the fit was observed not to alter significantly the general trend.

In Model C the yield surface is assumed to be constant in shape (Gottardi et al. 1997/99). Byrne & Houslsby (1999) however found that for circular surface footings on dense sand the shape changed with the vertical preload ratio, V_{pre}/V_0 . This change was fitted to the following expression:

$$\text{Equation 4.9} \quad \begin{aligned} h_0 &= h_{0,peak} \left(1 - 0.36 \ln \left(\frac{V_{pre}}{V_0} \right) \right) \\ m_0 &= m_{0,peak} \left(1 - 0.36 \ln \left(\frac{V_{pre}}{V_0} \right) \right) \end{aligned}$$

where $h_{0,peak}=0.11$ and $m_{0,peak}=0.08$ corresponding to the yield surface at peak bearing capacity. Equation 4.9 are validated for $0.025 > V_{pre}/V_0 < 1$.

The value of h_0 and $h_{0,peak}$ is from tests on bucket foundations in dense sand found to be enhanced significantly with an increase in the embedment ratio whereas the value of m_0 is found not to be affected from the embedment ratio, Byrne (2000).

This variation is also investigated for circular surface footings resting on loose sand by Byrne & Houlsby (2001) and Byrne (2000) who found a linear relation between the value of h_0 and the vertical settlement of the footing, w as given in Equation 4.10. The same behaviour was noticed by Tan (1990), though based on tests with moments that according to Byrne (2000) might be different from zero. No significant change in m_0 nor vertical peak bearing capacity was observed from these tests. Thus the variation observed can not directly be compared to Equation 4.9. Similarities are though noticed as the vertical preload is linked directly to the vertical plastic settlement and the vertical bearing capacity is linked to the diameter of the footing in Model C.

$$\text{Equation 4.10} \quad h_0 = 0.138 + 0.093 \frac{w}{D}$$

The eccentricity parameter, a is by comparing the results from tests with surface footings by Byrne (2000) on loose sand and Gottardi et al. (1997/99) on medium dense sand, found to depend on the vertical settlement of the foundation, Byrne (2000). The vertical settlement during the experiments is due to the loose sand tested significantly larger for the tests by Byrne (2000). As seen in Table 4.2 this (larger settlement) gives a decrease in a , i.e. an increased rotation of the yield surface in the radial plane.

From tests with surface footings on dense sand a value of a is found to -0.06 Byrne (2000). This differs significantly from the observations made by Gottardi et al (1997/99) on dense sand and Byrne (2000) on loose sand who found a value of approximately -0.25. The experiments on dense sand by Byrne (2000) are performed at a low preload ratio, V_{pre}/V_0 whereas the others are performed at a high value. Based on this Byrne (2000) states that it is likely that a is a function of V_{pre}/V_0 as well.

The values of $m_{0,peak}$, $h_{0,peak}$ and a derived from tests with bucket foundations in dense sand by Byrne (2000) can be seen in Table 4.2. The influence on these from the vertical settlement presented above can be compared with a similar dependence from d/D for the bucket foundations as seen in Table 4.2. Comparing the results from Byrne (2000) with Villalobos et al. (2005) and Byrne & Houlsby (2001) a dependence of D_r and V_{pre}/V_{peak} are also observed for bucket foundations.

The experimentally observed values of the yield surface parameters defined by Equation 4.8 from the literature are summarized in Table 4.2.

Table 4.2 Survey of results from combined small scale loading tests on footings and bucket foundations on sand.

Exp type and sand tested	Reference	b_1	b_2	ν	h_0	m_0	a
Strip footing surface and embedded. (Failure)	Butterfield & Ticof (1979)			0.5	0.12 d/D=0	0.10 d/D=0	
					0.18 d/D=0.5	0.14 d/D=0.5	
Dense sand					0.23 d/D=1	0.16 d/D=1	
Rectangular surface foundations (Failure)	Gottardi and Butterfield (1993)				0.12	0.09	
Rectangular footings L/B=5 (Failure)	Butterfield & Gottardi (1994)				0.13	0.088	-0.22
Dense sand Circular plates Medium dense sand $D_r=75\%$ High preload ratio	Gottardi et al. (1997/99)	1	1	0.5	0.1213	0.090	-0.2225
					$h_{0,peak}$ 0.11 for d/D=0	$m_{0,peak}$ 0.08 for d/D=0	-0.06 for d/D=0
Circular plates and Bucket foundations	Byrne (2000)				0.15 for d/D=0.17	0.074 for d/D=0.17	-0.25 for d/D=0.17
Very Dense sand $D_r=95\%$ Low preload ratio	Based on exp from Byrne & Houlsby (1998/2000)	1 for d/D=0	1 for d/D=0		0.17 for d/D=0.33	0.074 for d/D=0.33	-0.75 for d/D=0.33
					0.13 for d/D=0.66	0.09 for d/D=0.66	-0.93 for d/D=0.66
Circular plates -Vertical failure Based on exp from Byrne & Houlsby (1998/2000)	Byrne & Houlsby (2001) and Byrne (2000)	0.82/ 0.75	0.82/ 0.75		0.154/ 0.1505	0.094/ 0.089	-0.25/ -0.3
Loose dry sand $D_r=6\%$ Embedded to d/D=0.4 High preload ratio	Bold values is to be used together with Equation 4.19						
Bucket foundations d/D=0.5 Medium dense sand $D_r=75\%$ Low preload ratio	Villalobos et al. (2005)	0.99	0.99	0.5	0.337	0.122	-0.75

The experimental fitted value of a in Table 4.2 for relevant experiments is compared in Figure 4.9 with the change in embedment ratio.

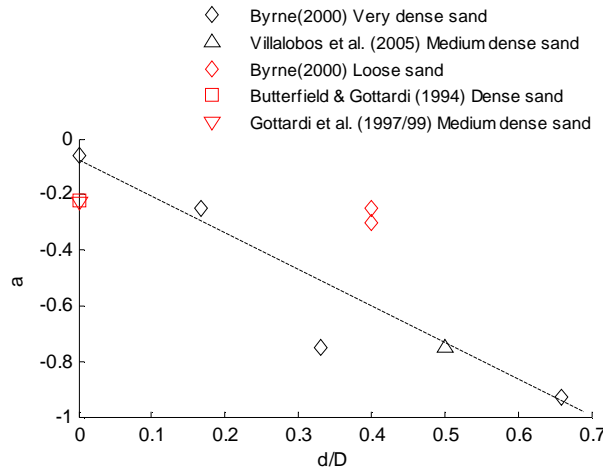


Figure 4.9 Variation of the eccentricity parameter for bucket-, surface and embedded foundations. Black colour indicates tests at low preload ratio and red tests at high.

From Figure 4.9 it can be seen that there seems to be a good relation between the embedment ratio and the eccentricity factor, a determined from tests on dense sand and with a low preload ratio, V_{pre}/V_{peak} . With exception of $d/D=0.33$ a linear relation is observed. This linear relation can clearly not continue due to the limiting value of a as explained earlier. For tests performed at large preload ratios the eccentricity factor seems to be unaffected of the embedment ratio. No information is available regarding the preload ratio for these experiments.

A similar comparison regarding the variation in $h_{0,peak}$ and $m_{0,peak}$ are shown in Figure 4.10.

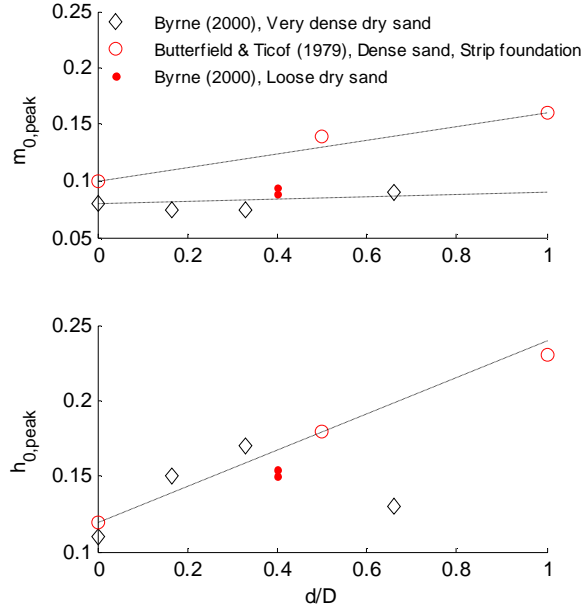


Figure 4.10 Variation of yield surface parameters for skirted and embedded foundations. Black colour indicates tests at low preload ratio and red tests at high.

From Figure 4.10 the variation of $m_{0,peak}$ is seen to be only slightly depended of the embedment ratio for the tests with the bucket foundations whereas an increase is seen for the skirted strip foundations. The variation of $h_{0,peak}$ is seen to follow the same linear tendency for the presented experiments with exception of the bucket tests with and embedment ratio of 0.66. No conclusion of the dependency of the preload ratio can be drawn at this point.

From the yield surface parameters by Byrne (2000), Byrne & Houlsby (1999) illustrated the change in shape of the yield surface with the embedment ratio by the normalized variables defined in Equation 4.11. The change in shape is illustrated in Figure 4.11.

$$\text{Equation 4.11} \quad h = \frac{H}{V_{peak} h_0 b_{12} v^{b_1} (1-v)^{b_2}}$$

$$m = \frac{M}{DV_{peak} m_0 b_{12} v^{b_1} (1-v)^{b_2}}$$

The Normalized variables in Figure 4.11 are seen to be almost independent of d/D for the loads relevant to offshore wind turbines, i.e. loads in the first or third quadrant. Whereas a significant change is observed in the second and fourth quadrant, with elongation of the surface. Furthermore the rotation of the normalized yield surface is seen to increase by the change in a .

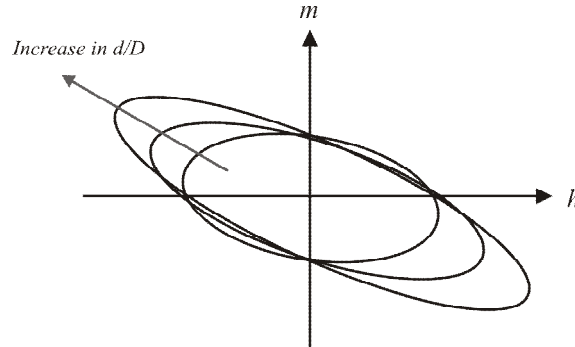


Figure 4.11 Experimental observed shape of normalized yield surface for bucket foundations, after Byrne and Houlsby (1999).

4.2.3. Failure surface

During loading of the foundation, the yield surface will expand until a stress level corresponding to an ultimate failure state is reached. This state can be expressed as a failure surface in the load space of force resultants. For a load state located on the failure surface the ultimate combined bearing capacity of the foundation is reached, and no further expansion of the yield surface will occur. Outside the failure surface, no loads can be sustained. If the formulas for the yield surface are used to describe the failure surface the size is merely related to the vertical peak bearing capacity instead of the vertical preload. The failure surface is in the literature also denoted the outer yield surface, whereas the expanding yield surfaces is denoted the inner yield surfaces.

Byrne & Houlsby (1999) found that the yield surface during expansion is actually not constant in shape as initially suggested by Gottardi et al. (1997) and used in Model C, but changes in a consistent way with the ratio V_{pre}/V_{peak} . This change corresponds well with the observed change in yield surface parameters controlling the shape in the radial plane as outlined previously. The change in shape is according to Byrne & Houlsby (1999) due to the dilatant behaviour of sand. The dilatant behaviour is specially pronounced at low preload ratios, as is the case of offshore wind turbine foundations. Based on their observations they suggest a hardening of the yield surface relative to the failure surface occurring according to Figure 4.12, for circular footings on dense sand in the (H, V) or $(M/D, V)$ planes. The yield surface is found to intersect the failure surface at low preload ratios as illustrated in the figure.

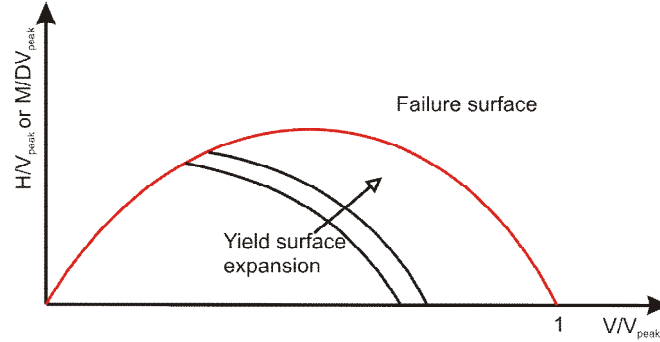


Figure 4.12 Observed yield surface hardening of circular surface foundations, after Byrne & Houlsby (1999)

The expansion of the yield surface in Model C with constant shape until failure is illustrated in Figure 4.13. Thus the observed variation of the yield surface parameters is neglected in the figure. The yield surface and failure surface are drawn using the expression for the yield surface after Cassidy (1999) in Table 4.1. Although this is not identical to the hardening observed by Byrne & Houlsby (1999) reasonable accordance with the behaviour outlined in Figure 4.12 is seen. The change in the yield surface as illustrated in Figure 4.12 is usually neglected, Houlsby (2003).

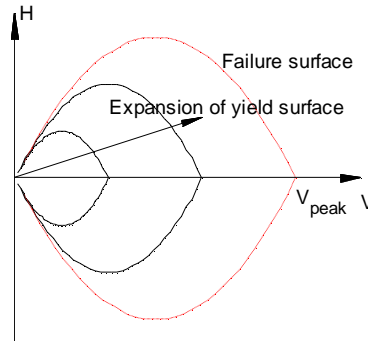


Figure 4.13 Illustration of the yield surface expansion of circular foundations in Model C.

Based on a limited number of experiments on bucket foundations located in loose dry sand ($D_r=20\%$) Byrne et al. (2003) found an approximately linear relation between the applied loads at failure. The experiments were performed with a small ratio of V/V_{peak} on a single bucket with a diameter of 293mm and an embedment ratio of 0.51. The values of $M/(DH)$ during the tests was held constant at 0.5, 1 and 2, corresponding to a height of impact at 150, 300 and 600 mm respectively. The density as well as the type of sand is not given for these experiments, i.e. the value of V/V_{peak} is not known. They found that the following linear relation would fit the experimental observations.

Equation 4.12

$$\frac{M}{D} = \left(f_1 + \frac{f_2}{k} \right)^{-1} (V + f_3 W)$$

where $k=M/(DH)$ is the ratio of moment to horizontal load and $W=1/4pD^2dg'$ is the weight of the soil plug inside the bucket. The parameters that fits the observations was found to $f_1=3.03$, $f_2=1$, $f_3=0.64$. The third parameter represents proportion of the soil plug weight mobilized under the action of moment loading.

Based on the results from Byrne et al (2003) and Byrne (2000) on bucket foundations values equals $f_1=3.26$, $f_2=1.073$ and $f_3=0.71$ are suggested by Byrne & Houlsby (2003). The tests are carried out on loose and dense sand respectively, thus the failure parameters are not suspected to be identical in the two cases as a dependency of D_r is observed. Only the parameters proposed by Byrne et al (2003) are compared with measured capacities in the references.

From the above observations it is clear that any vertical ballast on the structure is of great importance on the moment bearing capacity especially at low V/V_{peak} .

Equation 4.12 is seen to differ from the full three dimensional failure criteria used in the macro model with the absence of V_{peak} . Further more the observed influence on the peak parameters in the failure criteria presented in section 4.2.2 are not included. This is the embedment ratio and relative density of the soil.

Vertical bearing capacity

A special case of the combined loading is the situation where the foundation is loaded purely in the vertical direction ($H=M=0$), i.e. the upper apex of the complete three dimensional failure surface. The pure vertical bearing capacity, V_{peak} can be calculated by the general bearing capacity formula in Equation 4.1. The vertical bearing capacity is an important component in the macro model approach and is investigated for bucket foundations in chapter 5.

Tensile vertical capacity

The lower apex of the yield and failure surface is in most of the presented studies assumed to be located directly at the origo, since neither a horizontal or moment load can be sustained by a surface footing. This is however not the case for bucket foundations, where the earth pressure on the sides of the foundation will contribute to the horizontal and moment capacity, even at zero vertical load. The apex of the failure surface, i.e. intersection with the V-axis must therefore be given as the tensile capacity of the bucket foundation. If the

hardening of the yield surface is assumed to be isotropic and with constant lower apex this will also be the case for the expanding yield surfaces.

Whereas it is reasonable to assume that the vertical, moment and horizontal capacity of a bucket foundation is similar to an embedded foundation, the tensile capacity must clearly be different. Hence the friction resistance between soil and steel on the outside as well on the inside of the skirt to some extent are mobilized. The tensile capacity can be calculated assuming a limiting shear stress between the soil and skirt described by the coulomb failure criterion. This leads to a tensile capacity of a bucket foundation as follows:

$$\text{Equation 4.13} \quad V_t = \frac{g' d^2}{2} (K \tan d)_o (pD_o) + \frac{g' d^2}{2} (K \tan d)_i (pD_i)$$

where index o indicates the outside and i the inside of the bucket. K is the lateral earth pressure coefficient and d is the friction angle between the skirt and the soil.

When a vertical force is subjected to the bucket directed upwards, the stresses near the skirts are reduced due to the frictional forces further up the skirts. This change is not accounted for in Equation 4.13, and the tensile capacity is therefore non conservative. In order to account for this, Houlsby et al. (2005) suggests that the tensile capacity is calculated using the following formula.

$$\text{Equation 4.14} \quad V_t = g' Z_0^2 y_0 \left(\frac{d}{Z_0} \right) (K \tan d)_o (pD_o) + g' Z_i^2 y_i \left(\frac{d}{Z_i} \right) (K \tan d)_i (pD_i)$$

$$Z_i = \frac{D_i}{4(K \tan d)_i}$$

$$\text{where} \quad Z_0 = \frac{D_0(m^2 - 1)}{4(K \tan d)_o}$$

$$y_j \left(\frac{d}{Z_j} \right) = e^{-\left(\frac{d}{Z_j} \right)} - 1 + \left(\frac{d}{Z_j} \right)$$

where m defines the distance over which the stresses is reduced outside the foundation relative to the outer diameter, i.e. mD_o . Houlsby et al. (2005) suggests a value of m and $K \tan d$ at 1.5 and 0.7 from an analysis of laboratory tests given in Kelly et al (2004) on dense sand ($Dr=80\%$). Another proposal is given by Houlsby et al (2006) from a large scale test on dense sand ($Dr=80-85\%$), who suggests a value of m and $K \tan d$ of 2.0, and 1, respectively.

The tensile capacity after Equation 4.13 and Equation 4.14 is only valid as long as the contribution from the inside friction not exceeds the weight of the soil within the bucket, i.e. the soil plug. Thus in this case the inside friction is replaced by the weight of the soil plug.

4.2.4. Hardening law

During loading of the foundation the size of the yield surface at a given load state is given by the hardening law. Within the macro model approach the size is assumed to be controlled by the vertical preload of the foundation, i.e. the upper apex of the yield surface. The type of hardening law presently used is the strain hardening type, where the relation between the vertical plastic settlement and the vertical preload is used.

The relation between the vertical preload and the corresponding vertical plastic settlement can be determined from a pure vertical loading test. At all time the actual vertical load is equal to the vertical preload, in case the foundation is not unloaded during the entire test. In the following some proposal on how to describe this relation empirically is presented.

A linear relation is proposed by Byrne & Houlsby (1999) given by the following equation.

$$\text{Equation 4.15} \quad V_{pre} = k_p w_p$$

where k_p is the plastic stiffness which is assumed to be constant, w_p is the plastic component of the vertical settlement. This hardening law will result in a linear load-deflection curve for a vertical loading test which is well known not to be the case for soils. Hence this relation is not useful in practise.

Based on the results from vertical loading tests on circular surface footings on medium dense ($D_r=75\%$) and dry 14/25 yellow Leighton Buzzard Sand, Gottardi et al. (1997/99) fitted the following empirical expression.

$$\text{Equation 4.16} \quad V_{pre} = \frac{k w_p}{1 + \left(\frac{k w_{pm}}{V_{peak}} - 2 \right) \left(\frac{w_p}{w_{pm}} \right) + \left(\frac{w_p}{w_{pm}} \right)^2}$$

where k is the initial plastic stiffness and w_{pm} is the size of the vertical plastic settlement at failure.

Houlsby & Cassidy (2002) expanded this relation in order to describe not only the pre-peak behaviour but also the post-peak.

Equation 4.17

$$V_{pre} = \frac{k w_p + \left(\frac{f_p}{1-f_p} \right) \left(\frac{w_p}{w_{pm}} \right)^2 V_{peak}}{1 + \left(\frac{k w_{pm}}{V_{peak}} - 2 \right) \left(\frac{w_p}{w_{pm}} \right) + \left(\frac{1}{1-f_p} \right) \left(\frac{w_p}{w_{pm}} \right)^2}$$

where the post peak behaviour is described by the factor f_p which is a dimensionless constant that describes the magnitude of vertical load upon failure as a proportion of V_{peak} (that is $V_{pre} = f_p V_{peak}$ for $w_p = 0$), see Figure 4.14. If post-peak work softening is not essential a value of $f_p = 0$ can be chosen. Then the value of V_{pre} will go towards zero for w_p going towards infinity, which will lead to the relation by Gottardi et al. (1997/99).

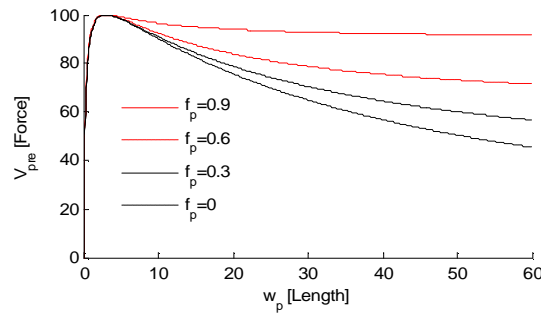


Figure 4.14 Illustration of hardening law including post peak behaviour.

Cassidy et al (2002) found that the following relative simple relation fits the results from vertical loading tests of circular footings on loose carbonate sand reported by Byrne & Houlsby (1998/2001):

Equation 4.18

$$V_{pre} = \frac{c w_p + k_2 w_p^2}{k_1 + w_p}$$

where c , k_1 and k_2 are constants.

Calculating the vertical preload as a function of the vertical plastic settlement solitarly is found to be too simple a relation. Byrne (2000) and Byrne & Houlsby (2001) found that the hardening of the yield surface is a function of the complete plastic displacements rather than the vertical solitarly. Based on their results they proposed a hardening law given by the following formula.

$$\text{Equation 4.19} \quad V_{pre} = f(x_p) = f(w_p + C_1|u_p| + C_2|Dq_p|)$$

where the constants is found to $C_1=0.5$ and $C_2=0.2$ in connection with the corresponding yield surface parameters in Table 4.2 (Bold values). Byrne & Houlsby (2001) suggests the use of Equation 4.18 as hardening law by replacing w_p with the weighted sum of the plastic displacements, x_p in Equation 4.19.

Though the relation given by Equation 4.19 is supported by experiments the hardening law as merely a function of w_p is generally supposed to be adequate in practical situations using the macro models, Cassidy et al. (2002) and Houlsby (2003).

4.2.5. Flow rule

During loading of a foundation when yielding occurs, the hardening rule determines the stiffness of the response, whereas the ratios between the plastic displacement components are determined by the flow rule. The plastic displacements including rotation are determined from a potential function by the flow rule given in the following formula.

$$\text{Equation 4.20} \quad \begin{bmatrix} dw_p \\ du_p \\ dq_p \end{bmatrix}_p = \lambda \begin{bmatrix} \frac{\partial g}{\partial V} \\ \frac{\partial g}{\partial H} \\ \frac{\partial g}{\partial M} \end{bmatrix}$$

where $g=0$ is a potential function and λ is a positive scalar that defines the magnitude of the plastic displacements, and is determined from the hardening law. The potential function is defined as a function that forms a potential surface in the load space on which the direction of the incremental plastic displacements is perpendicular.

If the potential function is chosen to be identical to the yield function this is denoted associated flow and non-associated flow otherwise. For circular footings on sand associated flow is observed in the radial planes and non-associated flow in the planes along the V -axis for both dense and loose sand. The same behaviour is observed for embedded- and bucket foundations as well, Gottardi et al (1997/99), Byrne & Houlsby (1999/2001), Byrne (2000) and Villalobos et al. (2004/2005).

Since associated flow is only observed in the radial plane the potential surface must differ from the yield surface in all terms containing V or V/V_{pre} . Houlsby and Cassidy (2002) suggest a non-associated potential function described as a modification of the yield function, by introducing an association parameter, a_v in the following way.

Equation 4.21

$$g = \left(\frac{H}{V' h_0} \right)^2 + \left(\frac{M}{V' m_0 D} \right)^2 - 2a \frac{H}{V' h_0} \frac{M}{V' m_0 D} - a_v^2 b_{34} \left(\frac{V}{V'} \right)^{2b_3} \left(1 - \frac{V}{V'} \right)^{2b_4} = 0$$

where...

$$b_{34} = \left(\frac{(b_3 + b_4)^{(b_3 + b_4)}}{b_3^{b_3} b_4^{b_4}} \right)^2$$

V' is the intersection of the plastic potential with the V -axis, determined by $g=0$, and is comparable with V_{pre} for the yield surface. The value of the b -factors can be chosen independently of the corresponding factors in the yield surface expression. It is noted that associated flow is obtained if $a_v = 1$, $b_1 = b_3$ and $b_2 = b_4$.

The association parameter a_v has two purposes:

1. It controls the relative magnitude of the vertical displacement. ($a_v > 1$ i increase in w_p)
2. It controls the position of the parallel point, defined by Tan (1990), which is the peak of the potential surface. For a_v less than unity the parallel point is moved to a lower value of V/V_{pre} .

The parallel point is defined as the point on the yield surface at which the foundation can rotate or move sideways at constant vertical load and constant vertical deformation. The parallel point describes the transition between heave and settlement of the foundation and for footings where sliding will occur.

Within the macro model approach the parallel point plays an important role regarding the plastic displacements, which is similar to the critical state in constitutive modelling of soils. The parallel point defines the peak value of the potential surface in the V -planes. At this point the increment in the plastic vertical settlement is zero due to the definition of the parallel point ($dw=0$ and $dV=0$ i $dw_e=0$ i $dw_p=1 dg/dV=0$).

It is noticed that the parallel point is in fact only linked to the failure surface since it only appears at large deformations, Byrne (2000).

The location of the peak relative to the apex of the potential surface, $v_{pp}=V_{pp}/V'$ is easily determined by the Equation 4.22, whereas the location relative to the apex of the yield surface, $z=V_{pp}/V_{pre}$ is very complex. Cassidy (1999) suggests a numerical method to compute the relation between the apexes of the potential- and yield surface, V/V_{pre} at a given load state from which z can be determined.

$$\text{Equation 4.22} \quad v_{pp} = \frac{V_{pp}}{V'} = b_3 / (b_3 + b_4)$$

where V_{pp} is the value of V for the parallel point at a given load state. It is clear that the location of the parallel point given by v_{pp} is independent of the association factor α_v . The location relative to the vertical preload given by z though can be found to depend on this as well as the values of the b -factors and the present load state. This is illustrated in Figure 4.15 in the (H, V) -plane, where it is seen that the location of the parallel point given by z is seen to decrease, i.e. moving left in the figure for an increase in α_v . Two potential surfaces with different association factors are plotted in the figure at a load state given by the same intersection with the yield surface.

In the special case where $a_v = 1$ and $b_1=b_3$ and $b_2=b_4$ or $b_1=b_2$ and $b_3=b_4$ the peak of the yield surface and the parallel point coincides i.e. $z = v_{pp} = b_1 / (b_1 + b_2)$.

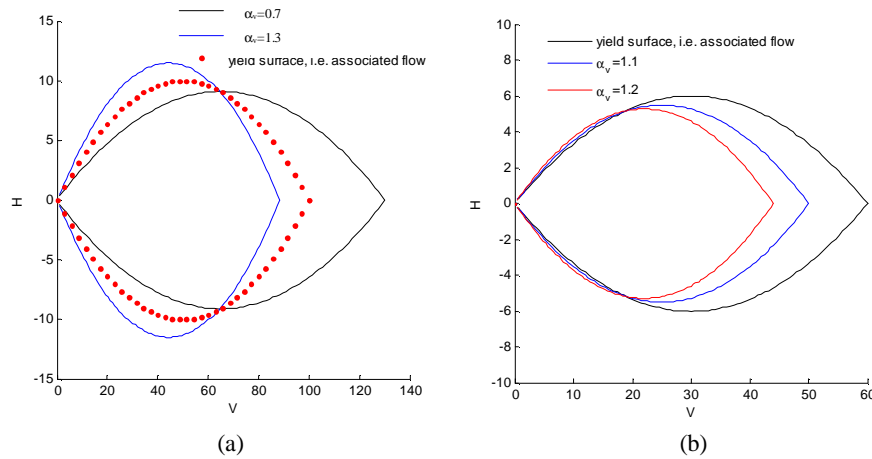


Figure 4.15 Illustration of the change in parallel point with the change in α_v in the $M=0$ -plane. $b_1=b_2=b_3=b_4=1$ (a) $V_{pre} = 130 [F]$ and (b) $V_{pre} = 60 [F]$

The association factor α_v is shown to determine the location of the parallel point for a given stress state. The same effect can be obtained by changing the

b -values differently from the yield function. The influence of the β -values on the shape of the potential surface is shown in Figure 4.16. From the figure it can be seen that the size of the b -factors changes the location of the peak on the surface and the inclination at intersections with the V -axis. A value of b_3 less than 1 gives a smoother crossing with the V -axis near the origin whereas this is the case for b_4 at the large apex i.e. V' . If a value of b_3 is chosen smaller than b_4 the value of v_{pp} i.e. the parallel point is seen to move to a lower value of z , i.e. left on the figure and opposite.

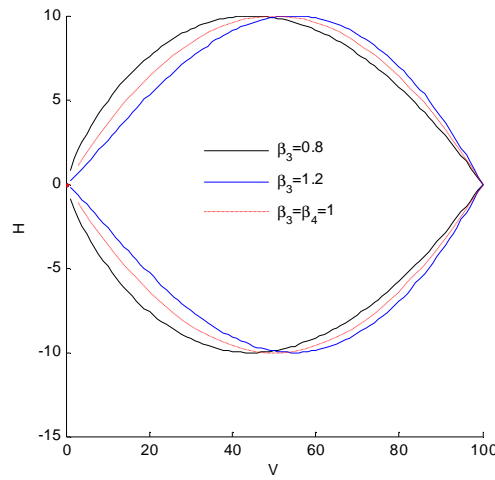


Figure 4.16 Illustration of the change in the shape of the potential surface with the change in b_3 . $b_4=1.0$, $a_v=1$ and $M=0$

The location of the parallel point given by z , if a_v is different from unity and the b -values are all different, becomes as mentioned earlier very complex. Which is a major drawback of the model since this point is very important in modelling the true behaviour.

Cassidy (1999) pointed out that Equation 4.21 is not capable of modelling both the magnitude of the vertical displacement and the location of the parallel point, v_{pp} correct with only one association factor. He therefore suggested that two association factors a_h and a_m is used instead in the following way.

Equation 4.23

$$g = \left(\frac{H}{V' h_0 a_h} \right)^2 + \left(\frac{M}{V' m_0 D a_m} \right)^2 - 2a \frac{H}{V' h_0 a_h} \frac{M}{V' m_0 D a_m} - b_{34} \left(\frac{V}{V'} \right)^{2b_3} \left(1 - \frac{V}{V'} \right)^{2b_4} = 0$$

where the two association factors enables the shape of the plastic potential surface to change in the radial plane corresponding to an increase in h_0 and m_0 which reduces the radial plastic displacements relative to the vertical.

Experimental investigations have shown that the location of the parallel point is different for pure horizontal loading and pure moment loading, i.e. the location is depended on the load path followed, Byrne (2000). The location of the horizontal parallel point is observed to be close to the origo whereas the moment parallel point is located at some distance, Byrne & Houlsby (1999) and Byrne (2000). For surface footings the location of the moment parallel point is found to $V/V_{peak}=0.26$ and $M/DV_{peak}=0.061$. With the introduction of the two association factors the model is capable of modelling the change in the parallel point with respect to the loading path in the radial-plane. If the two association factors are chosen to be identical i.e. $a_h = a_m$, Equation 4.23 corresponds to Equation 4.21 with $a_h = a_m = a_v$.

Based on loading tests with circular footings on dense sand Cassidy (1999) found that it was not possible to fit all the test results with Equation 4.23 without changing α_h and α_m during loading. Fitting the results from Gottardi & Houlsby (1995) he found that a_h and a_m could be described by hyperbolic functions of plastic displacement histories by the following formulas.

$$a_h = \frac{k' + a_{h\infty} (u_p / w_p)}{k' + (u_p / w_p)}$$

$$a_m = \frac{k' + a_{m\infty} (Dq_p / w_p)}{k' + (Dq_p / w_p)}$$

Equation 4.24

where k' determines the rate of change of the association factors. For no previous radial displacement a_h and a_m is equal to unity and gives associated flow. From the tests Cassidy found that the following parameters would fit the measured response well: $b_3=0,55$, $b_4=0,65$, $a_{h\infty}=2,5$, $a_{m\infty}=2,15$ and $k'=0,125$. The variation of a_h and a_m are shown in Figure 4.17. The degree of non-associated flow is seen from the figure to be most pronounced in the horizontal direction.

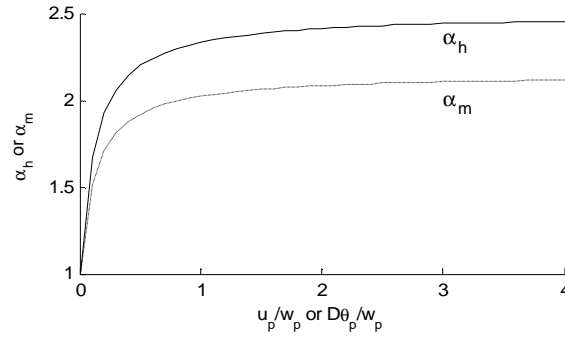


Figure 4.17 Variation of the association factors a_h and a_m proposed by Cassidy (1999).

The increase in the non-association factors during loading shown in Figure 4.17 must be compared with the observed degradation of the yield surface parameters h_0 and m_0 presented in section 4.2.2. The degradation of these are shown in Figure 4.18. If the change in yield surface parameters during loading is not included the increase in a_h and a_m will over-predict the degree of non-association.

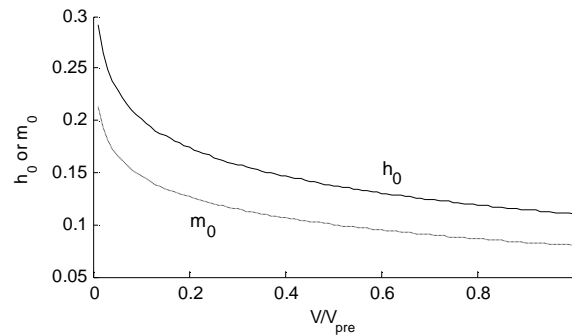


Figure 4.18 Variation of yield surface parameters for surface foundations by Equation 4.9.

The potential functions presented in the previous are very complex involving several parameters that need to be calibrated for each type of foundation and soil investigated. For the same tests on which Equation 4.24 is based Cassidy (1999) found, that a mean value of $a_h = a_m = 2.05$ would within reasonable tolerance fit the data as well.

In the literature several observations have been made indicating associated flow in the radial plane. In Figure 4.19 the shape of the yield surface is shown for different set of b -values within the yield function from Model C and the potential function in Equation 4.21 with $\alpha_v < 1$. The potential surface is shown

for $V_{pre}=V'$ and $V'>V_{pre}$. The latter is seen to cause intersection with the yield surface at $V/V_{pre} = 0.5$. From the figure it is seen that the shape of the potential surface is equal to the shape of the yield surface independent of V' , i.e. associated flow is obtained in the radial plane.

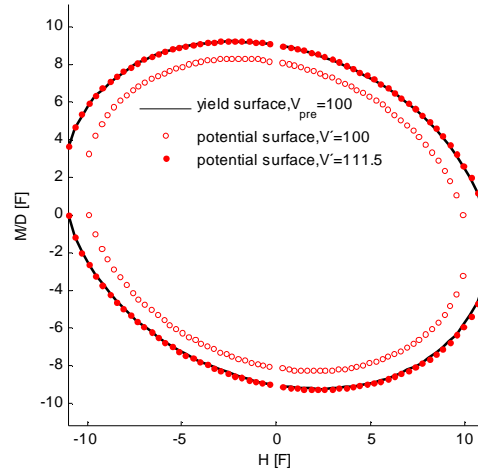


Figure 4.19 Comparison of yield surface and potential function in the radial plane. $D=100$ [L], $V/V_{pre}=0.5$, $b_1=1$, $b_2=1$, $b_3=0.1$, $b_4=0.1$, $a=-0.2$, $h_0=0.11$, $m_0=0.09$, $a_v=0.9$.

In Figure 4.20 the shape of the yield surface from Model C and the potential function in Equation 4.23 is drawn for different values of the association factors i.e. a_h and a_v and with the remaining values used in Figure 4.19. The plot is shown for different values of V' . It is clear from the figure that normality is not obtained in the radial plane for different values of the association parameters for this potential function, as observed experimentally. If the association factors are identical this potential surface is as earlier mentioned identical to the potential function given by Equation 4.21.

The b -values influences on the size of the potential- (b_3 and b_4) and yield surface (b_1 and b_2), for a given ratio of V/V' and V/V_{pre} , respectively, through b_{34} and b_{12} . The only change in the radial plane is the value of V' giving intersection with the yield surface at a given state. Thus the b -values does not change the shape of the surfaces in the radial plane only the size.

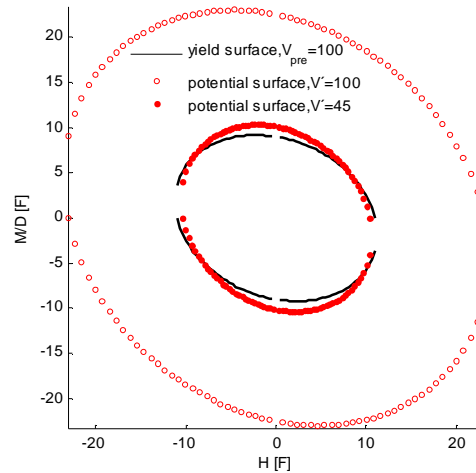


Figure 4.20 Comparison of yield surface and potential function in the radial plane. $a_h=2.5$ and $a_m=2.1$.

4.3. Influence from installation procedure on the behaviour of bucket foundations

In the laboratory the small scale bucket foundations are usually installed by pushing whereas in the field, the installation is carried out by suction within the bucket. The effect from these installation procedures on the static behaviour of the bucket is investigated experimentally by Villalobos et al. (2004/2005).

Static combined loading tests in oil-saturated Baskarp Cyclone sand ($D_r=69\%$) are presented in Villalobos et al. (2004). The bucket tested is a bucket with a diameter and a skirt height equal 200mm and 100mm respectively i.e. an embedment ratio equal 0.5. The bucket foundations is after installation loaded with a constant vertical load, $V=20\text{N}$ and radial load ratio, $M/(DH) = 0.5$. This corresponds to a constant height of impact of the horizontal load at $h=0.5D$. No information's are given on the vertical preload during the installation phase. No significant difference in the behaviour and moment capacity was observed from these tests.

Corresponding loading tests on bucket foundations in water saturated Redhill 110 ($D_r=75\%$) is presented in Villalobos et al. (2005). The buckets tested are 200 and 293 mm in diameter with an embedment ratio equal 0.5. The buckets are preloaded with a vertical load of approximately 400 and 1700N for the 200 and 293 mm buckets respectively. The tests are performed with a constant vertical load and a constant ratio of $M/(DH) = 1.0$ approximately. Plotting the load displacement response from some of these tests has shown a significant

effect of the installation method on the load-displacement behaviour including the capacity. Though the tests are performed at similar preload ratios some difference between the tests are measured. Normalizing the yield points with the actual vertical preload, smaller influence from the installation method was observed.

A set of large scale tests on a bucket foundation with $D = 3\text{m}$ and $d = 1.5\text{m}$ is performed in dense sand ($D_r = 80\text{-}85\%$). By comparing these experiments with similar laboratory tests, the influence from the installation procedure on the behaviour is found to be only small for large scale tests, Kelly et al. (2006). From these tests they conclude that the suction installation may create a localized zone of disturbance adjacent to the skirt, which does not increase in proportion to caisson diameter. The disturbance will thereby influence less on the behaviour of large bucket foundations.

4.4. Summary

A literature review concerning the behaviour of relevant foundations subjected to combined loads has been carried out.

Two methods presented are generally used to predict the behaviour of foundations:

1. The classical approach
2. The macro model approach

The first method is only capable of determining the capacity of foundations and not the pre-peak behaviour. The macro model approach is however capable of predicting the complete behaviour until failure is reached. The yield-, potential- and failure surface is found to follow a cigar shaped surface in the (M, H, V) - space.

The macro model approach is estimated capable of describing the static behaviour of bucket foundations including surface foundations. The shape of the yield-, potential- and failure surfaces is in this connection found to be dependent of D_r , d/D , V_{pre}/V_{peak} and HD/M . More research on the variation of these parameters in details is however estimated necessary.

The intersection of the yield and failure surface with the V -axis is only to a limited extend investigated. Especially the intersection at low V is to be pursued further.

For the investigated foundation types associated flow is observed to be plausible in the radial planes whereas non-associated flow is observed in the

planes along the V -axis. At the time being this is modelled by a modification of the yield surface expression by introduction of one or more association factors. The presented modification involving two association factors have shown to entail non-associated flow in the radial planes which disagrees with the experimental observations.

5. Vertical bearing capacity of bucket foundations

The vertical bearing capacity of a bucket foundation located in saturated sand is investigated in this chapter. The vertical bearing capacity is an important component in the macro model approach described in chapter 4. Several loading tests on small scale bucket foundations including circular surface footings is performed in the laboratory using Aalborg University Sand No.0. The test results are compared with the general accepted theory of bearing capacity. The bearing capacity factors within this theory are investigated in the axis-symmetric case corresponding to vertical loading of circular foundations in homogenous and isotropic sand.

It is assumed that the bucket foundation in case of vertical loading behaves similar to an embedded circular foundation. Thus the soil trapped within the bucket is expected to behave as or nearly as a rigid cluster. The soil within the bucket foundation is during vertical loading constrained laterally by the skirt, preventing the soil from large deformations due to the high stiffness of dense sand. The vertical bearing capacity is in this case given as the sum of two contributions: 1) the bearing capacity at the base of the embedded foundation and 2) the friction between the outside of the bucket skirt and the surrounding soil. The vertical bearing capacity of a bucket foundation located in saturated sand can in this case be estimated by use of the general bearing capacity formula, based on the work by Terzaghi (1943):

Equation 5.1

$$V_{peak} = g' \frac{D}{2} N_g \left(\frac{pD^2}{4} \right) + q' N_q \left(\frac{pD^2}{4} \right) + \frac{pDg'd^2}{2} (K \tan \delta)$$

where g' is the effective unit weight of the soil.

D is the diameter of the bucket.

N is the bearing capacity factors which should be defined for circular footings or be included a shape factor if based on a plane strain solution.

q' is the effective overburden pressure, $q' = d \times g'$

d is the skirt length.

K is the coefficient of lateral earth pressure.

δ is the friction angle between the skirt and the surrounding soil.

In Equation 5.1 the depth factor is not included as well as the enhanced stresses that occurs due to the friction along the skirt during penetration of the bucket foundation. The increase in frictional resistance due to vertical movement of the bucket foundation is investigated by Houlsby & Byrne (2005) but will not be included in this chapter. The presence of the depth factor requires that the strength of the soil above the foundation level is at least as great as the strength below. This has been found not always to be the case in the laboratory due to the preparation techniques used.

Equation 5.1 is based on the principle of superposition which results in a conservative estimate of the bearing capacity, Hansen (1975). In spite of this it is often used due to its simplicity. Thus the vertical bearing capacity of a bucket foundation located in saturated sand is investigated using this principle.

The error introduced by the superposition principle can be avoided by calculating the bearing capacity by the use of e.g. the Finite Element Method or the freeware bearing capacity program, ABC by Martin (2004).

5.1. Skirt friction

The last term in Equation 5.1 is the surface resistance assuming a behaviour between the bucket skirt and the soil according to the Coulomb failure criterion. A value of $K \tan \delta$ equals 0.25 and 0.5 are suggested by Byrne & Houlsby (1999) and Byrne et al. (2003) respectively. Though also significantly higher values are suggested in the literature. The value of $K \tan \delta$ is in reality not a constant but depends on the soil properties as well as the density and the roughness of the skirt. Values of $K \tan \delta$ for an open ended driven pile are shown in Table 5.1, API (2002). The limiting unit skin friction, f_l in the design situation is shown as well.

The values of $K \tan \delta$ in Table 5.1 are given for a driven pile where the installation procedure will increase the lateral earth pressure given by K relative to the stresses at rest. During the installation of the bucket the lateral earth pressure on the skirt is not increased but expected to decrease due to water flow around the skirt tip. The laboratory bucket foundations are however installed by pushing. By employing the values in Table 5.1 the friction resistance in case of installation by suction is suspected to be over-predicted. The limiting value of K must instead be given as the lateral earth

pressure coefficient at rest, $K^0 = 1 - \sin j_{tr}$, which in all cases gives a value that is smaller than implied in Table 5.1.

Table 5.1 Skin friction in cohesion-less siliceous soil for an open ended pile driven, (API 2002)

Density	Soil description	d [m]	K_{tan}	f_t [kPa]
Very Loose	Silt	15	0.214	47.8
Loose	Sand-Silt			
Medium	Silt			
Loose	Sand	20	0.291	67
Medium	Sand-Silt			
Dense	Silt			
Medium	Sand	25	0.373	81.3
Dense	Sand-Silt			
Dense	Sand			
Very dense	Sand-Silt	30	0.46	95.7
Dense	Gravel			
Very dense	Sand			
		35	0.56	114.8

Alternatively, the contribution from the skirt friction on the bearing capacity can be estimated based on results from a cone penetration test by the following equation, DNV (1992):

Equation 5.2
$$V_{skin} = A_s \int_d^0 k_f(z) \bar{q}_c(z) dz$$

where A_s is the outside area of the skirt per unit penetration depth, i.e. the perimeter of the bucket.

\bar{q}_c is the average cone resistance from the CPT

k_f is an empirical coefficient relating the cone resistance to the skin friction

Instead of using Equation 5.2 to estimate the resistance from the skirt friction it would be obvious to use the measured sleeve friction from the CPT's directly instead of the cone resistance. This could be done by the following expression:

Equation 5.3
$$V_{skin} = A_s \int_d^0 k_s(z) \bar{q}_s(z) dz$$

where \bar{q}_s is the average skin friction from the CPT.

k_s is an empirical coefficient relating the sleeve friction to the skin friction

The cone resistance and sleeve friction from CPT's depends on the penetration rate, pore pressure development during penetration of the CPT-probe and differences in the material roughness between CPT probe and the steel skirts. Hence the coefficients in Equation 5.2 or Equation 5.3 must be calibrated. In the laboratory a small scale CPT-probe is used to estimate the density of the soil before each experiment with the buckets, see appendix A. This probe is not capable of measuring the skin friction and is not penetrated with the standard penetration rate as used in the field. If the friction resistance from the laboratory tests is to be determined from the laboratory CPT-probe the skirt friction given by Equation 5.2 must be used and calibrated.

Byrne & Houlsby (1999) noticed that the contribution from the skirt friction to the vertical bearing capacity is negligible for small scale tests on dense sand and insensitive to slight changes in the value of $K \tan \delta$. The influence of the skirt friction, is investigated in Figure 5.1 and Figure 5.2 assuming a sand with $j = 35^\circ$, $g' = 10 \text{ kN/m}^3$ and $K \tan(\delta) = 0.25$.

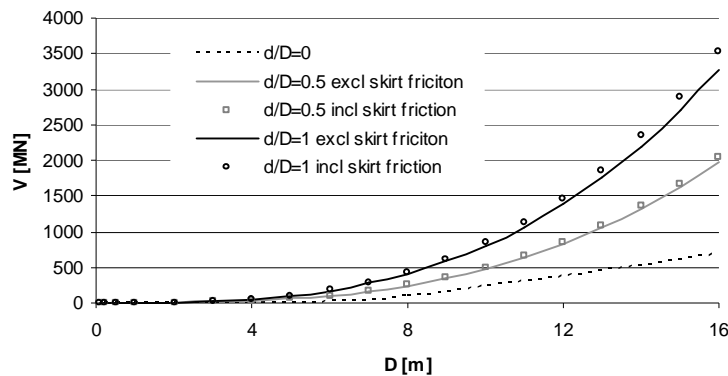


Figure 5.1 Calculated bearing capacity of bucket foundations assuming $j = 35^\circ$, $g' = 10 \text{ kN/m}^3$ and $K \tan(\delta) = 0.25$.

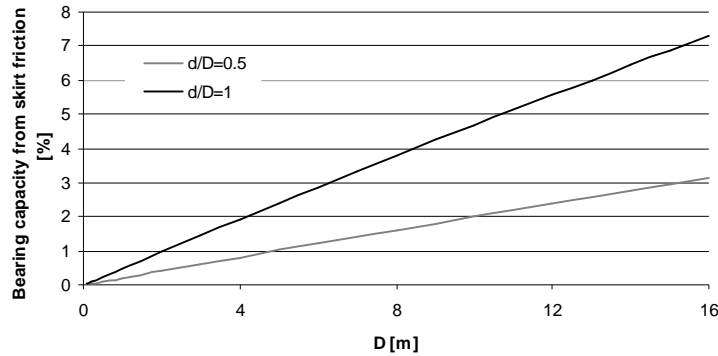


Figure 5.2 Calculated influence of the skirt friction on the bearing capacity of bucket foundations from Figure 5.1.

Figure 5.1 and Figure 5.2 shows that the influence of the skirt friction is clearly dependent of the bucket size including the embedment ratio. It can also be seen that the bearing capacity of a small scale bucket foundation tested in the laboratory is almost unaffected of the skirt friction as mentioned by Byrne & Houlsby (1999). The contribution from the skirt friction to the bearing capacity is less than 0.1% for a 200mm full bucket i.e. an embedment ratio equal 1. Furthermore the influence of the skirt friction is seen to be of greater importance for full size buckets in nature. From Equation 5.1 the influence of the skirt friction relative to the total vertical bearing capacity can be seen to be even smaller for sands with higher friction angles than the one used in the example. Thus the contribution from the skirt friction on the vertical bearing capacity is in the following only included if specified.

5.2. Bearing capacity factors for friction materials

The values of the bearing capacity factors in Equation 5.1 have been proposed by several authors in the literature since Terzaghi proposed the bearing capacity formula for a strip foundation in 1943. Some factors have been determined exact but some is still discussed. In the following some evaluated values of the bearing capacity factors are presented and selected values are investigated using the commercial finite element programs Plaxis and ABAQUS. The bearing capacity factors according to the bearing capacity formula by Terzaghi (1943), i.e. plane strain conditions are investigated in the following and used to verify the results from the FE-simulations. As less work is carried out on determining the bearing capacity factors of circular foundations this is later investigated by use of the FE-models verified.

5.2.1. Plane strain bearing capacity factors

Selected values of the bearing capacity factors determined under the assumption of plane strain conditions, i.e. a strip foundation, are presented in Figure 5.3 and Figure 5.6.

The value of the bearing capacity factor N_q can be determined analytically exact from the work by L. Prandtl (1920):

$$\text{Equation 5.4} \quad N_q = e^{p \tan j} \tan^2(45 + j/2)$$

The variation of N_q with the friction angle is shown in Figure 5.3, where also results from Plaxis calculations performed by the author and values determined by Bolton & Lau (1993) using the method of stress characteristics are shown. Results of calculations with both smooth and rough foundation bases by Bolton and Lau are shown in the figure. These calculations show that N_q is unaffected of the base roughness. Results from the Plaxis calculations are shown in the figure as well. These calculations are performed in order to verify the results from the Plaxis model created. The program is later used to calculate the values in the axis-symmetric case, i.e. circular foundations.

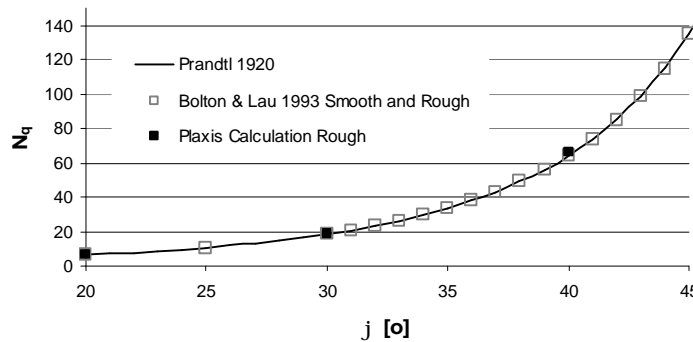


Figure 5.3 Variation of the plane strain bearing capacity factor N_q .

The Plaxis-model used to calculate the N_q values is shown in Figure 5.4. The foundation modelled is a 100 mm wide rough and rigid foundation resting on a Mohr coulomb material. The overburden pressure, q is after initializing of the initial stresses, applied to the surface of the soil including the area of the foundation. The applied foundation load (load A) is upon this increased until failure. The soil parameters used in the calculations are given in Table 5.2.

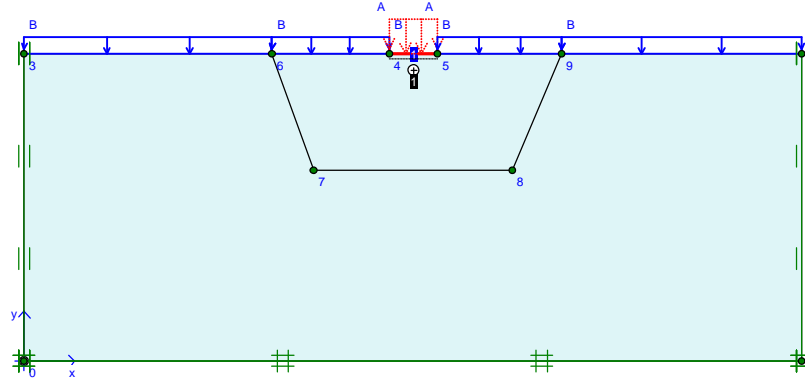


Figure 5.4 Plane strain Plaxis model used to calculate N_q . The overburden pressure, q is denoted B and the foundation load is denoted A .

The roughness of the interface between the foundation and the soil is given by R in Table 5.2 and is defined as:

Equation 5.5
$$R = \frac{\tan d}{\tan j}$$

Table 5.2 Soil parameters used in the Plaxis calculations.

c [kPa]	j [°]	γ [°]	n [-]	E [kPa]	g [kN/m ³]	R [-]
0.01	variable	$= \phi$	0.26	20000	0	1

The mesh used in the calculations in order to obtain a converged solution is shown in Figure 5.5. The elements used in the calculations are 15 node triangular standard elements within Plaxis.

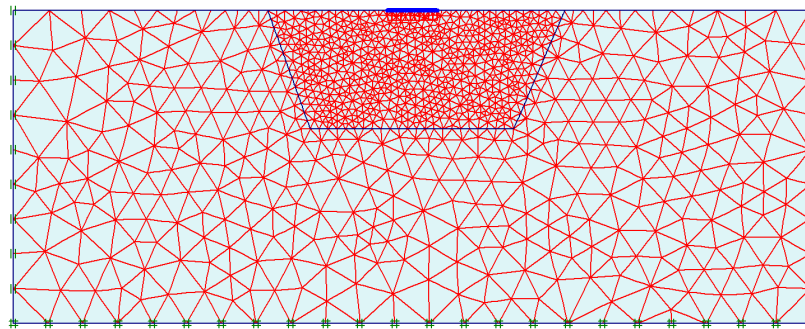


Figure 5.5 Mesh used for calculating the plane strain bearing capacity factor, N_q .

The results from the calculations are shown in Figure 5.3. The values of N_q are seen to correspond to the exact solution given by Equation 5.4 and the results by Bolton & Lau (1993).

Whereas the bearing capacity factor N_q is determined exactly, it has not yet been possible to determine the bearing capacity factor N_g exact with exception of a frictionless material, Prandtl (1920). A large number of attempts have been performed on calculating this in the past. Some of these are presented in Figure 5.6.

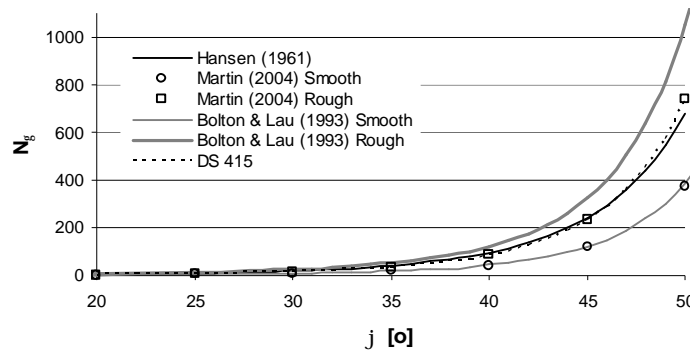


Figure 5.6 Plain strain values of N_g suggested by different authors.

One of the first expressions for N_g was proposed by Hansen (1961) by the following equation.

Equation 5.6
$$N_g = 1.8(N_q - 1) \tan j$$

The expression by Hansen (1961) is based on the results from Lundgren & Mortensen (1953) which is a lower bound solution and Meyerhof (1951) which is an upper bound solution which is presented in Figure 5.7. Only the value of $j = 30^\circ$ is given by Lundgren & Mortensen (1953). The corresponding values at $j = 20^\circ$ and $j = 40^\circ$ is calculated using the kinematically admissible rupture figure proposed by Lundgren & Mortensen, Hansen (1961). From Figure 5.7 it can be seen that the lower bound results by Lundgren & Mortensen fits the results from Martin (2004) and the relation given in the Danish Code of Practice for foundation engineering, DS 415 (1998). The results by Martin (2004) are converged solutions using the program ABC-Analysis of Bearing Capacity version 1.0. These results are argued to be exact values, Martin (2005a). The value of the bearing capacity factor N_g is according to DS 415 (1998) given by:

Equation 5.7
$$N_g = \frac{1}{4}((N_q - 1) \cos j)^\frac{3}{2}$$

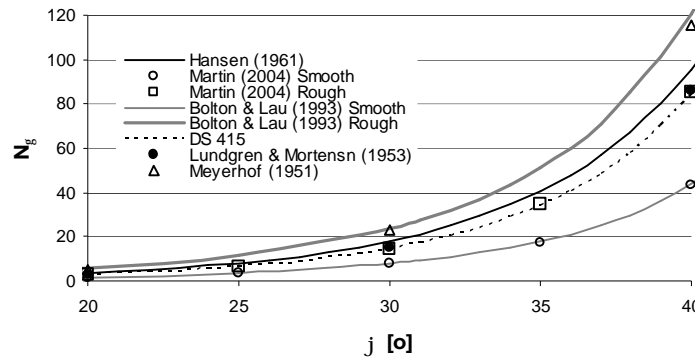


Figure 5.7 Values of N_g suggested by different authors compared with the lower and upper bound values by Lundgren & Mortensen (1953) and Meyerhof (1951) respectively.

From Figure 5.7 it is seen that in case of rough foundations the results by Bolton & Lau (1993) are higher than the corresponding values obtained by Meyerhof (1951), which is an upper bound solution. Hence the values for N_g proposed by Bolton & Lau are too high, which is also pointed out by Martin (2004). He also claims that the rupture figure used in the calculations by Bolton & Lau is incorrect in the case of rough base. For a smooth strip footing the values of the bearing capacity N_g given by Martin (2004) and Bolton & Lau (1993) are seen to be identical.

In order to give an estimate on the correct values of the bearing capacity factor N_g a set of FE-calculations is performed using the commercial FE-program ABAQUS. The soil is modelled as a Mohr-coulomb material by the means of the user material by Clausen et al. (2006). The calculations are carried out on a strip foundation with rough base resting on Mohr Coulomb material with a friction angle equal 40 degrees. The results are presented in appendix B where a value of N_g equal 86 is found. This corresponds to the values by both Lundgren & Mortensen (1953) and Martin (2004). The value of N_g for a friction angle equal 20 degrees given by both Martin (2004) and Bolton & Lau (1993) is verified for a smooth strip foundation from a corresponding FE-calculation by Clausen et al. (2007).

From the above it can be seen that the expression for the bearing capacity factor, N_g in the Danish Code of Practice for foundation engineering is valid for a strip foundation with a rough base.

5.2.2. Axis-symmetric bearing capacity factors

Vertical loading of a circular foundation or a bucket foundation induces an axis-symmetric stress situation in the soil below the bucket, assuming

isotropic and homogeneous soil. The bearing capacity factors in this case are investigated in the following. The values presented are including shape factors. In this case the bearing capacity is calculated using a foundation width equals the diameter of the foundation and by use of the triaxial measured friction angle. In Figure 5.8 the value of N_q for various friction angles is shown for some of the authors presented in the plane strain situation.

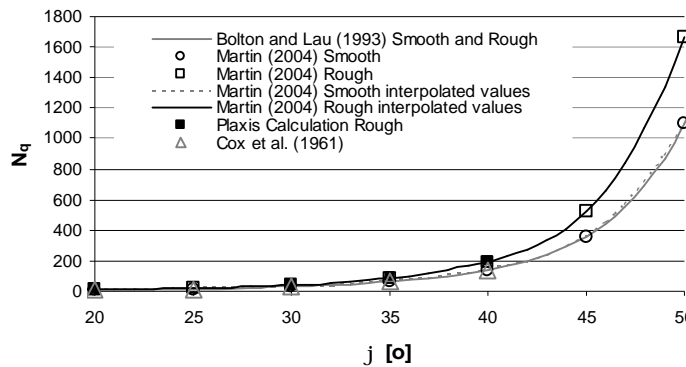


Figure 5.8 Values of the bearing capacity factor N_q for circular foundations.

The results from Martin (2004) illustrated by solid lines in Figure 5.8 is found using piecewise polynomial interpolation on the table values from Martin (2004) shown by marks.

Bolton & Lau (1993) assumes that the bearing capacity from the q -term in the bearing capacity formula is independent of the base roughness of the foundation. This is investigated using Plaxis with an axis-symmetric model identical to the one used in the plain strain situation. Due to symmetry only half a foundation, with a vertical line of symmetry in the centre of the foundation, is used in this case. The soil parameters from Table 5.2 are used, though with a friction angle equal 40 degrees and varying the interface roughness of the foundation base, R . The result is shown in Figure 5.9 where it is seen that the value of N_q actually increases with the roughness of the foundation base and goes towards the value given by both Bolton & Lau (1993) and Martin (2004) in the case of smooth base.

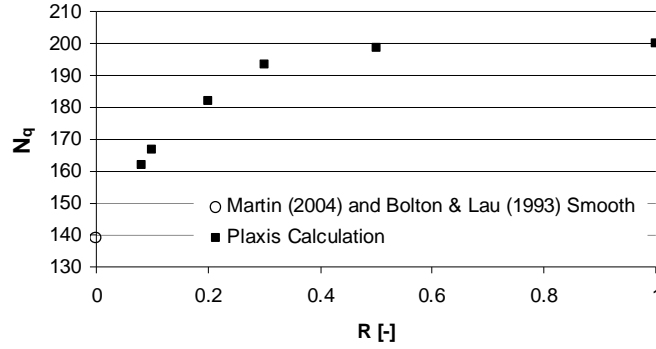


Figure 5.9 Value of the bearing capacity factor N_q for circular foundations with a varying base roughness, R for a friction angle at $j=40^\circ$.

The values of N_q for a rough and rigid circular footing are calculated using Plaxis and are presented along with results from the literature in Figure 5.8. The values from the Plaxis calculations are performed with the model described above and are seen to coincide with the values from Martin (2004) in case of rough base. The size of N_q for a circular foundation with smooth base is seen to be identical to the values by Martin (2004), Bolton & Lau (1993) and Cox et al. (1961). The values from Cox et al. is calculated using the following relation, since only the value of N_c is given in this reference, Prandtl (1920).

Equation 5.8
$$N_q = N_c \tan(j) + 1$$

The values of the axis-symmetric bearing capacity factors, N_g proposed by Bolton & Lau (1993) and Martin (2004) for both smooth and rough base are presented in Figure 5.10. The values of N_g are seen to coincide for circular footings with smooth base. In case of rough base the values of N_g by Bolton & Lau (1993) are though seen to be considerable higher then the values from Martin (2004). The difference was also noticed in the plane strain calculations. Since the assumptions made by Bolton & Lau (1993) in this case are the same as for the plane strain situation, these values are not reliable.

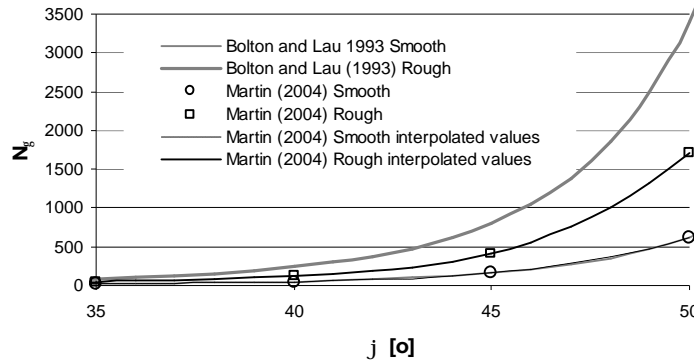


Figure 5.10 Values of the bearing capacity factor N_g for circular foundations.

The FE-program ABAQUS is used to give an estimate on the N_g -value at $j = 40^\circ$ for a circular rough and rigid foundation. The material model used is the user material, which was also used in the plane strain case. The material parameters used in the calculations are given in Table 5.3 and the results from the calculations are presented in appendix B. From the result of the analysis a value of N_g equal 125.5 is estimated, which corresponds to the value according to Martin (2004) equal 123.7. As in the plane strain case similar calculations is performed on a circular smooth footing with a friction angle of 20 degrees by Clausen et al. (2007). The results from these calculations also support the results from Martin (2004) as in the plane strain case.

Table 5.3 Soil parameters used in the ABAQUS calculation.

c [kPa]	ϕ [°]	ψ [°]	ν [-]	E [kPa]	γ [kN/m ³]	K^0 [-]
0	40	40	0.25	$1 \cdot 10^7$	9.82	0.36

As mentioned previously Martin (2004) claims that the figure of rupture assumed by Bolton & Lau (1993) is incorrect. These calculations are performed under the assumption that a trapped zone exists beneath the entire base. The size of this zone is investigated in Appendix B and confirms the postulate by Martin (2004).

5.2.3. Comparison of plane strain and axis-symmetric bearing capacity factors

In case of vertical loading of a circular or bucket foundation the stress situation is comparable with the one present in a triaxial test. Thus the friction angle to be used when determining the axis-symmetric bearing capacity factors is the triaxial determined friction angle, j_{tr} . If the bearing capacity of the bucket foundation is however estimated using the results from the plane strain assumptions, the plane friction angle, j_{pl} must be used together with

shape factors that accounts for the geometrical differences. The plane strain angle is generally assumed to be 10% higher than the triaxial measured friction angle, which is just an approximation as shown for instance by e.g. Stakemann (1976) and Larsen & Pedersen (2001).

The bearing capacity factors presented in section 5.2.1 based on plane strain assumptions are used in practice to calculate the bearing capacity of circular foundations. The bearing capacity of a circular embedded foundation or bucket foundation calculated in this way is in the following compared with the corresponding capacity based on the axis-symmetric values from section 5.2.2. In case the two methods imply identical capacities the following relations must according to Equation 5.1 be obeyed.

$$\begin{aligned} DN_{g,tr} &= BN_{g,pl} s_g \\ N_{q,tr} &= N_{q,pl} s_q \end{aligned}$$

Equation 5.9

where $B = D\sqrt{p/4}$ is the width of an equivalent foundation with identical area.

A comparison of the two methods presented, on calculating the bearing capacity of a rough circular foundation, is in the following carried out by investigating the relations in Equation 5.9

The values of $N_{q,tr}$ and $DN_{g,tr}$ for $j_{tr}=40^\circ$ can according to section 5.2.2 be determined to 192.7 and 123.7D respectively. The corresponding values based on the plane strain bearing capacity factors gives according to section 5.2.1 values of $N_{q,pl}s_q$ and $BN_{g,pl}s_g$ equals to 138 and 109D respectively for $j_{pl}=44^\circ$. It is clear from this example that the plane strain bearing capacity factors underestimates the correct bearing capacity if used on circular foundations. Hence it is recommended that the bearing capacity of circular foundations is calculated according to section 5.2.2.

5.2.4. New general expression for N-factors

Based on the performed study regarding the bearing capacity factors a new general expression is proposed on determining these. The expression is based on a modification of Equation 5.4 and Equation 5.7.

It has been shown that the bearing capacity factors from FE-calculations associated with this study and Martin (2004) should be used in connection with circular foundations. In the case of a smooth base the results from Bolton & Lau (1993) are seen to coincide with these results. In a plane strain situation the bearing capacity factors N_q and N_g can be calculated by Equation 5.4 and Equation 5.7 respectively. Though with exception of N_g which in case

of smooth base must be determined from Martin (2004) or Bolton & Lau (1993).

The values of the bearing capacity factors are fitted to the following expressions by minimizing the summed square of residuals.

$$\begin{aligned} N_g &= c_1 \cdot ((N_q - 1) \cos j)^{c_2} \\ N_q &= c_3 \cdot e^{c_4 \cdot P \cdot \tan j} \tan^2(45 + j/2) \end{aligned}$$

Equation 5.10

where the constants c_i are given in Table 5.4. The values of the bearing capacity factors given by Equation 5.10 are shown in Figure 5.11 and Figure 5.12. The expression for the bearing capacity factor N_q in case of both rough and smooth strip foundation and N_g for a rough strip foundation is identical to the corresponding expressions in section 5.2.1.

Table 5.4 Fitted values for constants in the formulas for the bearing capacity factors.

	Circular foundation		Strip foundation	
	Smooth	Rough	Smooth	Rough
c_1	0.1	0.16	0.12	0.25
c_2	1.33	1.33	1.51	1.5
c_3	0.715	0.8	1	1
c_4	1.42	1.5	1	1

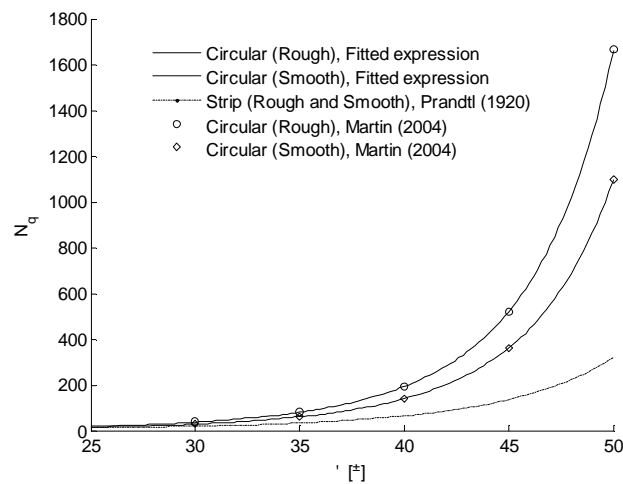


Figure 5.11 The bearing capacity factor N_q for circular and strip foundations with smooth and rough base.

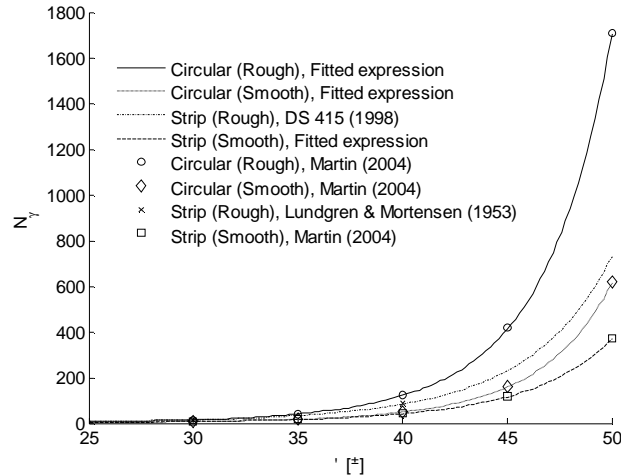


Figure 5.12 The bearing capacity factor N_g for circular and strip foundations with smooth and rough base.

The bearing capacity factors considered in the previous are valid in the extreme cases where the base of the foundation is completely rough or smooth. The bearing capacity factor, N_q for a strip foundation have been shown to be independent of the roughness. This is not the case for the corresponding N_g which is found to increase with the base roughness. The value of N_g for a strip foundation with an intermediate base roughness is presented by Martin (2005a,b) and is shown in Figure 5.13.

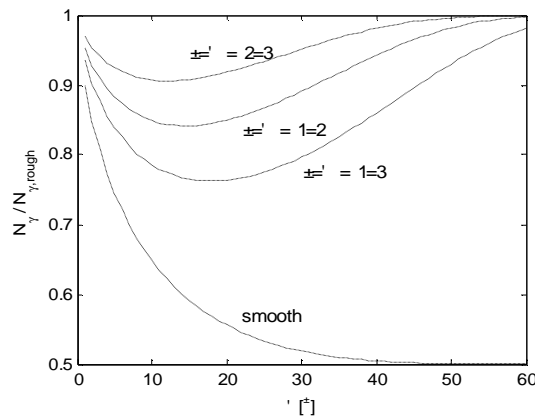


Figure 5.13 Influence of base roughness on N_g for a strip foundation, after Martin (2005a,b)

The base roughness for a circular foundation influences on both N_q and N_g . The influence on N_q is investigated in section 5.2 for circular foundation with a friction angle of the soil equal 40 degrees. The influence of the base

roughness on the bearing capacity factor N_g is to the knowledge of the writer not yet investigated for circular foundations.

5.3. Vertical bearing capacity of bucket foundations (Experimental observations)

The vertical bearing capacity of bucket foundations, V_{peak} is investigated in the following. Experimental observations are compared to the classical bearing capacity, using the bearing capacity factors according to Equation 5.10

5.3.1. Byrne & Houlsby (1999)

An investigation of the drained behaviour of bucket foundations in sand subjected to vertical load has been performed by Byrne & Houlsby (1999). The test series includes 17 tests on circular surface footings, i.e. $d=0$ with a diameter equals 50mm on very dense and dry sand. Based on these tests Byrne & Houlsby (1999) suggested the use of the general bearing capacity formula for estimating the vertical bearing capacity of a bucket foundation by the following formula.

Equation 5.11
$$\frac{V_{peak}}{V_0} = 1 + 0.89 \frac{d}{D}$$

where V_{peak} and V_0 is the vertical bearing capacity of bucket foundations and the corresponding surface foundation. The friction between the soil and skirt is ignored and a friction angle of approximately 46 degrees is used in the above equation. The friction angle is determined from the measured bearing capacities of surface foundations. The bearing capacity factors from Bolton & Lau (1993) are used to derive Equation 5.11.

The normalized bearing capacity of a bucket foundation is given by the following relation when all terms in Equation 5.1 are included:

Equation 5.12
$$\frac{V_{peak}}{V_0} = 1 + \frac{d}{D} \frac{2}{N_g} (N_q + \frac{d}{D} 2K \tan d)$$

Byrne and Houlsby have not succeeded in verifying the relation in Equation 5.11 experimentally since only the surface footings are loaded corresponding to failure due to limitations in the loading rig. Equation 5.11 is based on the values of the bearing capacity factors given by Bolton & Lau (1993), which is earlier found to be incorrect in case of a foundation with rough base. Since the bucket foundation is to be compared with an embedded foundation, the soil inside the bucket forms the base, thus the base is rough. Using the

recommended expression of N_q and N_g given by Equation 5.10, Equation 5.11 is rewritten as follows:

Equation 5.13
$$\frac{V_{peak}}{V_0} = 1 + 2.1 \frac{d}{D}$$

Equation 5.13 is derived using a friction angle of 48° , which is found by back calculation of the experiments from Byrne & Houlsby (1999) by use of the bearing capacity factors in section 5.2.2. The result from rewriting the relationship in Equation 5.11 shows that the vertical bearing capacity of a skirted foundation relative to the corresponding capacity of a circular plate is significantly larger than assumed by Byrne & Houlsby (1999). It must be noticed that the relation in Equation 5.13 is only valid for the small scale tests performed by Byrne & Houlsby (1999) and that Equation 5.12 should be used in all other situations that is not similar to this. The constant in Equation 5.13 is a function of the friction angle as shown in Figure 5.14.

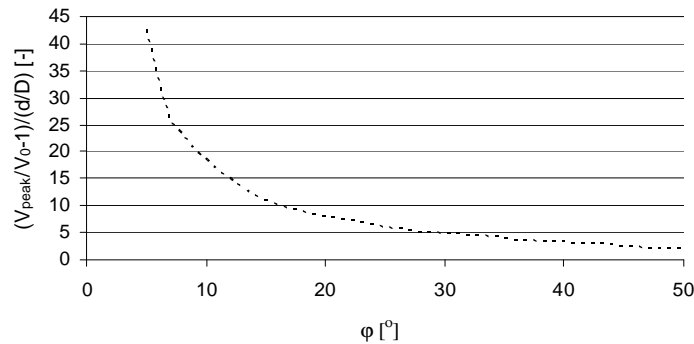


Figure 5.14 Value of the constant in the theoretical relation of V_{peak}/V_0 ignoring the skirt friction.

From Figure 5.14 it is seen that the size of V_0 relative to V_{peak} is decreasing with increasing friction angle, hence the advantage of using a skirted foundation is larger in sand with low friction angle.

5.3.2. Byrne et al. (2003)

A set of experiments investigating the vertical bearing capacity of bucket foundations as well as circular flat footings is presented in Byrne et al. (2003). The tests are carried out in dry sand with $D_r = 88\%$ with embedment ratios of the bucket foundation varying from zero to two. The results are shown in Figure 5.15 including the resistance measured during installation of the bucket.

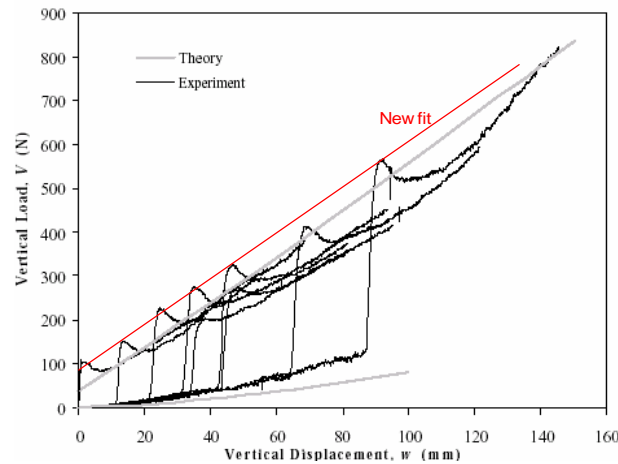


Figure 5.15 Vertical load-displacement response from bearing capacity tests, after Byrne et al. (2003).

The upper theoretical line (grey line), originate from calculations performed by Byrne et al. (2003) using bearing capacity factors from Bolton & Lau (1993). The lower theoretical line is the calculated penetration resistance during installation using the general bearing capacity formula for a strip foundation with plane strain bearing capacity factors. The penetration resistance during installation by pushing is investigated by Houlsby & Byrne (2005). They proposed a method that takes into account the enhanced stresses around the skirt and at the tip which is shown capable of describing the penetration resistance during installation, Villalobos et al. (2005). This method will not be included here as the concern is on the peak capacity upon installation. The bearing capacity factors from Bolton & Lau (1993) are previously shown to be incorrect for rough circular foundations. Using the bearing capacity factors proposed in section 5.2.4 a new fit to the peak capacity in Figure 5.15 is found using a friction angle equal 37.6° and an embedment depth corresponding to the vertical displacement. This new line of capacity is shown in the figure by a red solid line and is seen to capture the measured peak capacities well.

5.3.3. Vertical bearing capacity tests at AAU.

A set of vertical bearing capacity tests on buckets with varying size has been performed in the geotechnical laboratory at Aalborg University. The diameters of the buckets tested vary between 50 mm and 200 mm. The embedment ratios are 0, $\frac{1}{4}$, $\frac{1}{2}$, $\frac{3}{4}$ and 1. Results from the vertical bearing capacity tests can be found in Volume 2 of this thesis and in Larsen & Ibsen (2006a,b).

Bearing capacity of circular surface footings, V_0

Results from vertical load tests on circular surface footings with rough base are presented in the following figures. Failure is defined as the peak value of the vertical load or the residual value if no peak is obtained during further vertical deformation. The vertical load at failure is denoted V_0 for surface footings, i.e. bucket foundations with an embedment ratio of zero.

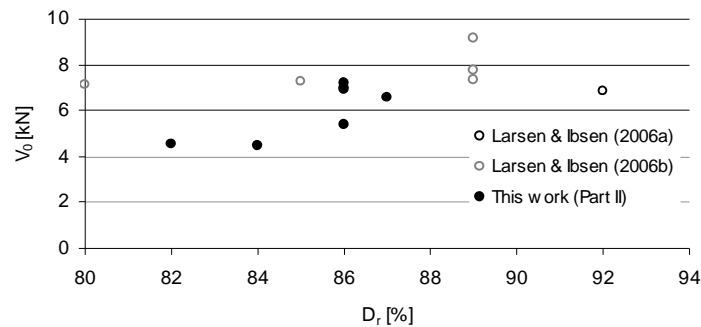


Figure 5.16 Results from vertical loading of flat circular footings with $D=200\text{mm}$.

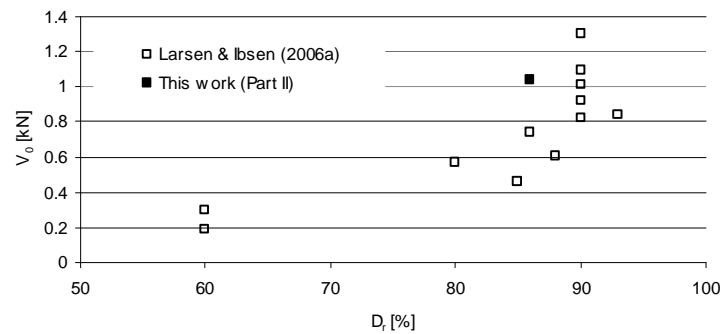


Figure 5.17 Results from vertical loading of flat circular footings with $D=100\text{mm}$.

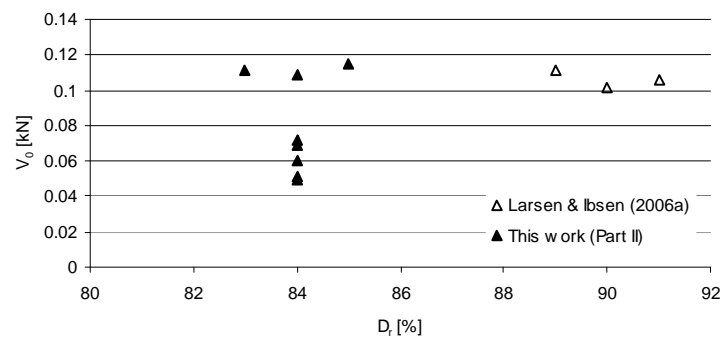


Figure 5.18 Results from vertical loading of flat circular footings with $D=50\text{mm}$.

From Figure 5.16 to Figure 5.18 it is seen that there is large scatter in the relation between the relative density and the vertical bearing capacity. The

vertical bearing capacity of surface footings, V_0 is usually calculated ignoring the influence of the overburden pressure caused by the settlements. The measured capacities in the above figures include the contribution from the settlements which varies significantly. Thus the experiments are actually not comparable. The measured capacities are in the following corrected for this contribution using the bearing capacity theory.

In order to subtract the contribution from the settlements on the bearing capacity, the friction angle needs to be determined. The bearing capacity formula in Equation 5.14 is used to determine the friction angle with the bearing capacity factors in Equation 5.10 for circular foundations. Sand is glued on to the base of the circular plates that are tested, thus the bearing capacity factors is determined in case of rough base.

Equation 5.14

$$V = g' \frac{D}{2} N_g \left(\frac{pD^2}{4} \right) + q' N_q \left(\frac{pD^2}{4} \right)$$

where $q' = w \times g'$ and w is the vertical settlement at failure. The unit soil weight, g' is known for each test from the void ratio determined using the laboratory-CPT probe, see appendix A. After determining the friction angle the corresponding V_0 -capacity can be determined using only the first term in Equation 5.14. This capacity is denoted the corrected V_0 -capacity, $V_{0,corr}$ in the following.

The friction angle is estimated from the bearing capacity formula under assumption of soil behaviour with associated flow. This means that the calculated friction angle does not correspond to the triaxial friction angle from chapter 2. Hansen (1979) suggested the use of a reduced friction angle in the bearing capacity formula to account for the degree of non-association given by the difference between the friction- and dilation angle. The value of this reduced friction angle by Hansen is given by:

Equation 5.15

$$\tan j_d = \frac{\sin j \cos \gamma}{1 - \sin j \sin \gamma}$$

The reduced friction angle, j_d is calculated from the bearing capacity tests with surface footings using Equation 5.14 and is shown in Figure 5.19 and Figure 5.20.

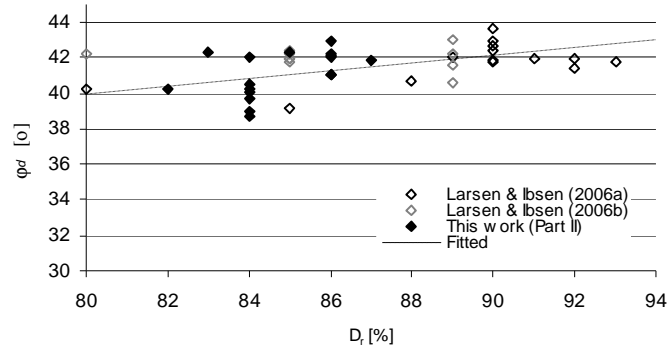


Figure 5.19 Reduced friction angle calculated from V_0 experiments.

In Figure 5.19 the calculated friction angle is differentiated with respect to the different data series from which the experiments originate. In order to investigate the reason of the scatter present, the results are in Figure 5.20 differentiated with respect to the diameter of the tested footings.

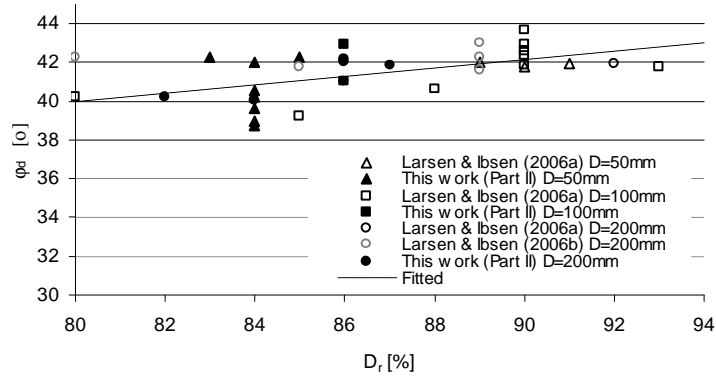


Figure 5.20 Reduced friction angle calculated from V_0 experiments.

From Figure 5.19 and Figure 5.20 it is seen that there is no systematic scatter that can be assigned to neither the size of the foundation nor the test series. The reason in the scatter is instead assumed to be partly due to the evaluation of the relative density from the laboratory-CPT. The relative density of the tested sand is determined as a mean value over depth. A small variation with depth is however observed in some tests. Another reason is ascribed the experimental errors, e.g. skew settlements of the plate and loads that are applied at an inclined angle from vertical.

The results from the laboratory tests are fitted to the following linear relation, which is also shown in Figure 5.19 and Figure 5.20:

Equation 5.16
$$j_d = 0.214D_r + 22.86$$

From the figures it can be seen that the linear relation between the relative density and the reduced friction angle is described within reasonable accuracy by Equation 5.16. It must be noticed that Equation 5.16 is only valid for stress levels under which the experiments are performed and for the sand tested. The linear fit is chosen based on the following example.

An often used estimate on the friction- and dilation angle of sand is assumed linear and is given by:

$$\text{Equation 5.17} \quad j_{tr} = 30^\circ - \frac{3}{U} + \left(14 - \frac{4}{U}\right) D_r$$

where U is the coefficient of uniformity. The dilation angle, ψ is assumed to follow $\psi = j_{tr} - j_{cl}$, see chapter 2. Where j_{cl} is the characteristic friction angle which is assumed constant for a given sand.

Combining Equation 5.15 and Equation 5.16 results in a linear relation between the relative density and the reduced friction angle as assumed in Equation 5.16. This linear relation is shown in Figure 5.21 for a sand with $U=3$ and $j_{cl}=30^\circ$.

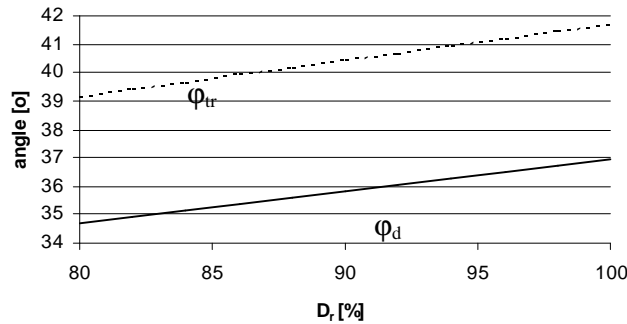


Figure 5.21 Theoretical variation of the friction angle for sand with $U=3$ and $j_{cl}=30^\circ$ according to Equation 5.15 and Equation 5.16.

The values of $V_{0,corr}$, i.e. the measured bearing capacity subtracted the contribution from the settlements are shown in Figure 5.22. The $V_{0,corr}$ bearing capacity is in the figure normalized with the diameter to the third power in order to compare the results.

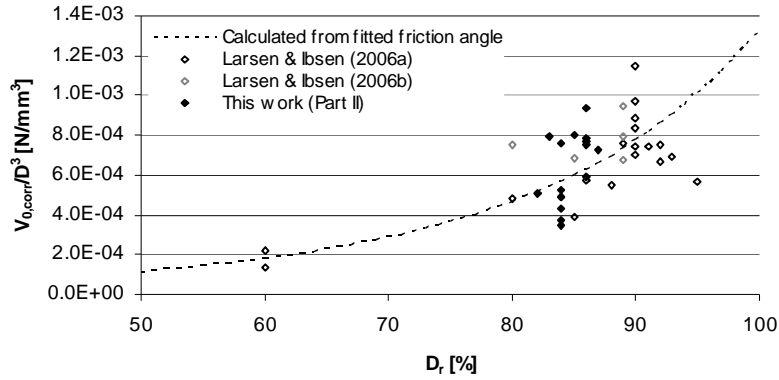


Figure 5.22 Corrected values of the measured V_0 bearing capacity relative to the relative density of the sand measured with the laboratory CPT-probe.

The corrected values of the vertical bearing capacity in Figure 5.22 shows, in spite of the scatter, good agreement with the variation of the theoretical line. The theoretical line in the figure is calculated using the fitted relation between the reduced friction angle and the relative density given by Equation 5.16.

Bearing capacity of bucket foundations with skirts, V_{peak}

The results from the bearing capacity tests on the skirted bucket foundations are used to calculate the reduced friction angle by Equation 5.14 as well. The weight of the soil plug inside the bucket foundation is ignored in the calculations as it is seen to only contribute slightly to the load on the foundation base. The reduced friction angle calculated from the measured capacities is shown in Figure 5.23 along with the corresponding results from the V_0 experiments.

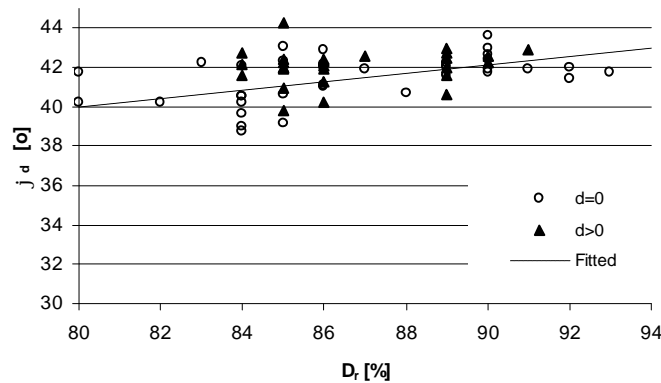


Figure 5.23 j'_d calculated from V_{peak} and V_0 experiments. The fitted relation is given by Equation 5.16.

From Figure 5.23 it is seen that also the experiments with the skirted foundations follows the relation between the friction angle and relative density given by Equation 5.16.

The results from the performed bearing capacity tests are all shown in Figure 5.24 to Figure 5.26 as a function of the embedment ratio, d/D . The values are all corrected for any settlements using the bearing capacity formula as explained earlier. The reduced friction angle is shown in Figure 5.23 to be between 40 and 44 degrees for the tests, approximately. The theoretical bearing capacity is shown in the following figures for friction angles equal 40, 42 and 44 degrees using Equation 5.1.

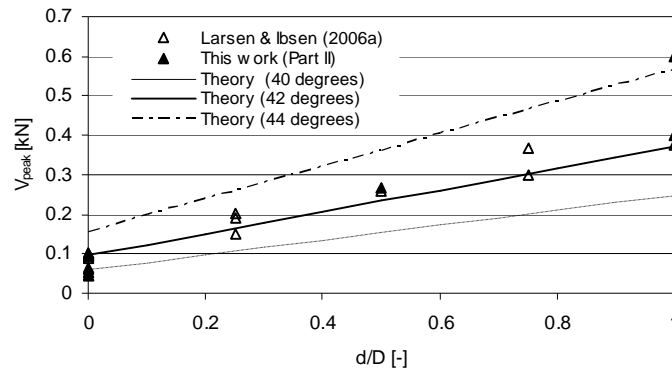


Figure 5.24 Results from bearing capacity tests on $D=50\text{mm}$ buckets corrected for settlements.

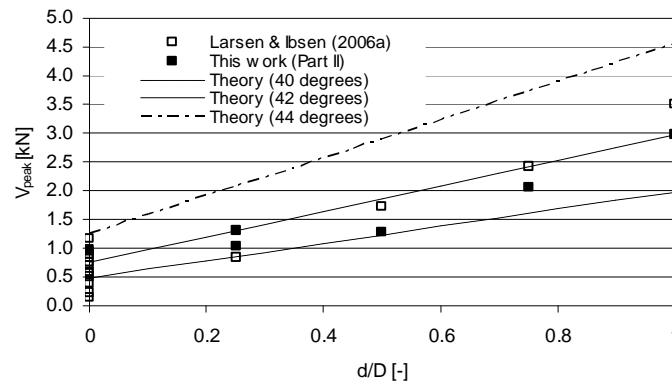


Figure 5.25 Results from bearing capacity tests on $D=100\text{mm}$ buckets corrected for settlements.

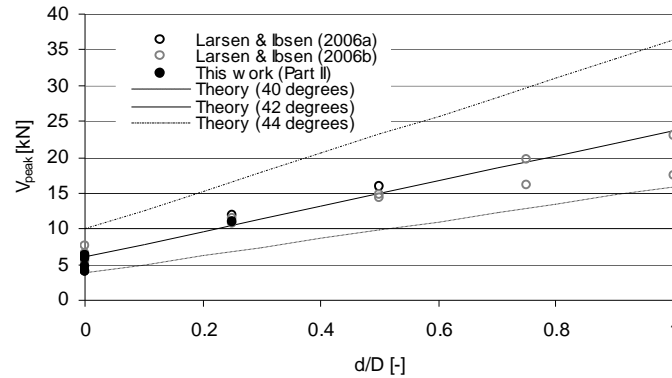


Figure 5.26 Results from bearing capacity tests on $D=200\text{mm}$ buckets corrected for settlements.

The theoretical bearing capacity, calculated using the bearing capacity factors from section 5.2, is shown to capture the measured capacities very well. As shown, the strength of the sand in-between the experiments vary, because different densities of the sand are obtained during preparation of the soil. The variation of the soil density in the prepared test boxes can be reduced significantly if the optimized preparation procedure of the test box, described in chapter 2, is followed. This procedure is optimized during this work and is therefore not used throughout all the experiments. Although the friction angle of the sand varies for the tests performed, a reduced triaxial friction angle equal 42° is seen to capture the measured failure values well for most of the experiments.

The measured capacities from the vertical bearing capacity tests on bucket foundations in the laboratory are in the following compared with the theoretical relation in Equation 5.12. The contribution from the skirt friction is ignored. The results from the tests are all corrected for settlements at failure and the comparison is shown in Figure 5.27. The value of V_0 is for each test estimated using the relation in Equation 5.16.

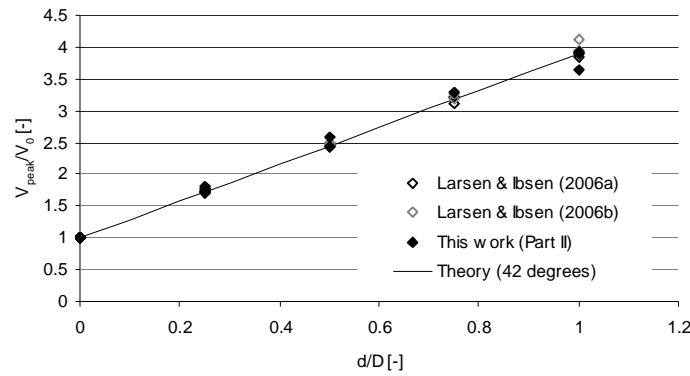


Figure 5.27. Vertical bearing capacity of bucket foundations normalized with the corresponding V_0 values. All values are corrected for settlements.

The normalized bearing capacities in Figure 5.27 is seen to support the linear relation determined theoretically from the bearing capacity formula. A mean friction angle equal 42 degrees yields the following relation:

Equation 5.18
$$\frac{V_{peak}}{V_0} = 1 + 2.9 \frac{d}{D}$$

A reduced triaxial friction angle equal 42 degrees is evaluated from the performed vertical bearing capacity tests on bucket foundation. The stress situation in the soil surrounding the foundation is unknown, but a mean value of the minor stress at failure can be estimated from Figure 5.28.

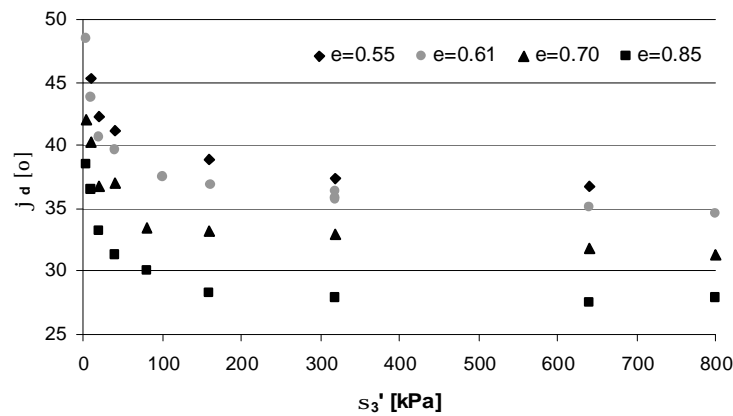


Figure 5.28. Reduced friction angle derived from triaxial tests.

The values of the reduced friction angles in Figure 5.28 are calculated from the triaxial measured friction- and dilation angle presented in chapter 2. The tested sand in the test box is deposited with a void ratio of 0.61

approximately. This corresponds to a mean value of the minor principal stress at failure of approximately 15 kPa for a reduced friction angle of $j_d = 42$ degrees, see Figure 5.28. From chapter 2 the corresponding triaxial and dilation angle at this stress level can be found to $j_{tr} = 47.5$ and $\gamma = 17.5$ degrees respectively for a void ratio equal 0.61.

5.4. Summary

The bearing capacity of bucket foundations including circular surface footings is investigated analytically and experimentally. The bearing capacity formula is found capable of determining the vertical bearing capacity of bucket foundations by use of axis-symmetric bearing capacity factors.

The commercial FE-codes Plaxis and ABAQUS are found capable of determining the value of N_q and N_g assuming both plane strain and axis-symmetric stress conditions.

A new general expression that describes the bearing capacity factors is proposed based on the FE- calculations carried out and values from the literature. The proposed expression applies to plane strain as well as axis-symmetric stress conditions for foundations with smooth or rough base.

The vertical bearing capacity of a bucket foundation is found to be larger than assumed in the literature. The increase in capacity is due to the use of incorrect bearing capacity factors in the literature.

The soil strength of the soil tested within this work is investigated using the results from the vertical loading tests. A triaxial friction angle of 47.5 degrees and a corresponding dilation angle of 17.5 degrees are determined from the performed vertical load tests.

6. Bucket foundation tests subjected to combined loading at AAU

An extensive number of loading tests with small scale bucket foundations are carried out in the geotechnical laboratory at Aalborg University within the past years. The tests are performed on buckets with varying size, embedment ratio and load paths. All tests are performed on saturated dense Aalborg University Sand No. 0. A description of the tested sand and the test setup can be found in chapter 2. In this chapter the static capacity and behaviour of bucket foundations subjected to combined loads are investigated based on the experimental results. The observations are compared with the available knowledge from the literature review in chapter 4.

The investigation of combined loaded foundations is in the past generally performed by the use of inclined loads, Gottardi & Butterfield (1993). At the University of Oxford and at Aalborg University the behaviour is investigated in a different way using load combinations that are similar to true loads. At the University of Oxford the oxford loading rig is used where a predefined load or deformation path can be tracked using stepper motors. At Aalborg University the test setup described earlier is used to investigate the behaviour of bucket foundations when exposed to combined loads. The tests are performed by loading the buckets with a load or deformation path that allows the bucket to move freely similar to the foundations in nature.

Within the work of this thesis several tests on bucket foundations exposed to low vertical load are performed. The diameters of the buckets are primarily 300mm and with varying embedment ratio. These tests are reported in part II of this thesis. The tests carried out in the laboratory are subjected to loads comparable with load from offshore wind turbines. Thus the vertical load applied is low relative to the vertical bearing capacity of the foundation and the load path given by M/DH varies between 0.37 and 8.7. The former corresponds to loads from waves and current whereas the latter corresponds to loads from wind.

Prior to this work a large set of experiments with a vertical load corresponding to 50% of the vertical bearing capacity is carried out in the laboratory on the same sand. These tests are performed on 200mm buckets with an embedment ratio varying from 0 to 1 and covers the entire radial plane. These tests have been evaluated during this work and are reported in Larsen and Ibsen (2006a,b)

6.1. Combined peak capacity

The experiments carried out at Aalborg University are especially relevant for considering the drained combined capacity of bucket foundations in sand. Two failure criteria's are considered in the following. The first criterion describes the capacity at low vertical load whereas the second describes the full capacity according to the macro model approach. At failure the yield surface according to the macro model corresponds to the failure surface by replacing V_{pre} with V_{peak} , i.e. the ratio of V_{pre}/V_{peak} is equal 1.

6.1.1. Linear failure criteria at low vertical load

A linear relation between the moment capacity and the applied vertical load are observed from tests subjected to low vertical load. The following equation is found to describe this relation, Byrne et al (2003). The equation is based on a limited number of tests with $d/D=0.5$.

Equation 6.1
$$\frac{M}{D} = \left(f_1 + \frac{f_2}{k} \right)^{-1} (V + f_3 W)$$

where k is the height of impact normalized with the diameter of the bucket foundation, h/D . The relation and the value of the parameters fitted are presented in chapter 4. The constants, f in Equation 6.1 are found to be independent of k , though only supported by a limited number of experiments. Equation 6.1 yields a failure criteria that is linear in not only the planes along the V -axis but also in the radial planes for constant values of f_i .

The linear relation between the moment capacity and the vertical load applied is supported by the results from laboratory tests on bucket foundations presented in Part II, see Figure 6.1. The capacities in the radial plane are shown in Figure 6.2. The linear relation in this plane can from the performed results not be validated nor rejected. The relation in Equation 6.1 is shown in the figures for comparison. The parameters used are given by Byrne & Houlsby (2003) for bucket foundations with an embedment ratio equal 0.5, see chapter 4.

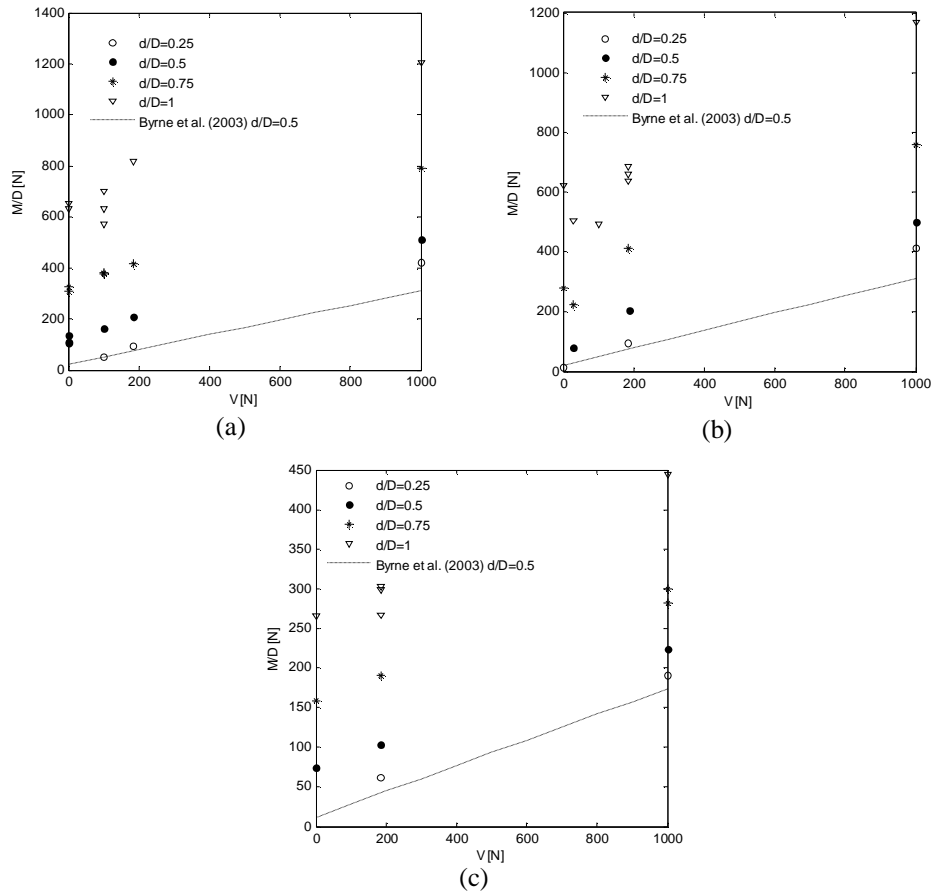


Figure 6.1 Failure values from tests with low V/V_{peak} values and a height of impact equal (a) $h=2610\text{mm}$, (b) $h=1740\text{mm}$ and (c) $h=110\text{mm}$.

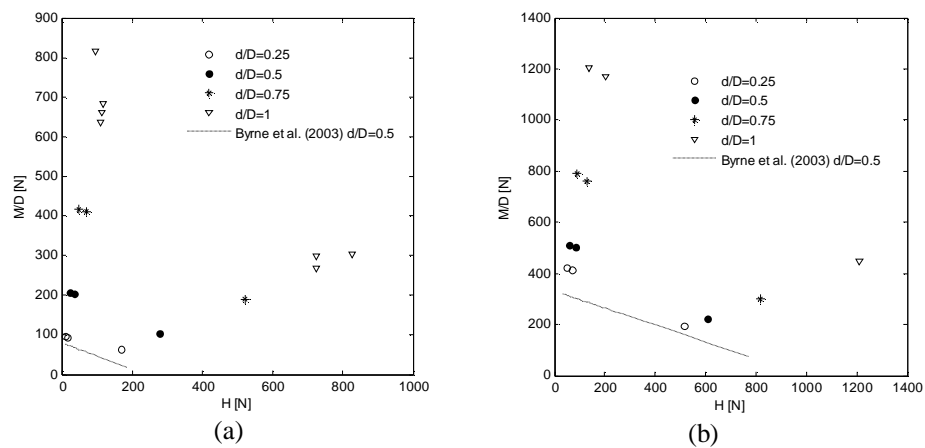


Figure 6.2 Failure values from tests with low V/V_{peak} values with a vertical constant load equal (a) $V=184\text{N}$, (b) $V=1000\text{N}$.

It is seen that Equation 6.1 does not fit the observed capacities with the given parameters. The failure surface after Equation 6.1 intersects the V-axis at a value corresponding to f_3W , which physically must correspond to the vertical tension capacity. It is therefore suggested to describe the combined capacity as a function of the tensile capacity, V_t instead of f_3W . The following linear relation is found to capture the capacities observed in the laboratory well.

$$\frac{M}{D} = a \cdot (V - V_t)$$

Equation 6.2

$$a = \left(f_1(k) + f_2(k) \frac{d}{D} \right)$$

where a is an inclination factor and V_t is the vertical tension capacity according to the standardized sign convention adopted.

Equation 6.2 is calibrated to the experimental data and is shown along the V-axis in Figure 6.3. The tensile capacity is evaluated from Equation 5.13. Alternatively the tensile capacity can be calculated using the method by Houlsby et al. (2005) in equation 4.14, which takes into account the reduction in stresses close to the skirts in tension. The first method has been found to fit the measured capacities at a much higher accuracy, with a value of $K \tan(d)$ equal 2. At this point it is estimated that both methods are equal accurate due to non experimental evidence available. A value of $K \tan(d)$ equal 2 though seems high and is ascribed the installation method.

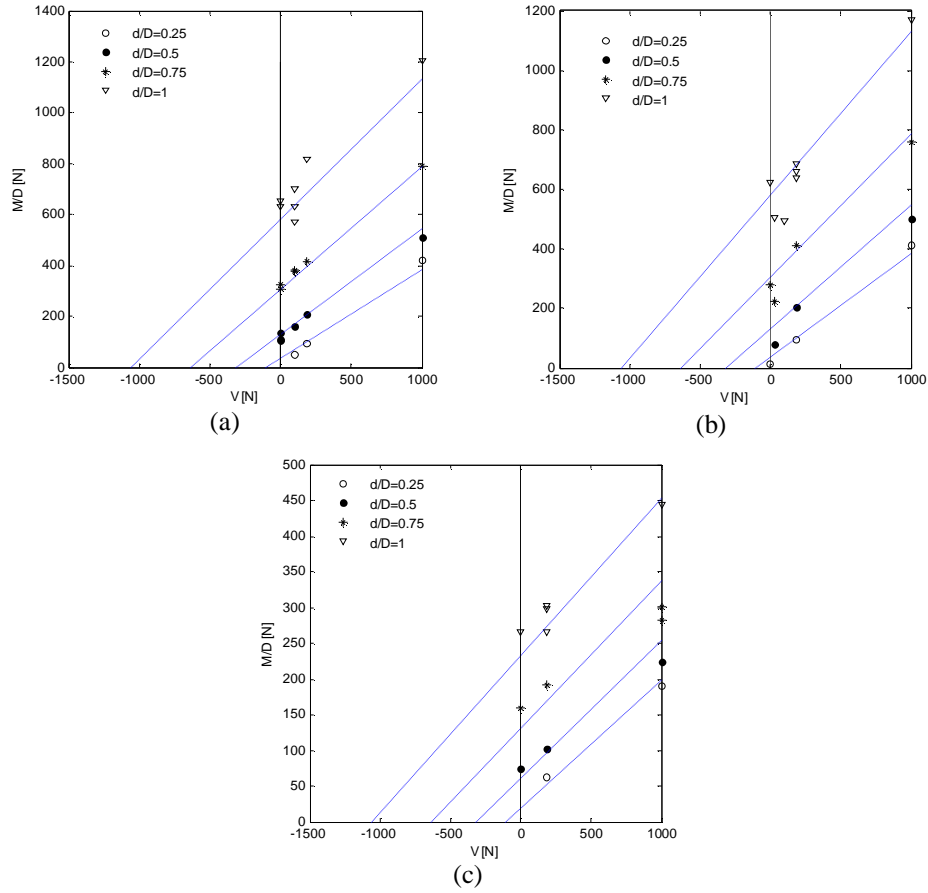


Figure 6.3 Proposed failure criterion compared with experimental failure values for tests with low V/V_{peak} values and a height of impact at (a) $h=2610\text{mm}$, (b) $h=1740\text{mm}$ and (c) $h=110\text{mm}$

The relation proposed in Equation 6.2 is seen to capture the observed capacities well. It is observed from the test results that the inclination factor, α is a function of both the embedment ratio as well as the height of impact, i.e. k . Unfortunately there are not enough information available to entirely determine this relation with the available test results. The value of α that fits the experiments is shown in Figure 6.4. It is clear from the figure that there is a linear relation between α and the embedment ratio as assumed in Equation 6.2. The relation with the height of impact, k is however less clear from the figure. An increase in α going towards an asymptotic value is observed for increasing k . Further experiments are necessary if this variation is to be pursued further.

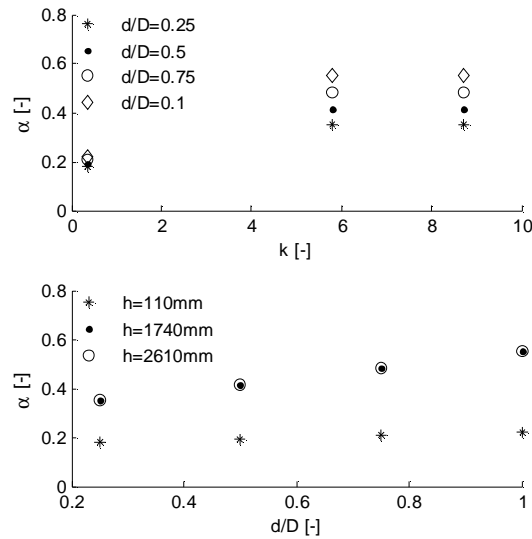


Figure 6.4 Variation of the measured failure parameter: α .

The parameters f_1 and f_2 in the proposed failure criterion are determined from the inclination factors, α above and are given in Table 6.1. The parameters are illustrated in Figure 6.5 with a proposal of a possible intermediate variation. The parameters are found to go towards an asymptotic value at high values of k . The reason for this is likely due to the change of failure mechanism, which for a given height of impact will be dominated by the moment and thereby becomes constant.

Table 6.1 Fitted failure parameters.

h [mm]	$k=h/D$	f_1	f_2
110	0.37	0.167	0.053
1740	5.8	0.283	0.267
2610	8.7	0.283	0.267

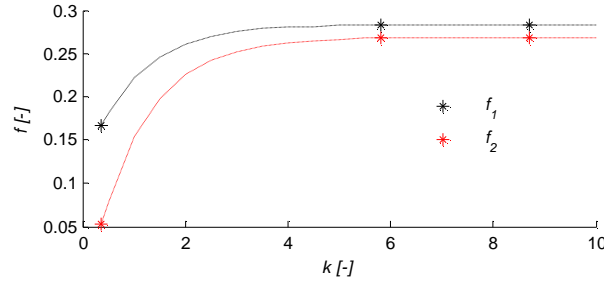


Figure 6.5 Parameters for proposed failure criterion given in Table 6.1. A Possible variation of f_1 and f_2 is shown as well.

The value of the failure parameters in Equation 6.2 is found to be a function of k , thus the relation in the radial plane is non-linear. The failure criteria in the radial plane with the variation of the failure parameters proposed in Figure 6.5 are shown in Figure 6.6. The proposed failure criterion is seen to capture the measured failure values well and gives a reliable intermediate variation of the failure criterion, cf. chapter 4. At low H values the fitted expression in Figure 6.6 though exhibits more curvature than expected cf. chapter 4.

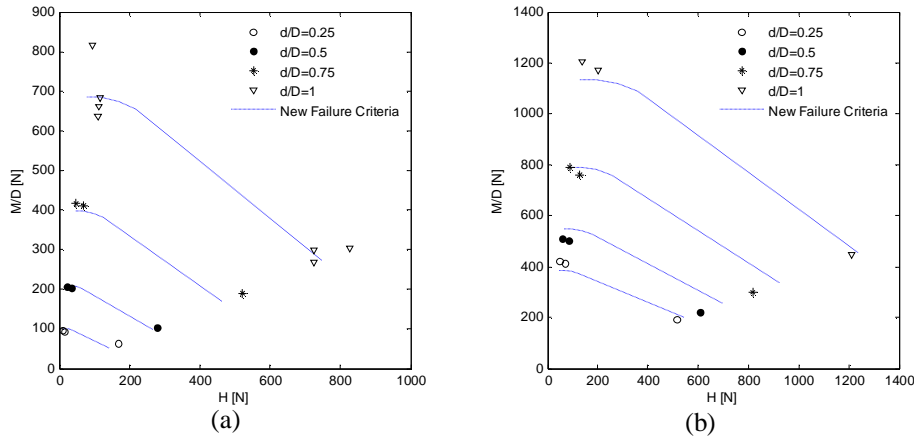


Figure 6.6 Measured loads and plastic displacement increments at failure, for tests with a vertical dead load of (a) 184N and (b) 1000N. Proposed failure criterion is shown as dotted lines.

The proposed failure criterion in Equation 6.2 is found to capture the static combined capacity of bucket foundations in saturated dense sand exposed to small vertical load well. Only few results from similar tests are available in the literature. Tests on bucket foundations subjected to low vertical load in loose dry sand are published in Byrne et al. (2003). These tests are performed on a bucket foundation with a diameter of 293mm, an embedment ratio equal

0.5 and with a low M/DH -ratio. The failure values from these tests can be used to determine the parameter, α in Equation 6.2 for loose sand. The tension capacity of these tests is assumed to correspond to the value of $f_3 W$ fitted from these tests. The result is shown in Figure 6.7 with the corresponding values from the tests presented above.

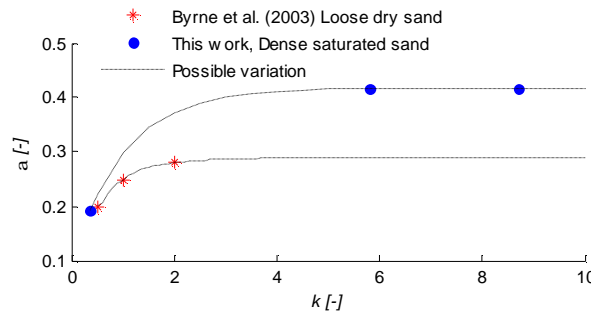


Figure 6.7 Value of inclination factor, α from bucket foundation tests $d/D = 0.5$.

A plausible variation of the inclination factors from Byrne et al. (2003) is proposed in Figure 6.7. The inclination factor is assumed to go towards an asymptotic value as shown previously. The asymptotic value of α is though smaller for these tests due to the difference in density and strength. At small values of k the inclination factors are seen to intersect for the two tests series.

If the variation of α is supposed to be unaffected of the soil strength the variation must according to Figure 6.7 be close to linear until reaching the asymptotic value at a value of k at approximately 4. This linear relation results in a failure criterion in the radial plane as shown in Figure 6.8. Both relations will fit the measured capacities at low and high height of impact. The combined capacity at low horizontal load is however seen to decrease abruptly with a slight decrease of k , corresponding to an increase in H in the figure. This failure criterion does not correspond to any other observations in the literature. Thus the curved variation in Figure 6.5 is concluded to be a plausible approximation to the correct variation of f_1 and f_2 .

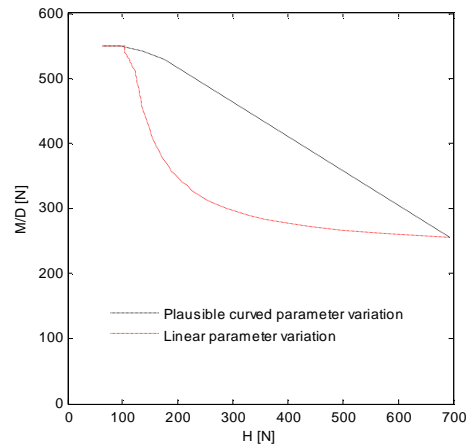


Figure 6.8 Failure criterion from proposed parameter variation compared with a linear parameter variation.

6.1.2. Complete 3-D failure criteria “Macro model approach”

A simple failure criterion is proposed above which is found to capture the measured capacities of bucket foundations subjected to combined loads well at low vertical load. Alternatively the yield surface expressions from the macro model approach can be used to describe the capacity in case of combined loading, see chapter 4. In case of failure the normalization with the vertical preload is replaced with the vertical bearing capacity in these expressions. The macro model approach is particular relevant if larger vertical loads is present, as it is supposed to capture the complete 3 dimensional combined capacity. A survey of the capacity of bucket foundations from loading tests performed in the geotechnical laboratory at Aalborg University prior to this work is shown in Figure 6.9 and Figure 6.10.

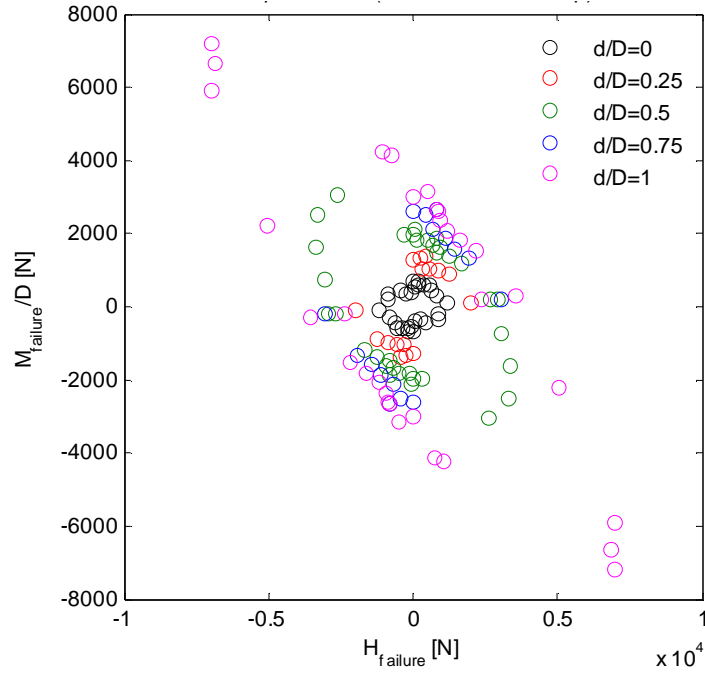


Figure 6.9 Survey of failure values from tests performed at $V/V_{peak}=0.5$. $D=200\text{mm}$.

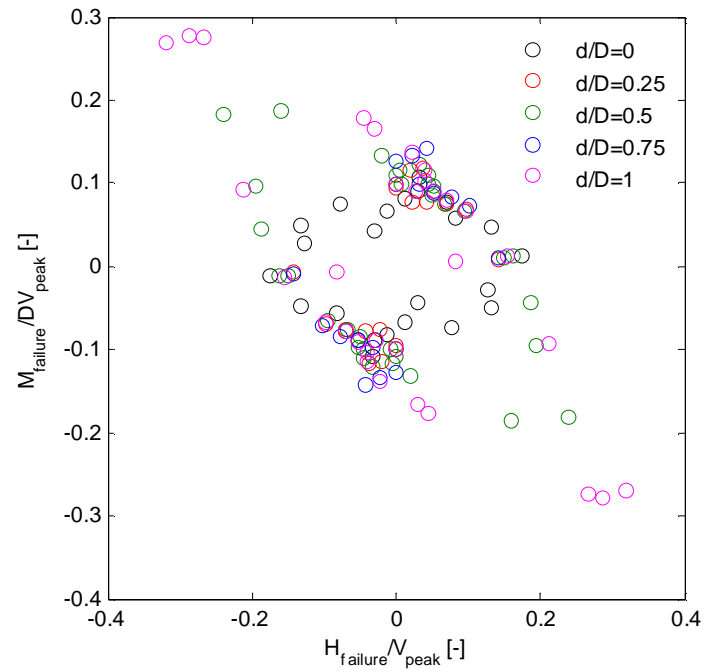


Figure 6.10 Survey of normalized failure values from tests performed at $V/V_{peak}=0.5$. $D=200\text{mm}$.

The failure values in Figure 6.9 are seen to agree with the observations made by Byrne and Houlsby (1999). The capacity is seen to form a rotated ellipse in the radial plane and the rotation increases for increasing embedment ratios. The loads relevant for offshore wind turbines are related to the first quadrant in Figure 6.9. From the figure it is seen that the increase in the combined capacity in this quadrant is most significant for low embedment ratios. The opposite is observed in case of low V (section 6.1.1) where the relative increase in capacity from e.g. Figure 6.6 is seen to increase for increasing embedment ratios.

In Figure 6.10 the capacities are normalized with the vertical bearing capacity determined from the relative density cf. chapter 5. It is clear from this figure that the normalized capacity does not give a unique failure surface. Thus the failure parameters vary with d/D . This corresponds well with the experimental observations from the literature as presented in chapter 4.

In the first quadrant the normalized capacities in Figure 6.10 are seen to be almost identical for all the tested values of d/D . This corresponds to the observations by Byrne and Houlsby (1999) regarding the yield surfaces. The tests in Figure 6.9 and Figure 6.10 are carried out with a vertical load corresponding to $0.5 \cdot V_{peak}$. At low vertical load the normalized capacities in the first quadrant is however different due to different values of V/V_{peak} . These normalized failure values are presented in Figure 6.11. From the figure it is clear that the normalized moment capacity is dependent of the embedment ratio. The capacities are all from tests carried out in the first quadrant in the radial plane. From the figure it can further more be seen that the normalized capacity for a given embedment ratio are unique for $h = 2610\text{mm}$ and $h = 1740\text{mm}$. This corresponds well with the observations in section 6.1.1. A unique failure criterion was found for tests exposed to large height of impact with a given diameter of the foundation. The obtained observations can be described as follows when any influence of the vertical preload and size effects are ignored.

Equation 6.3

$$\frac{M}{DV_{peak}} = f(d/D, V/V_{peak}, M/HD) \quad \text{for } M/HD < 5$$

$$\frac{M}{DV_{peak}} = f(d/D, V/V_{peak}) \quad \text{for } M/HD > 5$$

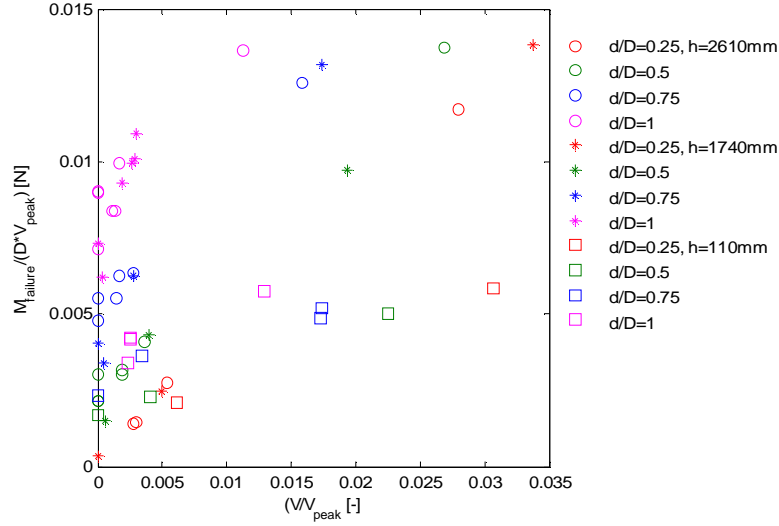


Figure 6.11 Survey of normalized failure values from tests with low V/V_{peak} , $D=300\text{mm}$.

Due to limited experience with the behaviour of bucket foundations only few yield surface expressions are proposed in the literature. Byrne and Houlsby (1999) initially suggested that the yield surface expression from the macro model “Model C” was used as a yield surface for bucket foundations, see Equation 6.4. This expression is presented in chapter 4 and is in Figure 6.12 compared with the capacities of bucket foundations measured in the laboratory. The results originate from tests with a value of V/V_{peak} at approximately 0.5. The values of V_{peak} are calculated using a reduced friction angle equal 42 degrees, cf. chapter 5.

Equation 6.4

$$f = \left(\frac{H}{h_0 V_{peak}} \right)^2 + \left(\frac{M}{m_0 D V_{peak}} \right)^2 - 2a \left(\frac{H}{h_0 V_{peak}} \right) \left(\frac{M}{m_0 D V_{peak}} \right) - b_{12} \left(\frac{V}{V_{peak}} \right)^{2b_1} \left(1 - \frac{V}{V_{peak}} \right)^{2b_2} = 0$$

$$\text{where } b_{12} = \left(\frac{(b_1 + b_2)^{b_1 + b_2}}{b_1^{b_1} b_2^{b_2}} \right)^2$$

The yield surface parameters a , h_0 and m_0 at failure can be determined from tests conducted at $V/V_{peak} = 0.5$ if $b_1 = b_2$. At failure the value of h_0 and m_0 corresponds to the peak value of these, i.e. $h_{0,peak}$ and $m_{0,peak}$. In chapter 4 a

linear relation between these yield-surface parameters and the embedment ratio was detected. The failure surfaces shown in Figure 6.12 are plotted using these and with a value of the curvature factors b_1 and b_2 equal to unity. The linear relation is determined from experiments with an embedment ratio between 0 and 0.66, thus only results from the experiments with embedment ratios of 0, 0.25 and 0.5 are shown in the figure (open circles). The measured capacities in the figure are mirrored in a line that divides the second and fourth quadrant equally.

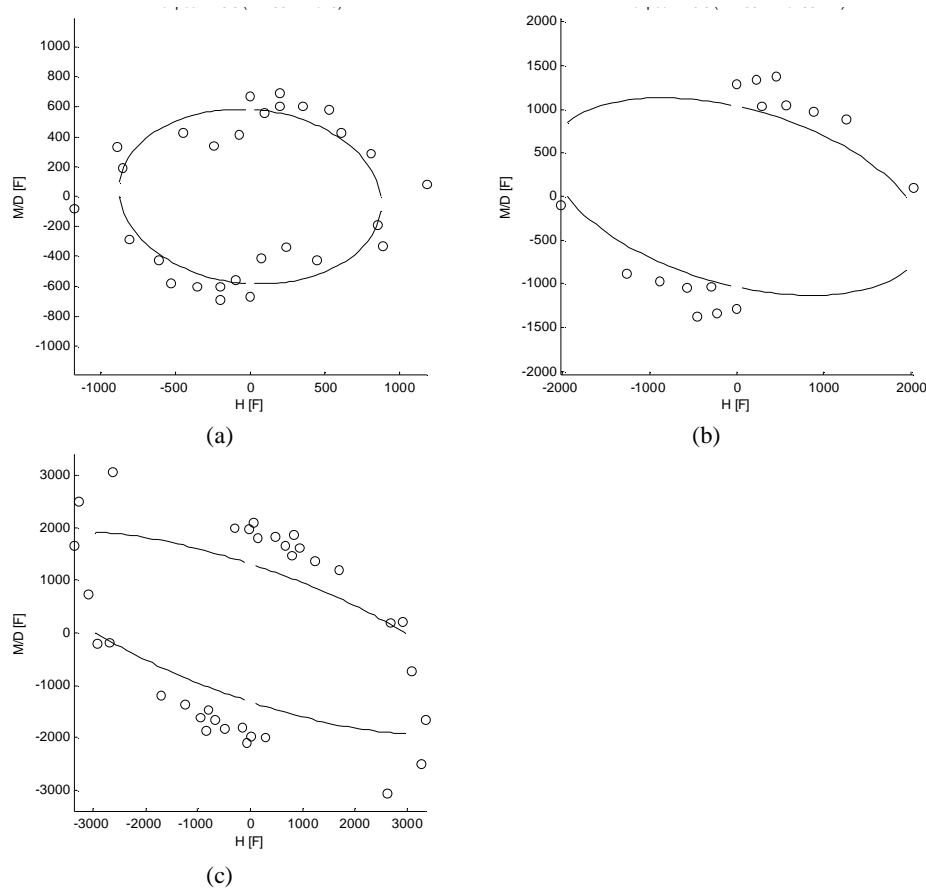


Figure 6.12 Comparison of measured failure values and yield surface at failure by Byrne and Houlsby (1999). $V/V_{peak} \gg 0.5$ and (a) $d/D=0$, (b) $d/D=0.25$ and (c) $d/D=0.5$.

The failure criterion from “Model C” is from Figure 6.12 seen not to describe the measured capacities of bucket foundations satisfactorily with the yield surface parameters from chapter 4. The results from experiments with surface footings, see Figure 6.12a are though seen to be fitted with a better accuracy than the rest. The yield surface expression from “Model C” is developed from

tests on surface footings which intersects the V -axis at the origo. This is however not the case for bucket foundations. Moreover numerous experimental results exist in the literature, which indicates that the combined capacity of surface footings normalized with the corresponding vertical bearing capacity yields a failure surface that is only slightly affected of the soil properties. Thus the accordance between the yield surface at failure from Equation 6.4 and the measured capacities of surface footings is expected, with the parameters used.

Only limited information on the normalization procedure in case of bucket foundations are available in the literature. From Figure 6.10 and Figure 6.11 the normalization procedure is clearly observed to yield different failure surfaces, depending of the embedment ratio. The combined capacity of bucket foundations is greatly affected by the lateral earth pressure on the skirt and not only the overburden pressure as the pure vertical bearing capacity. Thus different failure parameters depending on both the embedment ratio and soil strength are necessary to describe the combined capacity. This was also seen from the literature study in chapter 4. The failure surface in Figure 6.12 is based on parameters estimated from tests performed at low preload ratios, V_{pre}/V_{peak} , whereas experiments within this work at failure corresponds to $V_{pre}/V_{peak} = 1$. Hence the discrepancies in Figure 6.12 are ascribed the dependence of V_{pre}/V_{peak} and D_r or j on the capacity of bucket foundations.

A yield surface expression that is capable of describing the combined capacity at a vertical load less then zero is presented in chapter 4, see Equation 6.5. This expression is derived from a limited set of experiments with two different bucket foundations with $d/D = 0.5$, Villalobos et al. (2005).

$$\text{Equation 6.5} \quad f = \left(\frac{H}{h_0 V_{peak}} \right)^2 + \left(\frac{M}{m_0 D V_{peak}} \right)^2 - 2a \left(\frac{H}{h_0 V_{peak}} \right) \left(\frac{M}{m_0 D V_{peak}} \right) - \left(\frac{b_{12}}{(t_0 + 1)^{(b_1 + b_2)}} \right) \left(\frac{V}{V_{peak}} + t_0 \right)^{2b_1} \left(1 - \frac{V}{V_{peak}} \right)^{2b_2} = 0$$

Based on the experimental results Villalobos et al. (2005) found that the value of t_0 varies with the ratio between the diameter of the bucket foundation and the thickness of the skirt. The value of t_0 controls the lower intersection of the failure surface with the V -axis, i.e. the vertical tension capacity. It is unlikely that the value of this is related to the ratio D/t , hence the following definition of t_0 is suggested:

$$\text{Equation 6.6} \quad t_0 = -V_t/V_{peak}$$

Equation 6.5 is in the following used to fit the measured capacities in Figure 6.10 with the definition of t_0 proposed in Equation 6.6. The values of the fitted yield surface parameters a , $h_{0,peak}$ and $m_{0,peak}$ at failure are given in Table 6.2 assuming a value of b_1 , b_2 equal 1. A value of $Ktan(d) = 2$ is used to estimate V_t . The value of the failure parameters in Table 6.2 is however non-sensitive to the choice of b_1 , b_2 and $Ktan(d)$ for $V/V_{peak} = 0.5$, cf. chapter 4.

Table 6.2 Failure parameters determined from loading tests.

d/D	a	$h_{0,peak}$	$m_{0,peak}$	t_0 ($D=200\text{mm}$)
0	-0,1	0,15	0,08	0
0,25	-0,4	0,16	0,092	0,002
0,5	-0,65	0,165	0,125	0,006
0,75	-0,75	0,16	0,133	0,009
1	-0,86	0,15	0,135	0,0127

The failure criteria fitted are shown in Figure 6.13. The failure criteria are seen to describe the measured capacities of the tested bucket foundations well. The scatter in results is ascribed the difference in the soil density between the tested sand samples. The experiments are carried out with identical vertical loads for each embedment ratio. Thus a small variation in the normalized load applied to the bucket during loading is present.

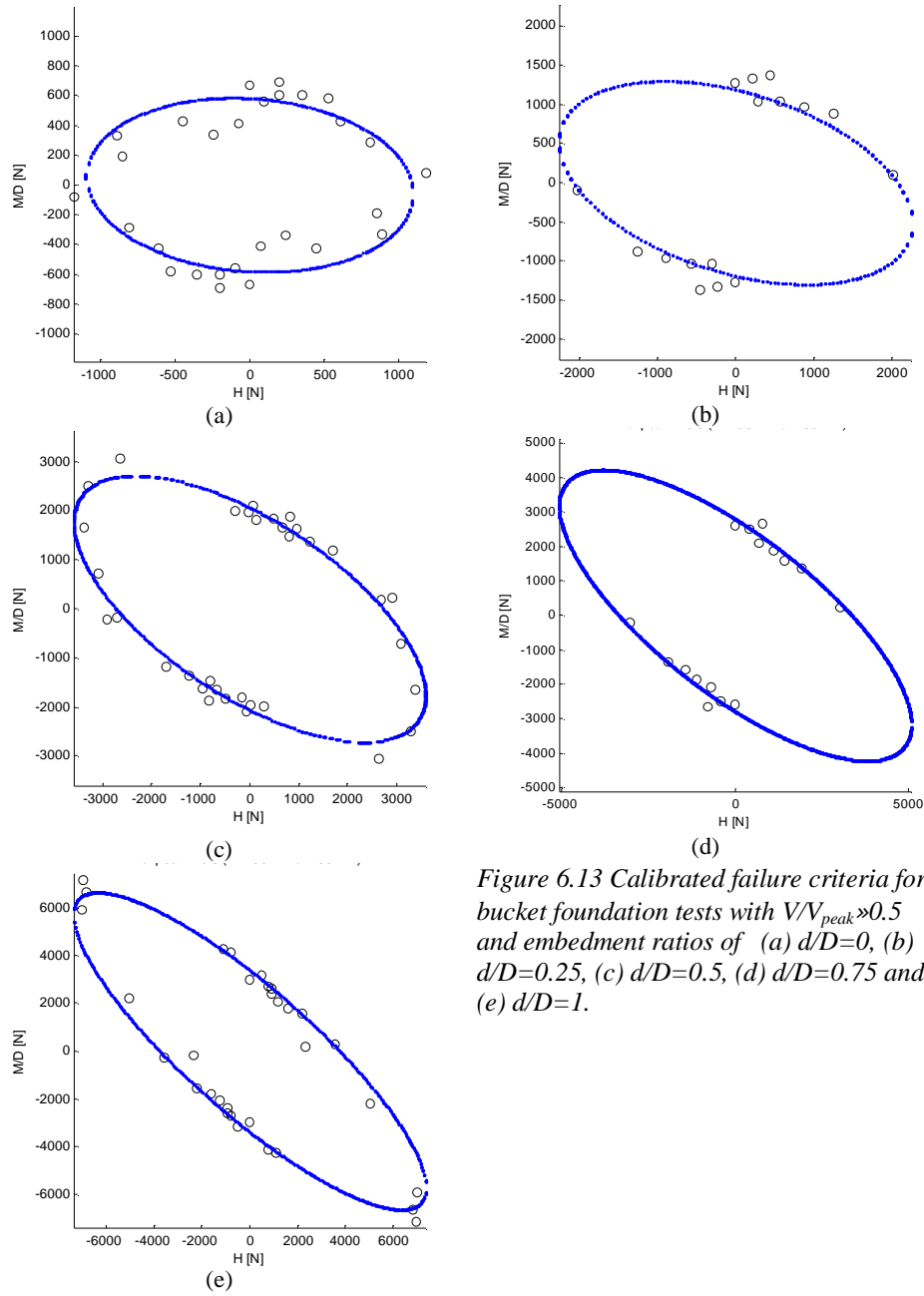


Figure 6.13 Calibrated failure criteria for bucket foundation tests with $V/V_{peak} \gg 0.5$ and embedment ratios of (a) $d/D=0$, (b) $d/D=0.25$, (c) $d/D=0.5$, (d) $d/D=0.75$ and (e) $d/D=1$.

The variation of the failure parameters in Table 6.2 are shown in Figure 6.14 to vary systematically with the embedment ratio of the bucket foundations. The value of $h_{0,peak}$ is seen to be almost constant at a value of 0.16 whereas $m_{0,peak}$ is increasing with the embedment ratio towards a value of 0.135 for

large embedment ratios. The opposite behaviour is observed from tests on bucket foundations in the literature, cf. chapter 4 where a constant value of $m_{0,peak}$ was found, Byrne (2000). The value of a is seen to decrease asymptotically towards a value larger than -1 for increasing embedment ratios. A value equal to -1 is shown in chapter 4 to change the shape of the yield surface from an ellipse in the radial plane to an open and convex surface.

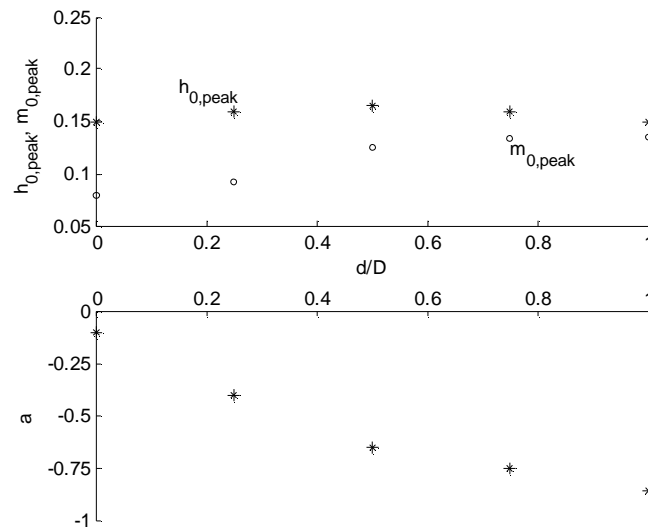


Figure 6.14 Variation of calibrated failure surface parameters.

The failure parameters determined in this section are compared with relevant values from chapter 4 in Figure 6.15 and Figure 6.16. From the figures no conclusions can be drawn, though the results support the assumption of a dependency with D_r and V_{pre}/V_{peak} . The values from Byrne (2000) in Figure 6.15 and Figure 6.16 are the only values determined from tests with bucket foundations. It must however be noticed that these are estimated from tests conducted at low preload ratio and extrapolated using Equation 5.9, which is based on tests with surface foundations. The above presented results are derived from loads at failure, i.e. V_{pre}/V_{peak} equal 1. Thus these corresponds to the peak values.

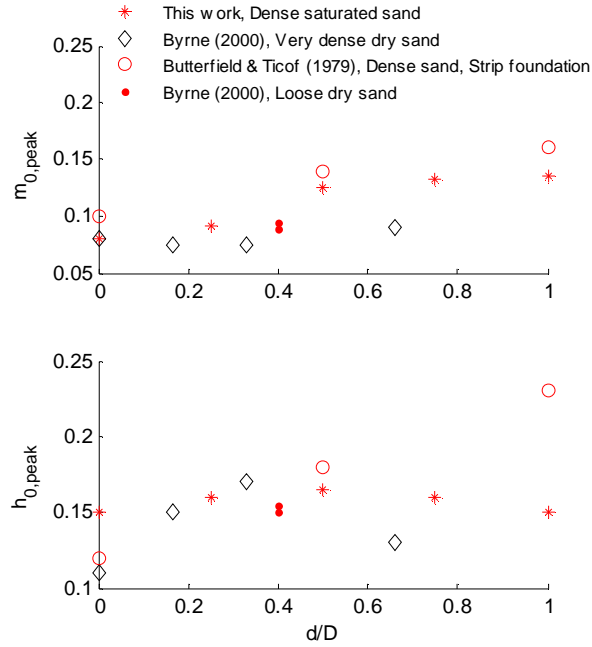


Figure 6.15 Comparison of failure parameters. Black colour indicates tests at low preload ratio and red tests at high

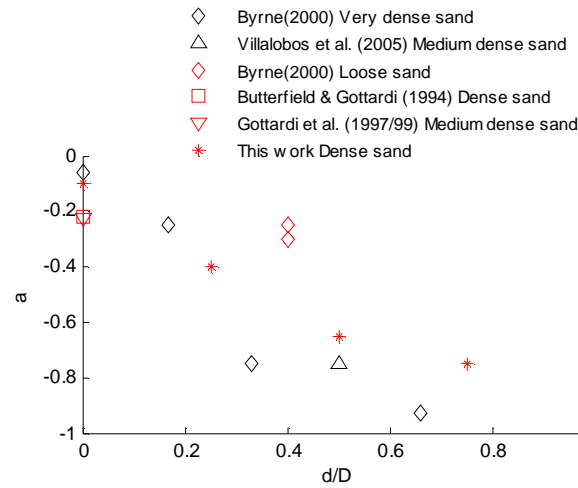


Figure 6.16 Comparison of the eccentricity parameter. Black colour indicates tests at low preload ratio and red tests at high

The shape of the failure surface in the radial plane is given by the parameters calibrated above. The shape along the V-axis is controlled by the value of b_1 , b_2 and the method used to estimate the vertical tension capacity. The value of b_1 can be calibrated from the laboratory tests presented in Part II performed at

low vertical load. The failure parameter b_2 is not possible to determine from the experimental data available, as tests with a vertical load close to the vertical bearing capacity is necessary. The failure surface at low vertical load is only minor influenced of the choice of b_2 , thus a calibration of b_1 is possible with the available test results. In Figure 6.17 and Figure 6.18 comparable failure values from the performed tests with low vertical load are compared with the failure criterion in Equation 6.5. A value of b_1 and b_2 equal 1 is used the tension capacity is estimated using Equation 4.13 with $K_{tand}=2$.

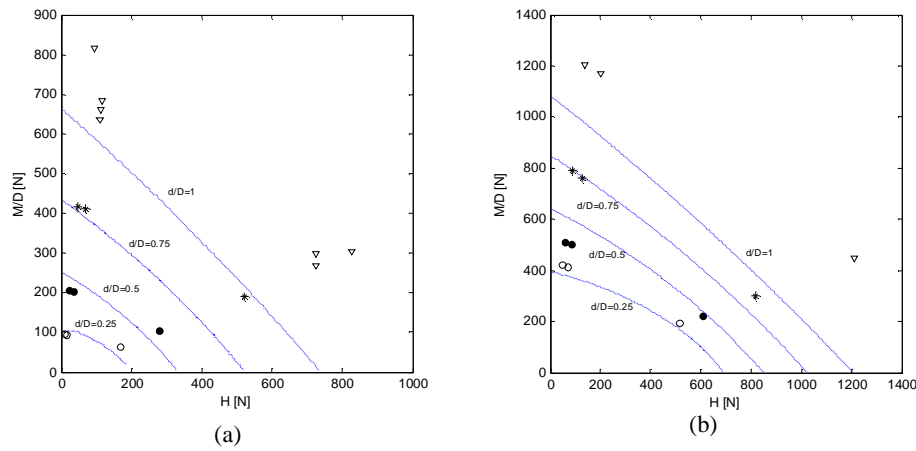


Figure 6.17 Failure values from tests performed at low V/V_{peak} values with (a) $V=184N$ and (b) $V=1000N$. The failure criteria (blue lines) are shown with parameters from Table 6.2, $K_{tand}=2$ and $b_1=b_2=1$.

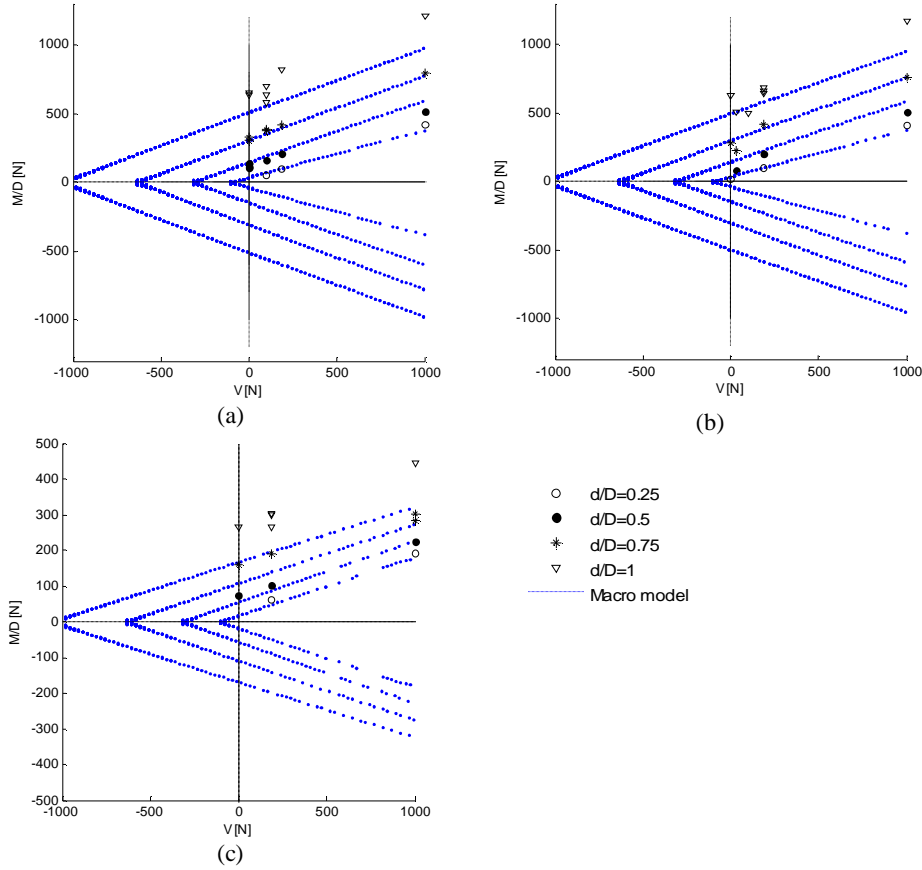


Figure 6.18 Failure values from tests performed at low V/V_{peak} value with a height of impact at (a) $h=2610\text{mm}$ (b) $h=1740\text{mm}$ (c) $h=110\text{mm}$. The failure criteria (blue lines) are shown with parameters from Table 6.2, $K\tan\theta=2$ and $b_1=b_2=1$.

The failure criterion in Equation 6.5 is seen from Figure 6.17 and Figure 6.18 to fit the observed capacities at low vertical load with the chosen parameters poorly. Especially at large embedment ratios the discrepancy are large. A better fit can be obtained by choosing a value of b_1 less than 1. The value of b_1 is calibrated against the experimental results in Part II and the corresponding failure criteria are shown in Figure 6.19.

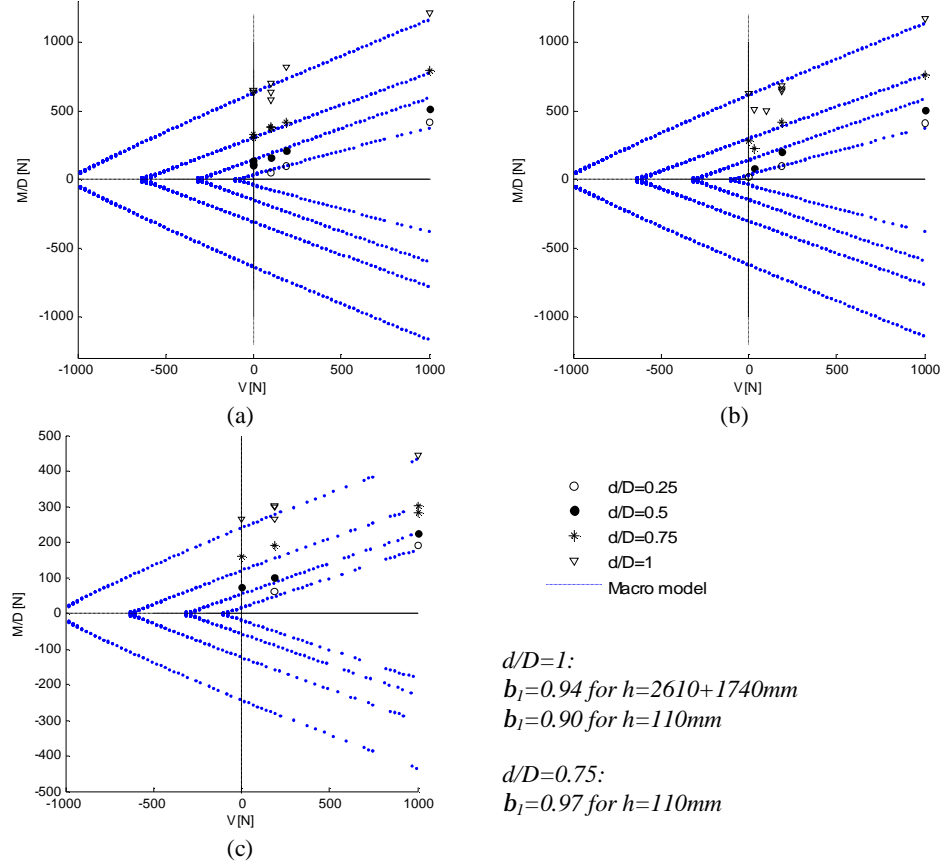


Figure 6.19 Failure values from tests performed at low V/V_{peak} values with a height of impact at (a) $h=2610\text{mm}$ (b) $h=1740\text{mm}$ (c) $h=110\text{mm}$. The failure criteria (blue lines) are shown with parameters from Table 6.2, $K_{tan}(b)=2$ and $b_2=1$. $b_I=1$ unless specified.

The proposed failure criterion is seen to fit the observed capacities at low vertical load with reasonable accuracy when the value of b_I is varied, see Figure 6.19. This corresponds to the observations by Cassidy (1999), who found a slight variation with the ratio H/DM corresponding to the height of impact normalized with the diameter of the foundation.

The fitted value of b_I in Figure 6.19 is unless specified 1.0. The value is seen to vary systematically to some extent with the embedment ratio and the height of impact. The value of b_I is generally seen to decrease with an increase in d/D and a decrease in h . The failure surfaces in the radial plane corresponding to Figure 6.19 are not plotted due to the dependence of h on b_I .

The investigated failure criterion is found capable of describing the combined capacity of the tested bucket foundations. A few test results are though seen from Figure 6.19 not to coincide with the calibrated failure parameters. Especially two tests are identified in this connection. These are test no. 0104-2002 and 0104-5601, which is test of bucket foundations with an embedment ratio of 0.5, a vertical load of 1000N and a height of impact at 1740 and 2610 respectively. The capacities of these two tests are systematically over predicted by the calibrated failure criteria, thus recurrence of the experiments is desirable.

The failure criterion has been calibrated using a vertical tension capacity, which is calculated from the stresses at rest by Equation 4.13. In this expression no account is taken on the reduction of vertical stress close to the skirt due to the frictional forces further up the skirt during uplift, cf. chapter 4. In Equation 4.14 this reduction of stresses near the skirt during tension is taken into account. The result of a calibration using this tension capacity with a value of $K \tan(\delta) = 1$ and $m = 2$ as suggested by Houlsby et al (2006) is shown in Figure 6.20. The values are based on tension capacity tests with a large scale bucket foundation in sand with a relative density corresponding to the tests within this chapter.

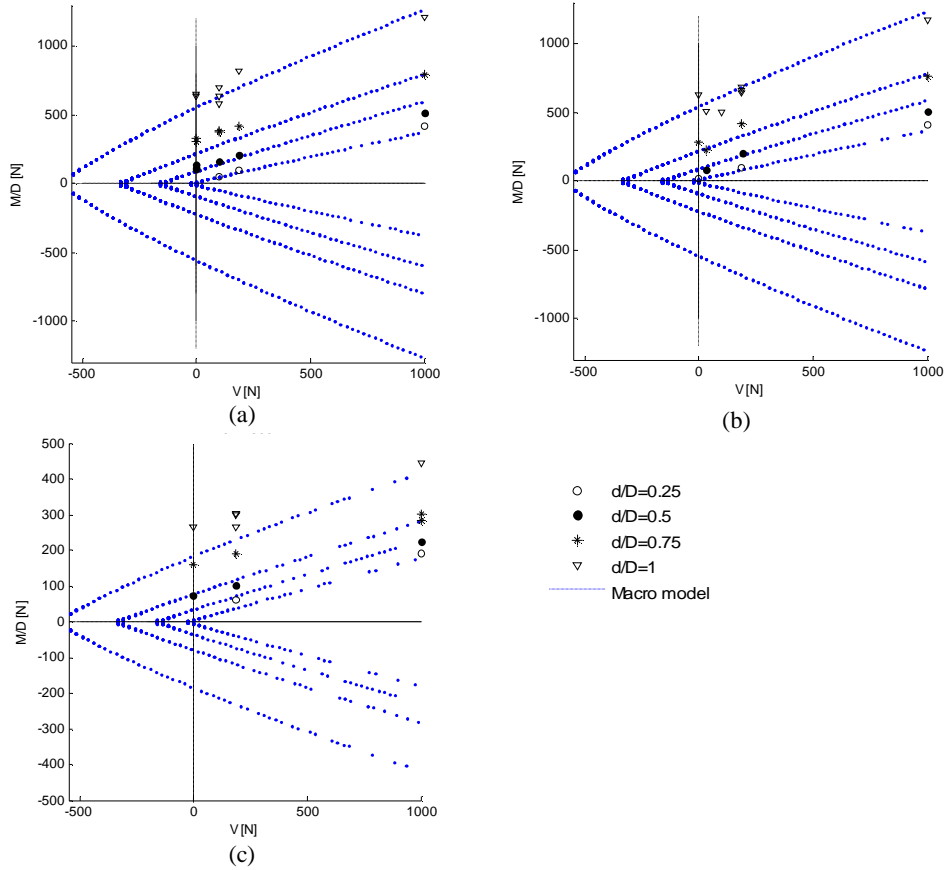


Figure 6.20 Failure values from tests performed at low V/V_{peak} values, with a height of impact at (a) $h=2610\text{mm}$ (b) $h=1740\text{mm}$ (c) $h=110\text{mm}$. The failure criteria (blue lines) are shown with parameters from Table 6.2, $K\tan(b)=1$, $m=2$ and $b_2=1$.

The calibration in Figure 6.20 using the modified expression for the tensile capacity is seen to give an overall good agreement with the measured capacities. Though at low V and h , the predicted capacity, is to some extent seen to under estimate the measured capacity. The calibrated values of b_1 are given in Table 6.3 and the variation with the embedment ratio is shown in Figure 6.21. The decrease in b_1 with increasing embedment ratio is recognized from the calibration in Figure 6.20, though it is more pronounced for this calibration. This dependence is in contrast with the observations from inclined loading tests of strip foundations on dense sand by Butterfield and Ticof (1979) who found that the end slopes of the failure surface along the V -axis are independent of d/D at failure.

Table 6.3 Calibrated values of b_l using a tension capacity calculated with $K_{tan}(d)=1$ and $m=2$

d/D	0,25	0,5	0,75	1
b_l	0,98	0,96	0,93	0,84

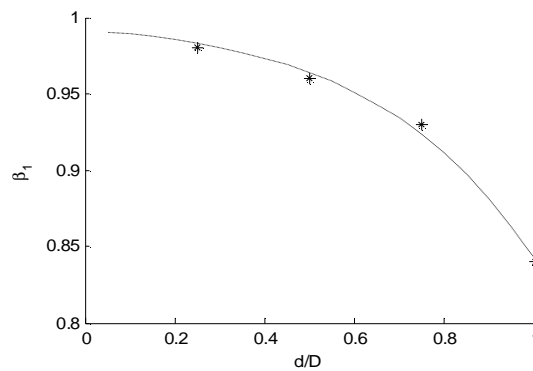


Figure 6.21 Calibrated values of b_l using a tension capacity calculated with $K_{tan}(d)=1$ and $m=2$

The values in Table 6.3 are calibrated without considering the differences in the height of impact. The calibrated failure criteria in Figure 6.20 indicates that there might be a slight tendency that b_l is dependent of h . For $d/D=1$ the capacity is for instance seen to be over-predicted at $h=2610\text{mm}$ and $h=1740\text{mm}$ while it is under-estimated at $h=110\text{mm}$.

The fitted variation of b_l in Figure 6.21 is seen to yield a value slightly different from 1 for a surface foundation. Combined loading tests with surface foundations subjected to low vertical load have not been performed during this work. A value of b_l close to unity for $d=0$ is however justified from results presented in chapter 4.

The calibrated failure planes in the radial plane corresponding to Figure 6.20 are shown in Figure 6.22. It is seen from the figure that the failure criterion underestimates the capacity at low V and h , thus there is an indication of a , $h_{0,peak}$ and $m_{0,peak}$ being dependent of the vertical load level, V/V_{peak} and the load path, $h=M/H$.

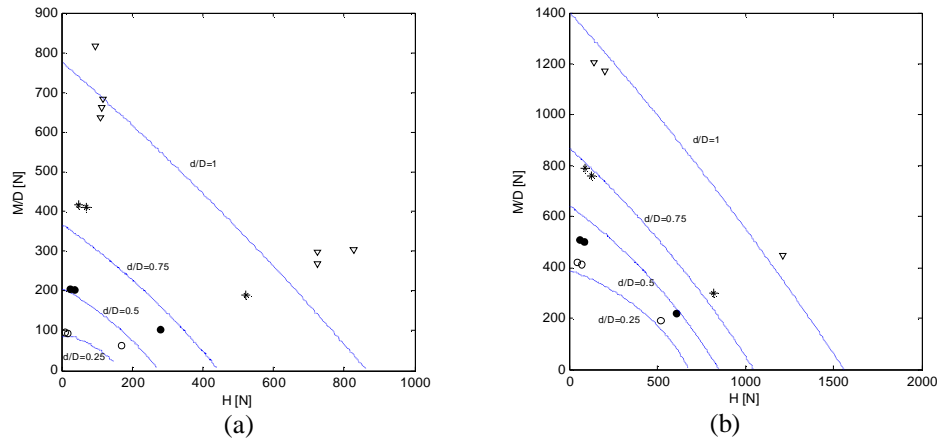


Figure 6.22 Parameters from Table 6.2 with $K_{\text{tand}}=1$ and $m=2$ (a) $V=184N$, (b) $V=1000N$.

The value of the failure parameter b_1 is shown to be sensitive to the calculation method used to estimate the vertical tension capacity. Two methods have been used in the calibration of the failure parameter. The first method assumes a frictional resistance between the soil and the skirt based on the Mohr Coulomb model and stresses calculated at rest. The second method used involves a stress situation that takes into account the reduction in stresses close to the skirts in tension. The second method is found to be capable of fitting the measured capacities with only minor variation of b_1 with the load path followed. This is however not the case for the first method where b_1 is found to change with the load path. Thus plotting the entire 3D failure surface with this method must be done partially.

The value of the failure parameter b_2 is not investigated since it requires a set of loading tests with a vertical load near the vertical bearing capacity. It is though found that $\beta_2 < \beta_1$, cf. chapter 4.

An investigation of the tension capacity of bucket foundations are undergoing at the time being at Aalborg University. Vertical tension capacity tests of a bucket foundation with $D=d=500\text{mm}$ is found to yield a capacity of approximately 2kN. From this result it is concluded that the vertical tension capacity should be estimated by including the stress reduction near the skirt in tension as this yields a tension capacity closer to the measured with the parameters used in this chapter.

6.2. Combined behaviour prior to failure

During loading of the bucket foundations the displacements, u , w and q are within the macro model approach assumed to be the sum of the corresponding elastic and plastic displacements. The elastic and plastic deformations are determined individually. The elastic deformations can be calculated as shown in appendix C from the elastic stiffness of the soil, i.e. Young's modulus, E or the shear modulus, G .

In Figure 6.23 the displacements from vertical loading tests are separated using an elastic stiffness that fits the unloading-reloading path. In some cases this stiffness is too small compared with the initial stiffness, causing negative plastic deformations in the initial state if used. The decrease in soil stiffness can be due to e.g. the dilation of the dense sand or the sliding between steel and soil, both occurring at large deformations. In case of negative plastic deformations, the shear stiffness is determined as the stiffness that gives zero plastic deformations prior to the preload.

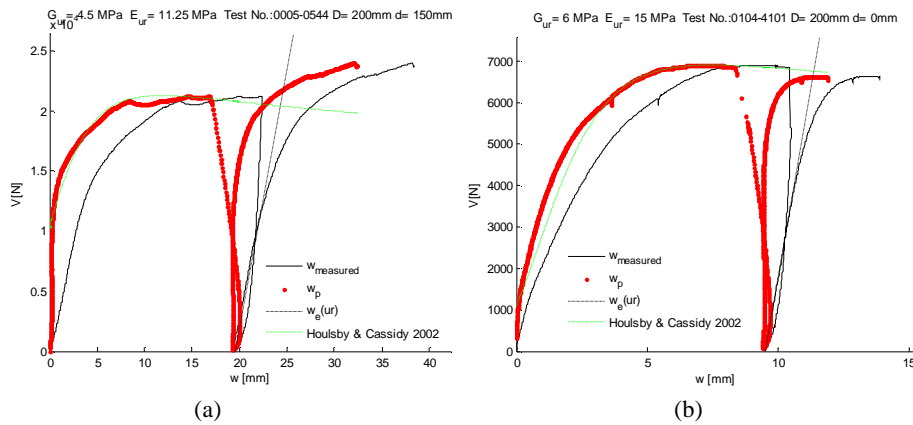


Figure 6.23 Separation of elastic and plastic displacements. (a) Test No. 0005-0544 $G=4.5 \text{ MPa}$ $D=200 \text{ mm}$ $d=150 \text{ mm}$ (b) Test No. 0104-4101 $G=6 \text{ MPa}$ $D=200 \text{ mm}$ $d=0$.

The vertical preload is used as hardening parameter in the macro model for combined loaded foundations. The vertical preload is generally determined merely from the vertical plastic displacement. The expression in Equation 6.7 by Housby and Cassidy (2002) is found to describe the vertical load tests carried out in the laboratory with a high degree of accuracy. This is tests with both surface foundations as well as bucket foundations. The function is presented in chapter 4.

Equation 6.7

$$V_{pre} = \frac{k w_p + \left(\frac{f_p}{1 - f_p} \right) \left(\frac{w_p}{w_{pm}} \right)^2 V_{peak}}{1 + \left(\frac{k w_{pm}}{V_{peak}} - 2 \right) \left(\frac{w_p}{w_{pm}} \right) + \left(\frac{1}{1 - f_p} \right) \left(\frac{w_p}{w_{pm}} \right)^2}$$

From the vertical load tests available the general bearing capacity formula is in chapter 5 found capable of estimating the vertical bearing capacity V_{peak} in Equation 6.7. The value of k and f_p that fits the experiments connected to this work has been found to 500 and 0.8 respectively.

The shear stiffness is generally found to vary excessively for the vertical load tests performed, see Figure 6.24. A tendency of a linear relation between the shear stiffness and the dimensions of the tested foundations is though observed and shown in the figure.

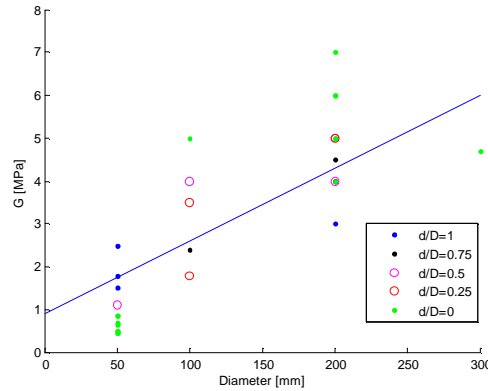


Figure 6.24 Shear stiffness of the tested soil based on vertical loading tests.

The vertical plastic displacement at failure, w_{pm} corresponding to the shear stiffness in Figure 6.24 is found to vary significantly between the tests. The value of w_{pm} is presented in Figure 6.25. The results indicate an increase in w_{pm} for large embedment ratios. No further conclusion regarding this can however be drawn from the figure. Thus a linear trend is suggested in the figure though large scatter is observed especially for bucket foundations with a diameter equal 200mm.

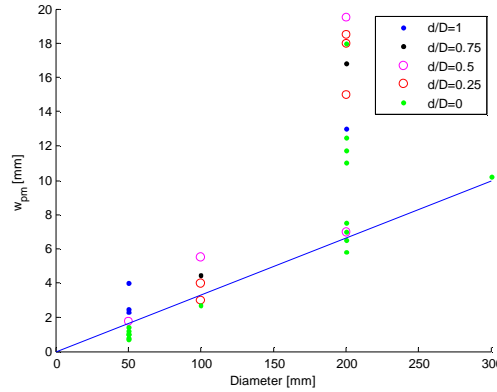


Figure 6.25 Plastic vertical settlement at failure from vertical loading tests, w_{pm} .

In fact both G and w_{pm} must be a function of the relative density of the tested sand which varies a little between the tests as well as the dimensions of the tested buckets. This is due to the dependency of the relative density and the stress level on the behaviour of sand, cf. chapter 2. The influence of the relative density has been investigated for the tests in Figure 6.24 and Figure 6.25. No systematic variation of the measured values of G and w_{pm} was however observed from this.

The elastic stiffness is also determined from the combined loading tests using the elastic stiffness matrix presented in appendix C. The elastic stiffness is determined from the unloading reloading paths where a general stiffness of $E = 15 \text{ MPa}$ is found corresponding to a shear modulus of $G = 6 \text{ MPa}$. An example of the separated displacements is shown in Figure 6.26, where also the directions of the incremental plastic displacements are shown at selected load levels. The vertical displacement, w is seen from the elastic stiffness matrix to be purely plastic due to constant vertical load during the tests. It is further more seen that for this experiment, the bucket foundation moves upward during loading. Hence the hardening law is not merely a function of the vertical plastic displacement as assumed in the macro model approach. This was also noticed by Byrne (2000) and Byrne & Houlsby (2001) who suggested a hardening law as a weighted sum of all the plastic displacement components. This relation is not pursued further here.

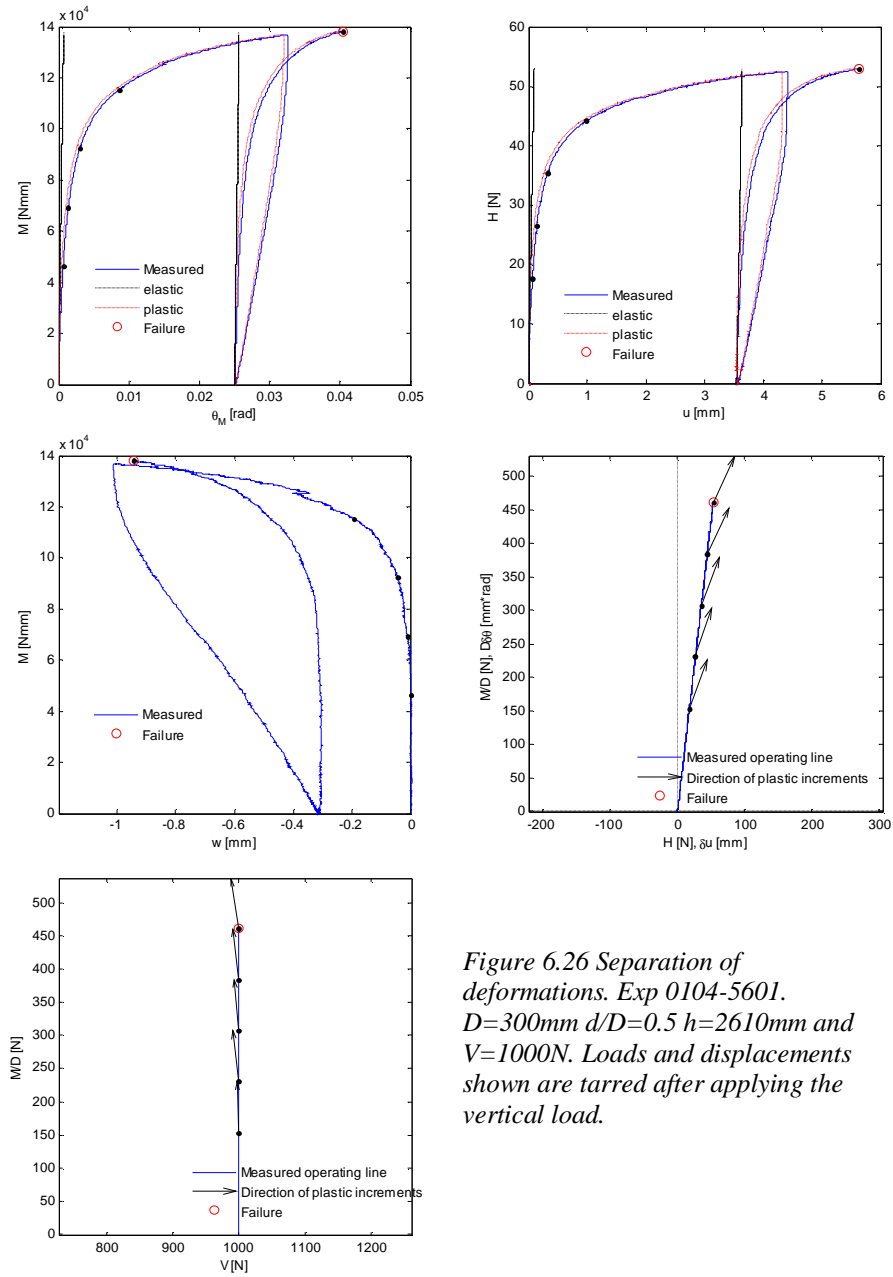


Figure 6.26 Separation of deformations. Exp 0104-5601. $D=300\text{mm}$ $d/D=0.5$ $h=2610\text{mm}$ and $V=1000\text{N}$. Loads and displacements shown are tarred after applying the vertical load.

The separation of displacements in Figure 6.26 is performed on all the test results available in order to investigate the plastic displacements. The direction of the plastic increments at failure in the radial plane is illustrated on Figure 6.27 for the tests subjected to low vertical load, and on planes along the V-axis in Figure 6.28. The linear failure criterion proposed in section 6.1.1 is shown for comparison. It is clear that the normality condition is not satisfied in the planes along the V-axis, whereas there is a good justification for normality in the planes in the radial plane. This corresponds well with the observations from tests with different foundation types published in the literature, cf. chapter 4.

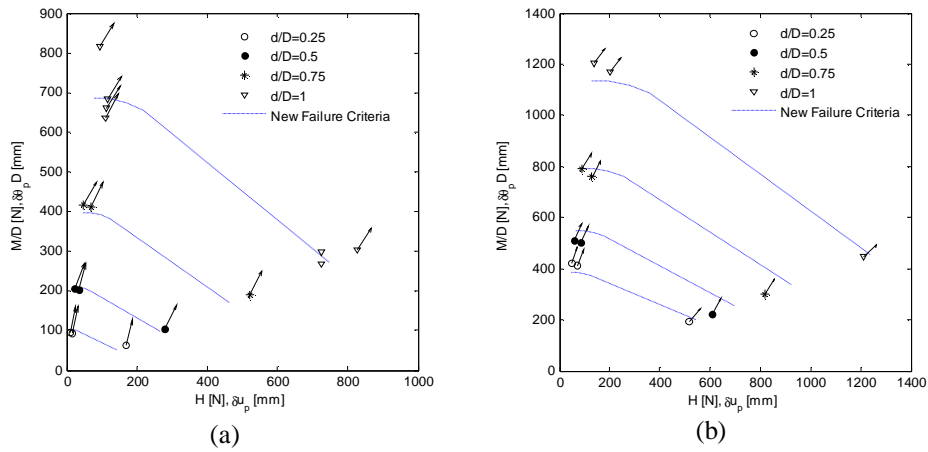


Figure 6.27 Measured loads and direction of plastic displacement increments at failure, for tests with (a) $V=184N$ and (b) $V=1000N$. Proposed linear failure criterion is shown as dotted lines. .

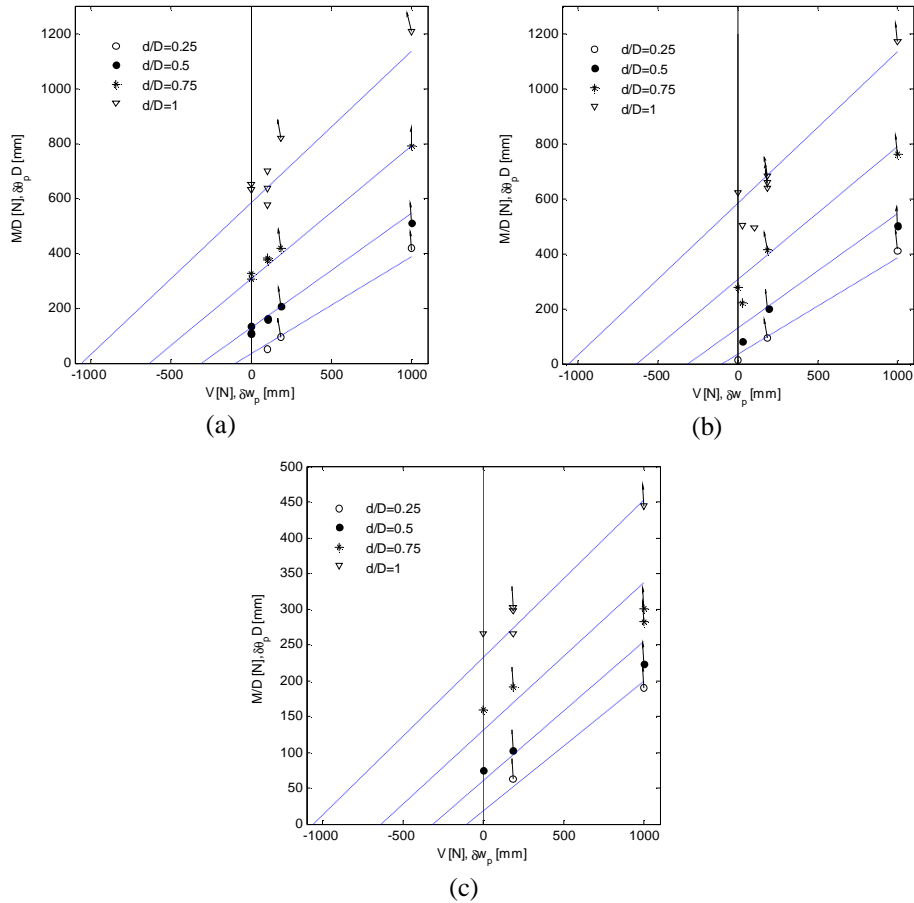


Figure 6.28 Direction of plastic displacement increments at failure for tests with low vertical load and a height of impact at (a) $h=2610\text{mm}$, (b) $h=1740\text{mm}$ and (c) $h=110\text{mm}$. Proposed failure criterion and experimental failure values are shown as well.

The experimental results in Figure 6.27 indicates that if the normality condition is true in the radial plane the failure criteria must be less curved at a large height of impact. This will result in a variation of the failure parameters proposed in Figure 6.5 that is slightly less curved. Due to the information available this is as previously mentioned not possible to determine, and is therefore not investigated further.

From Figure 6.28 the plastic displacement increments are shown to be almost vertical, thus the plastic displacements are dominated by rotational and translation displacements at low vertical load. The location of vertical increments is important as it defines the peak of the plastic potential surface also denoted the parallel point. The parallel point for a height of impact equal

110mm is seen from the plastic displacement increments to be located corresponding to a vertical load close to 1000N for a low embedment ratio. This corresponds to a value of $z = V_{pp}/V_{pre} = V_{pp}/V_{peak}$ equal 0.05 for $d=0$ and $h=110\text{mm}$ corresponding to $M/DH=0.55$. This corresponds with the observations from Byrne (2000) who found that z for small values of h was close to the zero and equal 0.26 for $d=0$ and $h=\infty$. From loading test on bucket foundations presented by Villalobos et al. 2005 a value of $z>0.15$ can be determined for $d/D=0.5$ and $M/DH=1$, i.e. $h=D$. The location of the parallel point at a low value of z entails that the problem is indeed very non-associated along the V-axis.

An increase in the height of impact is seen to rotate the plastic displacement increments anti-clockwise. Thus the location of the parallel point is moved to a higher value of z with increasing height of impact. This corresponds well with the observations by Byrne (2000), cf. chapter 4. In order to determine the location of the parallel point a large amount of experiments are required as it depends of the load path followed. The location of the parallel point for different densities of the sand is at this point unknown.

The direction of the plastic increments during loading is presented in Figure 6.29 for tests with a vertical dead load equal $V=1000\text{N}$. In order to compare the increments the loads are normalized with the respective failure values. From the figure on the left it can be seen that the ratio of the plastic increments $dw_p/(Ddq_p)$ is dependent of the embedment ratio and the preload ratio, V_{pre}/V_{peak} . The direction of these plastic increments is seen to rotate anticlockwise with an increase in embedment ratio. A failure the direction becomes almost constant independent of d/D . Thus moving the parallel point to a higher value of V . In the radial plane the direction of the plastic increments are shown in Figure 6.29 on the right. These show that the direction rotates clockwise with an increase in embedment ratio.

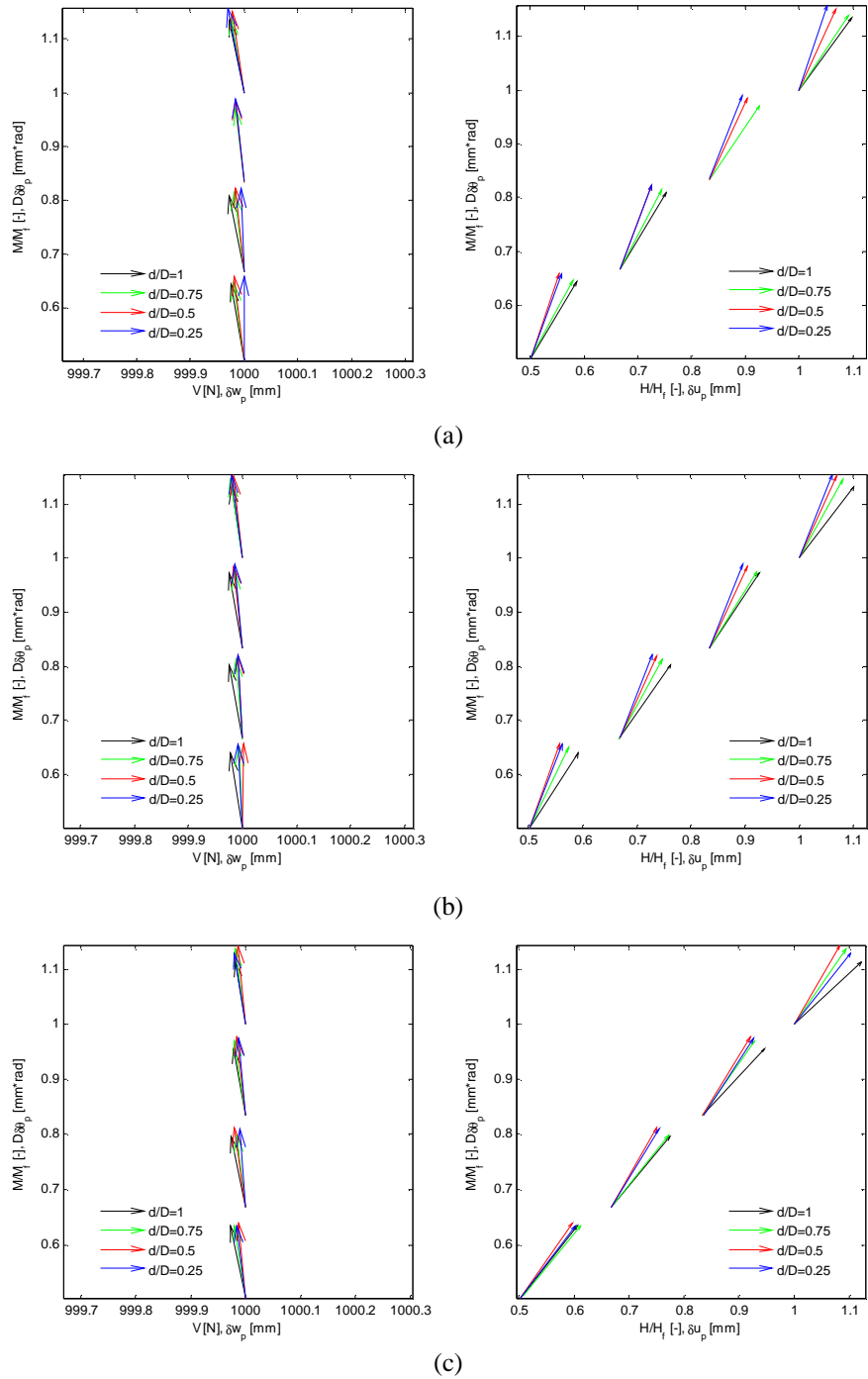


Figure 6.29 Direction of plastic increments during loading for tests with a vertical load of 1000N and a height of impact at (a) $h=2610\text{mm}$, (b) $h=1740$ and (c) $h=110\text{mm}$.

The direction of the incremental plastic rotation and horizontal displacement from H_{peak} and M_{peak} tests performed at $V/V_{peak}=0.5$ is shown in Figure 6.30.

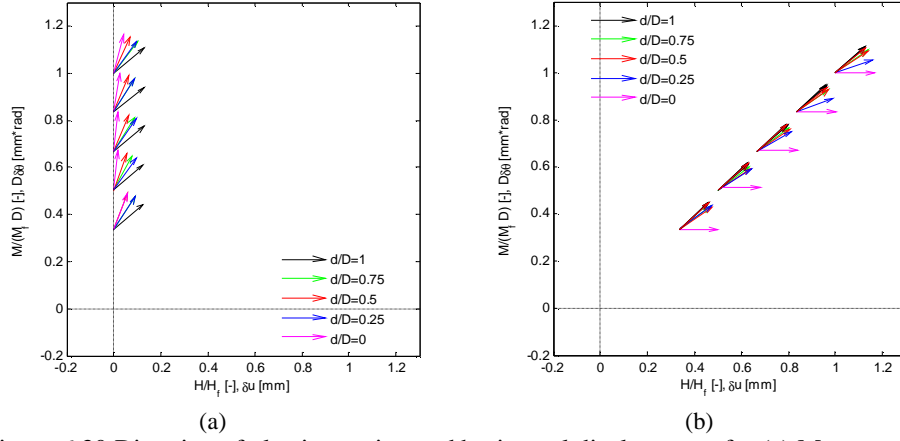


Figure 6.30 Direction of plastic rotation and horizontal displacement for (a) M_{peak} test (b) H_{peak} test. $V/V_{peak}=0.5$

The direction of the plastic increments in Figure 6.30 is seen to rotate clockwise for the M_{peak} tests and anti clockwise for the H_{peak} tests with an increase in embedment ratio. This corresponds to the observed increase in rotation of the yield surface with increasing d/D at failure in the radial plane assuming associated flow. Especially the $d=0$ tests is of interest since the plastic increments is almost parallel to the coordinate axis'. This indicates a value of the yield surface parameter a at failure close to 0 under assumption of associated flow, as also observed in section 6.1.2.

The direction of the plastic displacement increments during loading is from Figure 6.29 and Figure 6.30 seen to only change minor in the radial plane. This supports the assumption of isotropic hardening in the radial plane used in the Model C.

Associated flow in the radial plane for tests performed at low vertical load was found above using the linear failure criterion from Equation 6.2. Using the modified three dimensional failure criterion from the macro model approach proposed in section 6.1.2, the assumption of associated flow in the radial plane is investigated in Figure 6.31 for tests with $V/V_{peak}=0.5$.

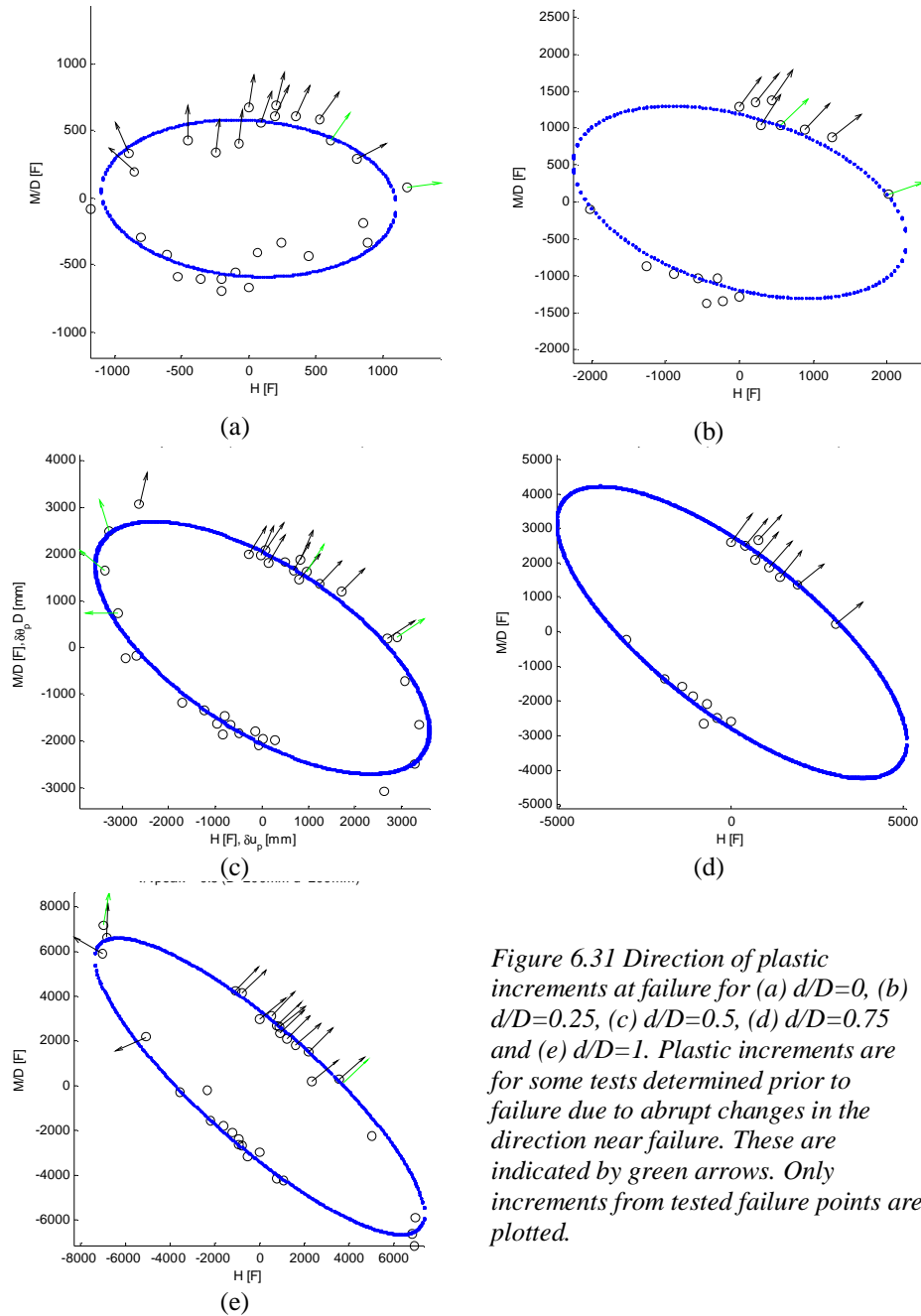


Figure 6.31 Direction of plastic increments at failure for (a) $d/D=0$, (b) $d/D=0.25$, (c) $d/D=0.5$, (d) $d/D=0.75$ and (e) $d/D=1$. Plastic increments are for some tests determined prior to failure due to abrupt changes in the direction near failure. These are indicated by green arrows. Only increments from tested failure points are plotted.

From Figure 6.31 it can be seen that the assumption of associated flow is validated from the tests performed with a vertical load corresponding to half the peak bearing capacity as well. For some experiments the direction of the plastic increments has shown to change significantly at failure compared to

the direction prior to failure. In these cases the direction is shown as the direction prior to this abrupt change, and is shown as green arrows. The corresponding plot for tests performed at low vertical load is shown in Figure 6.32. The failure criterion is shown using the calibrated values of b_1 in Figure 6.21. The assumption of associated flow is once again seen to be a reasonable assumption from the tests performed with large height of impact. At low height of impact the plastic increments are seen not to be perpendicular to the yield surface at failure, i.e. non-associated flow is present.

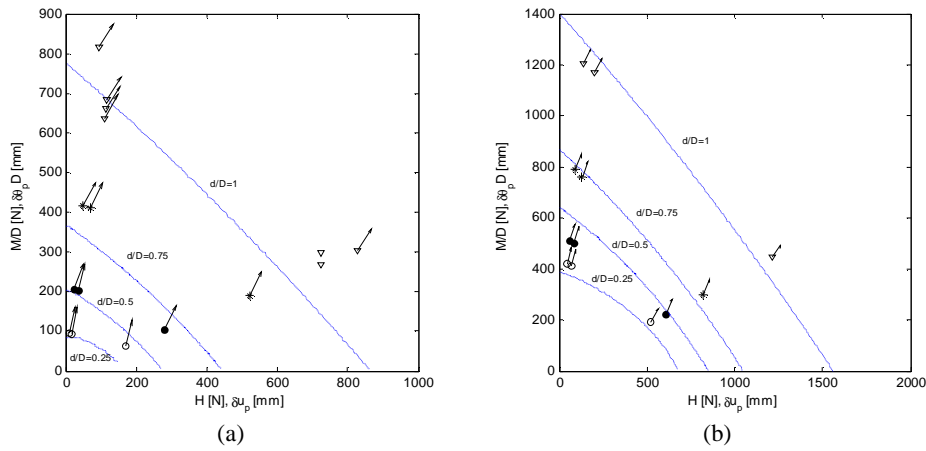


Figure 6.32 Direction of plastic increments at failure for tests performed with (a) $V=184N$ and (b) $V=1000N$. The failure criteria are shown with parameters from Table 6.2, $K\tan(b)=1$, $m=2$ and b_1 from Table 6.3.

6.3. Summary

The behaviour of bucket foundations in dense saturated sand subjected to combined static loads is investigated in the laboratory. Results from loading tests with a low vertical load and a vertical load corresponding to 50% of the vertical bearing capacity are presented. The tests are performed with varying embedment ratio, V/V_{peak} and M/DH ratio. The behaviour is investigated until failure with the applied load path. The variation of the failure parameters are not investigated regarding changes in D_r .

Especially the influence of the ratio M/DH and d/D of bucket foundations subjected to low vertical load has only to a limited extend been investigated prior to this work. The tests carried out in connection with this work are carried out with constant vertical load and M/DH ratio, whereas the majority of tests from the literature are swipe tests. The soil tested during this work is saturated sand, whereas the majority of the present work in the literature is based on tests on dry sand. Dry sand exhibits in some cases a behaviour that is similar to the presence of cohesion due to the humidity in the air. This is not

the case for saturated sand. The use of saturated sand is preferred as the location of bucket foundations is offshore.

The combined capacity is described by applying two failure criteria. A linear failure criterion is proposed in case of low vertical load and the yield criterion by Villalobos et al. (2005) is modified in order to describe the observed measured capacities at various vertical load ratios. The two failure criteria are calibrated from the test results. It is clear from the experiments that the values of the failure parameters are dependent of the embedment ratio and to some extent the load path. The normalized combined capacity in the first quadrant is shown not to be unique due to the tension capacity of bucket foundation, as previously assumed.

The behaviour prior to failure is clarified from the performed tests and is shown to be dependent of the embedment ratio as well as the load path followed. The assumption of associated flow in the radial planes is documented for large ratios of M/HD , though only at failure. At low M/HD ratio the assumption of associated flow in these planes are from the experiments less clear. Along the V -axis a high degree of non-associated flow is observed, which is accordance with observations in the literature. The hardening law is shown to be isotropic in the radial plane.

The macro model approach has been calibrated against laboratory tests on bucket foundations at failure. The parameters within the model however require numerous load tests in order to be calibrated for general situations. The macro model is furthermore with the present knowledge not capable of predicting the behaviour of bucket foundations prior to failure. Thus further research on this is necessary. Especially the effect of scale and V/V_{peak} which is expected due to the stress dependency in sand as well as the relative density or strength of the soil is to be pursued. Furthermore the hardening law requires attention, as it is shown that it is not merely a function of the vertical plastic settlement.

The increase in moment capacity is found to be most pronounced for low embedment ratios at a vertical load equal $0.5V_{peak}$. At low vertical load the opposite effect of the skirt length are observed. Thus the effect of the skirt is significant for loads relevant for offshore wind turbines.

7. FE-simulations of bucket foundations

As an alternative to the macro model approach used in chapter 6, e.g. commercial FE-programs can be used to estimate the behaviour of bucket foundations subjected to combined loading. Only limited experience is available on using FE-simulations in connection with combined loading of bucket foundations. Especially in case of foundation in sand and loads corresponding to offshore wind turbines (Only static loads are considered here). Finite Element calculations of the tested foundations are performed in order to investigate the applicability of this method in a design situation. A numerical study of the static behaviour of bucket foundations is performed using the commercial Finite Element code ABAQUS. The numerical models are three dimensional and the results from these are compared with selected loading tests performed at Aalborg University during this work. The capacity of bucket foundations in case of pure vertical loading have previously been compared with the capacity of a corresponding embedded solid foundation. The FE-models are in this chapter used to investigate whether an equivalent embedded solid foundation can predict the behaviour of a bucket foundation under combined loading as well.

In the following section FE-calculations are performed corresponding to the small scale tests performed in the laboratory. The results from these calculations are compared with the measured responses. The knowledge gained from these calculations is hereafter used in a simulation of the large scale test performed at the test site in Frederikshavn. All the tests are described in chapter 2 and 3 and the measured data for the small scale laboratory tests are reported in Volume 2.

7.1. FE-simulations of laboratory tests

The FE-models used in the simulations are described in the following and involves:

- Model assumptions
- Model Geometry
- Boundary Conditions
- Mesh and element Data
- Material Data
- Load Conditions and calculations phases

Model Assumptions

The constitutive model used in the simulations is the standard Mohr Coulomb material model within ABAQUS. The Mohr Coulomb model is briefly presented in Appendix B. The soil is regarded as an isotropic and homogenous material. The elastic deformations in connection with the Mohr Coulomb model is calculated using a linear elastic model defined by Young's modulus E and Poissons ration.

In ABAQUS the interaction between two surfaces (in this case soil and steel) is described with interaction properties orthogonal and tangential to the surfaces with the "Contact Pair" option.

The property orthogonal to the surface is denoted the "Normal Behaviour" in ABAQUS. As Normal behaviour the formulation denoted "Hard Contact" is used. The Hard Contact formulation defines that no contact pressure is transmitted with out contact between the surfaces, and that there is no limit to the contact pressure that can be transmitted when the surfaces are in contact. The Hard Contact formulation can be used along with the "Augmented Lagrange" surface behaviour. If the Augmented Lagrange option is chosen, some penetration of the soil nodes through the steel surface is allowed. The use of Augmented Lagrange surface behaviour is in some cases found to be a benefit or even necessary for obtaining equilibrium in the model.

As default the separation between the respective surfaces is allowed at all time. This can be changed by including the "No Separation" option where the surfaces are not allowed to separate once contact has been established. The choices are found in some cases to be superior in modelling the bucket foundation behaviour and obtaining equilibrium in the model.

As tangential behaviour between soil and steel the "Penalty Friction" formulation is used. This is given by the "Coulomb Friction" model where the limit of the shear stresses that can be mobilized is given by:

Equation 7.1
$$t_{\max} = m \cdot p$$

where

m is the friction coefficient given as $\tan(d)$, where d is the interface friction angle. p is the contact pressure between soil and steel perpendicular to the skirt.

The penalty friction formulation allows a small sliding of the surfaces relative to each other when $t < t_{\max}$. This has been seen to be necessary in order to obtain equilibrium during the calculations.

The use of the Penalty Friction, Augmented Lagrange surface behaviour and the No Separation option has been found not to influence on the simulated behaviour of the bucket foundations, see Appendix D.

When the “Contact Pair” option is used to describe the interaction between the skirt and the soil any initial gap between the surfaces must be removed. The surfaces must initially be forced to coincide precisely with the “Clearance” command in the input file as shown in Appendix D. If the surfaces don’t coincide precisely, the response of the bucket foundations is shown to be much softer due to the deformations necessary to establish full contact, see appendix D.

The Finite Element simulations are carried out on a half model because of symmetry in the plane of the horizontal loading as illustrated in Figure 7.1.

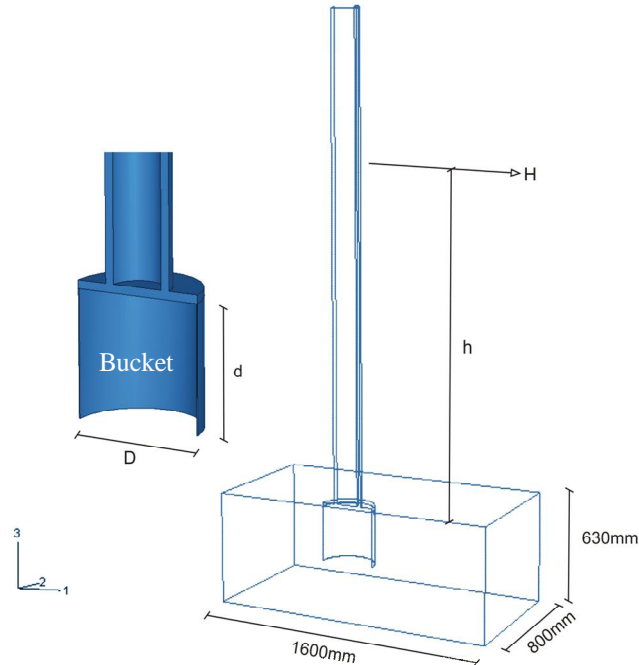


Figure 7.1 Problem modelled by use of a symmetry plane.

The calculations are carried out using effective stresses, since the load is applied at a rate slow enough to obtain a static response. Hence effective densities reduced for buoyancy are used.

Model Geometry

The FE-model is modelled with dimensions corresponding to the true situation in the laboratory. Thus the soil specimen modelled, corresponds to the size of the test box, see Figure 7.1. The bucket foundation is modelled with dimensions corresponding to the tested foundations whereas the tower and connection between the tower and bucket foundation are simplified as shown in Figure 7.1. The plate thickness used for the skirt and lid of the bucket is 2mm and 10mm respectively. The diameter of the bucket foundation in the tests simulated is 300mm, whereas the embedment ratio and height of impact are varied.

Boundary Conditions

The degrees of freedom in the problem are reduced by adding boundary conditions to nodes where the load or displacement is known in advance. The boundary conditions of the model are according to Figure 7.1 as follows:

Symmetry plane:	The deformations of nodes located on the symmetry plane are constrained in the x_2 -direction, i.e. in direction perpendicular to the symmetry plane.
Bottom of the soil:	The deformations of soil nodes located on the bottom of the soil specimen are constrained in all three directions.
Vertical sides of the soil:	The deformations of the soil nodes located on the vertical sides of the soil are constrained in the horizontal directions.

The influence of the boundary conditions specified at the bottom and vertical sides of the soil, with exception of the symmetry plane is investigated in Appendix D. From this it is found that the simulated behaviour is unaffected of the degree of constrained deformations in the plane of the soil boundaries. This indicates that the boundaries of the test box doesn't influence on the behaviour measured in the laboratory, i.e. the size of the test box is adequate.

Mesh and Element Data

The problem is discretized by means of first order solid elements, denoted C3D8R in ABAQUS, corresponding to a linear displacement field. Reduced integration is used because of the risk of locking problems. The elements are used to model the bucket foundation, tower and the surrounding soil. A convergence study has shown that these elements are superior regarding the stability of the calculations, calculation time and convergence rate, see Appendix D. This is assumed to be due to the complexity of the problem which involves elasto-plastic soil combined with slender elements and interface problems between the bucket and soil. Second order elements are often preferred, but the benefit from second order elements is not utilized to its full potential because of the interaction problems present. The interface model used to describe the behaviour between skirt and soil is linear and uses linear interpolation across the element length in case the nodes on adjacent surfaces are not coinciding.

A convergence study of the laboratory bucket foundations with an embedment ratio equal 0.25 and 1 with first order elements are presented in Appendix D. The mesh's shown in Figure 7.2 is from this study found to yield an acceptable degree of convergence and is used throughout the calculations performed.

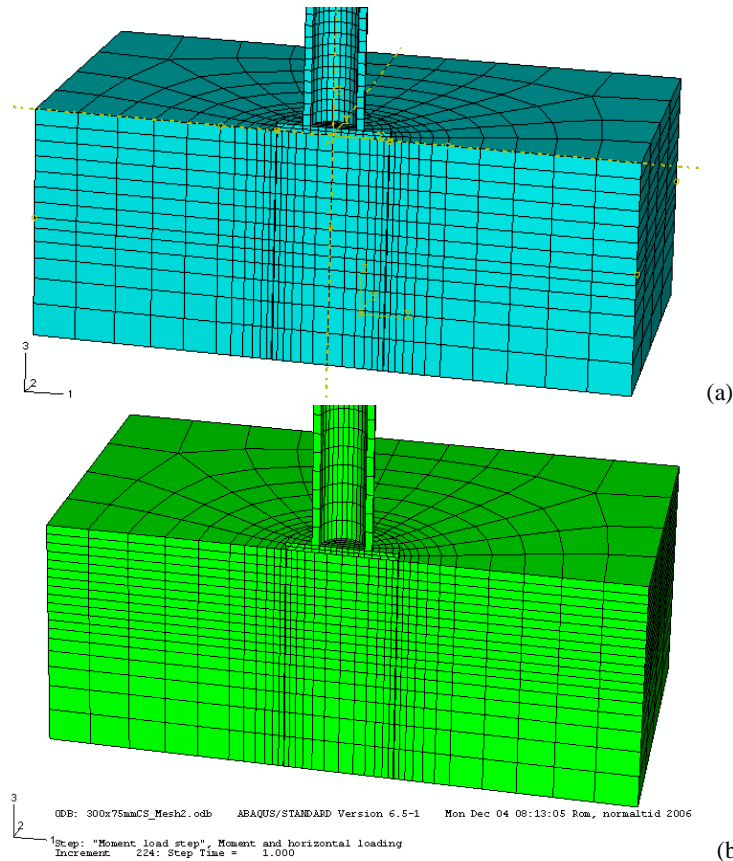


Figure 7.2 Converged meshes in case of embedment ratios equal (a) $d/D=1$ and (b) $d/D=0.25$.

The slender elements present in the soil below the skirt, see Figure 7.2, are seen from the calculations to induce stress concentrations in the soil in this area. Feld (2001) suggests that soft elements are modelled below the skirt tip to avoid this. In Appendix D the use of soft elements is investigated by introducing soft and anisotropic elements at the lower part of the skirt tip. The material used is an anisotropic elastic material so that the soft elements can be implemented without any influence on the lateral earth pressure on the skirt. The stiffness in the lateral direction is given as the stiffness of steel whereas the vertical stiffness is lowered in the calculations. The results from these calculations show that there is no effect on the calculated behaviour when these soft elements are introduced. The influence of the stress concentration might be of importance, if bucket foundations with large vertical load are to be simulated. This is however not investigated here.

Material Data

The characteristics of Aalborg University Sand No. 0 are shown to be a function of the stress level present, see chapter 2. The material data used in the calculations must therefore be chosen so that it represents a weighted mean stress level in the soil influenced by the foundation during loading. This weighted mean stress level is however unknown. The value of Poissons ratio and Young's modulus for the sand is determined in chapter 2 and 6 from the small scale tests performed in the laboratory. The elastic values determined and used through out the analysis of the small scale tests are $E=15\text{MPa}$ and $\nu=0.25$. The effective unit weight of the prepared sand is $\gamma' = 10\text{kN/m}^3$ approximately.

The soil strength parameters of the Mohr Coulomb material in connection with the small scale laboratory tests are investigated by a parameter study. The strength of the tested sand has previously been assumed to be related to the secant values, i.e. the cohesion must be minimized in the simulations. The interface friction and friction angle is calibrated from this parameter study and the measured behaviour of the bucket foundations. The dilation angle is throughout the calculation calculated from the friction angle by a reduction of 30 degrees corresponding to the characteristic state angle, cf. chapter 2.

The bucket foundation and loading tower are modelled with a linear elastic material assuming $\nu=0.3$ and a stiffness corresponding to steel. The large difference between the elastic stiffness of the soil and steel has shown in some case to cause numerical problems. It has been found that this can be overcome by changing the stiffness of the steel skirt without any influence on the output, see Appendix D. The optimal steel stiffness has been found to $2 \cdot 10^7 \text{ MPa}$ which is used in the majority of the calculations.

Load Conditions and Calculations Phases.

In order to model the experiments, as true as possible the following calculation phases are carried out in the FE-model:

1. Initial phase: The effective stresses in the soil are generated. In this phase ABAQUS calculates a stress situation by means of the soil unit weight that is in equilibrium with the initial stress situation. The initial stress situation must be given manually by the user in the input file, see appendix D.
2. Vertical loading phase: The vertical load on the bucket foundation is applied as a uniform distributed pressure on top of the bucket lid. The "pressure" load in ABAQUS is used in this phase. The load is with this method applied to the bucket foundation perpendicular to the

bucket lid and not vertically. The error introduced by this method is investigated in Appendix D and is shown to have only insignificant effect on the result.

3. **Moment loading phase:** In this phase the moment and horizontal load are applied. The moment and horizontal load are applied by a prescribed horizontal displacement of the tower until failure, see Figure 7.1. The load is applied at a height of impact, defined by the load path by the ratio M/H . During this phase the foundation is free to move, only affected by the interaction with the soil.

7.1.1. Parameter study

A parameter study is performed in the following in order to calibrate the material parameters of the soil and interfaces according to the situation present in the laboratory. The elastic properties of the soil are given above and the influence of this will therefore not be investigated here. From the work with ABAQUS it has however been found that the influence of the elastic stiffness only affects the combined capacity of the bucket foundations minor for moderate changes in the stiffness. The overall stiffness of the response prior to failure is however found to be significantly influenced by the Young's modulus. No influence of poisons ratio on the response is observed within the interval relevant for drained conditions in sand.

The influence of the soil strength parameters and the interface roughness is investigated in the following. Unless specified the parameters in Table 7.1 are used in the calculations. The friction and dilation angle used in this basic case is determined from the vertical bearing capacity tests in chapter 5. The cohesion and interface friction are chosen equals 1 kPa and 30 degrees respectively. During the generation of the initial stresses in the soil prior to loading of the bucket foundation a lateral earth pressure coefficient K^0 is calculated as:

$$\text{Equation 7.2} \quad K^0 = 1 - \sin(j)$$

Table 7.1 Initial values of parameters used in parameter study

$j [^\circ]$	$\gamma [^\circ]$	$c [\text{kPa}]$	$d [^\circ]$	$g' [\text{kN/m}^3]$	$E [\text{MPa}]$	$n [-]$
47.5	17.5	1	30	10	15	0.25

The result from a FE-calculation of a bucket foundation with the parameters given Table 7.1 and a vertical load and height of impact equal 1000N and 2610mm respectively is shown in Figure 7.3. The diameter and embedment ratio of the bucket foundation are 300mm and 1 respectively. The measured response from the corresponding loading test in the laboratory is shown for

comparison. This experiment is used as reference test in the following parameter study.

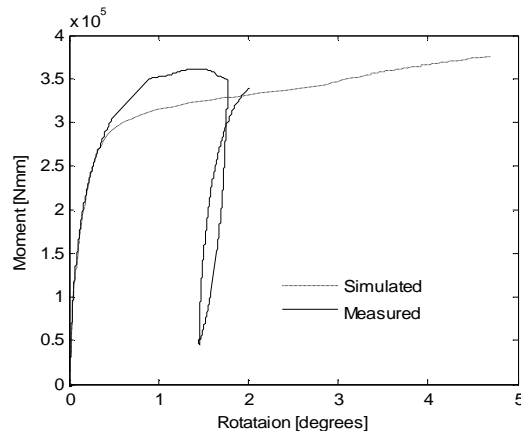


Figure 7.3 Calculated behaviour using parameters from Table 7.1. The measured response of the corresponding loading test No. 0104-6901 is shown as well. $D=300\text{mm}$, $d/D=1$, $V=1000\text{N}$ and $h=2610\text{mm}$.

From the simulated behaviour of the basic case shown in Figure 7.3 it is seen that there is no indication of a peak capacity as observed in the laboratory nor is it expected. The Mohr Coulomb material model used in the simulations is not capable of simulating the post peak softening that dense sand exhibit, cf. chapter 2. The failure capacity is instead determined from the vector plot of the displacements shown in Figure 7.4 for the same calculation a failure. At this state a point exists, around which the soil and bucket foundation rotates. The location of this point is from the model seen to become constant as a complete failure mechanism is developed. In the basic case it is found that a complete failure mechanism is developed at a rotation of 2° approximately.

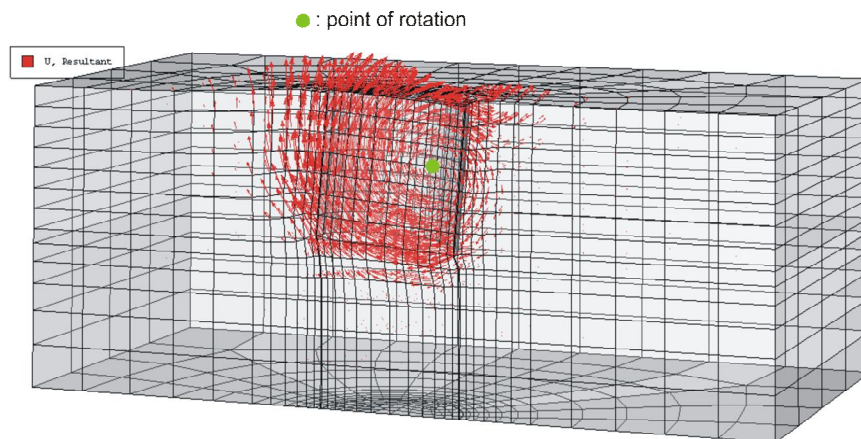


Figure 7.4 Vector plot of displacements at failure.

Influence of cohesion on the simulated behaviour

A value of the cohesion equal 1 kPa is used in the above calculation. Since sand is assumed to be a pure frictional material this should actually be excluded in the calculation. A cohesion of only 1 kPa is very low and is not supposed to affect the behaviour in case of a prototype. In the laboratory where the stress level is very low this will however greatly affect the behaviour due to the failure criterion used. It has been found that ABAQUS is not capable of creating equilibrium in the model using zero cohesion with the standard Mohr Coulomb material model used. Thus the influence of the cohesion on the behaviour is investigated. The influence of the cohesion in the basic case is shown in the following figure.

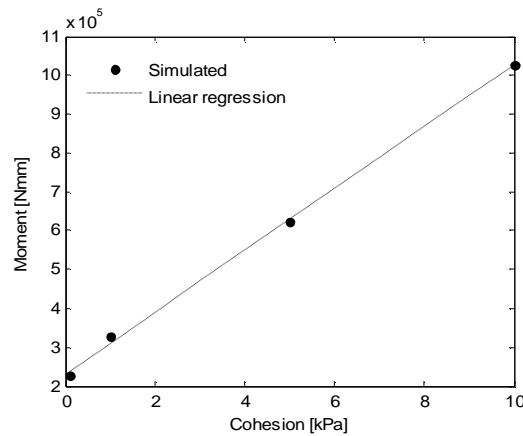


Figure 7.5 Calculated influence from the cohesion on the simulated response in the basic case. The moments are shown corresponding to a rotation equal to 2 degrees.

In Figure 7.5 the calculated moment is for comparison plotted at a rotation equal 2 degrees for different values of the cohesion in the FE-simulations. The influence from the cohesion on the response is seen to be linear in the interval examined. It is clear that the capacity of the bucket foundation at this low stress level is indeed sensitive to even slight changes in the cohesion.

Influence of interface roughness on the simulated behaviour

The influence of the interface friction angle δ is investigated from a set of calculations with the parameters from Table 7.1 though with varying roughness of the interface. The results from the calculations are summarized in Figure 7.6.

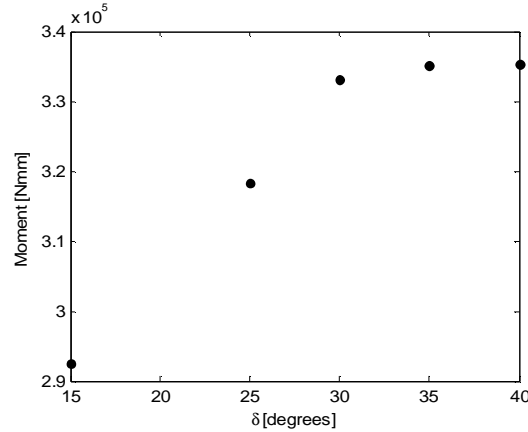


Figure 7.6 Calculated influence from δ on the simulated response in the basic case. The moments are shown corresponding to a rotation equal to 2 degrees.

In Figure 7.6 the calculated moment is for comparison once again plotted at a rotation equal 2° for different values of the interface roughness. From the figure it can be seen that the influence is negligible for a roughness of the interface above 30 degrees. For lower interface roughness a clear influence on the capacity is however seen from the figure.

Influence of friction angle on the simulated behaviour

The influence of the friction angle is summarized in the following figure from simulations of the basic case. In order to simulate the influence under assumption of a frictional material, low cohesion is used in these calculations. It is not possible to complete the calculations with zero cohesion, thus a cohesion of 0.1 kPa is used.

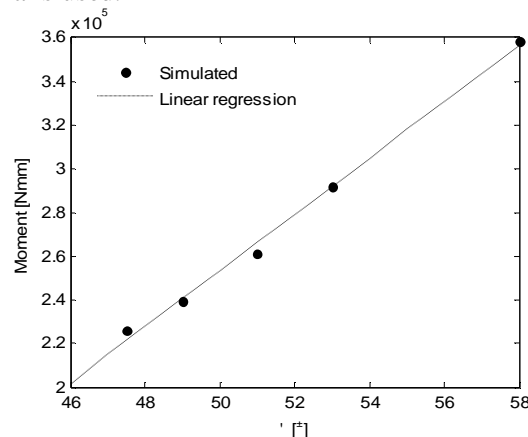


Figure 7.7 Calculated influence from the friction angle on the simulated response in the basic case. The moments are shown corresponding to a rotation equal to 2 degrees.

In Figure 7.7 the calculated moment is once again for comparison plotted at a rotation equal 2 degrees for different values of the friction angle used in the FE-simulations. The dilation angle used in these calculations is changed according to a characteristic state angle equal 30 degrees by subtraction, cf. chapter 2. Within the interval examined the relation between the friction angle and the moment capacity is seen to be almost linear. The capacity is from the figure seen only to be moderate sensitive to slight changes in the friction angle.

Influence of K^0 on the simulated behaviour

During the first calculation phase the initial stress situation in the soil is generated from equilibrium between the prescribed stress distribution and the characteristics of the soil. The prescribed stress distribution is entered manually by the user with a linear variation in the vertical direction. The initial stress distribution in the horizontal direction is calculated by the lateral earth pressure coefficient at rest, K^0 . Calculations shows that the capacity of the bucket foundation is independent of the value of K^0 used, see Figure 7.8. At low deformations a slightly stiffer response is seen for a large value of K_0 , which is also expected, since this gives a higher mobilization of the interface friction at this state.

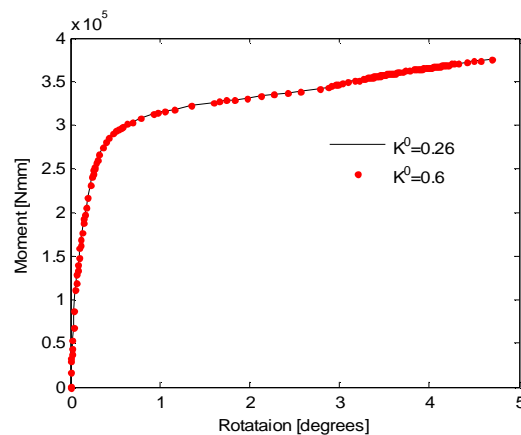


Figure 7.8 Calculated response of the basic case with different values of K^0 .

Calibration of soil parameters

From the parameter study above it is clear that the cohesion of the material dominates the response of the bucket foundation at the low stress level present in the laboratory. In order to simulate the laboratory experiments according to the assumption of a pure frictional material a very low cohesion is necessary. It has not been possible to complete calculations with zero cohesion. A value of 0.1 kPa is instead recommended in order to minimize the influence of the

cohesion. A low cohesion is found to increase the number of iterations as well as the number of time steps necessary to obtain equilibrium of the model during loading. This results in a significant increase in the calculation time and number of numerical problems. The experience gained during this work on how to cope with the numerical problems that arises is presented in appendix D. In large scale or prototype simulations the cohesion is expected to have less influence on the simulated behaviour. A larger (though small) cohesion can therefore with advantage be used in these simulations.

The interface roughness between the skirt and the soil is not known for the tests in the laboratory. But is shown to influence on the behaviour for $d < 30^\circ$. A value of $d = 20$ degrees is chosen in the following calculations based on experience gained from large scale tests with bucket foundations, Larsen and Ibsen (2005). It was found that no significant influence is present from the lateral earth pressure prior to loading on neither the deformations nor the capacity. A value of K^0 is based on this chosen equal 0.5.

It is clearly evident that a reduction of the cohesion and interface roughness requires an increase in the friction angle relative to the basic parameters if the measured response is to be simulated. In Figure 7.3 the result from the calculation of the basic case is seen to coincide well with the measured response in the laboratory. Similar accordance is however not found in simulations of additional tests with the basic parameters. The friction angle used in the basic case is determined from the bearing capacity tests in chapter 5 under assumption of a non-cohesive material. The increase necessary to capture the response during combined loading can be explained by the lower stress level in these tests compared to the vertical load tests in chapter 5, from which the friction angle used in the basic case originate.

A calibration of the friction angle and the corresponding dilation angle is performed with the above presented parameters. A value of the friction and dilation angle is found to 58 and 28 degrees respectively, when calibrated against the measured response in Figure 7.3. A friction angle equal 58 degrees for sands is in true scale problems regarded as extremely high. The stress level in the soil during the small scale tests performed within this thesis is however very small. The stress level corresponding to a friction angle equal 58 degrees and an elasticity modulus equal 15MPa can be found, from the presented behaviour of Aalborg University Sand No. 0 in chapter 2. The stress level is found to correspond to a minor principal stress level equal 0.5 kPa for $e = 0.61$ corresponding to a relative density of 80%, for both the friction angle and the elasticity modulus. The minor principal stresses in the soil at failure from the basic case are shown in Figure 7.10. The stresses are seen to be only locally high. The mean stress level is difficult to establish but the minor stresses in the soil are though in the affected area seen to mainly be between 1 and 3 kPa.

A friction angle equal 58 degrees is however found necessary to capture the behaviour with the model when the soil is regarded as a purely frictional material. This large friction angle is assumed to be caused by installation method, choice of interface roughness and a stress situation in the soil which is differently from the triaxial stress conditions.

The friction angles evaluated in chapter 2 is the triaxial friction angles. In case of combined loading the stress situation in the soil is not corresponding to a triaxial test. Thus the friction angle used in ABAQUS is not fully comparable with the triaxial friction angle which is then less than 58 degrees. It is a well known fact that the friction angle changes with an increase in the intermediate principal stress s_2 relative to the triaxial case. The influence of the intermediate principal stress on the friction angle at peak is shown in Figure 7.9. The friction angles are measured using the true triaxial apparatus in the geotechnical laboratory at Aalborg University with a constant mean effective stress equal 160 kPa. The influence of s_2 is in the figure given according to Equation 7.3.

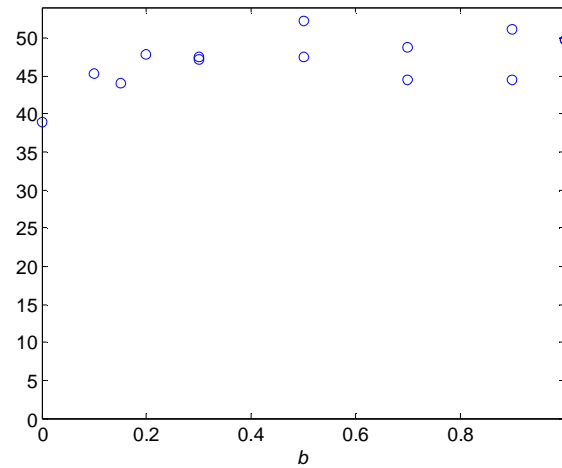


Figure 7.9 Friction angles of Aalborg University Sand No. 0 measured in the true triaxial apparatus. $D_r=80\%$ after Larsen & Pedersen (2001)

Equation 7.3

$$b = \frac{s_2 - s_3}{s_1 - s_3}$$

It is seen from Figure 7.9 that the friction angle for most values of b is larger than the triaxial angle ($b=0$) and assumes an almost constant value which is equal to the plane strain angle. Thus the friction angle equal 58 degrees used in ABAQUS more likely corresponds to the plane strain angle. It is moreover observed from Figure 7.9 that the difference between the plane and triaxial friction angle are larger than 10% which is often assumed.

The friction angle necessary to simulate the measured response moreover depends on the interface friction angle used. Further research is estimated necessary in order to determine this. Further more it is plausible that the installation procedure affects the measured capacity, cf. chapter 4 corresponding to a higher friction angle in the finite element model.

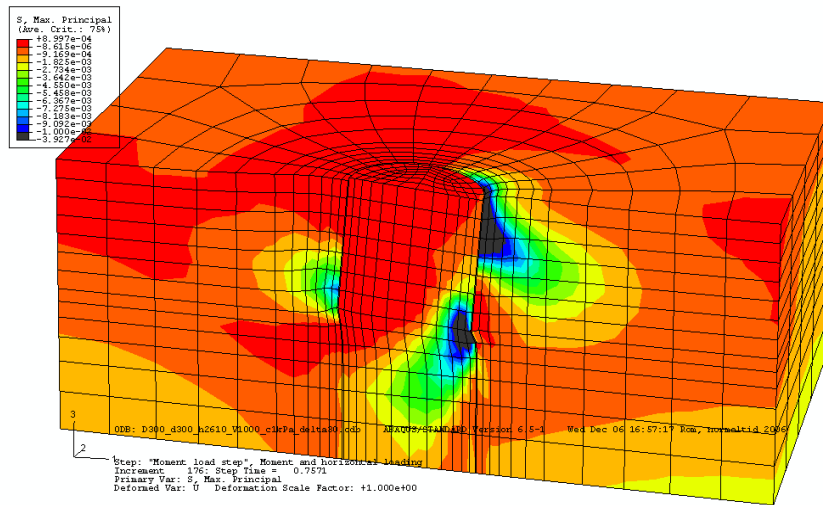


Figure 7.10 Minor principal stress at the end of the basic calculation.

The soil parameters presented above are used in the following section to simulate selected experiments in the laboratory.

7.1.2. Comparison of small scale tests and FE-simulations

The laboratory loading tests performed on 300 mm bucket foundations with an embedment ratio equal 0.25 and 1 are simulated in Abaqus with the in section 7.1.1 calibrated parameters. The results from the calculations are compared with the measured behaviour in the laboratory in Figure 7.11 and Figure 7.12. In connection with the use of bucket foundations for offshore wind turbines, the rotation is the most critical in a design situation. Thus only this is presented in relation to the moment applied. Some calculations have stopped due to equilibrium problems when the failure mechanism is fully developed. These are not restarted as only the behaviour prior to failure is relevant. The state at which a failure mechanism is developed is shown in the figures as circles.

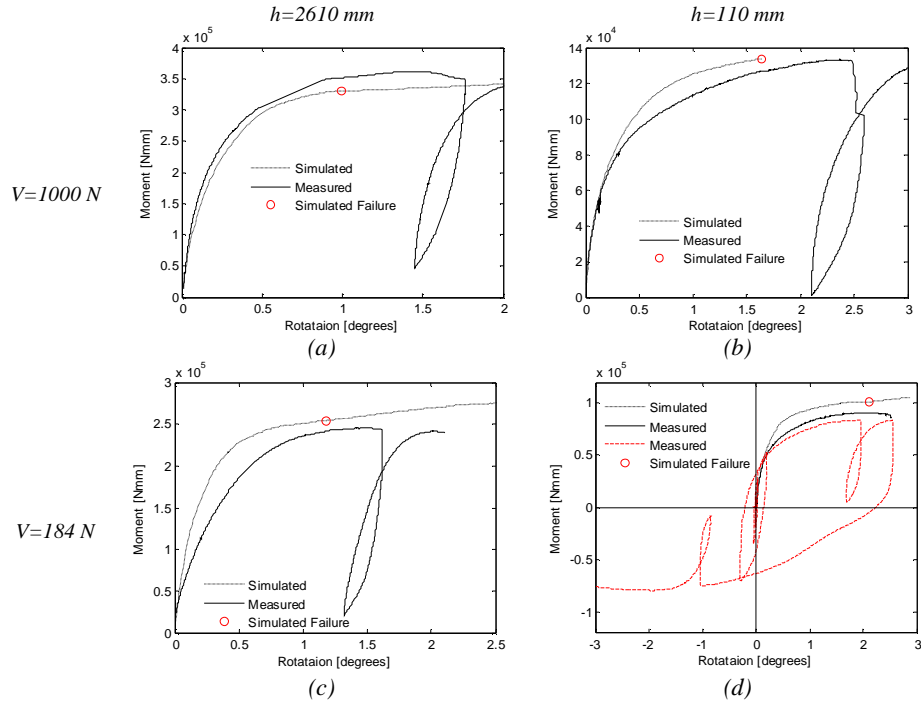


Figure 7.11 Simulation of selected laboratory tests. $d/D=1$

The results from the FE-calculations of the tests with an embedment ratio equal 1 are seen from Figure 7.11 to simulate the measured behaviour very well. The moment at failure is for all the calculations seen to be determined within 10 percent of the measured. Also the rotation at failure is seen to be simulated in accordance with the measured.

The results from corresponding FE-calculations with an embedment ratio equal 0.25 are presented in Figure 7.12. The results from these calculations are seen also to simulate the measured behaviour with an acceptable accuracy, with exception of the simulation with $h=2610$ and $V=1000\text{N}$, Figure 7.12(a). The simulated response is seen to deviate significantly from the measured response for this test. The simulated behaviour in Figure 7.12 is generally seen to yield capacities that are below the measured

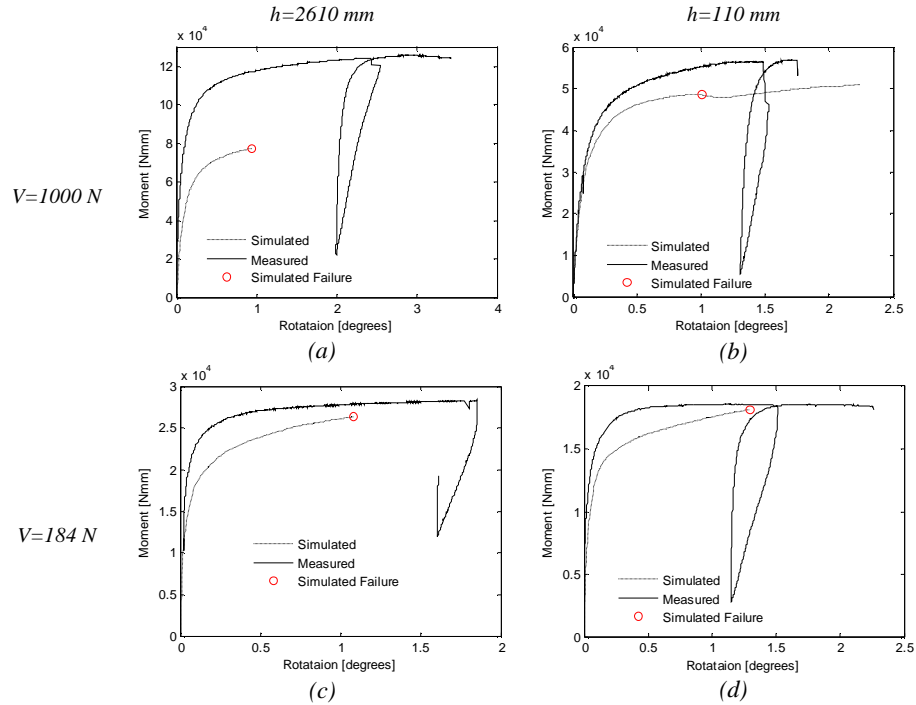


Figure 7.12 Simulation of selected laboratory tests. $d/D=0.25$

The stress level at failure from simulations with low embedment ratio is shown in Figure 7.13 corresponding to Figure 7.12 (a). The limits of the contours are for comparison identical to Figure 7.10. From this it is clear that the stress level is smaller in this test, than in the corresponding test with a full bucket in Figure 7.11(a). The stress level in the soil at failure with a vertical load equal 184N is generally found to yield smaller stresses in the soil than corresponding simulations with $V=1000\text{N}$, as would be expected. These observations correspond with the under-predicted capacity as a higher friction angle should be used in these tests due to the lower stress level.

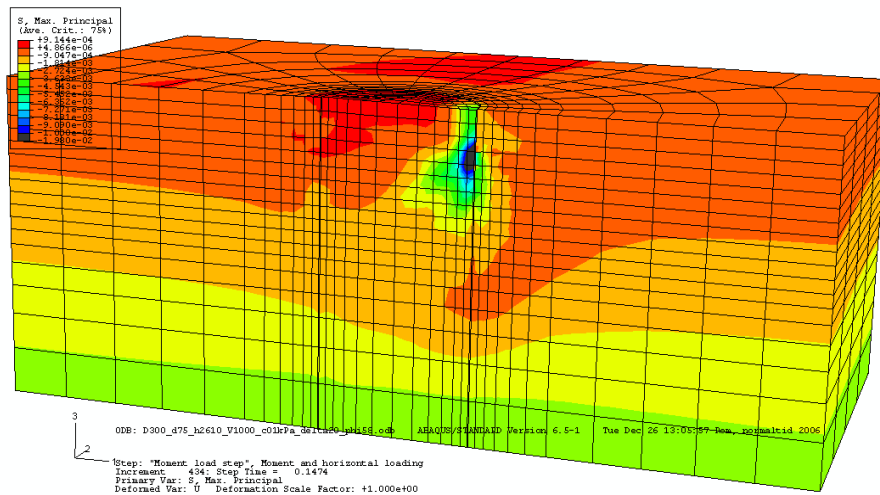


Figure 7.13 Minor principal stress at failure. $D/d=0.25$ $h=2610$ and $V=1000N$

The above presented results from the performed FE-simulations are carried out with the calibrated values using secant strength parameters. Alternatively the calculations can be carried with tangent parameters as shown in chapter 2. Simulations of the experiments in Figure 7.11 and Figure 7.12 are carried out using tangent strength parameters calibrated against the test in Figure 7.11(a). The results from these simulations have however shown in larger extend to disagree with the measured behaviour from the tests. Thus this is not pursued further

7.1.3. Failure modes

The bucket foundations have previously been assumed to behave similar to embedded solid foundations. Proposed failure modes for combined loads of embedded foundations are presented by Feld (2001), see Figure 7.14. These are found to correspond to the failure modes for combined loading of bucket foundations subjected to large vertical load, Feld (2001). This similarity is investigated in the following from FE-simulations with embedded foundations subjected to low vertical load.

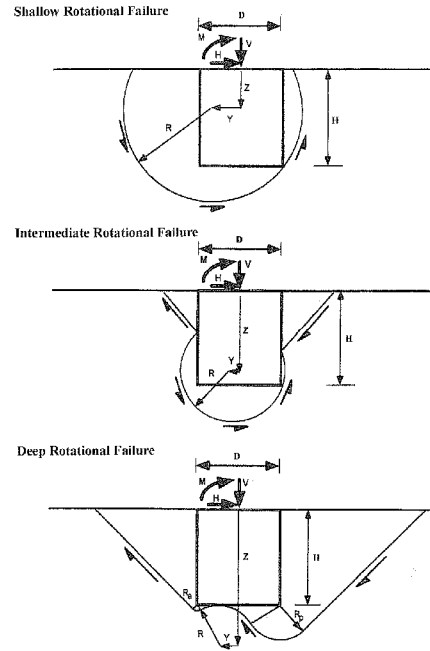


Figure 7.14 Failure modes of embedded foundations, after Feld (2001).

The failure mode obtained from the FE-simulation of loading test 0104-6901 in Figure 7.11(a) with $V = 1000\text{N}$, $h = 2160\text{mm}$ and $d/D = 1$ respectively is shown in Figure 7.15. The failure mode is shown as a contour- and vector plot of the magnitude of displacements.

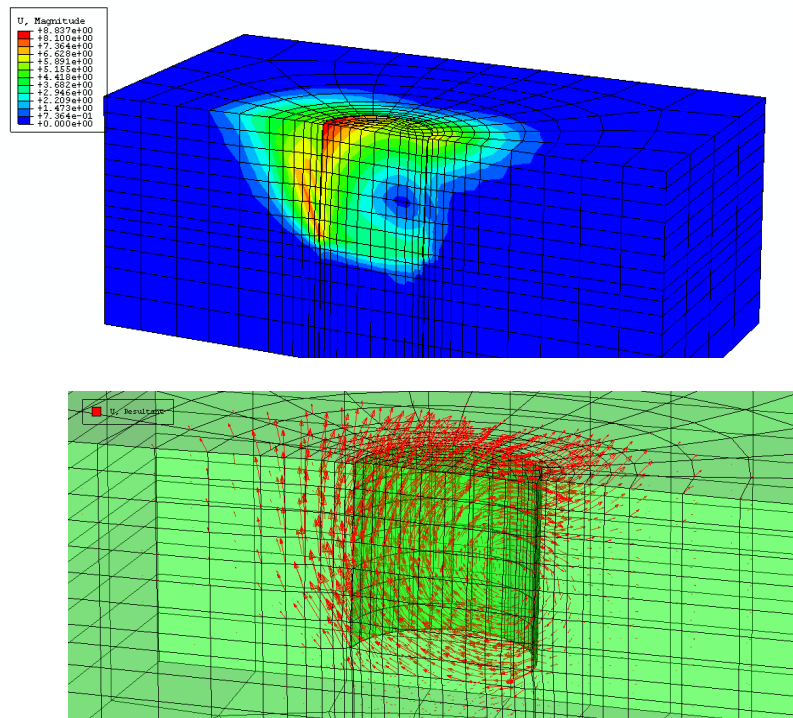


Figure 7.15 Failure mode observed from simulation of bucket foundation. $V=1000N$, $d/D=1$ and $h=2610mm$.

The failure is seen to be caused by a rotation of the bucket foundation around a centre located inside the bucket. The point of rotation at failure is located at a depth corresponding to half the embedment depth near the skirt in direction of the impact. During loading this point is found to move as illustrated in Figure 7.16. During loading active earth pressure zones are initially developed as these only requires small deformations. The zones of active earth pressure are mainly located at the backside of the bucket near the soil surface and at the front near the skirt tip. At further loading passive zones are developing at the front side of the bucket above the point of rotation and below at the backside. The final rotational mechanism creates a rupture figure consisting of a slightly curved slip line beneath the foundation base that connects the failure zones on the outside of the skirt, see Figure 7.15 and Figure 7.17. The soil within the bucket foundations is from Figure 7.17 seen to behave nearly as a rigid body with only a slight influence from the rupture figure near the base.

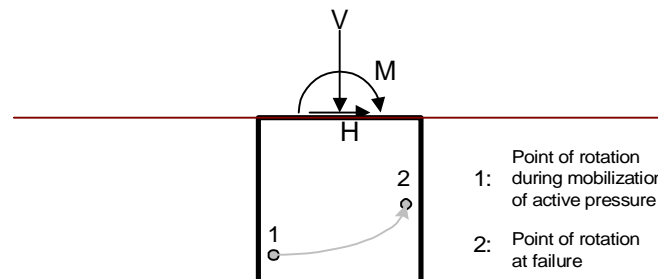


Figure 7.16 Location of the point of rotation during moment loading.

The bucket foundation is from both simulation and experiment seen to move upward during moment loading. The soil beneath the bucket foundation below the skirt tip is therefore unloaded creating an almost horizontal slip line beneath the level of the skirt tip, see Figure 7.17. The failure mode observed is illustrated in Figure 7.18. An identical failure mode is observed for the simulation with $V=184\text{N}$. The horizontal location of the point of rotation is though located nearer to the skirt in the direction of the horizontal load. Corresponding simulations with a height of impact equal 110mm yields similar failure modes. The point of rotation though moves downward to a depth of approximately $2/3d$.

In the case of moment loading combined with large vertical load the buckets are seen from the experiments to move downward and thereby changing the curvature of the lower slip line. In this case the horizontal location of the point of rotation is located according to Figure 7.14.

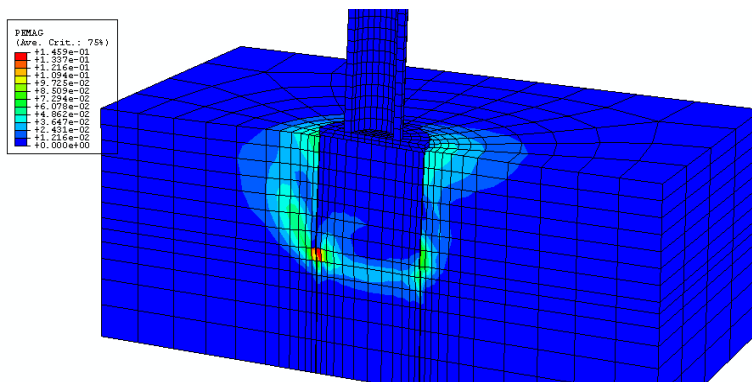


Figure 7.17 Magnitude of plastic strains at failure. $V=1000\text{N}$, $d/D=1$ and $h=2610\text{mm}$.

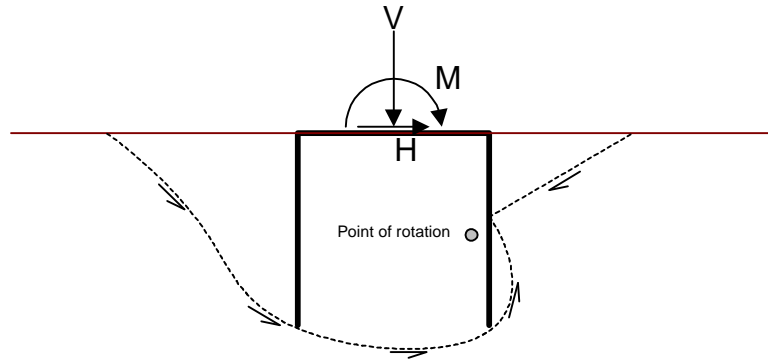


Figure 7.18 Failure mode observed for full bucket foundation with low vertical load and large height of impact.

The failure modes observed from simulations with $V = 1000\text{N}$ and $d/D = 0.25$ are shown in Figure 7.19 and Figure 7.21 for $h = 2610\text{mm}$ and $h = 110\text{mm}$ respectively.

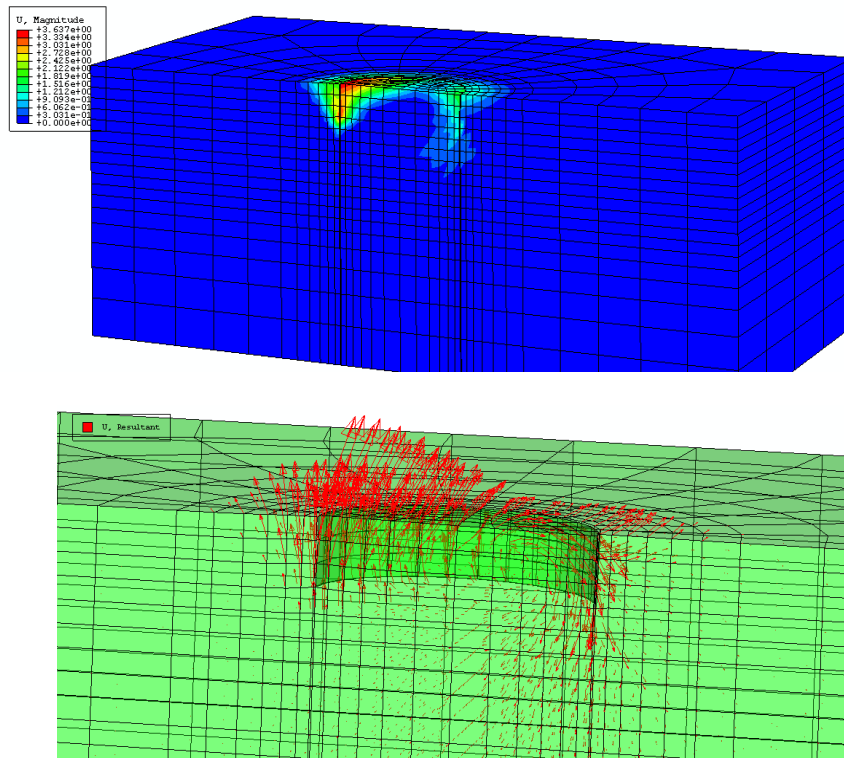


Figure 7.19 Failure mode figure for simulation of bucket foundation with $V = 1000$ $d/D = 0.25$ and $h = 2610$.

The failure is from Figure 7.19 and Figure 7.21 also seen to be caused by a rotation and vertical uplift of the bucket foundation. The rotational centre is located near the bucket lid, at a horizontal distance from the middle of approximately $0.5R$ in direction of the loading. The rupture figure is from Figure 7.20 seen to include the soil inside the bucket foundation, and are seen to mainly consist of active and passive earth pressures on the inside and outside of the skirt. During loading and mobilization of the pressure zones the point of rotation is found to move in direction of the load similar to the observations made from the bucket with $d/D = 1$.

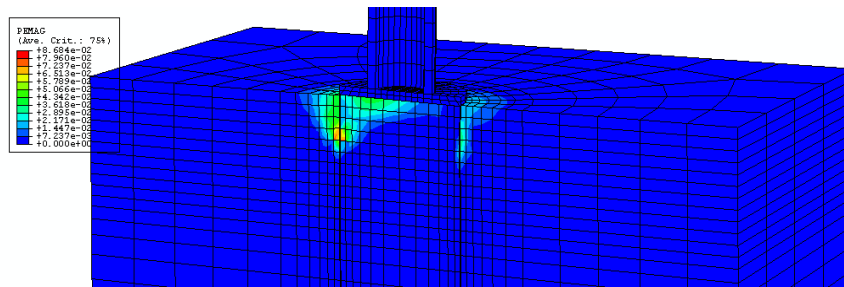


Figure 7.20 Magnitude of plastic strains at failure from simulation of bucket foundation with $V = 1000N$ $d/D = 0.25$ and $h = 2610mm$.

The failure mode for the simulation with low height of impact is shown in Figure 7.21 and is seen to increase the volume of soil within the bucket foundation that is affected by the rupture zone. The point of rotation is found to move a small distance downward with decreasing height of impact. This corresponds with the observations from the simulations with $d/D = 1$.

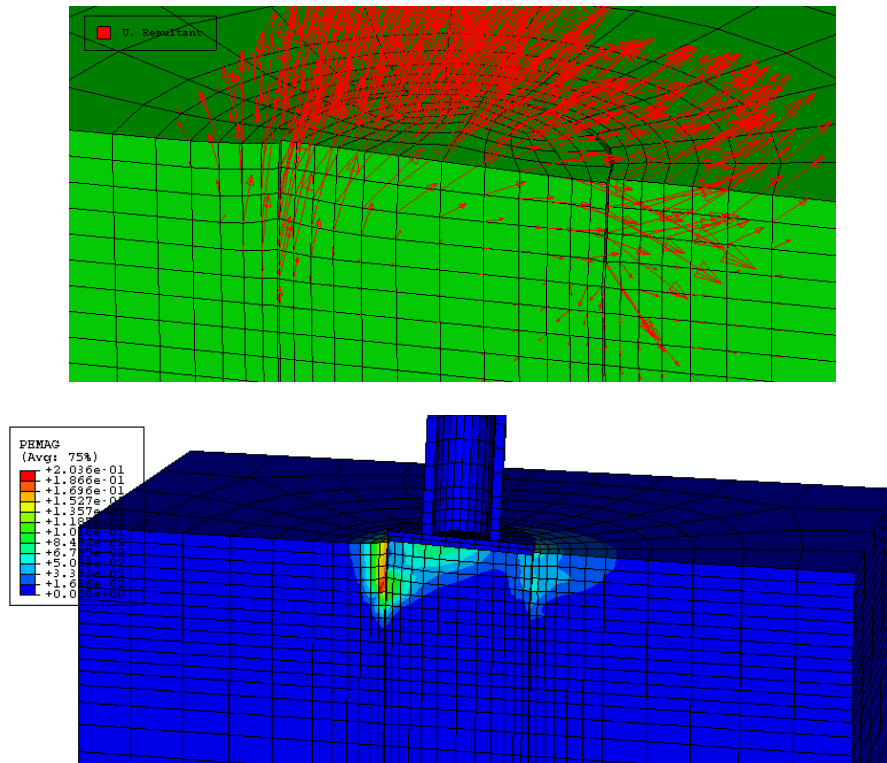


Figure 7.21 Failure mode and magnitude of plastic strains for simulation of bucket foundation with $V = 1000\text{N}$ $d/D = 0.25$ and $h = 110\text{mm}$.

The failure modes observed is caused by a rotation of the bucket foundation around a point located inside the bucket. In chapter 4 a suggested method for predicting the pure horizontal capacity was presented based on a point of rotation located below the skirts. Thus this method does not yield the correct failure. The rotational failure modes observed at low height of impact corresponds to the failure mode observed experimentally for pure horizontal loading of bucket foundation by Yun and Bransby (2003), cf. chapter 4.

A point of rotation located inside the bucket can be modelled with the method proposed by Ibsen (2002) on predicting the combined capacity, cf. chapter 4. In case of low embedment ratio the failure mode must however be altered to include the earth pressure zones inside the bucket observed.

7.1.4. FE-simulations of embedded solid foundations

The behaviour of shallow bucket foundations are from the failure modes observed not suspected to be comparable with a solid circular embedded foundation as initially assumed. A set of FE-simulations are performed by replacing the bucket foundation and internal soil with a solid structure

consisting of a stiff material, e.g. concrete. The results from these calculations are compared to the respective simulations with bucket foundation in Figure 7.22 and Figure 7.23.

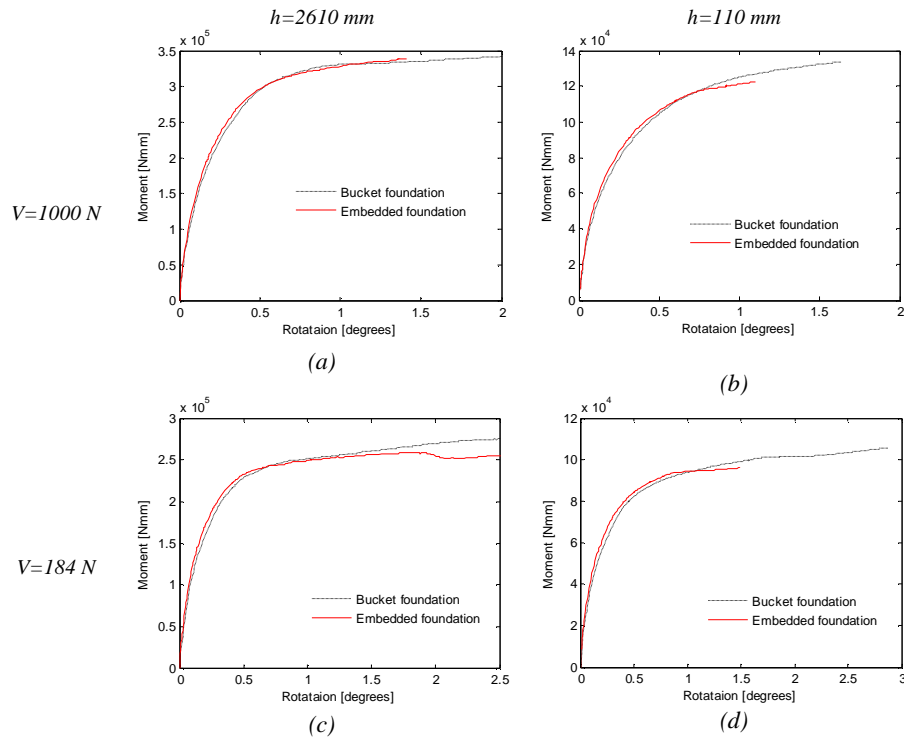


Figure 7.22 Comparison of bucket- and embedded foundation simulations. $d/D=1$

From Figure 7.22 it can be seen that the simplified FE-model, i.e. embedded foundation, results in a behaviour similar to the one observed from the FE-calculations with the bucket foundations. Only a slight underestimation of the moment capacity is seen at low height of impact with this model. This difference is a result of change in the geometry of the slip line below the base of the foundation. This slip line is forced a distance below the foundation base for the embedded model. The slip line below the base is when compared, found to be more curved then observed for the bucket foundations. The remaining parts of the rupture figures have from the simulations shown to be identical to the ones observed in the simulations performed with the bucket foundation.

From the failure modes and the results in Figure 7.22, the soil inside the bucket is proved to behave nearly as a rigid body. The simulations of the embedded foundations are less complicated in geometry as well as concerning interaction problems. The simulations are moreover found to be significant

less time consuming in both modelling phase as well as the calculation phase. The simulation time varies between 4 hours and several days on a 2.8MHz PC with 2GB Ram depending on the load conditions and embedment ratio. Further more the embedded model is generally found to be more stable and therefore useful in a design situation.

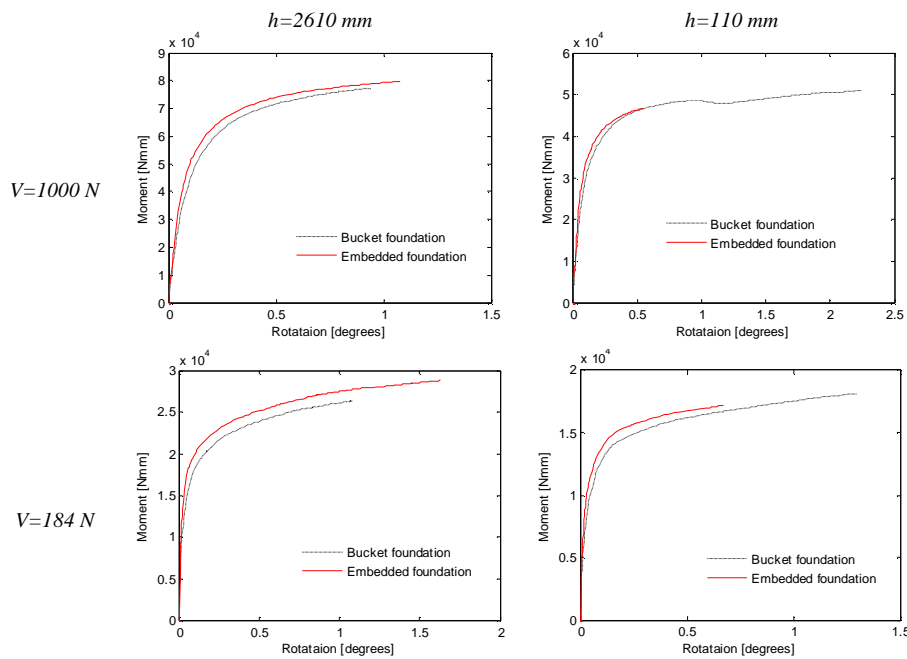


Figure 7.23 Comparison of bucket - and embedded foundation simulations. $d/D=0.25$

The results from the embedded simulations with $d/D = 0.25$ are presented in Figure 7.23. Also in this case the behaviour of embedded foundations is seen to correspond to the simulated behaviour of bucket foundations. A slight decrease in the initial stiffness and increase in the capacity are observed in these simulations when compared to bucket foundations. These differences are subscribed to a change in failure mode. The influence on the overall behaviour from this change in failure mode is however seen to be small. Thus in spite of the difference in failure modes the simulations of the embedded foundations are found applicable to simulate the behaviour of corresponding bucket foundations, even at low embedment ratios.

Intermediate embedment ratios

The behaviour of bucket foundations with loads corresponding to the ones presented above is simulated for intermediate embedment ratios equal 0.5 and 0.75 and with $D = 300\text{mm}$. The simulations are carried out using an embedded model. The results from the simulations are presented in Figure 7.24 and

Figure 7.25 where they are compared with the measured response from the corresponding load tests.

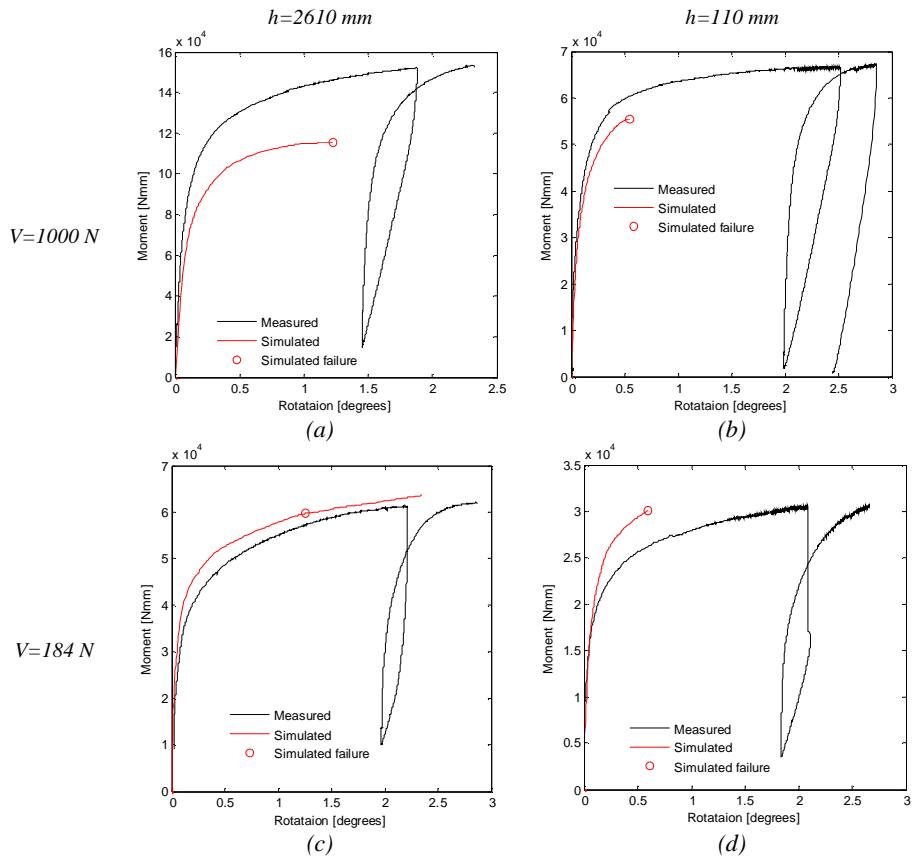


Figure 7.24 Simulation of laboratory tests using an embedded FE-model. $d/D=0.5$

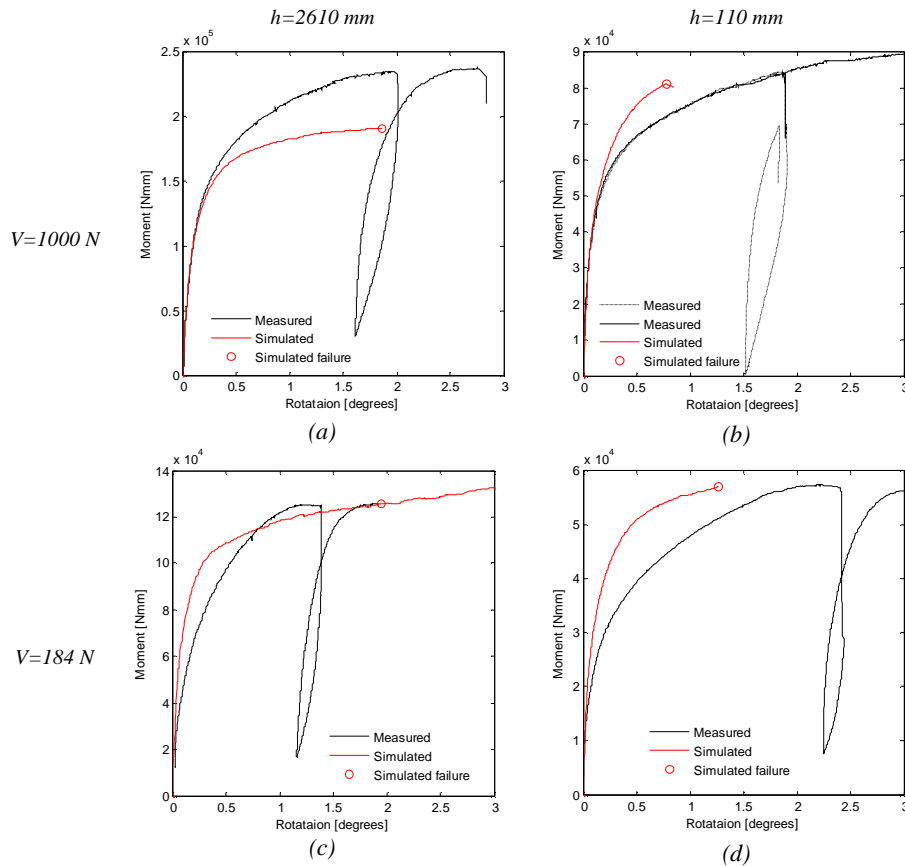


Figure 7.25 Simulation of laboratory tests using an embedded FE-model. $d/D=0.75$

The simulations performed with embedded foundations in Figure 7.24 and Figure 7.25 are seen to predict the overall capacities well, with exception of tests performed with $V=1000$ N and $h=2610$ mm. This was also seen for the corresponding test with $d/D=0.25$.

It is clear from the performed simulations that the calibrated soil parameters are not capable of predicting the behaviour of bucket foundations measured in the laboratory precisely. The degree of accuracy observed is though in geotechnical problems assumed to be acceptable for most of the simulations.

The deviation between the measured and simulated results is assumed to be caused by the material model used to simulate the soil behaviour and the installation method. The Mohr Coulomb material model has several disadvantages in relation to the true behaviour of soil. Firstly the stress dependency is not included in the model. The stress level in the soil is shown to vary between the tests simulated. Thus this dependency is of great

importance as the stress level is small in the small scale tests. Secondly the post peak softening that dense sand exhibits is not possible to model since the model behaves as an ideal plastic material at yield. The installation method is in the literature shown to influence the response of small scale tests, cf. chapter 4. This corresponds well with the large strength parameters necessary to predict the capacity. Information's on the value of the interface friction between the soil and skirt are only limited. The interface friction is shown to influence on the response, thus further research regarding this is desirable.

Attempts have been made on simulating the response using a more advanced material model, Feld (2001) and Hansson et al. (2005). The model used is the Single Hardening model which is generally capable of simulating the basic behaviour of soil better than the Mohr Coulomb material model, Lade & Kim (1988). The Single Hardening model is implemented in ABAQUS as a user material model by Jakobsen (2002). Attempts on three dimensional modelling of bucket foundations with this model have shown that the model is presently not capable of performing a complete simulation of the problem until failure with the mesh fineness necessary, Feld (2001) and Hansson et al. (2005).

7.2. Simulation of large scale loading test

The large scale loading test presented in chapter 3 is simulated in the following section using soil parameters derived from CPT's performed at the site prior to the test. The bucket foundation is a full bucket with a diameter and skirt length equal 2 meters and is loaded horizontally 11.6 meters above the bucket lid. The geometry of the FE-model and the mesh constructed is presented in Figure 7.26 and Figure 7.27 respectively. The vertical loads on the bucket are 23.1kN and 21.6kN from self weight of the bucket foundation including measuring equipment and the loading tower respectively. The model and mesh are constructed according to the experience gained from the simulations of the small scale tests.

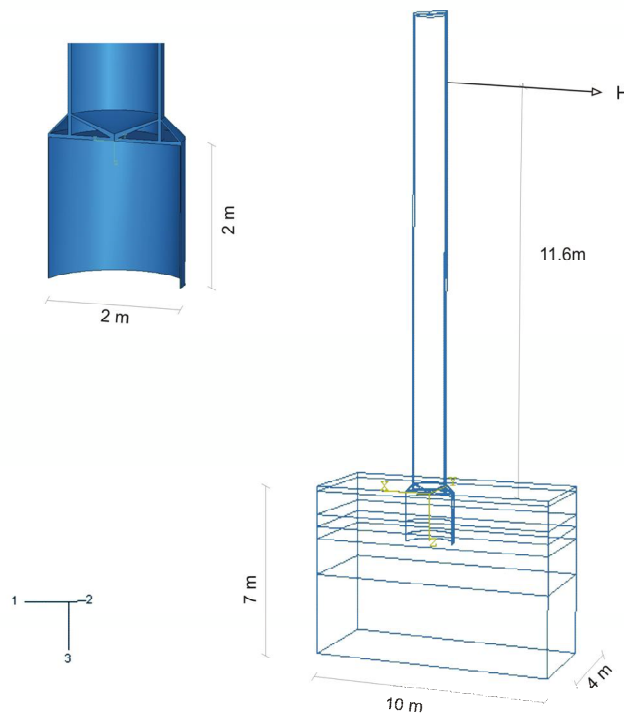


Figure 7.26 Geometry used in FE-simulation of large scale test.

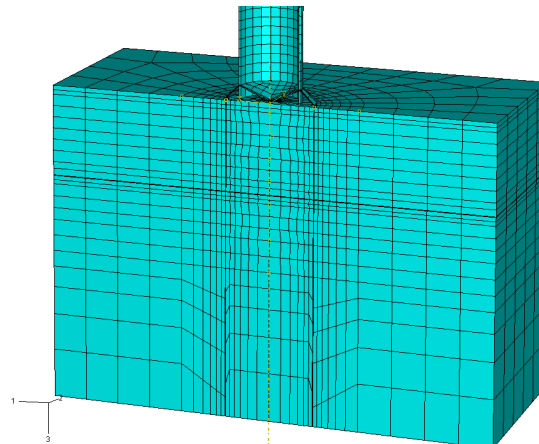


Figure 7.27 Constructed mesh used in the simulation of the large scale test.

The soil parameters used in the simulation are derived from the CPT response as given in the following. The soil is divided into 6 layers containing similar soil characteristics, see Figure 7.26. The location of the stratum boundaries are given in Table 7.2, where the foundation level corresponding to the mud

line is located in level -1.8m. The soil parameters are derived from several CPT's. The CPT-results are reported in Larsen & Ibsen (2005). From each CPT the mean soil parameters are determined within each layer. The soil parameters used in the simulation are the 55% fractile of the mean values in each layer assuming t-distribution. The soil parameters are presented in Table 7.2 where also the 95% fractile is shown.

Relative density

The relative density, D_r of the sand is determined from the cone resistance using the following expression, Baldi et al. (1986).

$$\text{Equation 7.4} \quad D_r = \frac{1}{C_2} \ln \left(\frac{q_c}{C_0 (s'_v)^{C_1}} \right)$$

where values of the constants equals $C_0=181$, $C_1=0.55$ and $C_2=2.61$ valid for sands are used.

Triaxial friction angle

The triaxial secant friction angle is determined from the relative density using the following expression, Schmertmann (1978).

$$\text{Equation 7.5} \quad j_{tr} = aD_r + b \quad \left. \begin{array}{l} a = 0.14 \\ b = 28 \end{array} \right\} \quad \text{Valid for fine uniform sands}$$

From the simulations of the small scale tests in section 7.1.1 it was argued that the friction angle in the FE-model more likely corresponds to the plane friction angle than the triaxial angle. Thus the simulation of the large scale test is carried out with both the triaxial friction angle as well as the plane. The plane friction angle is in the model approximated by $j_{pl}=1.1j_{tr}$.

Young's modulus

The Young's modules as secant and initial stiffness are determined from the following expression, Plaxis (2003).

$$\text{Equation 7.6} \quad E_s = C_s \cdot q_c \left(\frac{q_c}{\sqrt{s'_v}} \right)^{-0.5}$$

$$E_0 = C_{ur} \cdot q_c \left(\frac{q_c}{\sqrt{s'_v}} \right)^{-0.75} \cdot 2(1+n)$$

where

q_c , s'_v and E is in kPa.

C_s and C_{ur} are constants.

E_s is the secant stiffness modulus determined at 0.1% axial strain. The secant modulus is often assumed to correspond to the modulus at 50% strength, E_{50} . E_0 is the initial stiffness modulus corresponding to the unloading reloading stiffness.

The values of C_s and C_{ur} are based on triaxial tests on the sand and are estimated to a value equal 320 and 1600 respectively. The results from the triaxial tests are presented in Hansson et al. (2005).

Table 7.2 Characteristic material properties determined from CPT.

Soil Layer; Level	I_D [%]		j [o]		E_s, E_{50} [MPa]		E_0 [MPa]		$\tan(d)$
	t_{55}	t_{95}	t_{55}	t_{95}	t_{55}	t_{95}	t_{55}	t_{95}	
Layer 0: -1.8;-2m			28		10		20		0.42
Layer 1: -2;-3.0m	85.2	80.4	39.9	39.3	26.4	23.8	52.6	48.2	0.42
Layer 2: -3.0;-3.5m	66.1	58.4	37.3	36.2	32.9	29.9	72.9	69.6	0.42
Layer 3: -3.5;-4m	94.6	86.5	41.2	40.1	56.1	51.4	103.6	99	0.42
Layer 4: -4;-5.5m	76	71.8	38.6	38.1	56	54	115.9	113.3	0.42
Layer 5: -5.5;-7m	61.8	56.1	36.7	35.9	59.6	57.1	133.3	127	0.42

Layer 0 consists of disturbed material due to work during installation of the bucket foundation and loading tower. The soil parameters used for this layer is estimated. A cohesion and overburden pressure equal 1kPa is used in the simulation for easier equilibrium. The interface friction angle, d in Table 7.2 is determined from measurements during removal of the bucket foundation, which can be found in Larsen & Ibsen (2005). The result from FE-simulations with the secant stiffness modulus is compared with the measured response in the following figures.

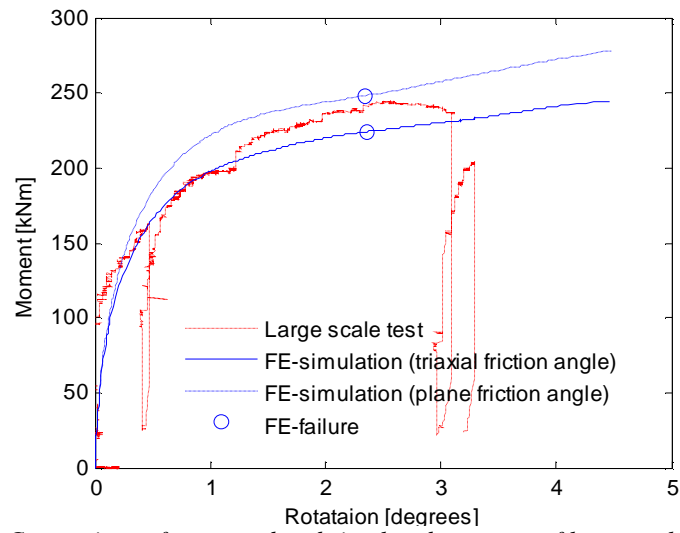


Figure 7.28 Comparison of measured and simulated response of large scale bucket foundation subjected to combined loading.

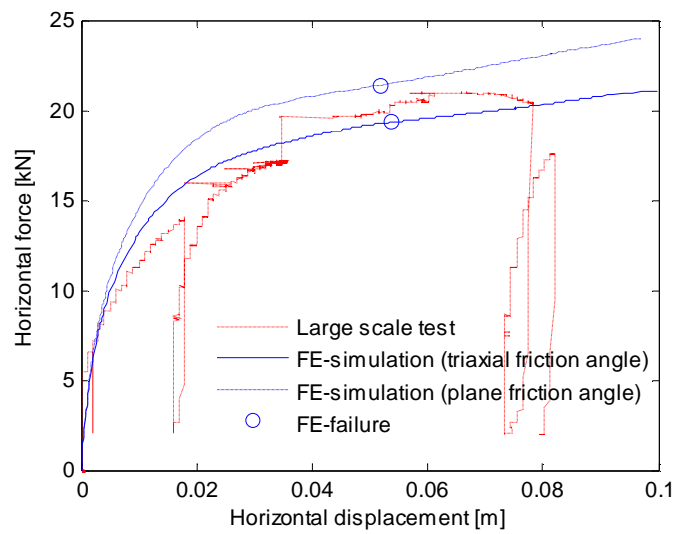


Figure 7.29 Comparison of measured and simulated response of large scale bucket foundation subjected to combined loading.

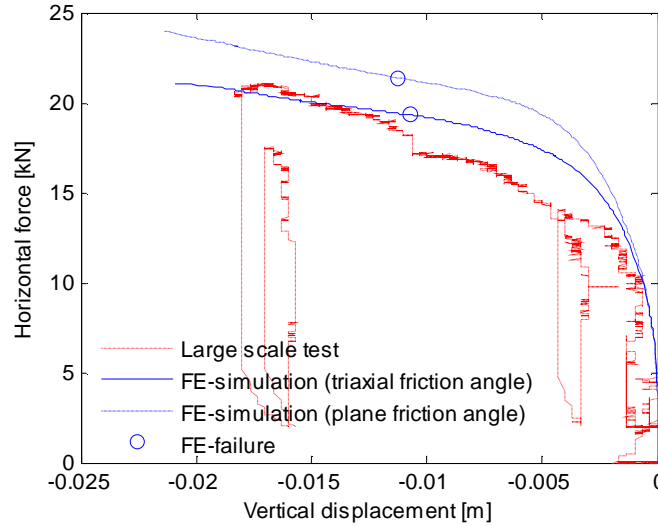


Figure 7.30 Comparison of measured and simulated response of large scale bucket foundation subjected to combined loading.

The FE-simulation with j_{pl} is from Figure 7.28 to Figure 7.30 seen to estimate the measured capacity of the bucket foundation well, with the soil parameters derived from the performed CPT's. The simulation with the triaxial friction angle, j_{tr} is seen to underestimate the capacity of the foundation, which supports the argument stated regarding the influence of the intermediate stress in section 7.1.1.

The pre peak behaviour of the bucket foundation is though seen to deviate slightly from the measured response. This is ascribed the constitutive model used. The response is generally too stiff compared to the measured results, with exception of the initial rotational stiffness which is softer in the simulation.

The FE-simulation stopped at failure due to equilibrium difficulties. The simulation was hereafter restarted by changing the extrapolation procedure, as explained in appendix D. The state of failure is specified by circles in the above figures and is determined as described in the previous section.

The failure mode observed in the simulation is shown in Figure 7.31 and is seen to correspond to the one observed from the corresponding small scale simulations.

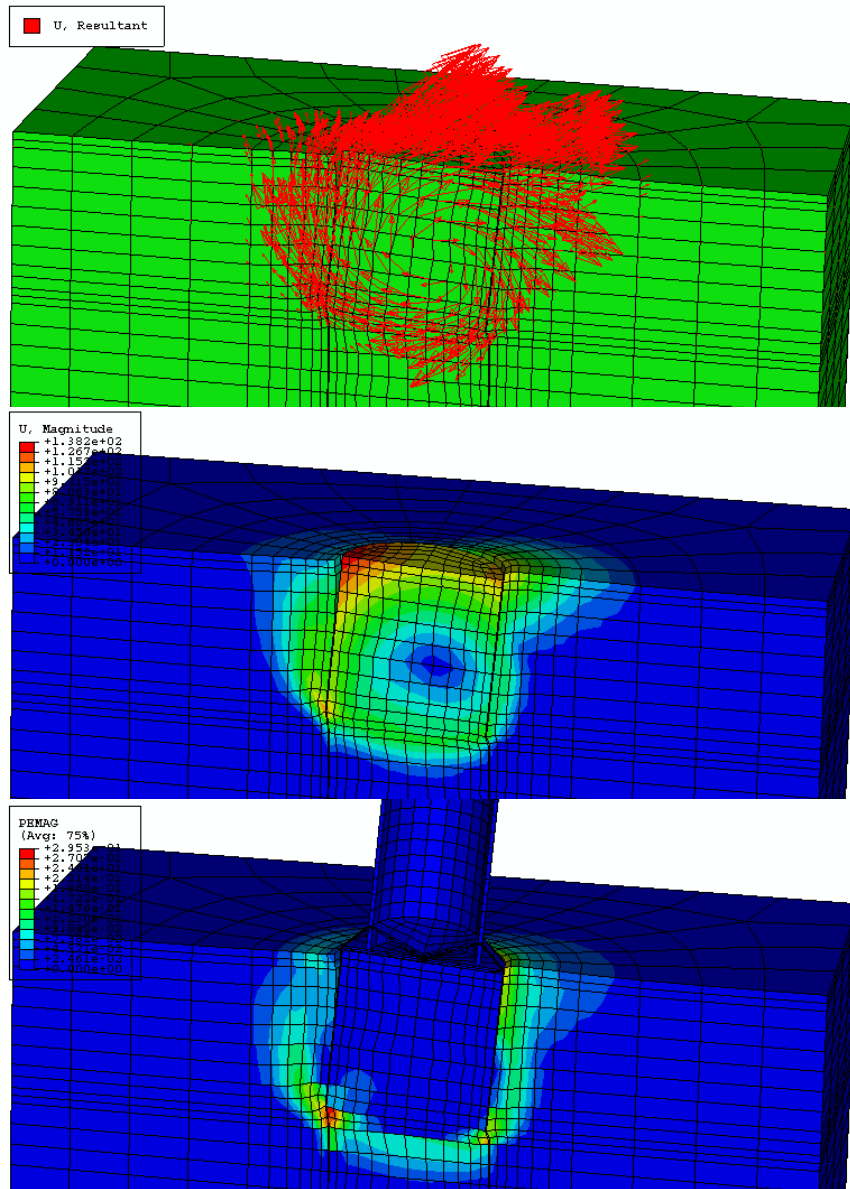


Figure 7.31 Deformations and plastic strains at failure.

Comparison with embedded behaviour

The behaviour of the large scale bucket foundation is in Figure 7.32(a) compared with the behaviour of a corresponding embedded solid foundation. From the figure it is clear that only minor deviation in the behaviour is present which also was found for the small scale buckets. The simulations presented

in Figure 7.32 are performed with a vertical load corresponding to twice the load applied to the large scale experiment i.e. $V=89.4$ kN.

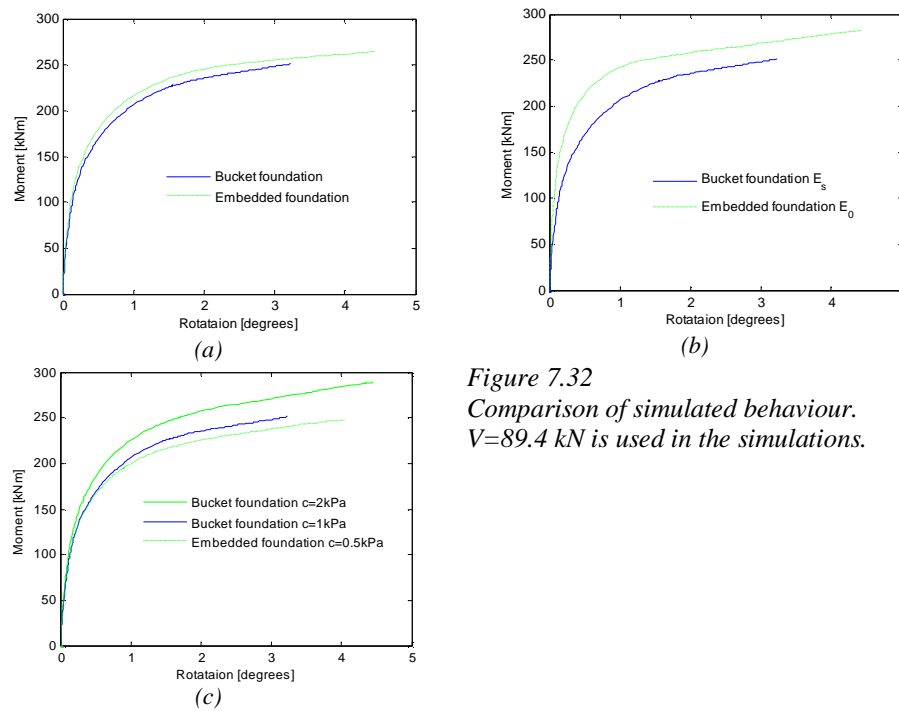


Figure 7.32
Comparison of simulated behaviour.
 $V=89.4$ kN is used in the simulations.

Influence of stiffness modulus

The secant stiffness modulus is used in the simulation of the large scale loading test. If the unloading reloading behaviour is desired the elastic stiffness modulus E_0 is to be used instead. A simulation of an embedded foundation is performed with the elastic stiffness', E_0 from Table 7.2. The results are shown in Figure 7.32(b) where the global stiffness of the behaviour and the capacity is seen to increase significantly. Thus the secant modulus is to be used in order to predict the overall behaviour of large scale bucket foundations. This is in contrast with the results from the simulations of the small scale tests where an unloading reloading stiffness was found to simulate the overall behaviour.

The difference between the small- and large scale tests is the installation procedure. The bucket foundations in the laboratory are installed by means of pushing whereas the large scale test is installed by applying suction to the bucket. Installation by pushing is assumed to increase the density of the soil adjacent to the skirt and is thereby assumed to entail an increasing stiffness as well as strength of the soil. The installation procedure is only assumed to have an significant effect on the response in case of small scale tests, cf. chapter 4.

Influence of cohesion

A small cohesion is used in the simulation of the large scale bucket foundation test. The influence from the cohesion on the behaviour is therefore investigated, see Figure 7.32(c). The influence of the cohesion used is from the figure estimated to be 8%, assuming a linear relation, cf. section 7.1.1. It has unfortunately not been possible to complete a simulation with a cohesion less than 1kPa in combination with the small vertical load applied in the large scale test.

FE-simulations of additional large scale loading tests

The presented load test is only one from a test series with different heights of impact carried out at the test site. Based on the CPT's performed before each test, corresponding simulations of the individual tests are carried out. The results from the simulations of the remaining test entails results that are similar to the one presented above.

7.3. Simulation of swipe test

The hardening law controls the size of the yield surface at a given load state within the macro model approach as described in chapter 6. The macro model assumes that the vertical preload of the foundation controls the expansion of the yield surface during loading. The yield surface is in the literature investigated based on this assumption by carrying out swipe tests in the laboratory. The swipe test is assumed to follow the yield surface. This assumption is investigated in the following.

A FE-model of a bucket foundation with $D = d = 300\text{mm}$ is used to simulate a side swipe test with pure horizontal load, i.e. $h = M = 0$. A corresponding simulation is hereafter performed by preloading the foundation corresponding to the swipe test. The vertical load is then lowered to a level below this, after which the bucket foundation is loaded with a horizontal force applied at height of impact $h = 0$ until failure. During this the bucket is free to move in all directions. If the assumption above is true the response of the second simulation should be purely elastic until reaching the load path from the swipe test. The results from the simulations are shown in Figure 7.33 .

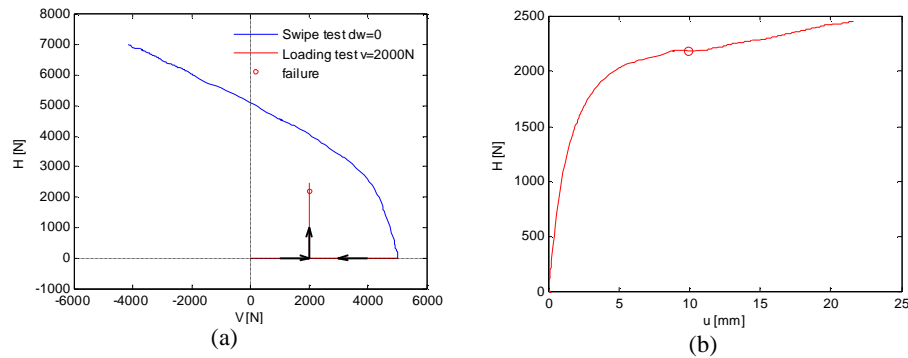


Figure 7.33 (a) Simulated swipe test and (b) load test with corresponding vertical preload, $V_{pre}=5000N$.

From the simulated tests in Figure 7.33 it is clear that the swipe test doesn't follow the yield surface, as failure is reached within the supposed present yield surface, although $V_{pre} \ll V_{peak}$.

7.4. Summary

Evidence has been given that a three dimensional FE-model is capable of predicting the combined behaviour of bucket foundation subjected to low vertical load when the material properties of the soil are defined corresponding to the stress level present.

The results from the simulations indicate that the behaviour of small scale tests are influenced by the installation procedure used. Thus large strength and stiffness are necessary in the simulations.

The performed FE-simulation has shown that the behaviour of bucket foundations under the given load conditions are very similar to a circular and solid embedded foundation. The simulations of embedded foundations are found to be significantly more stable and easy to carry out. Thus the embedded calculations are recommended especially in the initial part of a design phase.

The failures mode of bucket foundations analyzed are found to be caused by a rotation around a point located inside the bucket foundation. The point of rotation is for low vertical load found to be located at a distance from the vertical centre line in direction of the horizontal load. An increase in the height of impact is found to move the point of rotation upward and an increase in the vertical load moves the point horizontally in the direction opposite of the horizontal load. For large embedment ratios the soil trapped within the bucket foundation is found to behave as a rigid cluster during loading whereas

it is in case of low embedment ratios are found to be affected by the failure mode.

A FE-model of the bucket foundation has been used to investigate whether the load path followed in swipe tests corresponds to the yield surface according to the macro model approach. The simulations yield results that do not support this assumption.

8. Concluding remarks

The bucket foundation is expected to have great potential as foundation principle for offshore wind turbines. The purpose of this thesis was to investigate the static behaviour of bucket foundations as monopods in dense saturated sand subjected to combined loads relevant for offshore wind turbines. An extensive test program have been carried out during this work on both small scale foundations in the laboratory and large scale foundations at the test facility in Frederikshavn. The tests are carried out in saturated dense sand using a test setup that is significantly different from the majority of other studies. The static behaviour is evaluated based on these results in relation to the macro model approach and finite element calculations. The main conclusions of this work are presented in this chapter, and directions for future work are given.

8.1. Conclusion- main findings

The conclusions gained from the work carried out during this Ph.D. study are given in the following with respect to the research aims stated in chapter 1.

8.1.1. Experimental work

The experimental work carried out during this Ph.D. study constitutes a major part of the total work. More than 100 loading tests on bucket foundations with different geometry and load paths are carried out in both the laboratory and at the test facility in Frederikshavn. Moreover a corresponding amount of experiments performed prior to this work at the geotechnical laboratory at Aalborg University are evaluated and reported during this work. From this a large database on bucket foundations has become available. The database consists of results from more than 200 experiments with a diameter varying from 50 millimetres to 2 metres. The embedment ratio of the tested bucket foundations varies from 0 to 1.

The test setup in the laboratory has during this work been optimized and the procedure for preparation of the sand is optimized to yield homogenous sand

samples. The characteristics of the tested sand have been evaluated from available triaxial tests.

Laboratory CPT-calibration

A method is proposed on predicting the relative density and strength of the prepared sand samples using a laboratory CPT-probe.

The method is based on Terzaghi's bearing capacity formula and involves a depth factor that is calibrated from results of 12 test series with the laboratory probe.

The proposed method is based on the triaxial friction angle at large stresses since Kerisel's relationship in this case gives a unique result. From this friction angle the method can be used to estimate the void ratio and the complete variation of the triaxial friction angle with the stress level for the tested sand.

8.1.2. Vertical bearing capacity of bucket foundations

The bearing capacity of bucket foundations including circular surface footings is investigated analytically and experimentally. The bearing capacity formula is found capable of determining the vertical bearing capacity of bucket foundations by use of axis-symmetric bearing capacity factors. Selected values of these are investigated using the commercial FE-codes Plaxis and ABAQUS. These calculations yield results that are in accordance with newly published values.

A new general expression that describes the bearing capacity factors is proposed based on the FE- calculations carried out and values from the literature. The proposed expression applies to plane strain as well as axis-symmetric stress conditions for foundations with smooth or rough base. The influence of the base roughness on the bearing capacity factor N_q is discussed in the literature. The influence has been investigated numerically for circular foundations from which it is concluded that there is a significant effect from this.

Plane strain calculations have shown to yield a conservative bearing capacity of circular foundations (including bucket foundations). Hence factors evaluated from axis-symmetric stress condition are proposed with a reduced triaxial friction angle.

The vertical bearing capacity of a bucket foundation is from the bearing capacity formula as well as the experiments found to be larger than generally

assumed in the literature. The increase in capacity is due to the use of incorrect bearing capacity factors throughout the literature.

8.1.3. Combined behaviour of bucket foundations

The behaviour of bucket foundations in dense saturated sand subjected to combined static loads is during this work investigated experimentally. The entire behaviour is investigated until failure from the applied load paths.

Especially the influence of the ratio M/DH and d/D of bucket foundations subjected to low vertical load has only to a limited extend been investigated prior to this work. The tests carried out in connection with this work are carried out with constant vertical load and M/DH ratio, whereas the majority of tests from the literature are swipe tests. Moreover the soil tested during this work is saturated sand, whereas the majority of the present work in the literature is based on tests in dry sand. Dry sand exhibits in some cases a behaviour that is similar to the presence of cohesion due to the humidity in the air. This is not the case for saturated sand. Thus this is preferred.

The experimental results available from the database are within this thesis analyzed in relation to the macro model approach. The components within the macro model approach have been examined and further knowledge on these is gained during this work.

Combined Capacity of bucket foundations

The combined capacity of the bucket foundations from the experimental results has been evaluated by applying two failure criteria. A simple failure criterion is proposed in case of low vertical load, which is linear in planes along the V-axis and non-linear in the radial planes. The criterion is calibrated from the test results in volume 2 on dense sand and from test results on loose sand ($d/D=0.5$) after Byrne et al. (2003). The three dimensional yield criterion according to the macro model approach by Villalobos et al. (2005) is modified in order to describe the observed measured capacities at various vertical load ratios, V/V_{peak} . Both criteria are proposed depended of the tensile capacity of the bucket foundations. It is clear from the experiments that the capacities are dependent of the embedment ratio and to some extend the load path as well as the load ratio.

The two failure criteria are calibrated from the test results, and are found capable of describing the measured capacities, though with some scatter. The failure criterion according to the macro model approach is when compared with existing results found to some extend to deviate from these. The experiments within this work are expected to yield the correct criteria as only few tests in the literature have actually been brought to failure.

Initial experiments on bucket foundations available from the literature have shown, that the combined capacity of bucket foundations from loads relevant to offshore wind turbines are, when normalized with the corresponding vertical bearing capacity, independent of the embedment ratio. From the experiments performed the normalized capacity is however in case of low vertical load found to be significantly dependent of the embedment ratio. This is found to be due to the tension capacity of bucket foundations.

Behaviour of bucket foundations

The behaviour prior to failure is clarified from the performed tests and is shown to be dependent of the embedment ratio as well as the load path followed. The behaviour of the bucket foundations tested in the laboratory is analyzed according to the macro model approach.

The hardening of the yield surface is according to the macro model approach controlled by the vertical plastic settlement during loading. Preliminary investigations have indicated that this is not correct, which is also found from loading tests with low vertical load within this work as these yields negative vertical displacements.

Experimental evidence has indicated that the plastic potential and yield surface of circular and bucket foundations are identical in the radial planes of the load space, i.e. associated flow. The assumption of associated flow in the radial planes is within this thesis validated for large ratios of M/HD at failure. At low M/HD and V/V_{peak} ratios the assumption of associated flow in these planes are from the experiments however less clear. Along the V-axis a high degree of non-associated flow is observed, which is in accordance with observations from earlier studies in the literature. From the development of the plastic displacements during loading, the hardening law is shown to be isotropic in the radial planes.

The macro model approach is from the experimental work generally found to be capable of simulating the behaviour of bucket foundations. The yield surface at failure is calibrated from the experiments, and the peak of the potential surface along the V-axis is investigated for low embedment ratios. At large embedment ratios ($d/D > 0.25$) the peak is found to be located at a vertical load larger than 1000N.

In a design situation the macro model is only to a limited extend applicable at the time being. In order to calibrate the model, a numerous model parameters are still to be evaluated. At the time being the available knowledge is insufficient to describe the entire behaviour of e.g. a bucket foundation without an extensively test program. Further more a macro model is often

only useful in the conceptual design phase since this model assumes homogenous and isotropic soil.

8.1.4. Numerical simulations

Numerical simulations of selected small scale loading tests are performed using ABAQUS. The soil is modelled as a Mohr-Coulomb material. Evidence has been given that a three dimensional FE-model is capable of predicting the complete combined behaviour of bucket foundation subjected to low vertical load, when the material properties of the soil are defined corresponding to the stress level present. Small scale as well as large scale tests has been compared to the numerical simulations. The soil characteristics of the sand tested in the laboratory have been estimated from triaxial tests whereas the results from CPT's have been used for the large scale tests.

First order cubical solid elements and reduced integration have shown to be superior in modelling the problem which involves elasto-plastic behaviour of the soil combined with interface problems and slender elements below the skirt tip.

The results from the simulations indicate that the behaviour of small scale tests are influenced by the installation procedure used. Thus large friction angles and stiffness' are necessary in the simulations. The large friction angle, is besides the installation method, argued to be due to the influence of the intermediate principal stress.

The performed FE-simulations have shown that the behaviour of bucket foundations under the given load conditions are similar to an equivalent circular and solid embedded foundation.

The numerical simulations of embedded foundations are found to be significantly more stable and user friendly. The embedded calculations are therefore recommended especially in the initial part of a design phase.

The failure modes of bucket foundations are analyzed from the performed simulations with low vertical load. The failure mechanisms causing failure are found to be induced by a rotation of the construction around a point located inside the bucket foundation. The point of rotation is found to be located at a distance from the vertical centre line in direction of the horizontal load. An increase in the height of impact is found to move the point of rotation upward and an increase in the vertical load is found to move the point horizontally in the direction opposite of the horizontal load. In case of low embedment ratios the failure modes observed from simulations of bucket foundations and embedded foundations are found not to be identical. The overall response is though found only to be insignificantly affected by this difference.

The majority of available information's regarding the behaviour of bucket foundations available in the literature are based on swipe tests. A FE-model of the bucket foundation has been used to investigate whether the load path followed in swipe tests corresponds to the yield surface according to the macro model approach. The simulations have shown to yield results that do not support this assumption. Thus these tests will yield an incorrect shape of the yield surface.

8.2. Directions for future work

Based on the knowledge and experience gained through the work, connected with this thesis, the following directions for future work are suggested.

The vertical bearing capacity of bucket foundations has been investigated omitting the influence of the depth factor in the bearing capacity formula. The estimated bearing capacity of bucket foundations will in this case be underestimated. Hence an investigation of the depth factor correlated to the axis-symmetric bearing capacity factors is suggested.

The behaviour of bucket foundations is during this work linked to the vertical tension capacity. Two methods have been used within this work, though more experience on this is important as the modelled behaviour of bucket foundations subjected to low vertical load is significantly dependent upon this.

The macro model approach has been calibrated against laboratory tests with bucket foundations at failure. The parameters within the model however still require numerous load tests in order to be calibrated for general situations. The tests carried out during this work are optimal for estimating the shape of the yield surface at failure. Further experiments are necessary to describe the complete influence of the relative density (D_r), effect of scale (D), load level (V/V_{peak}) and load path (M/DH). As initially tests the laboratory tests series carried out are proposed expanded with following conditions: 1) Intermediate vertical load e.g. $V=500N$ and 2) Intermediate height of impact e.g. $h=M/H=1000mm$. Hence the curvature of the failure criteria suggested can be evaluated.

The flow potential and the hardening law is during this thesis only to a limited extend analyzed. In order to describe the entire behaviour of bucket foundations, further research on this is necessary. The use of finite element is based on the presented results suggested in this connection.

The macro model approach described is only valid for a planar loading of the bucket foundations. The full six-degree of freedom behaviour of shallow foundations is investigated at Oxford University and University of Western Australia at the time being, e.g. Byrne & Houlsby (2005) and Bienen et al.(2006). The investigation is however based on swipe tests which have shown to introduce errors.

The soil conditions present in connection with prototypes are often layered, within the depth corresponding to the skirt length of the bucket foundation. The use of the macro model approach is only relevant for homogenous soils, whereas the finite element method is capable of including layered soil. The influence of layered soil is only to a limited extend investigated during this work from the simulation of the large scale test. The influence of layered soil on the behaviour of bucket foundations is of great importance, as the presence of layers with soft soil in many cases is expected. The influence of layered soil is according to the failure modes observed mainly supposed to influence on the behaviour when located above or near the level of the skirt tip.

Bibliography

Abaqus (2004) *Abaqus Documentation Version 6.5 (Manual)*. Abaqus inc. 2004

American Petroleum Institute (API) (2002), *Recommended Practice for Planning, Designing and Constructing Fixed Offshore Platforms- Working Stress Design 2A-WSD* 21st edition December 2002

Andersen A.T., Madsen E.B. & Schaarup-Jensen A.L. (1998) *Data Report Part 1 Eastern Scheldt Sand, Baskarp Sand No. 15*. January 1998 Geotechnical Engineering Group, Aalborg University.

Baldi, G. Bellotti, R. Ghionna, V. Jamiolkowski, M & Pasqualini, E (1986) *Interpretation of CPT's and CPTU's; 2nd part: Drained penetration of sands*. Proceedings of the 4th International Geotechnical Seminar pp. 143-156.

Bell R.W. (1991) *The analysis of offshore foundations subjected to combined loading*. M.Sc. Thesis, Oxford University

Bienen B., Byrne B.W., Houlsby G.T. & Cassidy M.J. (2006) *Investigating six-degree-of-freedom loading of shallow foundations on sand*. Géotechnique **56**, No. 6, 367-379.

Bolton M.D. (1986) *The strength and dilatancy of sands*. Géotechnique, **36**(1): 65-78

Bolton M.D. & Lau C.K. (1993) *Vertical bearing capacity factors for circular and strip footings on Mohr-Coulomb soil* Can. Geotech. J. 30 pp. 1024-1033.

Borup M. and Hedegaard J. (1995) *Data Report 9403, Baskarp Sand No.15*, Geotechnical Engineering Group, Aalborg University.

Butterfield R. (1981) *Another look at gravity platform foundations. Soil mechanics and foundation engineering in offshore technology*. Udine, Italy: CISM

Butterfield R., Houlsby G.T. & Gottardi G. (1997) *Standardized sign conventions and notation for generally loaded foundations*. *Géotechnique* **47**, No. 5, 1051-1054.

Butterfield R. & Gottardi G. (1994) *A complete three dimensional failure envelope for shallow footings on sand*. *Géotechnique* **44**, No.1, 181-184.

Butterfield R. & Ticof J. (1979) *The use of physical models in design*. Discussion. Proc. 7th Eur. Conf. Soil. Mech., Brighton 4, 259-261

Byrne B.W. (2000) *Investigation of Suction Caissons in Dense Sand*. Ph.d. thesis University of Oxford

Byrne B.W. and Houlsby G.T. (1998) *Model testing of circular flat footings on uncemented loose carbonate sand: experimental data*. Report N° OUEL 2192/98. Department of Engineering Science, University of Oxford.

Byrne, B.W. & Houlsby G.T. (1999) *Drained Behaviour of Suction Caisson Foundations on Very Dense Sand* Offshore Technology Conference May 1999 OTC 10994

Byrne B.W. and Houlsby G.T. (2000) *Investigation of suction caissons in dense sand: experimental data*. Report N° OUEL 2227/00. Department of Engineering Science, University of Oxford.

Byrne B.W. & Houlsby G.T. (2001) *Observations of footing behaviour of loose carbonate sands*. *Géotechnique* **51** No.5 463-466

Byrne B.W. & Houlsby G.T. (2002a) *Experimental investigations of the response of suction caissons to transient vertical loading* Proc. ASCE, Jour. of Geotech. Eng. **128**, No. 11, Nov., pp 926-939

Byrne B. W. & Houlsby G.T. (2002b) *Investigating novel Foundations for Offshore Windpower Generation*. Proceedings of OMAE'02 21st International Conference on Offshore Mechanics and Arctic Engineering June 2002- Oslo, Norway.

Byrne B.W. & Houlsby G.T.(2003) *Foundations for offshore wind turbines*. Phil. Trans. R. Soc. of London Ser. A **361**, pp.2909-2930

Byrne B.W. & Houlsby G.T. (2005) *Investigating 6 degree-of-freedom loading on shallow foundations*. Frontiers in Offshore Geotechnics: ISFOG 2005.

Byrne B.W., Villalobos F., Houlsby G.T. & Martin, C.M. (2003) *Laboratory Testing of Shallow Skirted Foundations in Sand*. Proc BGA International Conference on Foundations, Dundee, September 2003 pp.161-173

Casagrande A. (1940) *Characteristics of cohesionless soils affecting the stability of slopes and earth fills*. Contributions to soils mechanics, 1925-1940, Boston Society of Civil Engineers, Boston Mass., 257-276.

Cassidy M.J. (1999) *Non-linear analysis of jack-up structures subjected to random waves*. DPhil thesis, Oxford University.

Clausen J., Damkilde L. and Andersen, L. (2006) *Efficient return algorithms for associated plasticity with multiple yield planes*. International Journal for Numerical Methods in Engineering. Vol 66, No. 6 pp. 1036-1059

Clausen J.C., Damkilde L. and Krabbenhøft K. (2007) *Efficient finite element calculation of Ngamma*. Proceedings of the Eleventh International Conference on Civil, Structural and Environmental Engineering Computing. Barry H.V Topping (Ed.). Civil-Comp Press. 2007. (Accepted)

Cook R.D, Malkus D.S. and Plesha M.E. (1989) *Concepts and Applications of Finite Element Analysis*. Wiley 1989 Third edition ISBN 0-471-848788-7

Coulomb C.A. (1776) *Essai sur une Application des Règles des Maximis et Minimis à quelques Problèmes de Statique*, Mémoires, Académie Royale des Sciences, Vol. 7, Paris.

Cox A.D., Eason G. and Hopkins H.G. (1961) *Axially Symmetric Plastic Deformations in Soils*. Philosophical Transactions of the Royal Society of London. Series A, Mathematical and Physical Sciences, Vol. 254, No. 1036

DGF-Bulletin (2001) *DGF- Bulletin 15, Laboratoriehåndbogen (Handbook for laboratory work)*. Danish Geotechnical Society. In Danish.

Didriksen L.R. & Kristensen J. (2000) *Konceptvurdering af bøttefundament til en offshorevindmølle*. M.Sc. Thesis, Aalborg University. In Danish

DNV (1992) *Foundations, Classification Notes No. 30.4*. Det Norske Veritas Classification A/S February 1992

DNV (2004) *Design of offshore wind turbine structures Offshore Standard*. DNV-OS-J101 Det Norske Veritas

Doherty J.P. & Deeks A.J. (2003) Elastic response of circular footings in a non-homogeneous half-space. *Geotechnique* 53 No 8 703-714.

Doherty J.P. & Deeks A.J. (2006) *Stiffness of a Flexible Circular Footing Embedded in an Elastic Half-Space*. Int Journal of Geomech. ASCE 2006

Doherty J.P., Houlsby G.T. & Deeks A.J. (2005) *Stiffness of Flexible Caisson Foundations Embedded in Nonhomogeneous Elastic Soil*. Journal of Geotechnical and Geoenvironmental engineering. ASCE 2005

DS 415 (1998) *Norm for fundering (Code of Practice for foundation engineering)*, 4th. edition, Danish standard Copenhagen, In Danish

Energy 21 (1996) *The Danish governments energy action plan 1996 (Regeringens energihandlingsplan 1996)* In Danish. Miljø og Energiministeriet. ISBN 87-7844-057-2

Energy Plan 2030 (2006) *The Danish Society of Engineers' energy plan 2030 (Ingeniørforeningens energiplan (2030))* In Danish (Resume in English are available), The Danish Society of Engineers, IDA. Available on www.ida.dk

Feld T. (2004) *State-of-the-art design standard specific developed and applicable for offshore windturbine structures*. North American Wind Power.

Feld T. (2001) *Suction Buckets, a new Innovative Foundation Concept, applied to Offshore Wind Turbines*, Ph.D. Thesis atv project ef675, Joint Project between ATV, Rambøll and Aalborg University, Denmark.

Georgiadis M. & Butterfield R. (1988) *Displacements of footings on sand under eccentric and inclined loads*. Can. Geotech. J. **25**,199-212.

Georgiadis M. (1993) *Settlement and rotation of footings embedded in sand*. *Soils and Foundations* **33**, No. 1, pp. 169-175.

Gottardi G. & Butterfield R. (1993) *On the bearing capacity of surface footings on sand under general planar loads*. *Soils Fdns* **33**, No. 3, 68-79.

Gottardi G. & Houlsby G.T.(1995) *Model tests of circular footings on sand subjected to combined loads*, Report No. OUEL 2071/95; University of Oxford U.K.

Gottardi G., Houlsby G.T. & Butterfield R. (1997) *The Plastic Response of Circular Footings on Sand under General Planar Loading*. Report No. OUEL 2143/97 University of Oxford U.K.

Gottardi G., Houlsby G.T. & Butterfield R. (1999) *The Plastic Response of Circular Footings on Sand under General Planar Loading*. *Géotechnique* **49**, No. 4, 453-469.

Gottardi G. Ricceri G. & Simonini P. (1994) *On the scale effect of footings on sand under general loads*. XIII ICSMFE New Delhi India.

Hansen A. & Jakobsen K.P (1995) *Fundamenters stødbæreevne ved plasticitetsteoriens øvre værdisætning*. M.sc. Thesis Aalborg University Denmark. In Danish.

Hansen B. (1958) *Line ruptures regarded as narrow rupture zones, basic equations based on kinematic conditions*, Proceedings on Conference on Earth Pressure Problems, Vol. 1, Brussels, pp.38-47.

Hansen B. (1975) *The Bearing Capacity of Footings*. First Baltic Conference on Soil Mechanics and Foundations Engineering Gdansk, Poland, 22-25 September 1975.

Hansen B. (1979) *Definition and use of frictional angles*, Proc. Int. Conf. VII ECSMFE Brighton, U.K.

Hansen J.B. (1953) *Earth Pressure Calculation*, Teknisk Forlag, Copenhagen

Hansen J.B. (1961) *Bulletin No. 11, a General Formula for Bearing Capacity*. The Danish Geotechnical Institute Copenhagen 1961.

Hansson M., Hjort T.H. & Thaarup M. (2005) *Static and Transient Loading of the Bucket Foundation*. Ms.c. Thesis Aalborg University.

Houlsby G.T. (2003) *Modelling of Shallow Foundations for Offshore Structures*, Int Conf on Foundations, Thomas Telford, London.

Houlsby G.T. and Byrne B.W. (2000) *Suction caisson foundations for offshore wind turbines and anemometer masts*. *Journal of Wind Engineering* 24 (4) pp 249-255

Houlsby G.T. Byrne B.W. & Martin C.M. (2001) *Novel Foundations for Offshore Wind Farms*. Research Proposal to EPSRC (Aug 2001)

Houlsby G.T. & Byrne B.W. (2005) *Calculation procedures for installation of suction caissons in sand*. Proc. ICE Geotechnical Engineering 158, July 2005 Issue GE3. pp. 135-144

Houlsby G.T. & Cassidy M.J. (2002) A plasticity model for the behaviour of footings on sand under combined loading. *Géotechnique* **52** No.2 117-129

Houlsby G.T., Ibsen L.B. & Byrne B.W. (2005a) *Suction caissons for wind turbines*. Frontiers in Offshore Geotechnics: ISFOG 2005 London.

Houlsby G.T., Kelly R.B. and Byrne B.W. (2005) *The tensile capacity of suction caissons in sand under rapid loading*. Frontiers in Offshore Geotechnics: ISFOG 2005.

Houlsby G.T., Kelly R.B., Huxtable J. & Byrne B.W. (2006) *Field trials of suction caissons in sand for offshore wind turbine foundations*. *Géotechnique* **56** NO. 1, 3-10

Ibsen L.B., Borup, M. & Hedegaard, J. (1995) *Data Report 9501 Triaxial tests on Baskarp Sand No. 15*. Geotechnical Engineering Group, Aalborg University.

Ibsen L.B. (2002) *Bilag til Bøttefundament Frederikshavn Havn*. (Enclosure for Bucket Foundation Harbour of Frederikshavn; In Danish) Internal Report R0206 ISSN 13986465 R0206 Aalborg University (Confidential)

Ibsen L.B. & Bødker L. (1994) *Data Report 9301 Baskarp Sand No. 15* August 1994, Geotechnical Engineering Group, Aalborg University.

Ibsen L.B., Lade P.V. (1998) *The Role of the Characteristic Line in Static Soil Behavior*. 4th Workshop on Localisation and Bifurcation Theory for Soils and Rocks, A. A. Balkema.

Ibsen L.B., Larsen K.A. & Nielsen S.A. (2005a) *Joint R&D-Program: Innovative Foundation Solutions, The Novel Bucket Foundation*. Copenhagen Offshore Wind Conference & Exhibition, 26-28 October 2005, Denmark

Ibsen L.B., Liingaard M. & Nielsen S.A. (2005) *Bucket Foundation, a status*. Conference Proceedings Copenhagen Offshore Wind 2005, 26-28 October 2005, Copenhagen, DK.

Ibsen L.B., Schakenda, B & Nielsen S.A. (2003) *Development of the bucket foundation for offshore wind turbines, a novel principle*. Proc. USA Wind 2003 Boston.

Jacobsen M. (1970) *New oedometer and New Triaxial apparatus for firm soil*. DGI Bulletin No. 27 Danish geotechnical society.

Jakobsen K.P. (2002) *Elements of Constitutive Modelling and Numerical Analysis of Frictional Soils*. Ph.D. Thesis Aalborg University Denmark.

Janbu N. (1963) *Soil compressibility as determined by oedometer and triaxial tests*. Proceedings, European Conference on Soil Mechanics and Foundation Engineering, Wiesbaden, Vol. 1. and 2.

Jostad H.P. (2004) *Plaxis 3D foundation* Presentation Slides. Norsk Plaxis Brukermøte Trondheim 19. Oktober 2004

Kelly R.B., Byrne B.W., Houlsby G.T. & Martin C.M. (2003) *Pressure Chamber Testing of Model Caisson Foundations in Sand*. Proc.BGA Int. Conf. On Foundations, Dundee, UK.

Kelly R.B., Byrne B.W., Houlsby G.T., and Martin C.M. (2004) *Tensile loading of model caisson foundations for structures on sand*, Proc. ISOPE, Toulon, Vol., 638-641.

Kelly R.B., Houlsby G.T. & Byrne B.W. (2006) *A comparison of field and laboratory tests of caisson foundations in sand and clay*. Géotechnique **56** No. 9 617-626

Lade P.V. & Kim M.K. (1988) *Single hardening constitutive model for frictional materials –II Yield criterion and plastic work contours*. Computers and Geotechnics, Vol. 6, 1998, pp. 13-29

Larsen K.A. & Ibsen L.B. (2005) *Combined Loading Test of Large Scale 2-meter Full Bucket in Sand - H=11.6m Test No.2* Report 0505 ISSN 1398-6465 R0505 Aalborg University.

Larsen, K.A. & Ibsen L.B. (2006a) *Data Report 0202: Static experiments on bucket foundations placed in Aalborg University Sand No. 0 Version 2* Aalborg University, May 2006, ISSN 1398-6465-R0202

Larsen, K.A. & Ibsen L.B. (2006b) *Data Report 0203: Bucket foundations on Aalborg University Sand No.0 Version 2* Aalborg University, May 2006, ISSN 1398-6465-R0203

Larsen, K.A. & Pedersen L. (2001) *Tredimensionel analyse af krydsanisotropisk sand i drænet og udrænet tilstand*. M.sc. Thesis Aalborg University, June 2001. In Danish.

Liingaard M. (2006) *Dynamic Behaviour of Suction Caissons*. Ph.D. Thesis Aalborg University Denmark.

Loung M.P. (1982) *Stress-strain aspects and cohesionless soils under cyclic and transient loading*. International Symposium on Soils under Cyclic and Transient Loading, 1982, s. 315-324

Lundgren H. & Mortensen K. (1953) *Determination by the Theory of Plasticity of the Bearing Capacity of Continuous Footings on Sand*. Proc. Third Int. Conf. Soil Mech., Vol I, Zürich

Martin C.M. (1994) *Physical and numerical modeling of offshore foundations under combined loads*. DPhil Thesis, University of Oxford.

Martin, C.M. (2004) *User guide for ABC-Analysis of Bearing Capacity Version 1.0* Department of Engineering Science University of Oxford Revised version October 2004 OUEL Report No.2261/03

Martin C.M. (2005a) *Exact bearing capacity calculations using the method of characteristics*. Issues lecture, 11th Int. Conf. of IACMAG, Turin

Martin C.M. (2005b) Exact bearing capacity factors for strip footings –notes downloaded from <http://www-civil.eng.ox.ac.uk/people/cmm/>

Meyerhof G. (1951) *The ultimate bearing capacity of foundations*. Géotechnique Vol.II, Dec 1951

Ngo-Tran C.L. (1996) *The analysis of offshore foundations subjected to combined loading*. DPhil thesis Oxford University.

Poulos H.G. & Davies E.H. (1974) *Elastic solution for soil and rock mechanics*, John Wiley & Son, New York

Plaxis (2003) *Plaxis Bulletin No. 13*. Bulletin of the Plaxis Users Association (NL)

Prandtl L. (1920) *Über die Härte plastischer Körper*, Nachr. D. Ges.D.Wiss, Göttingen 1920.

Rasmussen M. S. (1996) *Behaviour of structures subjected to cyclic loadings*. Ph.D. Thesis Aalborg University

Roscoe K.H. & Schofield A. N. (1956) *The stability of short pier foundations in sand*. Br. Weld. J., August 343-354.

Schmertmann, J.H. (1978) *Guidelines for cone penetration test, performance and design*. US Federal Highway Administration, Washington DC, Report, FHWA-TS-78-209, 145.

Seed H.B. & Lee K.L. (1967) *Undrained strength characteristics of cohesionless soil*. Journal of Soil Mechanics and Foundations Division, ASCE 93(6), 333-360.

Spence D.A. (1968) *Self similar solutions to adhesive contact problems with incremental loading*, Proc. Roy. Soc. A **305** 55-80

Stakemann, O. (1976) *Brudbetingelse for G12 sand og plane modelforsøg* (Failure condition for G12-sand and plane strain model tests; in Danish) Internal Memo Danish Geotechnical Institute.

Steenfelt J.S. (1992) *Strength-strain properties of crushed stone*. DGI/POS Report 158. Danish Geotechnical Institute.

Tan F.S.C. (1990) *Centrifuge and theoretical modelling of conical footings on sand*. PD thesis University of Cambridge.

Tani K. & Craig W.H. (1995) *Bearing capacity of circular foundations on soft clay of strength increasing with depth*. Soil and Foundations Vol. 35, No. 4, 21-35.

Terzaghi K. (1943) *Theoretical soil mechanics* John Wiley and sons, inc., New York

Villabolos F.A., Houlsby, G.T. & Byrne B.W. (2004) *Suction caisson foundations for offshore wind turbines*. Proc. 5th. Chilean Conference of Geotechnics, Santiago.

Villabolos F.A, Byrne B.W. & Houlsby, G.T. (2005) *Moment loading of caissons installed in saturated sand*. ISFOG Perth WA.

Yun G.J. & Bransby M.F. (2003) *Centrifuge modelling of the horizontal capacity of skirted foundations on drained loose sand*. BGA International Conference on Foundations, Thomas Telford, London.

Zaharescu E. (1961) *Sur la stabilité des fondations rigides*. Proc 5th Int. Conf. Soil Mech. Fndn Engng, Paris, Vol.1, pp. 867-871.

GEOTECHNICAL ENGINEERING
DEPARTMENT OF CIVIL ENGINEERING
AALBORG UNIVERSITY

Appendix A.

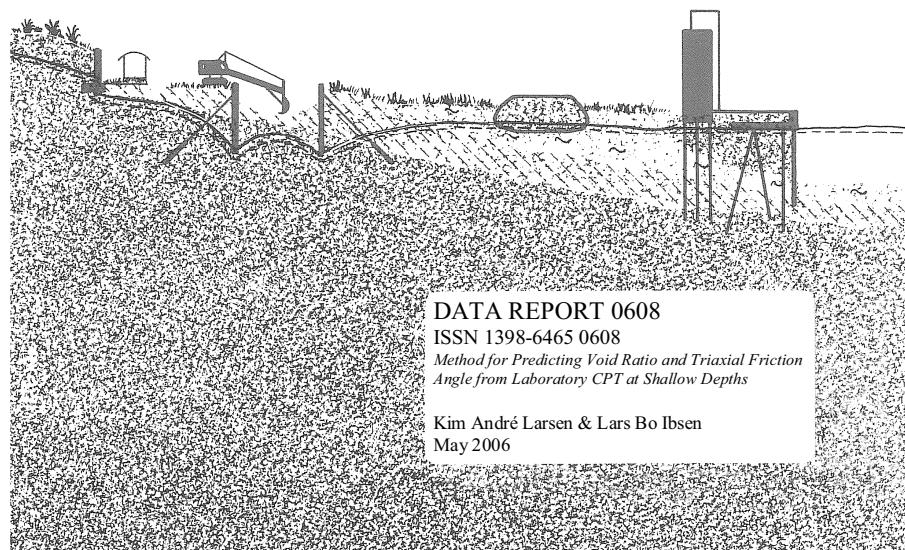


Table of content

1	Introduction	3
2	Laboratory Cone Penetration Testing Probe.....	4
2.1	Construction of the Laboratory Cone Penetration Probe.....	4
2.2	Tests with the laboratory CPT-probe	5
3	Aalborg University Sand No. 0	9
3.1	Description of Aalborg University Sand No.0.....	9
3.2	Behaviour of Aalborg University Sand No.0.....	10
4	Interpretation of CPT	14
4.1	Presentation of selected method from the literature.....	14
4.1.1	Janbu and Senneset (1975).....	15
4.1.2	Lunne and Christoffersen (1983).....	15
4.1.3	Bolton and Lau (1993).....	16
4.2	Comparison of methods from literature with test results.....	17
4.3	Calibration of CPT-test for shallow depths	18
5	Conclusion	22
6	References	23
7	Appendix I: Results from tests.	25
8	Appendix II: Evaluation of tests.	37

1 Introduction

In this report an investigation of the relationship between the tip resistance, q_c of a laboratory CPT-probe versus the relative density, D_r and friction angle, ϕ of Aalborg University Sand No. 0 is carried out. A method for estimating the relative density and the triaxial friction angle from the cone resistance of the laboratory probe is proposed.

The suggested method deals with the fact that the friction angle is depended of the stress level especially at low stresses. The method includes a calibration of the cone resistance from the laboratory CPT at shallow depths i.e. low values of d/D against the properties of Aalborg University sand No. 0.

2 Laboratory Cone Penetration Testing Probe

In connection with a Ph.D-study on CPT-testing, a small scale CPT-probe was manufactured at the geotechnical laboratory at Aalborg University, Luke (1994). The probe was manufactured with a length of the shaft at 400mm, but due to the need for investigations in greater depths the probe is modified regarding the shaft length. A presentation of the new probe is given below.

2.1 Construction of the Laboratory Cone Penetration Probe

The laboratory CPT-probe is only capable of determining the tip resistance in contrary to the probes used in the field. These probes are also capable of determining the pore pressure and the sleeve friction during penetration. An illustration of the modified laboratory CPT- probe is shown in Figure 2.1

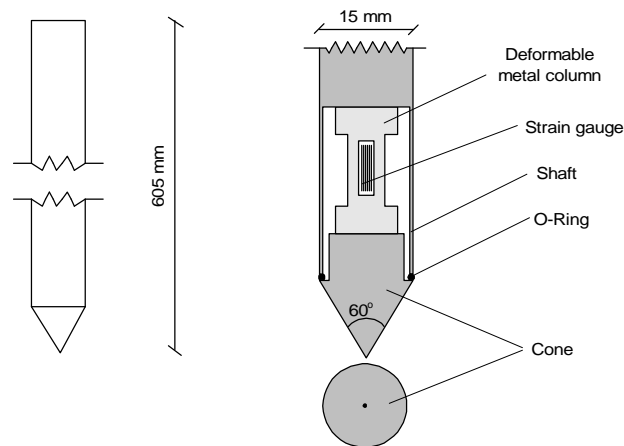


Figure 2.1 Illustration of the modified laboratory cone penetration probe.

The new laboratory CPT-probe has the following geometrical measures:

- Penetration length: 605 mm
- Cone diameter: 15 mm
- Cone area: 176,7 mm²
- Cone angle: 60°

Appendix A

The diameter of the laboratory CPT-probe was originally predetermined to 15mm to avoid influence from the calibration chamber used, Luke (1994).

A deformable metal column and four strain gauges constitute the load cell in the probe as shown on Figure 2.1. The four strain gauges work as two active and two passive gauges. The two active gauges are attached to the deformable metal column vertically and the two passive is attached horizontally. The strain gauges are coupled in a full-bridge connection as shown in Figure 2.2.

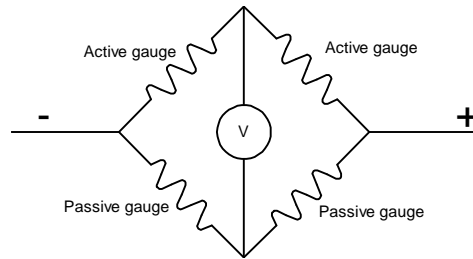


Figure 2.2 Full-bridge connection for the load cell in the CPT-probe.

During the penetration tests the cone resistance, q_c and the penetration depth, d are measured using a computer. The displacement transducer and the strain gauges are connected to the computer through a “spider 8” sampling device.

The constructed load cell is calibrated by use of a calibration bench where the tip is loaded with a known external force in the direction of the probe. The laboratory CPT-probe is found to have a maximum loading capacity of 1200N.

2.2 Tests with the laboratory CPT-probe

Several penetration tests are performed using a cylindrical test box (calibration chamber) and a larger test box, developed for small scale testing of foundations. The construction of the large test box and the procedure for preparation of the sand in this test box is described in Larsen & Ibsen (2006). The large test box is shown in Figure 2.3. All tests in connection with this report are carried out in water saturated sand.

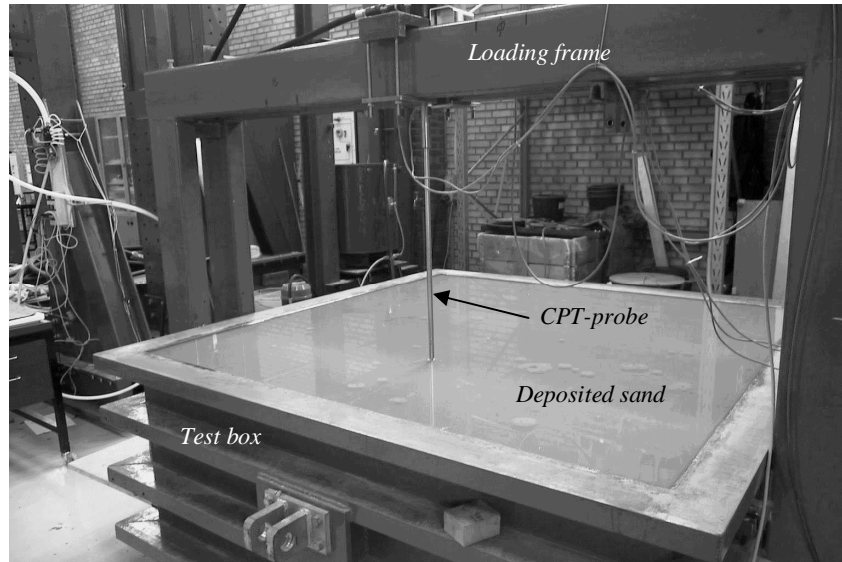


Figure 2.3 The large test box used for the tests with the laboratory CPT-probe. The probe is seen in the middle of the picture ready for penetration.

The calibration chamber is constructed in a way similar to the test box. The inner diameter of the calibration chamber is 525mm and the inner depth is 600mm. The calibration chamber is illustrated in Figure 2.4.

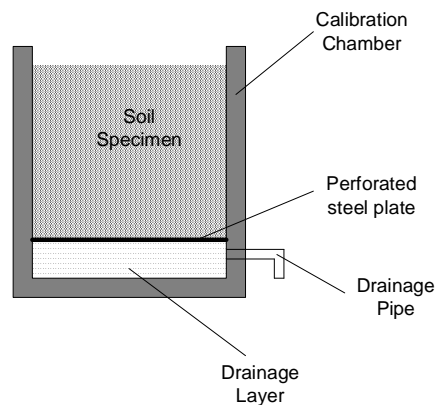


Figure 2.4 Illustration of calibration chamber.

The calibration container consists of a thick steel cylinder with a corresponding steel plate welded at the lower end as bottom. A drainage layer consisting of small stones is used for distributing the water before entering the soil sample above. Between the drainage layer and the soil sample a perforated steel plate is placed to prevent the sand from entering the drainage layer. The water is led in and out of the calibration chamber through a drainage pipe in the side of the chamber, through the drainage layer.

Appendix A

In order to vary the void ratios of the soil samples, different compactness methods are used throughout the study. The location of samples extracted and CPT's performed etc. is defined according to Figure 2.5.

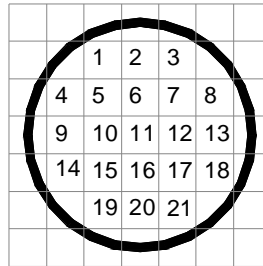


Figure 2.5 Discretization of the soil surface in the calibration container.

The following preparation procedures are used to compact the soil sample during the test program:

- Water pluviation. The sand is deposited with a very large void ratio by dropping the sand through water. This method gives a small relative density.
- Compactness using a rod vibrator. The sand is compacted by vibrating saturated sand with a rod vibrator. The method is described in Larsen & Ibsen (2006) for the large test box. This method gives a large relative density.
- Compactness of the sand by vibrating the container externally with a hydraulic hammer located on the side of the calibration chamber. This method gives intermediate values of the relative density.

The cone penetration tests in the laboratory are performed with a penetration rate of 5 mm/s, with the use of a hydraulic cylinder, see Figure 2.6. The standard CPT's in the field are normally carried out with a penetration rate of 20 mm/s.



Figure 2.6 Left: Hydraulic cylinder used to penetrate the probe with a constant penetration rate. Right: Laboratory CPT-probe ready for penetration

After each test with the laboratory CPT-probe the void ratio is measured by extracting samples with known volume in different depths. The void ratio is measured from each sample by weighing and drying the soil.

The results from the test series are presented in the data sheets in appendix I. The preparation procedure and the location of CPT and samples for each set of experiment are given in the data sheets. In total 12 set of experiments is executed in sand samples prepared with the above mentioned methods and a combination of these.

3 Aalborg University Sand No. 0

The sand used in the experiments is Aalborg University Sand No. 0 (Baskarp Sand No. 15). Results from several triaxial tests are summarized in the following to determine the behaviour of the sand. A description of the sand is given below.

3.1 Description of Aalborg University Sand No.0

Aalborg University Sand No. 0 is a graded sand from Sweden. The shape of the largest grains is round while the small grains have sharp edges. The main part of Aalborg University Sand No. 0 is quartz, but it also contains feldspar and biotite.

The properties of Aalborg Universitet Sand No.0 are well-known because of available results from triaxial, cubical and other tests. All tests are performed in the laboratory at Aalborg University. Information's from triaxial tests are used to correlate the response of the tests with the laboratory CPT-probe to the relative density and strength of the sand.

For classification of the sand the performed tests are:

- Sieve test
- Grain density, d_s
- Maximum, e_{\max} and minimum, e_{\min} void ratio

From the sieve test the following parameters have been determined:

- $d_{50} = 0.14 \text{ mm}$
- $d_{60}/d_{10} = U = 1.78$

The distribution of the grains is illustrated in Figure 3.1.

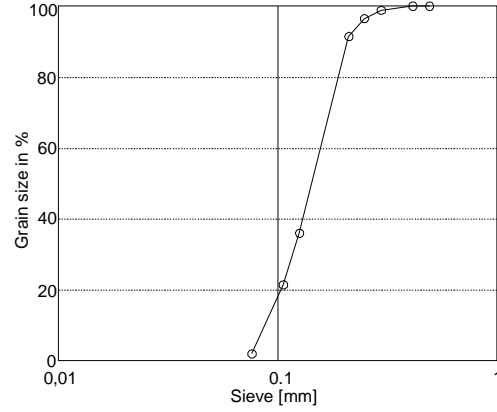


Figure 3.1 Distribution of grains for Aalborg University Sand No. 0.

The grain density, maximum and minimum void ratios have been determined to:

- $d_s = 2.64$
- $e_{\max} = 0.858$
- $e_{\min} = 0.549$

All the tests have been performed according to the standard procedures used in the laboratory, DGF-Bulletin (2001).

3.2 Behaviour of Aalborg University Sand No.0.

Since the void ratio is known with depth for each CPT the correlation between the void ratio and the friction angle can be investigated. The friction angle is throughout the report determined as the effective secant friction angle, j'_s from a triaxial test by the following equation:

$$\sin(j'_s) = \frac{s'_1 - s'_3}{s'_1 + s'_3} \quad (3.1)$$

where s'_1 and s'_3 is the major and minor effective principal stress at failure.

The following results are derived from previous performed triaxial tests on Aalborg University Sand No. 0 with different void ratios and different confining pressures, Ibsen & Bødker (1994), Borup & Hedegaard (1995), Ibsen et al. (1995) and Andersen et al. (1998).

The influence from the minor effective principal stress, σ'_3 on the strength of the sand is investigated using the results from the above mentioned triaxial experiments. A description of this influence has been proposed by Jacobsen (1970) by the following equation.

Appendix A

$$q' = s'_1 - s'_3 = \frac{\sin(j'_{t,a})}{1 - \sin(j'_{t,a})} s'_3 \left(1 + \frac{c'_{t,a} \cdot \cot(j'_{t,a})}{m \cdot s'_3} \right)^m \quad (3.2)$$

where q' is the deviatoric stress and c' is the effective cohesion. The index t and a denotes that the parameter is the tangent parameter at high stresses (asymptote) and m is a parameter that describes the curvature of the failure envelope at low stress levels.

The enveloping surface given by equation (3.2) is fitted to the result from the triaxial tests. For void ratios of 0.61, 0.7 and 0.85 the calibration are performed by Didriksen and Kristensen, (2000). The fitted parameters are listed in Table 3.1.

Table 3.1 Fitted strength parameters for Aalborg University Sand No.0.

Void ratio, e	$j'_{t,a}$ [°]	$c'_{t,a}$ [kPa]	m
0,55	41,00	19,90	0,350
0,61	38,60	34,57	0,197
0,70	34,21	40,42	0,187
0,85	30,93	7,00	0,451

The failure envelopes according the fitted strength parameters in Table 3.1 can be seen in Figure 3.2 where the stress situations at failure for the performed triaxial tests are plotted as well.

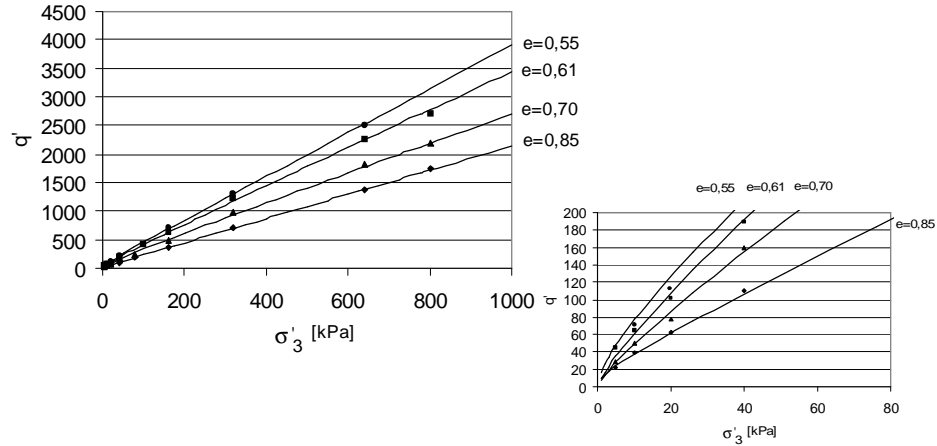


Figure 3.2 Failure envelopes from triaxial tests on Aalborg University Sand No.0. The line represents the fitted envelopes and the markers represent failure values from performed triaxial tests.

The variation of the triaxial secant friction angle with respect to the minor principal stress, s'_3 can be calculated when equation (3.1) is transcribed into a function of s'_3 and the deviatoric stress, q' according to equation (3.2):

$$\sin(j'_s) = \frac{q'}{2 \cdot s'_3 + q'}$$

or

$$\sin(j'_s) = \frac{\frac{\sin(j'_{t,a})}{1 - \sin(j'_{t,a})} s'_3 \left(1 + \frac{c'_{t,a} \cdot \cot(j'_{t,a})}{m \cdot s'_3} \right)^m}{2 \cdot s'_3 + \frac{\sin(j'_{t,a})}{1 - \sin(j'_{t,a})} s'_3 \left(1 + \frac{c'_{t,a} \cdot \cot(j'_{t,a})}{m \cdot s'_3} \right)^m} \quad (3.3)$$

The fitted variation of the triaxial secant friction angle for different void ratios after equation (3.3) are shown in *Figure 3.3*

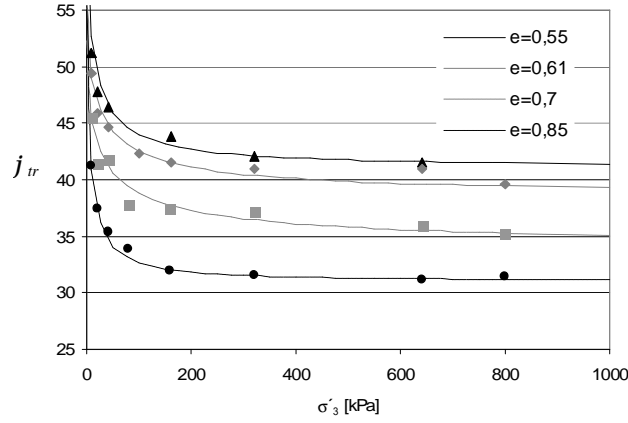


Figure 3.3 Variation of the triaxial secant friction angle with the minimal stress at failure after equation (3.3). The results from the triaxial tests are shown as marks.

The triaxial secant friction angle is from *Figure 3.3* seen to depend on both the stress level as well as the void ratio. The relation between the void ratio and the friction angle can be described using Kerisel's formula.

$$e \cdot \tan(j) = C \quad (3.4)$$

where C is a constant which for sand usually is between 0.4 and 0.5. In *Figure 3.4* the constant in Kerisel's formula is fitted to the triaxial results at different stress levels i.e. the confining pressure. The constants are fitted according to the failure envelopes from equation (3.2). Selected failure values from these envelopes are shown in the figure as well.

Appendix A

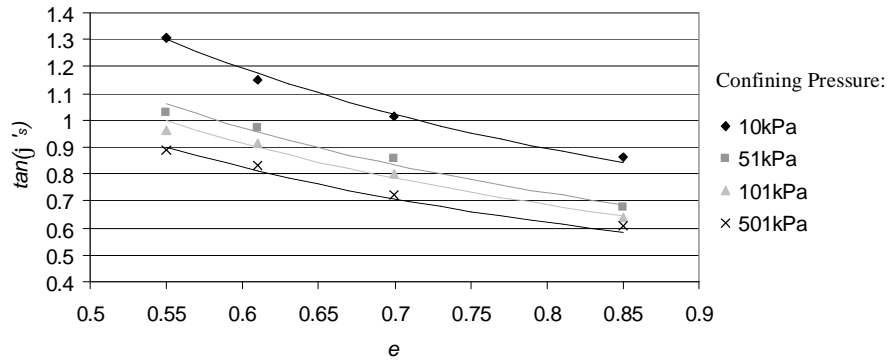


Figure 3.4 Relationship between the void ratio and $\tan(\phi_s)$ from equation (3.2) (grey scale marks) at different confining pressures. The relationship suggested by Kerisel is shown for the respective stress levels by lines.

From Figure 3.4 it can be seen that the relationship proposed by Kerisel fits the results from the triaxial tests very well. Though it is found that the constant in equation (3.4) varies with the stress level. The value of the constant C as a function of the minor principal stress is shown in Figure 3.5.

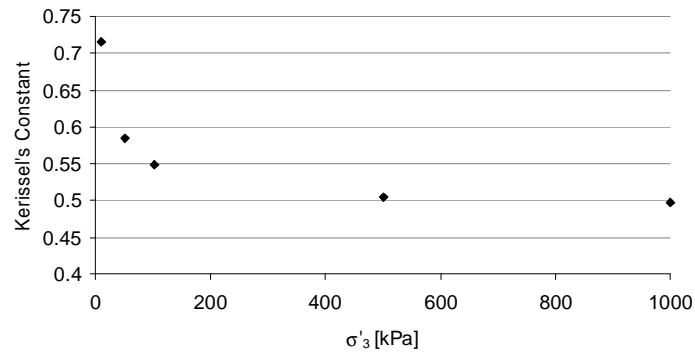


Figure 3.5 Variation of Kerisel's constant with respect to the minor principal stress.

The constant in Kerisel's formula is seen to decrease with increasing stress level, until reaching a constant value of $C = 0.496$ at large stresses.

4 Interpretation of CPT

The resistance against penetration of the CPT-probe into the sand depends on several factors. Some of these factors are the geometry and material of the probe. The geometrical factors are the angle of the wedge on the cone, the diameter of the probe and the material property are reflected by the roughness of the cone. Furthermore the conditions of the soil are reflected in the penetration resistance. This is the density, the friction angle, the compressibility and the stress conditions in the soil. Besides this the degree of saturation, the size of the grain particles as well as the relative penetration depth and penetration rate is of importance.

4.1 Presentation of selected method from the literature

Different methods of predicting the strength parameters of soils from cone penetration tests are proposed in the literature. Some of these suggestions are presented in the following, and will be investigated for their usefulness in the prediction of the friction angle from the laboratory CPT's.

Methods used to calculate the cone resistance of the cone probe, $q_c = Q/A$ presented in this report are all based on the classical bearing capacity formula by, Terzaghi (1943):

$$\frac{Q}{A} = \frac{1}{2} g' B N_g + q' N_q + c' N_c \quad (4.1)$$

where g' is the effective unit weight of the soil, B is the width of the foundation, q is the overburden pressure and N_g , N_q and N_c are bearing capacity factors. The bearing formulation in equation (4.1) assumes that the bearing capacity can be divided into three terms. The first term is the bearing capacity of a surface foundations resting on a cohesion-less soil. The second term is the bearing capacity from the overburden pressure and the last term is the bearing capacity from the cohesion in the soil. Equation (4.1) can for a friction or cohesion-less material be reduced to:

$$\frac{Q}{A} = \frac{1}{2} g' B N_g + q' N_q \quad (4.2)$$

The last term (q -term) in equation (4.2) can be shown to dominate as the CPT is penetrated into the soil. Thus γ -term is often ignored, and the relation between the tip resistance of the CPT and the bearing capacity factor N_q is merely expressed by:

$$N_q = \frac{q_c}{s_v} \quad (4.3)$$

Appendix A

where N_q , for a pure friction material, is given by the cone resistance divided by the effective stresses at rest in the depth equal to the position of the cone.

Selected correlations between the bearing capacity factor N_q and the friction angle relevant for CPT's from the literature are presented in the following sections.

4.1.1 Janbu and Senneset (1975)

Janbu and Senneset (1975) suggested an expression for the bearing capacity factor N_q , determined from the stress field illustrated in Figure 4.1. The expression are evaluated assuming plain strain conditions. Thus the plane friction angle must be used along with an appropriate shape-factor on N_q .

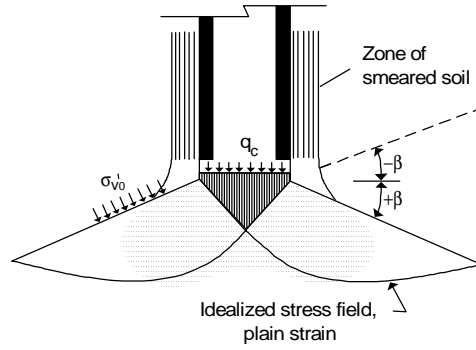


Figure 4.1 Idealized stress field used to determine N_q after Janbu & Senneset (1975)

The evaluated expression of N_q from the stress field in Figure 4.1 is given as follows:

$$N_q = \tan^2 \left(\frac{p}{4} + \frac{1}{2}j \right) \cdot e^{(p-2 \cdot b) \tan(j)} \quad (4.4)$$

Where b is the angle of plastification in the idealized stress field geometry shown in Figure 4.1. The value of b for sand is usually between 15° and -15° . The value of b is observed to change with the angle of internal friction, which must be taken into account.

4.1.2 Lunne and Christoffersen (1983)

Lunne and Christoffersen (1983) suggested a modified version of the expression by Janbu and Senneset (1975) presented above, and is given as follows.

$$N_q = \tan^2 \left(\frac{p}{4} + \frac{1}{2}j \right) \cdot e^{(p/3+4j) \tan(j)} \quad (4.5)$$

Equation (4.5) is modified in order to describe the variation of b with the change of j .

4.1.3 Bolton and Lau (1993)

A set of bearing capacity factors for strip and circular footings is evaluated by Bolton and Lau (1993). The values derived for circular footings with smooth base are given in Table 4.1. These values are determined from an axis-symmetric stress situation, thus the factors include shape factors and is a function of the triaxial friction angle. The width of the foundation in equation (4.1) and (4.2) is equal to the diameter of the cpt-probe if these values are used.

Table 4.1 Bearing capacity factors for circular smooth footings, after Bolton and Lau (1993).

j [°]	N_q	N_g
	Smooth or rough base	Smooth base
5	1.65	0.06
10	2.80	0.21
15	4.70	0.60
20	8.30	1.30
25	15.2	3.00
30	29.5	7.10
31	34	8.60
32	39	10.3
33	45	12.4
34	52.2	15.2
35	61	18.2
36	71	22
37	83	27
38	99	33
39	116	40
40	140	51
41	166	62
42	200	78
43	241	99
44	295	125
45	359	160
46	444	210
47	550	272
48	686	353
49	864	476
50	1103	621
51	1427	876
52	1854	1207

The values in Table 4.1 are evaluated assuming a flat base of the foundation, i.e. a wedge angle = 180 degrees.

4.2 Comparison of methods from literature with test results.

The values of the bearing capacity N_q presented in section 4.1 are compared in Figure 4.2.

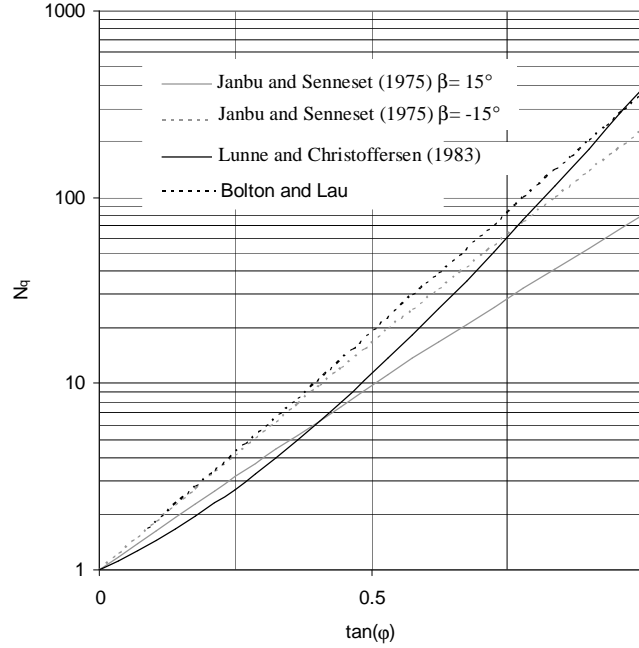


Figure 4.2 Comparison of the bearing capacity factors, N_q .

The values of N_q in Figure 4.2 are evaluated assuming associated flow. Sand is known to exhibit a behaviour that is non-associated. Thus a reduced friction angle, j_d should be used to estimate the value of N_q . A relation that accounts for this is given by the following relation, Jakobsen (1989).

$$\tan(j'_d) = \frac{\sin j'_r \cos y}{1 - \sin j'_r \sin y} \quad (4.6)$$

where y is the dilation angle of the sand.

The friction angle is in chapter 3 shown to vary extensively with the stress levels at a low stress level. The friction angle that corresponds to the measured cone resistance is unknown during penetration of the CPT-probe due to the variation with stresses. The friction angle at large stress levels is however unique for a given compactness of the soil sample. In appendix II this friction angle is used to compare the measured cone resistance with the proposed values of N_q in Figure 4.2. The friction angle used is the reduced friction angle according to equation (4.6) assuming $y = j'_r - 30^\circ$.

The results clearly shows that this friction angle gives a penetration resistance that is too low compared with the measured resistance. The variation of N_q proposed by Bolton & Lau (1993) is in appendix II used to estimate the reduced as well as the triaxial friction angle from the measured cone resistance. This friction angle is seen to be significantly higher then the measured triaxial friction angle determined at large stresses, also presented in appendix II. Thus the stress level in the soil during penetration of the CPT-probe is lower than the stress level that entails a constant value.

The mean stress level in the soil affected by the penetration of the CPT-probe is not known. Hence the estimated friction angle from e.g. Bolton and Lau (1993) is not useful for characterizing the soil tested.

4.3 Calibration of CPT-test for shallow depths

The stress levels present in the laboratory during small scale testing of geotechnical problems are extremely small compared to true scale. Thus the friction angle must be determined at a corresponding stress level. The friction angle determined from the above presented methods corresponds to a stress level that often is different from e.g. a loading test on a surface foundation. Hence this is not useful in evaluating the measured results

Because of this a method for determining the triaxial friction angle at a known stress level for CPT-tests at shallow depths is suggested and calibrated against Aalborg University Sand No.0. As shown in section 3 the influence of stress level on the friction angle is different for different void ratios. At large stresses a unique relation between the void ratio and the friction according to Kerisel's formula was observed. This relation is used to propose a method that is based on equation (4.3) using a bearing capacity factor N_q^* . The bearing capacity factor N_q^* is calibrated against the triaxial friction angle at large stresses according to the following definition:

$$N_q^* = N_q \cdot d_q \quad (4.7)$$

where N_q is the bearing capacity suggested by Bolton & Lau (1993) for a circular and smooth footing and d_q is a depth factor that takes into account the effect of the penetration depth i.e. the stress level on the friction angle. The bearing capacity factor is a function of the triaxial friction angle and is shown in Figure 4.3.

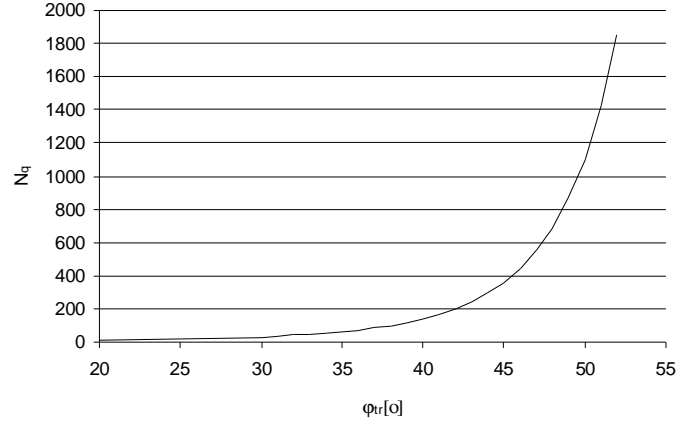


Figure 4.3 Bearing capacity factor for smooth circular footings after Bolton & Lau (1993).

The depth factor is from the tests in Appendix I found to be a function of the friction angle and the penetration depth according to the following relation:

$$d_q = 1 + a(j) \cdot \frac{d}{D} \quad (4.8)$$

The value of α in equation (4.8) has been investigated by back calculation of the cone resistance from the tests with the laboratory CPT-probe. From the measured void ratios the corresponding triaxial friction angles at high stresses are determined from equation (3.4). The variation of α has been found to follow:

$$a = 3 \cdot 10^{-16} \cdot j^{9.4176} \quad (4.9)$$

The variation of α is shown in Figure 4.4. The value of α is seen to increase with increasing friction angle. The back calculated values from the laboratory CPT's are shown in the figure as well. The fitted expression of α is seen from the figure to capture the variation well with exception of a few outliers. The outliers are identified to originate from measurements at low penetration depths.

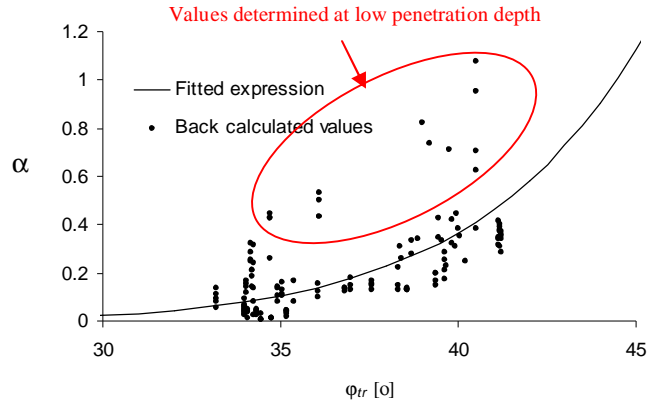


Figure 4.4 Variation of α with the triaxial friction angle at large stress levels.

The proposed method is in appendix II compared with the tests carried out. The method is from comparison with measured results shown capable of predicting the void ratio and friction angle at large stress levels as well as the cone resistance.

From the comparisons carried out in appendix II, it is seen that for penetration depth below 100mm the proposed method generally overestimates the friction angle and there by underestimates the void ratio.

The cone resistance from the laboratory CPT-probe has been calibrated against the triaxial friction angle at large stresses. From this the void ratio and the stress dependency of the friction angle can be determined according to Figure 4.5, cf. section 3.2.

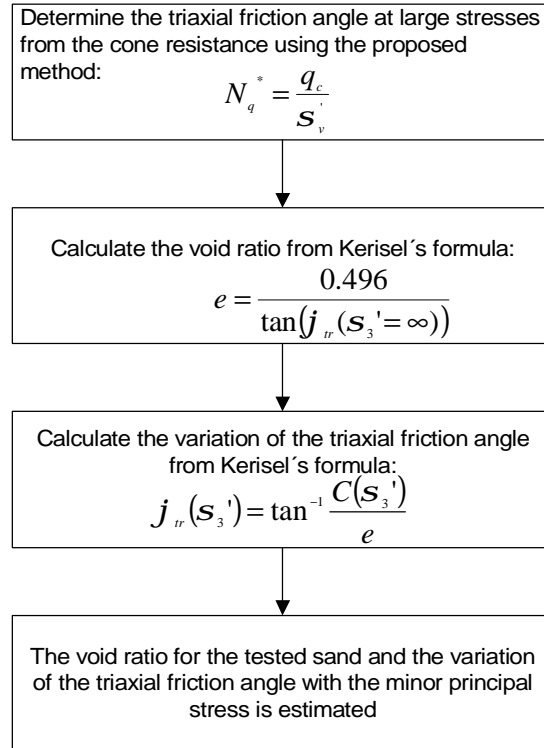


Figure 4.5 Proposed evaluation procedure for determining the void ratio and the triaxial friction angle from a test with the laboratory CPT-probe in Aalborg University Sand No. 0 at shallow depth.

5 Conclusion

A method to estimate the void ratio and the triaxial friction angle from the cone resistance using a laboratory CPT-cone in Aalborg University Sand No. 0 is proposed.

The method is based on Terzaghi's bearing capacity formula using the values of the bearing capacity factors given by Bolton & Lau (1993) for circular and smooth footings including a depth factor. The depth factor is calibrated from the results of 12 test series with the laboratory probe.

The proposed method is based on the triaxial friction angle at large stresses since Kerisel's relationship in this case gives a unique result. From this friction angle the method can be used to estimate the complete variation of the triaxial friction angle with the stress level for the tested sand.

6 References

- Andersen, A.T. ; Madsen, E.B & Schaarup-Jensen, A.L. (1998)
Data Report 9701, Eastern Scheldt Sand, Baskarp Sand No. 15
Geotechnical Engineering Group, Aalborg University
- Bolton & Lau (1993)
Vertical bearing capacity factors for circular and strip footings on Mohr-Coulomb soil
Canadian Geotechnical Journal 30. (1993)
- Borup, M. & Hedegaard, J. (1995)
Data Report 9403, Baskarp Sand No. 15
Geotechnical Engineering Group, Aalborg University
- Det Norske Veritas, (1992) [DNV (1992)]
Foundations, Classification Notes No. 30.4
Det Norske Veritas, Norway.
- Didriksen, L.R. and Kristensen, J. (2000)
Konceptvurdering af bøttefundament til en offshorevindmølle.
M.sc.-thesis. Aalborg University. In Danish.
- Ibsen, L.B. ; Borup, M. & Hedegaard, J. (1995)
Data Report 9501, Triaxial Tests on Baskarp Sand No. 15
AAU Geotechnical Engineering Papers ISSN 1398-6465 R9501
Geotechnical Engineering Group, Aalborg University
- Ibsen, L.B. & Bødker, L. (1994)
Data Report 9301, Baskarp Sand No. 15
Geotechnical Engineering Group, Aalborg University
- Jacobsen M. (1970)
New oedometer and New Triaxial apparatus for firm soil. DGI
Bulletin No. 27 Danish geotechnical society.
- Jacobsen, M. (1989)
Lærebog i videregående geoteknik I "Brud i jord".
Aalborg Universitet In danish

- Larsen, K.A. & Ibsen, L.B. (2006)
Data Report 0201, Bucket foundations on Aalborg University Sand No. 0.
ISSN 1398-6465 R0201. Department of civil engineering, Aalborg University Version 4 May 2006
- Luke, K. (1994)
The use of CPT in Danish soils with special emphasis on measuring the undrained shear strength.
Ph.D. Thesis ATV Project EF 368, Aalborg University
- Lunne and Christoffersen., (1983)
Interpretation of Cone Penetrometer Data for Offshore Sands
Offshore Technology Conference OTC 4464
- Terzaghi K. (1943)
Theoretical soil mechanics John Wiley and sons, inc., New York

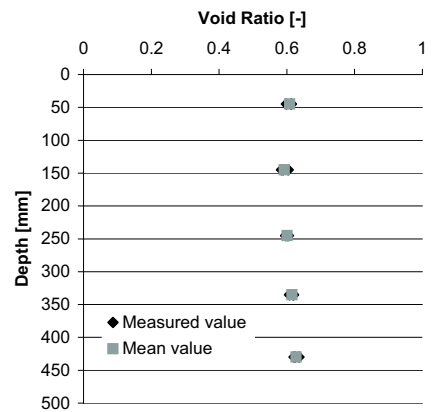
7 Appendix I: Results from tests.

The results from the performed CPT's with Aalborg University Sand No.0 are presented in this appendix.

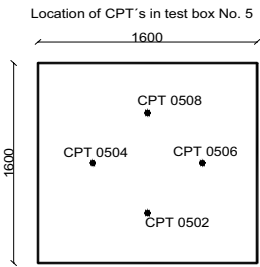
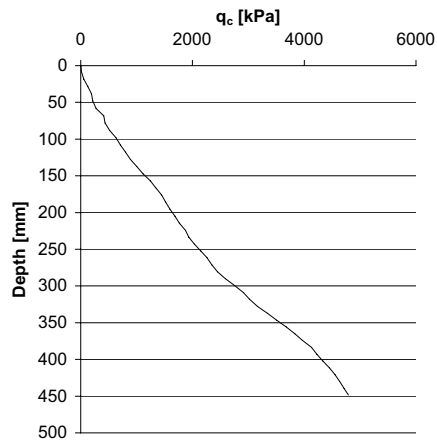
The method of compactness is given in the table at the top of each data sheet.

The measured void ratios in different depths are presented, and the results from the tests with the laboratory CPT-probe, i.e. the cone resistance, q_c is shown.

Description of soil Aalborg University Soil No. 0	Date: 05.12.01	Test box used: Large test box No. 5 Test serie 1
Preperation procedure: Standard preperation procedure using rod vibrator.	Location of samples for void ratio: Samples is taken with in a radius of 200mm around the respective CPT.	

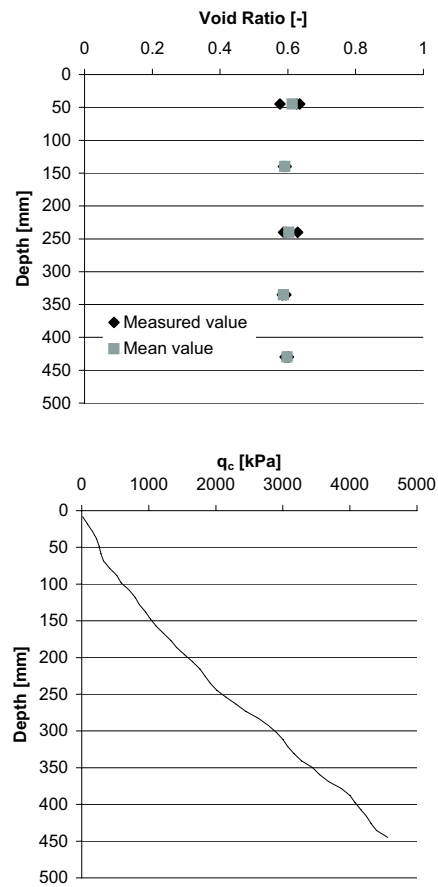


Depth [mm]	Void ratio
45	0.613
	0.613
	0.599
145	0.604
	0.589
	0.584
245	0.605
	0.596
	0.602
335	0.618
	0.62
	0.608
430	0.636
	0.621
	0.625

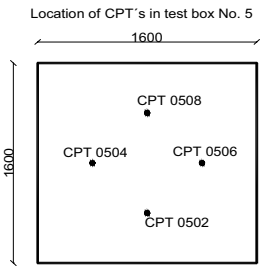


Job: Laboratory CPT-test		Remarks: 4 set of experiments is performed in this test box.
Exc: KAL	Eval: KAL	

Description of soil Aalborg University Soil No. 0	Date: 05.12.01	Test box used: Large test box No. 5 Test serie 2
Preparation procedure: Standard preparation procedure using rod vibrator.	Location of samples for void ratio: Samples is taken with in a radius of 200mm around the respective CPT.	

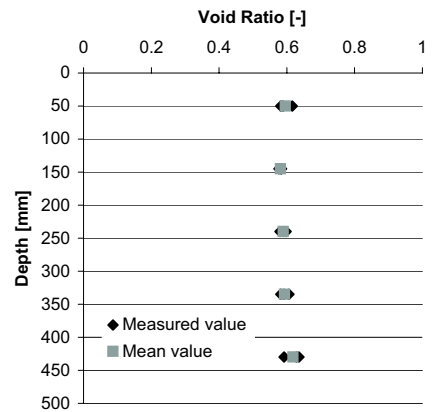


Depth [mm]	Void ratio
45	0.577
	0.635
	0.626
140	0.595
	0.587
240	0.594
	0.587
	0.629
335	0.584
	0.584
	0.594
430	0.602
	0.6
	0.592

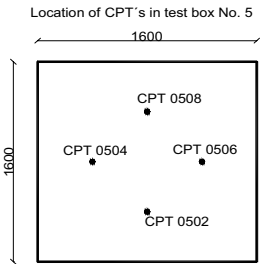
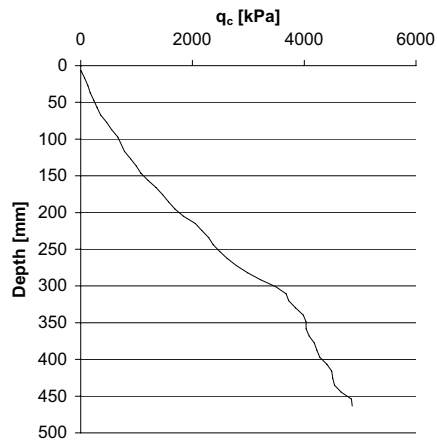


Job: Laboratory CPT-test		Remarks: 4 set of experiments is performed in this test box.
Exc: KAL	Eval: KAL	

Description of soil Aalborg University Soil No. 0	Date: 05.12.01	Test box used: Large test box No. 5 Test serie 3
Preparation procedure: Standard preparation procedure using rod vibrator.	Location of samples for void ratio: Samples is taken with in a radius of 200mm around the respective CPT.	

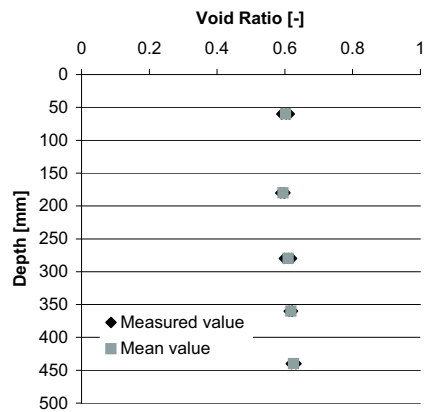


Depth [mm]	Void ratio
50	0.589
145	0.577
240	0.598
335	0.606
430	0.628

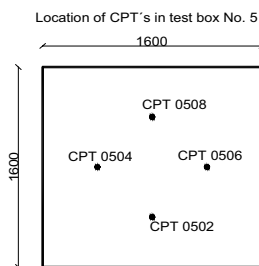
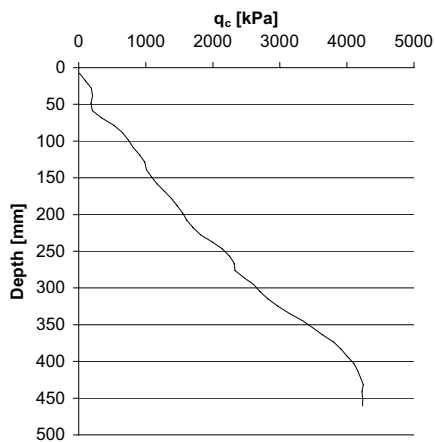


Job: Laboratory CPT-test		Remarks: 4 set of experiments is performed in this test box.
Exc: KAL	Eval: KAL	

Description of soil Aalborg University Soil No. 0	Date: 05.12.01	Test box used: Large test box No. 5 Test serie 4
Preparation procedure: Standard preparation procedure using rod vibrator.	Location of samples for void ratio: Samples is taken with in a radius of 200mm around the respective CPT.	

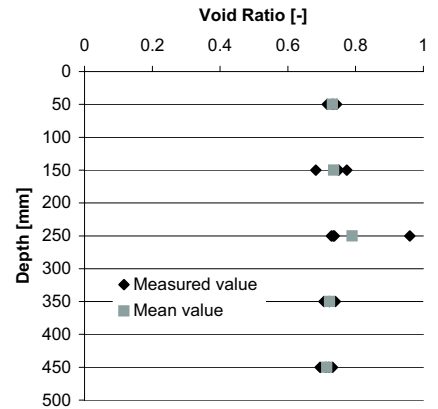


Depth [mm]	Void ratio
60	0.604
	0.613
	0.591
180	0.588
	0.6
	0.597
280	0.599
	0.62
	0.611
360	0.613
	0.622
	0.621
440	0.633
	0.619

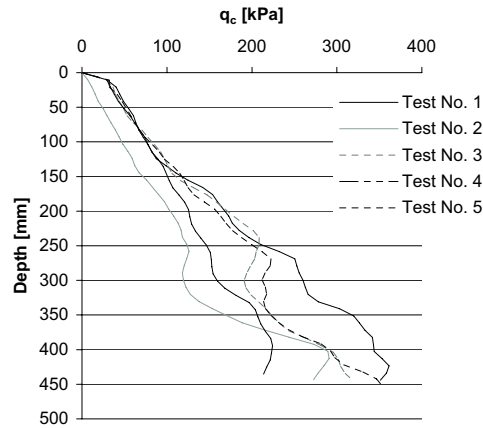


Job: Laboratory CPT-test		Remarks: 4 set of experiments is performed in this test box.
Exc: KAL	Eval: KAL	

Description of soil Aalborg University Soil No. 0	Date: 11.10.01	Test box used: Calibration container No. 2
Preperation procedure: Water pluviation		

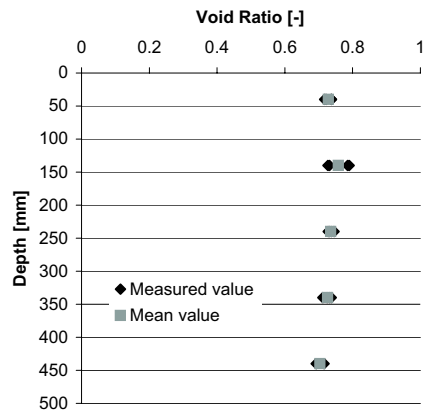


Depth [mm]	Void ratio
50	0.7299 0.7168 0.7355 0.7436
150	0.7496 0.774 0.6827
250	0.96 0.7283 0.7339 0.737
350	0.74 0.707 0.7224 0.7229
450	0.6952 0.7208 0.7124 0.7316

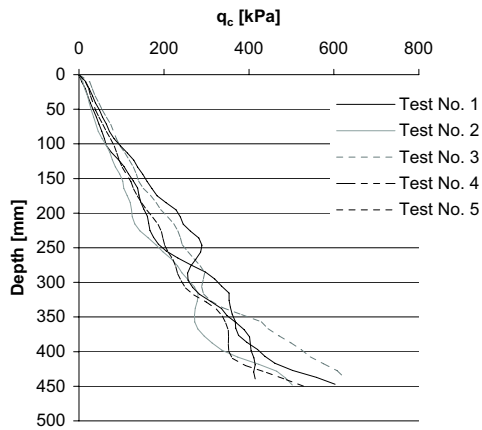


Job: Laboratory CPT-test		Remarks: One of the CPT's show a considerable lower resistance then the rest.
Exc: KAL	Eval: KAL	

Description of soil Aalborg University Soil No. 0	Date: 17.10.01	Test box used: Calibration container No. 3
Preperation procedure: Water pluviation followed by 2x1 sec ext vibration (wood between) 1/3 down at 5 pos.		

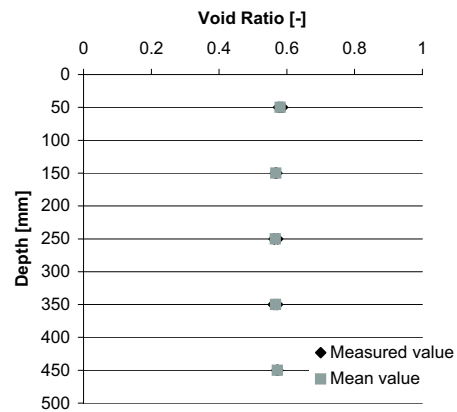


Depth [mm]	Void ratio
40	0.722
	0.717
	0.737
	0.738
140	0.785
	0.727
	0.79
	0.732
240	0.732
	0.737
	0.728
	0.745
340	0.732
	0.737
	0.725
	0.712
440	0.692
	0.716

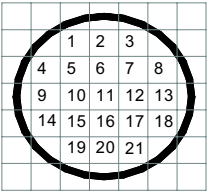
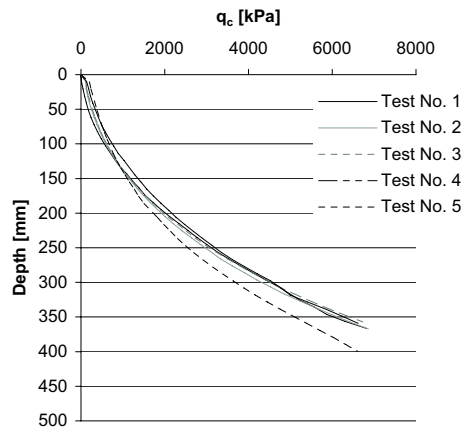


Job: Laboratory CPT-test		Remarks: No clear influence of external vibration.
Exc: KAL	Eval: KAL	

Description of soil Aalborg University Soil No. 0	Date: 22.10.01	Test box used: Calibration container No. 4
Preperation procedure: Water pluviation followed by two times vibration with rod vibrator of all squares.		

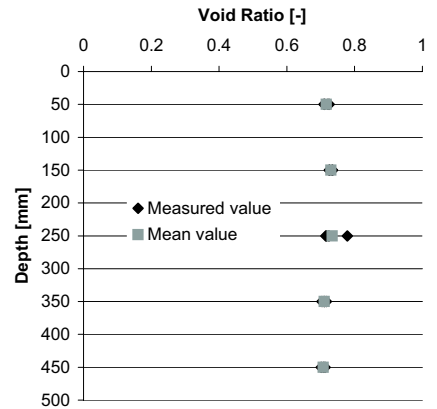


Depth [mm]	Void ratio
50	0.576
	0.582
	0.587
	0.577
150	0.566
	0.567
	0.571
250	0.562
	0.573
	0.564
350	0.571
	0.56
	0.565
	0.572
450	0.572
	0.574
	0.571
	0.572

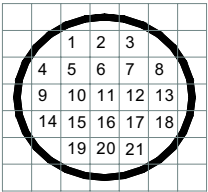
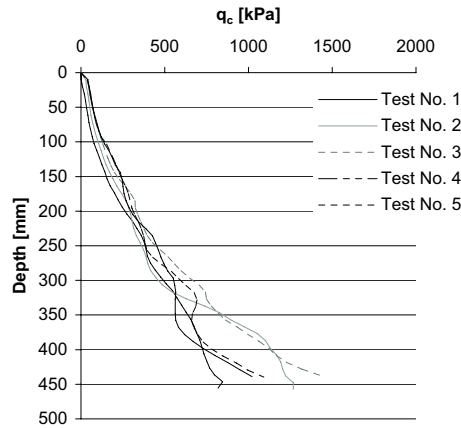


Job: Laboratory CPT-test		Remarks:
Exc: KAL	Eval: KAL	

Description of soil Aalborg University Soil No. 0	Date: 25.10.01	Test box used: Calibration container No. 5
Preparation procedure: Water pluviation followed by 3x3 sec ext. vibration (directly on chamber) 1/3 down at 6 pos.	Location of CPT: 11, 13, 20, 9, 2	Location of sample for void ratio: 5, 7, 15, 17

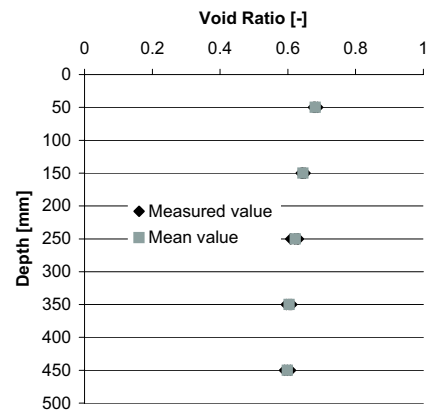


Depth [mm]	Void ratio
50	0.7095
	0.7248
	0.7212
	0.7113
150	0.7255
	0.7338
	0.7258
	0.7348
250	0.7173
	0.7244
	0.7788
	0.7151
350	0.7114
	0.7037
	0.7095
	0.716233
450	0.7124
	0.7082
	0.7017

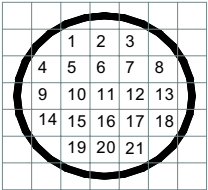
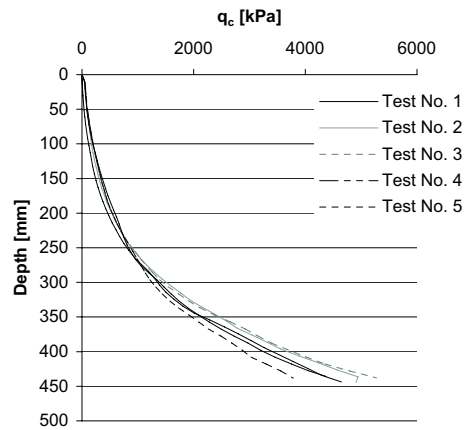


Job: Laboratory CPT-test		Remarks:
Exc: KAL	Eval: KAL	

Description of soil Aalborg University Soil No. 0	Date: 07.11.01	Test box used: Calibration container No. 6
Preparation procedure: Two times vibration in: 5, 7, 15, 17	Location of CPT: 20, 13, 2, 9, 11	Location of sample for void ratio: 6, 10, 12, 16

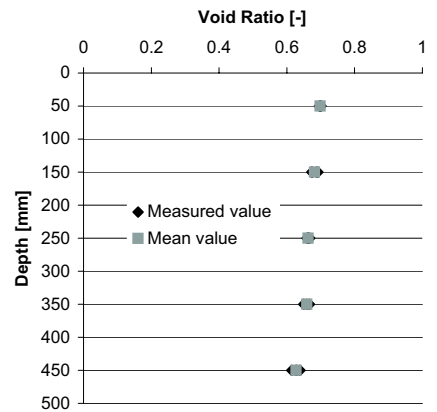


Depth [mm]	Void ratio
50	0.680788 0.678619 0.676053 0.688034
150	0.643287 0.644978 0.650816 0.639566
250	0.627363 0.608602 0.630925 0.620182
350	0.602991 0.611609 0.595261 0.606582
450	0.590269 0.598584 0.607827

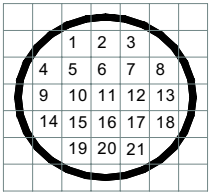
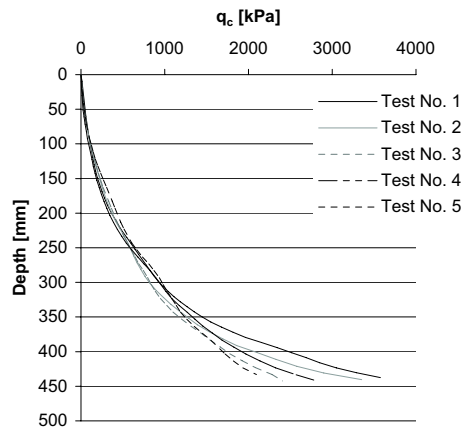


Job: Laboratory CPT-test		Remarks: The void ratio is decreasing with the depth. CPT-test No.5 is close to a vibration hole.
Exc: KAL	Eval: KAL	

Description of soil Aalborg University Soil No. 0	Date: 15.11.01	Test box used: Calibration container No. 7
Preparation procedure: One time vibration in: 5, 7, 15, 17	Location of CPT: 20, 13, 2, 9, 11	Location of sample for void ratio: 6, 10, 12, 16



Depth [mm]	Void ratio
50	0.695793
	0.698946
	0.698495
	0.70098
150	0.674371
	0.686996
	0.674006
	0.691345
250	0.659634
	0.66269
	0.667314
	0.662618
350	0.649965
	0.659239
	0.666988
450	0.629263
	0.638971
	0.614321
	0.626569



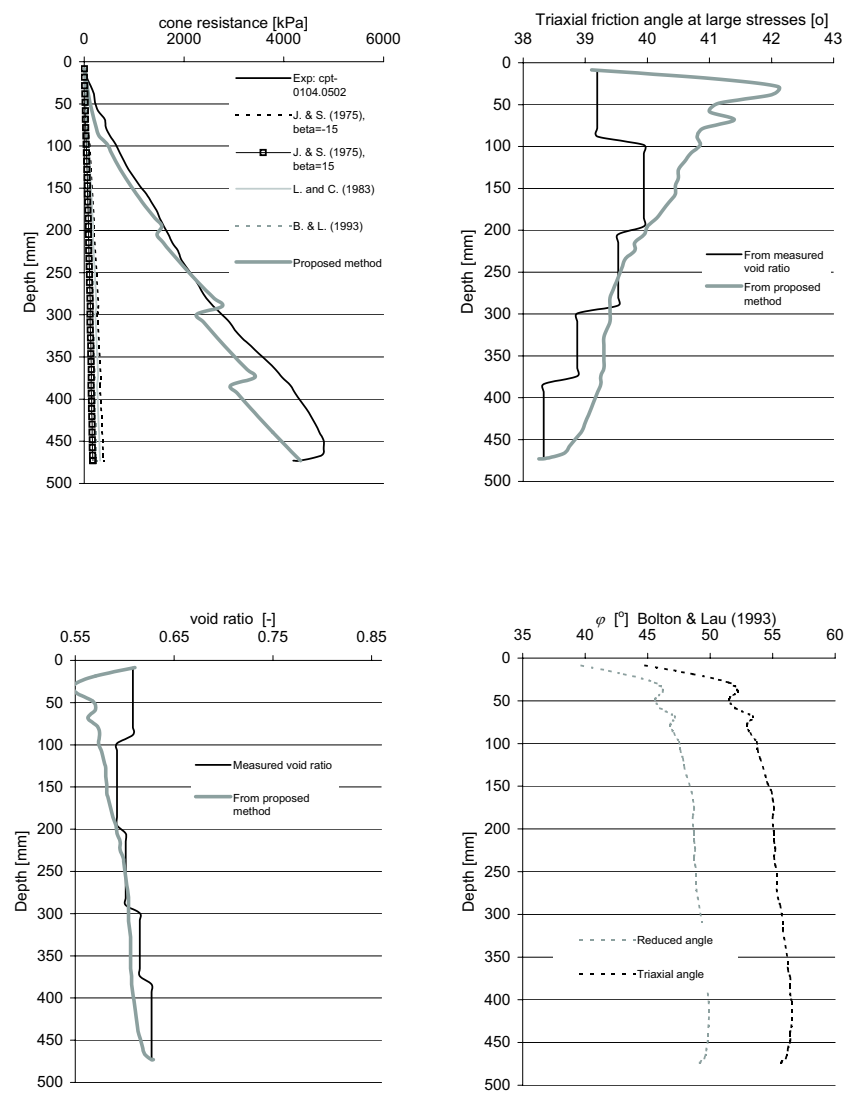
Job: Laboratory CPT-test		Remarks: The void ratio is decreasing with the depth.
Exc: KAL	Eval: KAL	

8 Appendix II: Evaluation of tests.

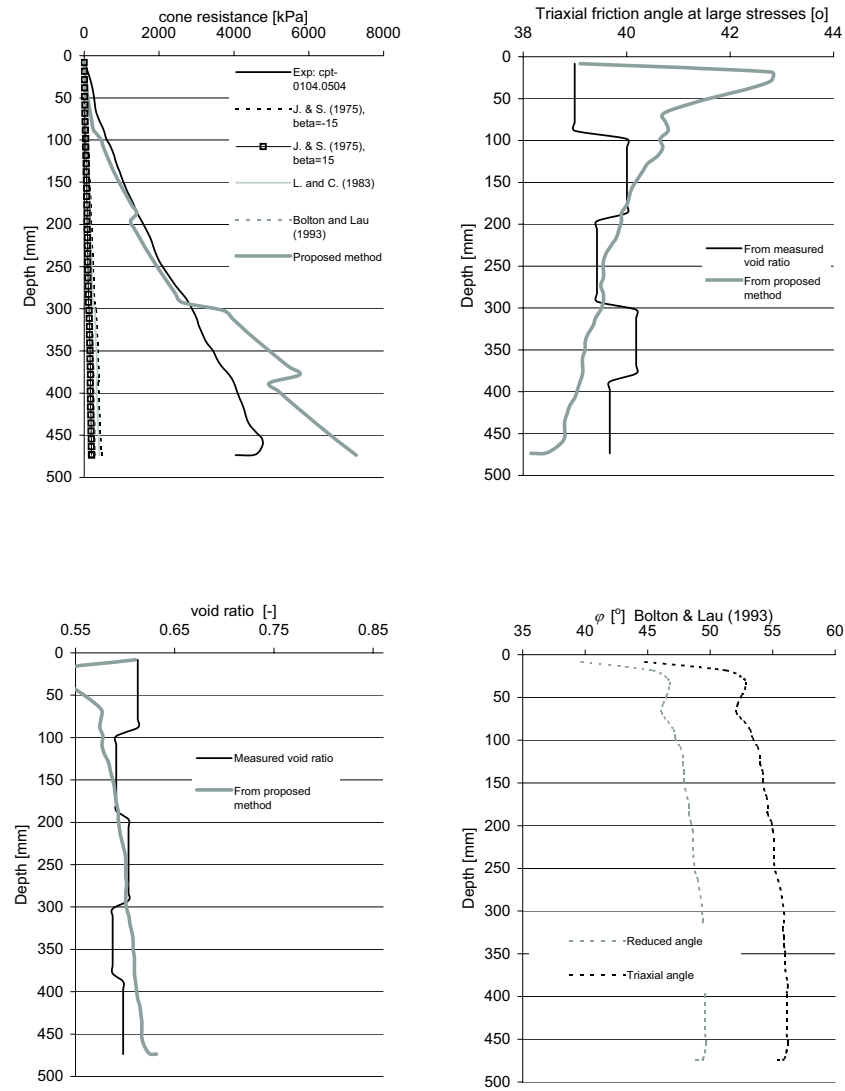
For each of the test series in Appendix I, a comparison is given between the measured results and the corresponding values predicted by the presented methods including the method proposed in this report.

On each data sheet four set of curves is shown.

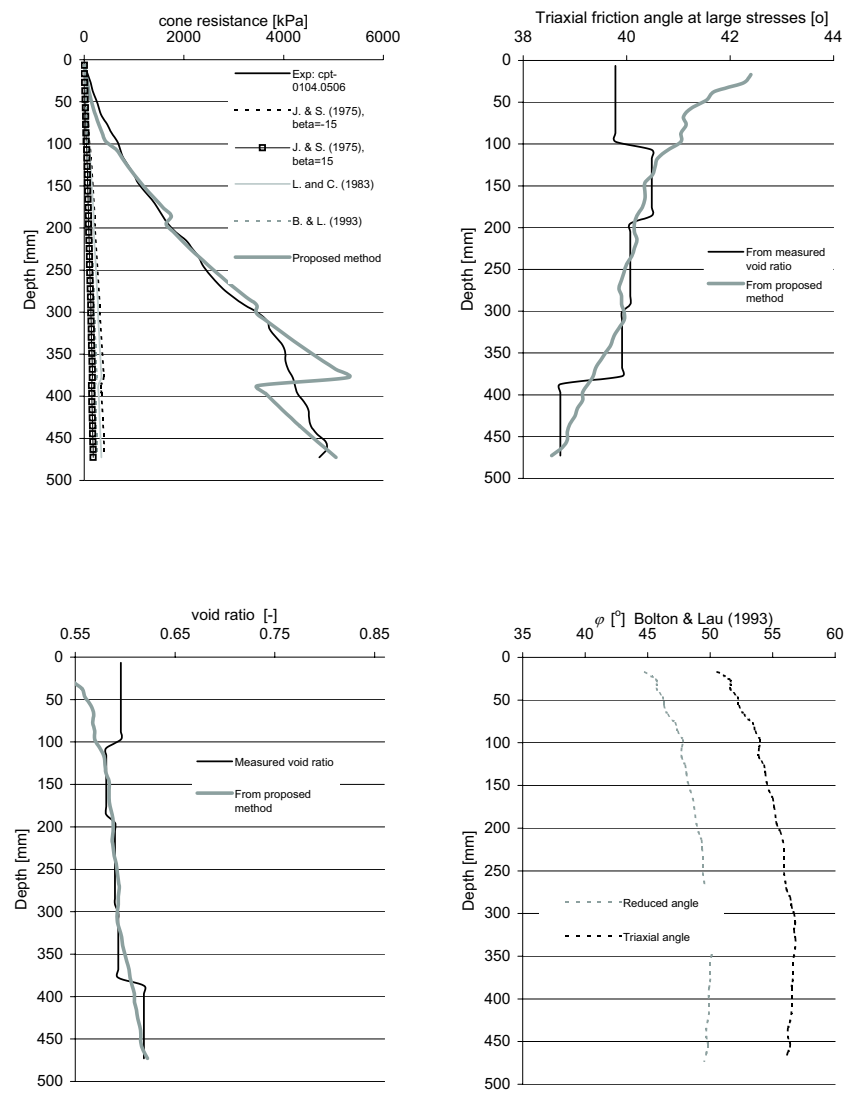
- The predicted values on the curve at the top left side of the data sheets is estimated using the respective methods from the friction angle measured at large stresses in chapter 3.
- On the top right curve the method proposed in this report is used to predict the triaxial friction angle at large stresses from the performed CPT's.
- The lower left figure shows the measured void ratio at a given depth compared with the void ratio estimated from the proposed method.
- The values of the bearing capacity factors N_q given by Bolton & Lau (1993) is used on the lower right figure to predict the reduced and triaxial friction angle. These angles correspond to the present stress level in the soil during penetration.



Job: Laboratory CPT-test		Remarks:
Exc: KAL	Eval: KAL	



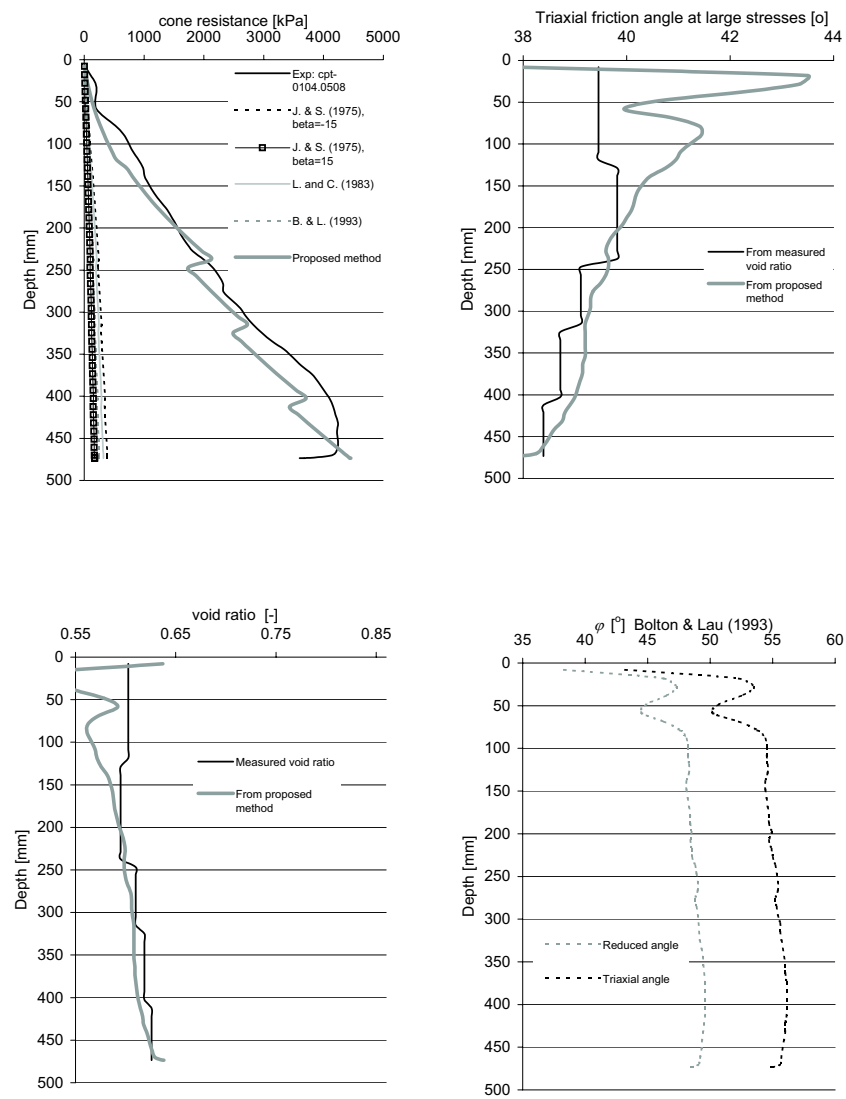
Job: Laboratory CPT-test		Remarks:
Exc: KAL	Eval: KAL	



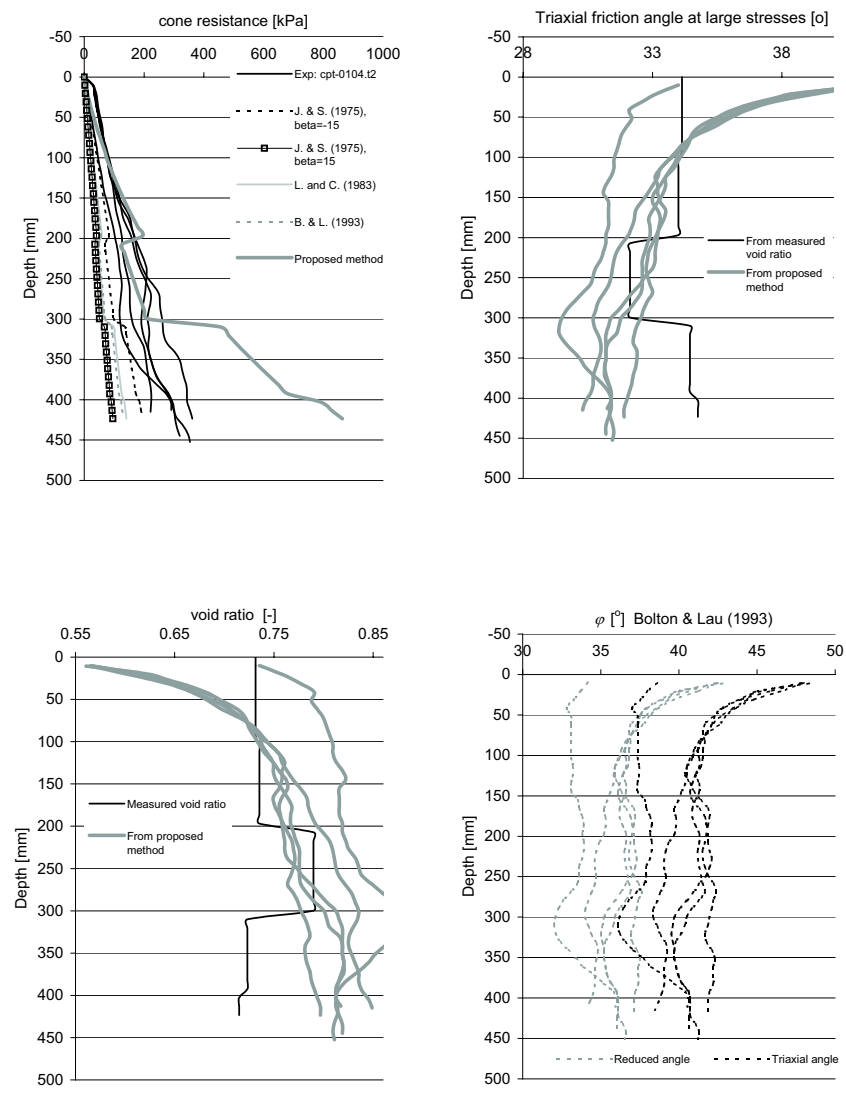
Job: Laboratory CPT-test		Remarks:
Exc: KAL	Eval: KAL	

Theory on laboratory CPT-TEST SERIE NO.

0104.05-cpt-08



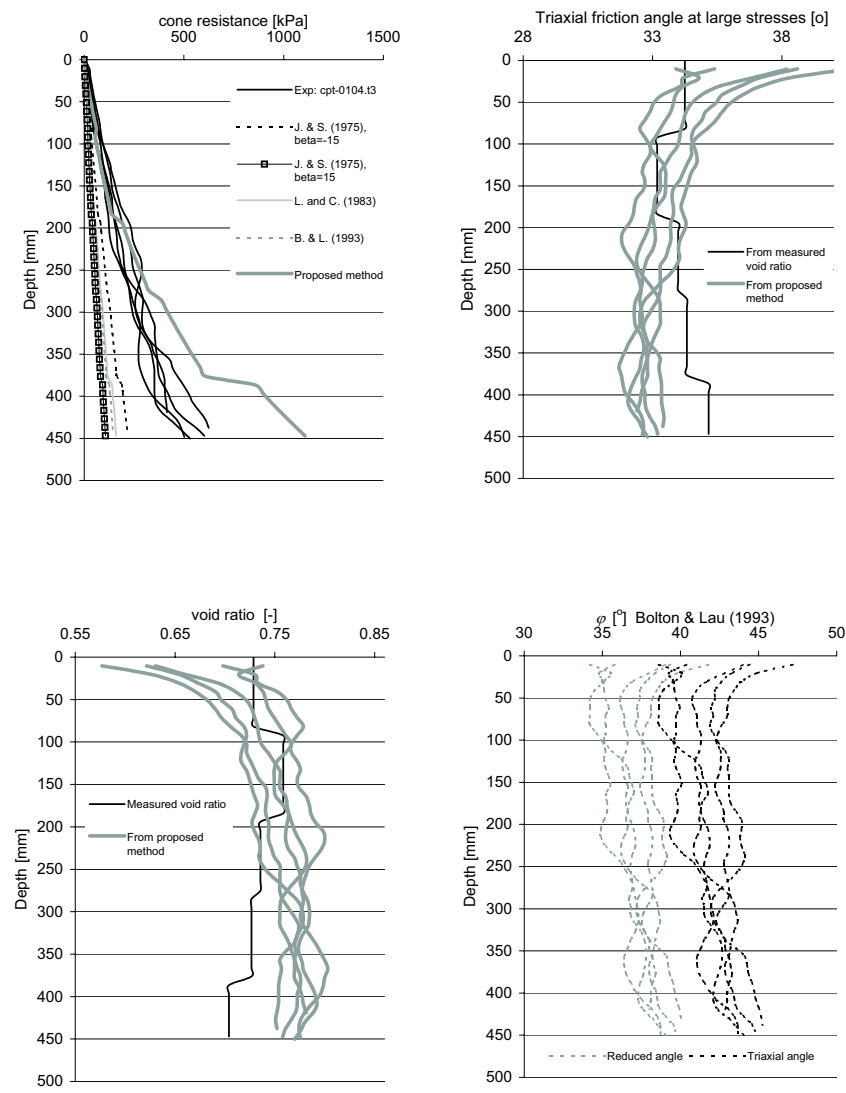
Job: Laboratory CPT-test		Remarks:
Exc: KAL	Eval: KAL	



Job: Laboratory CPT-test		Remarks:
Exc: KAL	Eval: KAL	

Theory on laboratory CPT-TEST SERIE NO.

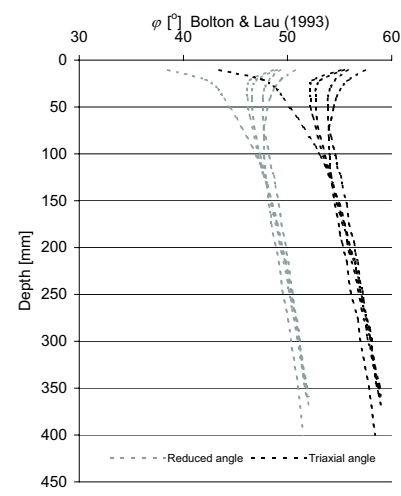
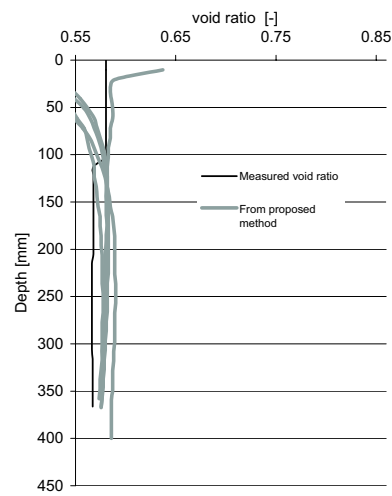
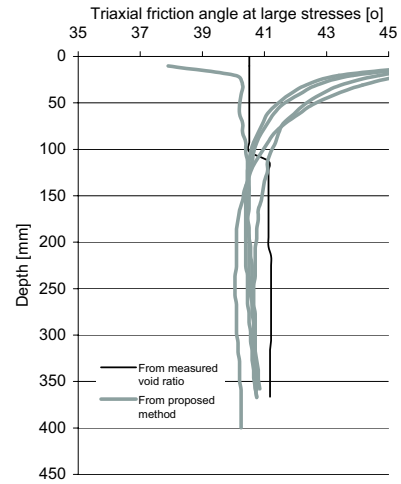
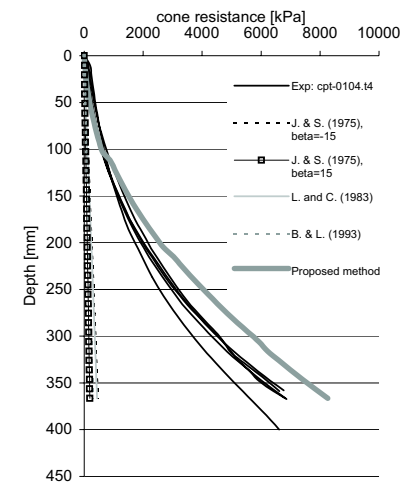
0104-cpt-t3



Job: Laboratory CPT-test		Remarks:
Exc: KAL	Eval: KAL	

Theory on laboratory CPT-TEST SERIE NO.

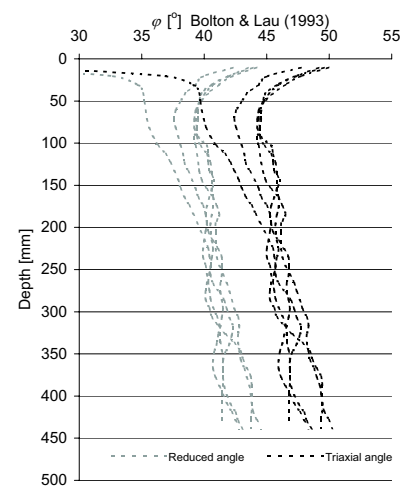
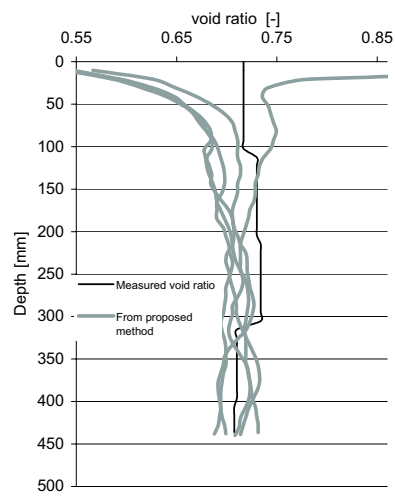
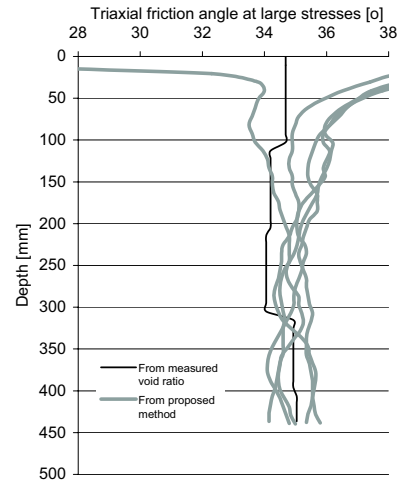
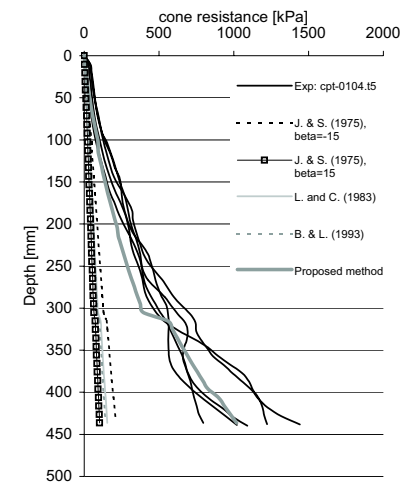
0104-cpt-t4



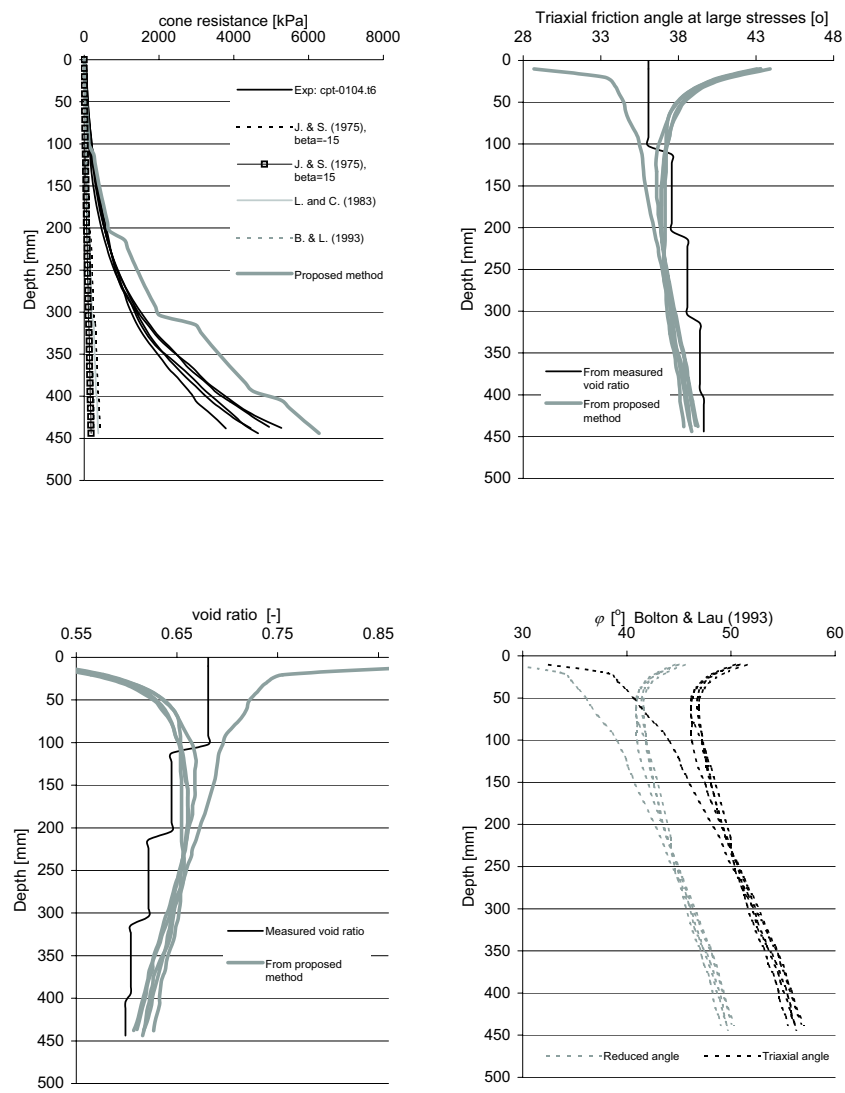
Job: Laboratory CPT-test		Remarks:
Exc: KAL	Eval: KAL	

Theory on laboratory CPT-TEST SERIE NO.

0104-cpt-t5



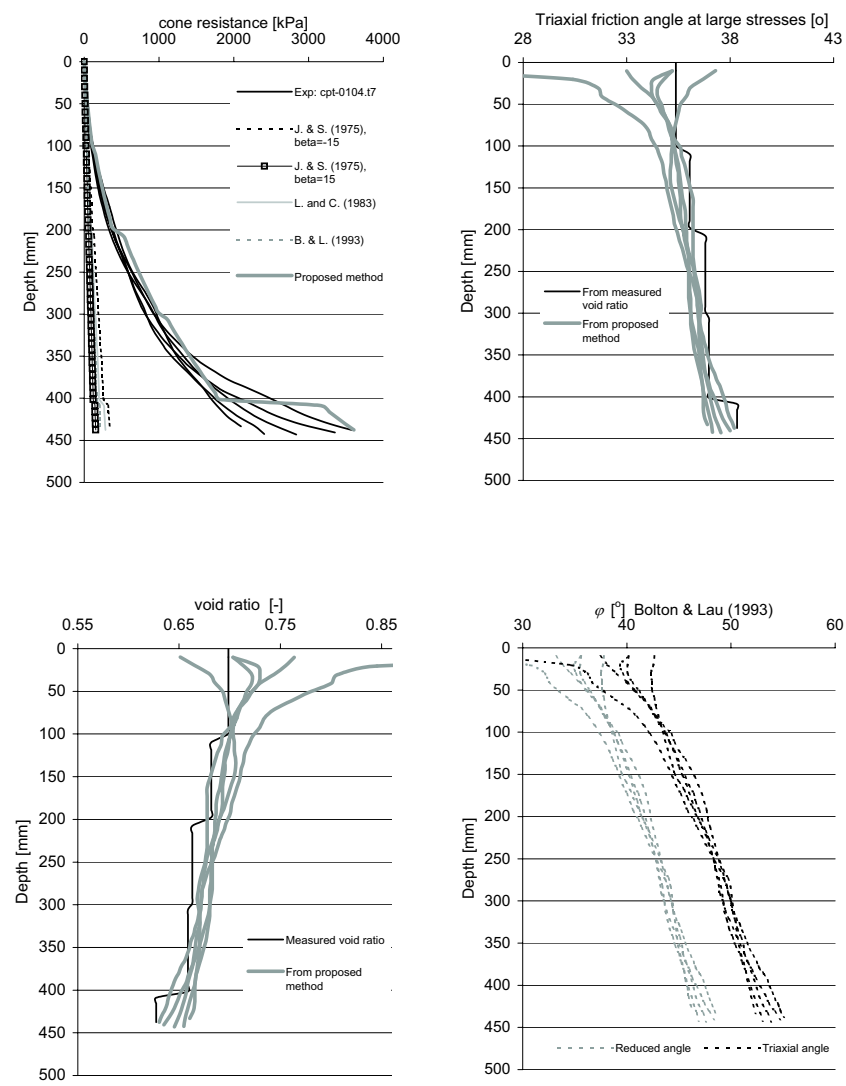
Job: Laboratory CPT-test		Remarks:
Exc: KAL	Eval: KAL	



Job: Laboratory CPT-test		Remarks:
Exc: KAL	Eval: KAL	

Theory on laboratory CPT-TEST SERIE NO.

0104-cpt-t7



Job: Laboratory CPT-test		Remarks:
Exc: KAL	Eval: KAL	

B. Appendix FE-Calculations of N_g

The commercial FE-program ABAQUS is used to determine the value of N_g in the plane strain and axis-symmetric stress cases assuming a soil behaviour according to the Mohr Coulomb material model. Associated flow with a friction angle equal 40 degrees is investigated.

B.1. Material model

The FE-program ABAQUS is used to calculate the value of N_g for a cohesionless soil with a dilation and friction angle equal 40 degrees. The user material mcdp.for by Clausen et al. (2006) is used in the calculations. The model uses the Mohr-Coulomb failure criterion given by Equation B.1, which is illustrated in Figure B.1. The figure is shown with the definitions used in ABAQUS, thus stresses are positive in extension.

Equation B.1
$$t = c + s \tan j$$

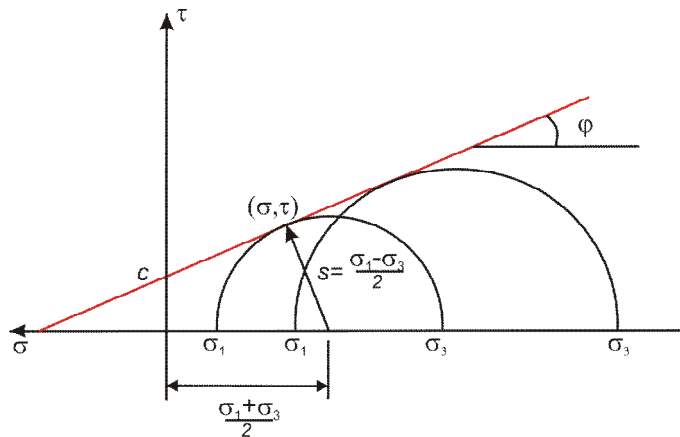


Figure B.1 Illustration of the Mohr-Coulomb failure criterion using Mohr's circles, after ABAQUS (2004).

The yield surface in the deviatoric stress plane for the Mohr Coulomb material model is shown in Figure B.2.

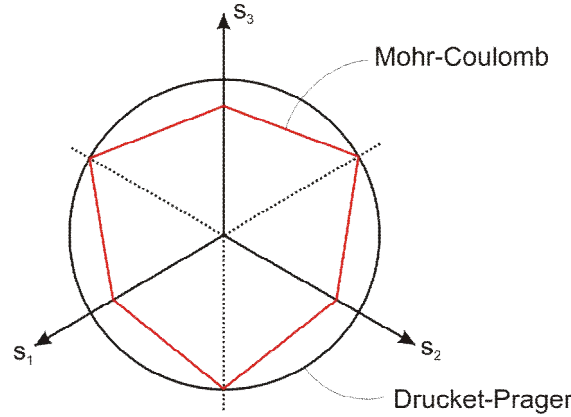


Figure B.2 Illustration of the Mohr-Coulomb yield surface in the deviatoric stress plane, after ABAQUS (2004).

The deviatoric stresses in Figure B.2 are defined according to the definitions used in Abaqus as follows:

Equation B.2
$$\bar{\mathbf{S}} = \bar{\mathbf{S}} + p\bar{\mathbf{I}}$$

where $\bar{\mathbf{S}}$ is the stress tensor, p is the negative trace of the stress tensor (p is positive in compression) and $\bar{\mathbf{I}}$ is the identity matrix. The deviatoric stresses can be expressed by the principle stresses as:

Equation B.3
$$\begin{bmatrix} S_1 \\ S_2 \\ S_3 \end{bmatrix} = \begin{bmatrix} s_1 \\ s_2 \\ s_3 \end{bmatrix} + p \begin{bmatrix} 1 & 0 & 0 \\ 0 & 1 & 0 \\ 0 & 0 & 1 \end{bmatrix} = \begin{bmatrix} \frac{2}{3}s_1 - \frac{1}{3}s_2 - \frac{1}{3}s_3 \\ \frac{2}{3}s_2 - \frac{1}{3}s_1 - \frac{1}{3}s_3 \\ \frac{2}{3}s_3 - \frac{1}{3}s_1 - \frac{1}{3}s_2 \end{bmatrix}$$

where $p = -\frac{1}{3}(s_1 + s_2 + s_3)$

The user material model uses a flow potential that is identical to the yield function, defined by the dilation and friction angle respectively, thus it is possible to perform calculations with associated flow. The flow potential within the ABAQUS standard Mohr Coulomb material is a modification of the yield surface presented above. The sharp edges present on the yield surface are rounded off in the flow potential function. The flow potential in ABAQUS is completely smooth and, therefore, provides a unique definition of the direction of plastic flow, Abaqus (2004). Hence the flow potential surface diverges from the yield surface. This model is therefore prevented from calculations with associated flow.

The Mohr Coulomb material model is used to calculate the bearing capacity factor N_g which is historically determined using the theory of plasticity under assumption of associated flow. Since this is possible with the material model by Clausen et al. (2006), this is chosen in the following calculations. Furthermore it has been found that the model seems more stable than the standard Mohr Coulomb model within ABAQUS under the given circumstances.

During the work concerning these calculations, the user material implemented has shown not to be capable of performing calculations with non-associated flow.

The input parameters to the user material are the same as for the corresponding standard ABAQUS material model. The material parameters used in the calculation are shown in Table B.1.

Table B.1 Soil parameters used in the calculations

E [MPa]	n [-]	c [kPa]	j [°]	ψ [°]	K^0 [-]	g' [kN/m ³]
10000	0.25	0	40	40	$1-\sin\phi$	9.82

Performing calculations in ABAQUS with a user material is done in a slightly different way than standard. The input parameters for the user material are defined in the input file for the model in the following way.

```

-----
** MATERIALS
**
*Material, name=Mohr_Coulomb_User
*Density
1.,                               **  $\rho = \gamma'/g$ 
*Depvar
3,                               ** No of SDV in the output file.
*User Material, constants=5
1e+07, 0.25, 0., 40., 40.       **  $E, \nu, c, \phi, \psi$ 
-----

```

It is very important that the material name of the soil in the input file starts with the letter m. This is because the routine also contains a corresponding Drucker Prager material model which is called if this is not obeyed.

The number of variables, Depvar specified in the input file defines the number of solution dependent state variables, SDV that is saved to the output file. Three variables is defined in the user material denoted SDV 1, SDV 2 and SDV3. SDV 1 is a variable that locates the current stress state relative to the yield surface:

SDV 1=0: Elastic stress state

SDV 1=1: Stress state on yield surface

SDV 1=2: Stress state on yield surface where $S_1 > S_2 = S_3$ (triaxial compression)

SDV 1=3: Stress state on yield surface where $S_1 = S_2 > S_3$ (triaxial extension)

SDV 1=5: Stress state on the apex of the yield surfaces

The second variable, SDV2 is only defined for the user material in case the Drucker Prager material model is used. The third variable SDV3 reports the plastic incremental shear strain, de'_{12} .

In order to save the defined variables in the output file the solution dependent state variables, SDV is requested in the input file with the following command.

```
-----
** OUTPUT REQUESTS
*Restart, write, frequency=0
** FIELD OUTPUT: F-Output-1
*Output, field
*Node Output
RT, U
*Element Output, directions=YES
E, S, SDV ** E: strain, S: stress and SDV: solution dependent state variables.
** HISTORY OUTPUT: H-Output-1
*Output, history, variable=PRESELECT
*End Step
-----
```

The input file is submitted to the ABAQUS solver using the command window in Abaqus as shown in Figure B.3.

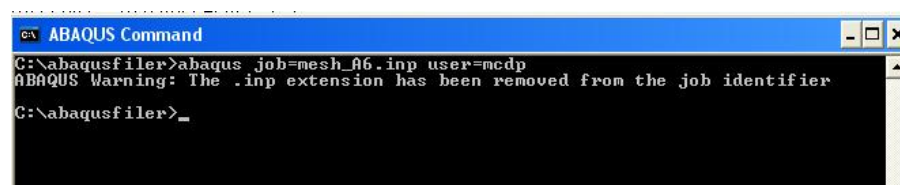


Figure B.3 Procedure for submitting an input-file with a user material.(First line)

B.2. Plane strain calculations

The bearing capacity of a strip foundation resting on cohesion-less soil with a width equal 2 meter is evaluated using the described user material in ABAQUS. The foundation is modelled as a rigid and rough foundation by applying a prescribed vertical deformation of nodes located on the soil surface, within the region of the foundation. Only half the foundation is modelled by use of a vertically symmetry line beneath the centre of the foundation, see Figure B.4. The soil considered is 20 meter wide and 10 meter deep. The ABAQUS element CPE6 which is a 6 node triangular second order plane strain element is used in the calculations.

The calculations are divided into three phases by the following three steps:

1. Initial step
2. Geostatic step
3. General static step

The initial step is used to activate the boundary conditions on the considered soil. The nodes on the lower boundary of the soil are constrained horizontally and vertically, whereas the nodes on the vertical boundaries are only fixed horizontally, thus are free to move vertically as illustrated in Figure B.4.

The second phase, i.e. the geostatic step is used to initialize the initial stress situation in the soil at rest. In this phase the unit soil weight is applied to the model and is to be balanced with a prescribed initial stress situation given by the user. Thus deformations are avoided in the soil during this phase. The initial conditions are defined manually in the input file as follows, where the element set in this case is all the elements in the considered soil named “_PickedSet39”.

```
-----
*Initial conditions, type=stress, geostatic
**Element set, stress at level 1, level 1, stress at level 2, level 2, K0
_PickedSet39, 0, 0, -98.2, -10, 0.36
-----
```

Using this procedure it is important to arrange the model in such a way that the direction of the global axis denoted 2 in the model is in the direction of the gravity for a two dimensional problem. In three dimensional problems the gravity is orientated in the direction of the global axis denoted 3.

The foundation is loaded vertically during the third phase, i.e. the general static step. This is done by a prescribed vertical deformation of the nodes, on the soil surface within the area of the foundation, until failure. Thus the

foundation is rigid. The nodes are fixed laterally in order to simulate the rough base of the foundation.

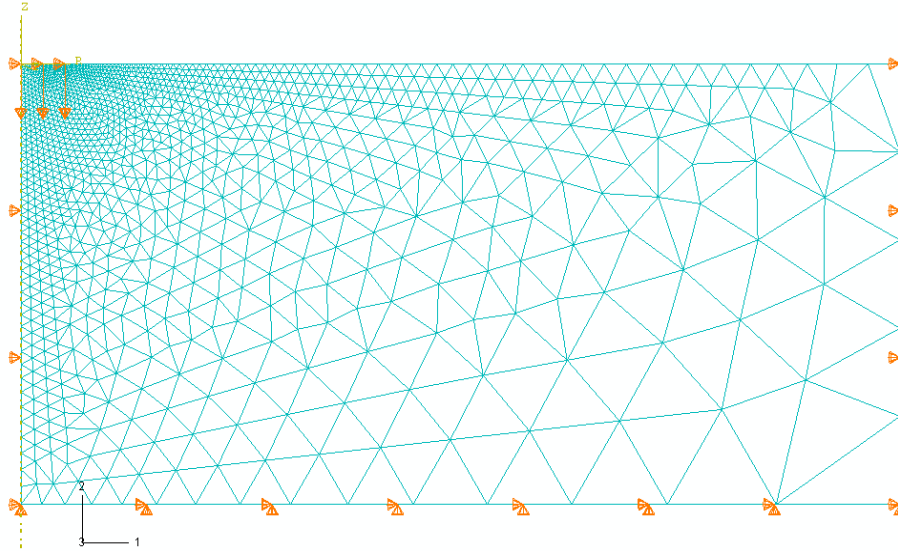


Figure B.4 FE-Model showing Mesh3F with a total of 2932 elements.

The model is used to calculate the bearing capacity with different coarseness of the mesh as given in Table B.2 in order to estimate the converged value of the bearing capacity. The bearing capacity is calculated from the output data as twice the sum of the foundation reactions due to symmetry.

The number of elements, $N_{el, line}$ is changed along the symmetry line and the soil surface as given in Table B.2. From this abaqus creates a mesh and the total number of elements in the model, N_{el} is shown in Table B.2 as well. The symmetry line is denoted line d , the line on the surface representing the foundation is denoted line a and the remaining surface is denoted line b .

Table B.2 Mesh information's and corresponding calculated value of N_g

	Mesh3	Mesh 3A	Mesh 3B	Mesh 3C	Mesh 3D	Mesh 3E	Mesh 3F
$N_{el, line a}$	12	13	14	11	15	16	17
$N_{el, line b}$	50	55	60	45	65	70	75
$N_{el, line d}$	25	30	35	20	40	45	50
$N_{el, model}$	1313	1592	1907	1052	2228	2575	2932
Results from calculations							
N_g	92.8	92.2	91.2	95.4	91.0	90.4	90.3

The bearing capacity factor N_γ in Table B.2 is calculated from the FE-simulations using the bearing capacity formula. The bearing capacity of the strip footing is determined as the maximum or residual value of the

foundation load. The result from the calculation with Mesh 3F is shown in Figure B.5.

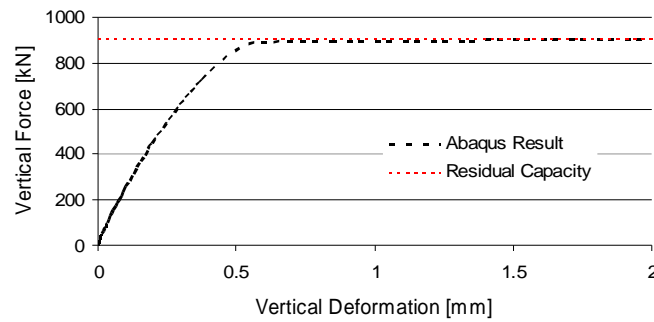


Figure B.5 Output from Abaqus calculation with Mesh 3F.

As seen in Table B.2 and Figure B.6 the size of the elements near the edge of the foundation needs to be very small in order to obtain a converged solution. The deformation of these elements is from Figure B.6 seen to go towards infinity, which often results in numerical problems especially for surface footings. The user material model used in these calculations however has shown to be superior regarding this problem.

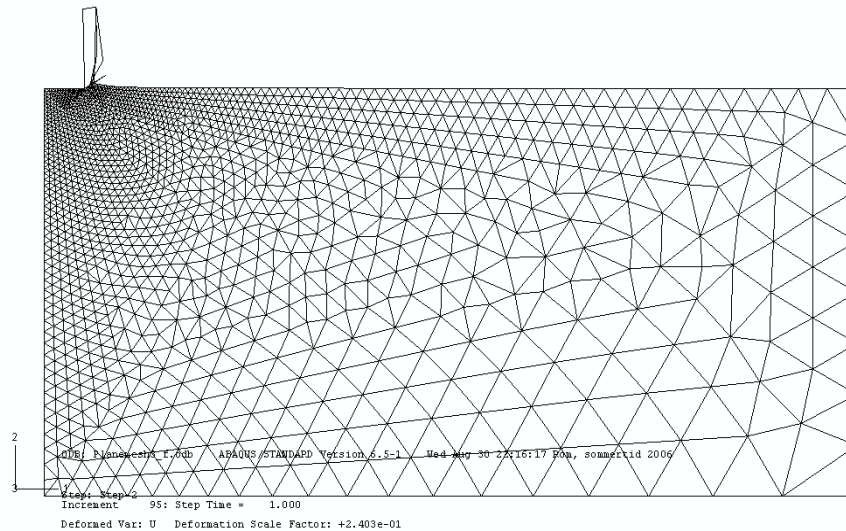


Figure B.6 Deformed mesh from Abaqus calculation with Mesh3F.

The solution dependent state variables, SDV1 and SDV3 defined in the input-file are shown in Figure B.7 and Figure B.8. From the figure it can be seen that an elastic zone beneath the foundation is present and that this only spans part of the footing width, also noticed by Martin (2004) for rough footings.

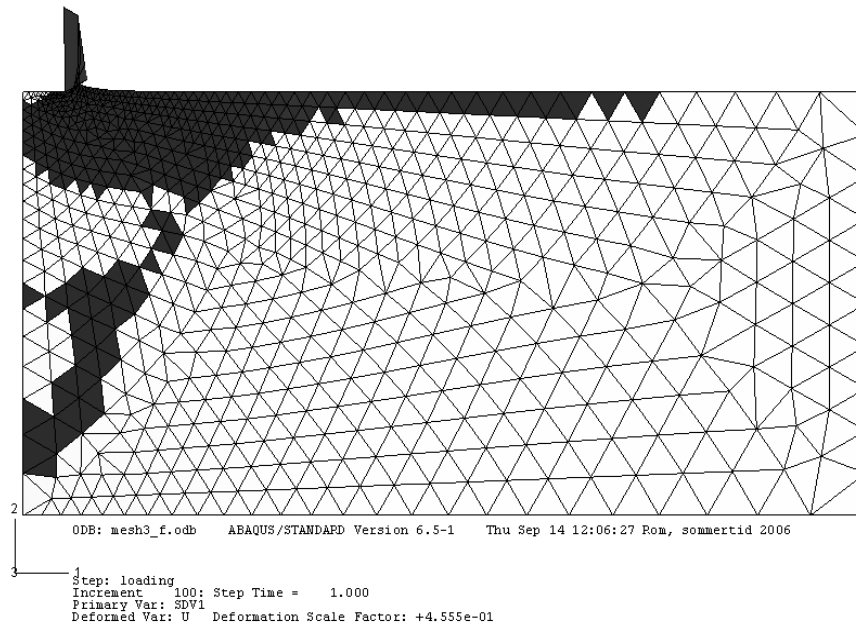


Figure B.7 Result from Abaqus calculation with Mesh3F. Colored elements show elements where the stress state is located on the yield surface, i.e. plastic stress state.

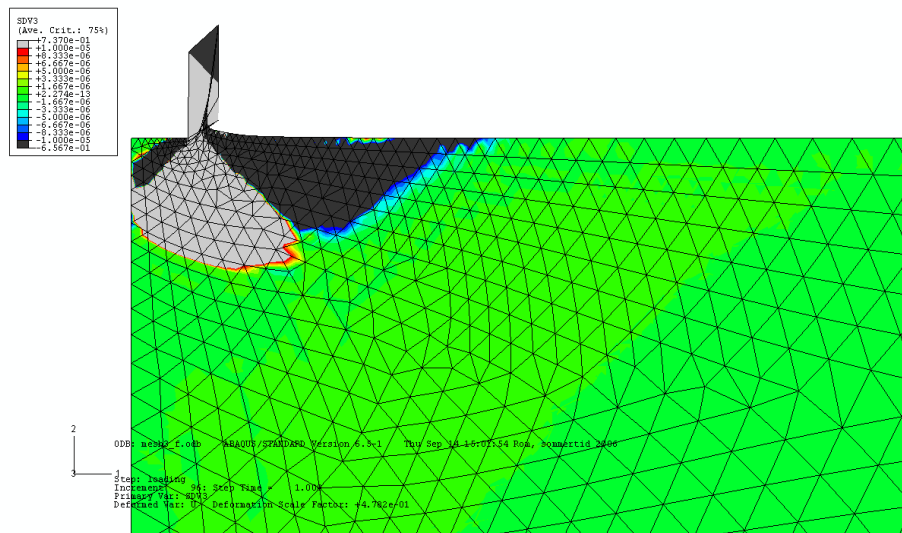


Figure B.8 Incremental shear strain at failure for Mesh 3F.

The plot of the incremental shear strain at failure in Figure B.8 for the bearing capacity problem indicates the figure of rupture for the problem. The figure is seen to be in accordance with the figure of rupture proposed by Lundgren and Mortensen (1953), see Figure B.9.

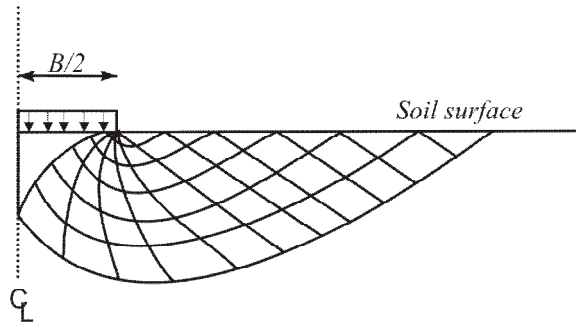


Figure B.9 Rupture Lines under Rough Bases for $j = 30^\circ$ after Lundgren and Morten (1953)

B.3. Axis-symmetric calculations

The axis-symmetric calculations are performed using the same model, thus with a radius of the foundation equal 1 meter. The Abaqus element CAX6 is used in these calculations which is the axis-symmetric version of the one used in the plane strain model. It has not been possible to complete the axis-symmetric calculations with the same meshes as in the plane strain case. Instead the calculations are carried out with the meshes defined in Table B.3 according to the description given previously.

Table B.3 Mesh information's and corresponding calculated value of N_g

	Nel,line a	Nel,line b	Nel,line d	N _{el,model}	Calculated N_g
Mesh 2				1151	141.26
Mesh 3	12	50	25	1315	135.56
Mesh 3a	11	45	20	1219	137.76
Mesh 3b	10	40	15	972	150.82
Mesh 3e	13	50	30	1712	140.48
Mesh 3f	11	50	20	1346	137.28
Mesh 3g	14	50	35	1902	139.87
Mesh 3i	15	50	40	2084	138.73
Mesh 3ii	15	50	45	2287	138.90
Mesh 3k	13	50	25	1513	141.91
Mesh 3l	13	50	35	1893	140.45
Mesh 3m	13	50	40	2072	140.71
Mesh 3n	11	50	25	1497	135.14
Mesh 3p	14	50	25	1526	140.81
Mesh 3q	15	50	25	1537	140.13
Mesh 3s	12	50	30	1695	134.75
Mesh 3t	14	50	30	1723	140.13

Mesh number 2 is structured differently from the rest and is shown in Figure B.10.

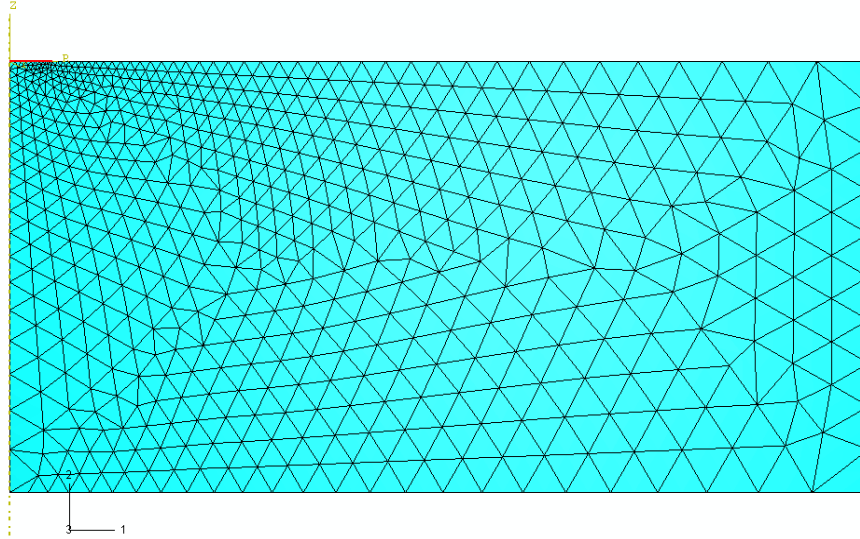


Figure B.10 FE-Model showing Mesh2 with a total of 1151 elements.

The bearing capacity is calculated directly from the output data by the sum of the foundation reactions since ABAQUS integrates the reaction force in the radial direction. The bearing capacity factor N_γ derived from the FE-calculations is shown in Table B.3.

B.4. Extrapolation to full converged values

If full convergence of a modelled problem is not achieved the converged solution can be estimated using the following principle, known as Richardson extrapolation. The converged value, f^0 is estimated based on two calculated set of values using meshes larger than the one necessary to obtain a converged solution, Cook et al. (1989):

$$\text{Equation B.4} \quad f^0 = \frac{f_1 h_2^p - f_2 h_1^p}{h_2^p - h_1^p}$$

where h is a dimensionless length that characterizes the mesh, that gives the corresponding value of f and $p = 1$ for $e = O(h)$ and $p = 2$ for $e = O(h^2)$ etc. see Figure B.11.

The dimensionless length, h is defined by:

$$\text{Equation B.5} \quad h = \frac{1}{N^{1/n}}$$

where N is the number of elements in the mesh and n is 1,2 and 3 for line, plane and solid problems, respectively.

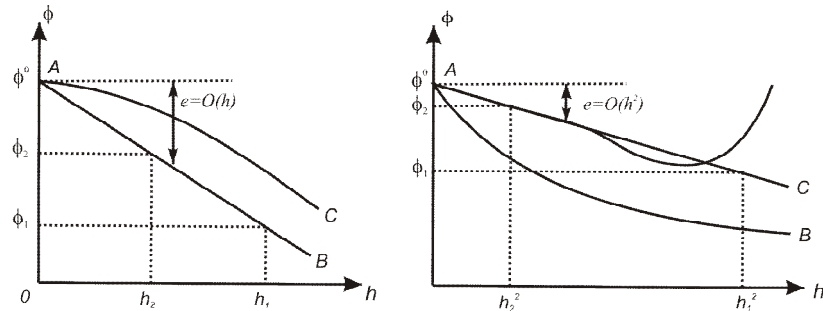


Figure B.11 Convergence of a quantity f with mesh refinement. AB: linear convergence. AC: quadratic convergence. AD: non-monotonic convergence for $h > h_D$, after Cook et al. (1989)

In order to obtain reliable values with the given method the convergence must be monotonic. A too coarse mesh may fail to display a definite trend and is in this case left out from the analysis.

B.4.1. Plane strain results

The results from the calculations with the plane strain model in Table B.2 are summarized in Figure B.12.

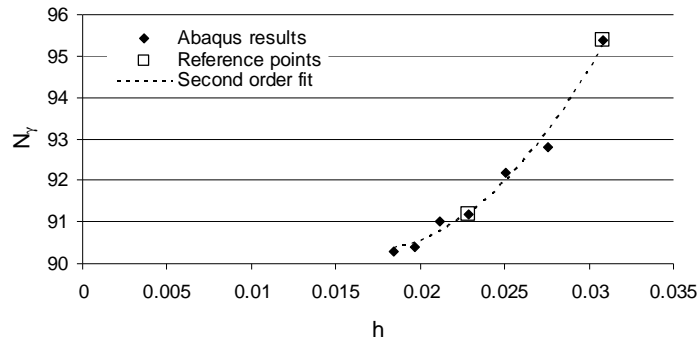


Figure B.12 Results from Plane strain calculations.

From Figure B.12 it can be seen that the convergence rate is quadratic, i.e. $e = O(h^2)$ for the plane strain calculations, which means that $p = 2$ and $n = 2$. The described method is used to extrapolate the calculated values to a full converged value of N_g . A value of 86 is found using the reference points shown in Figure B.12. These values are chosen because they lie directly on the fitted line and with some distance between them. The converged value of N_γ for a rough strip foundation is found to be in accordance with the value by Lundgren and Mortensen (1953), see chapter 4.

B.4.2. Axis-symmetric results.

The results from the calculations with the axis-symmetric model in Table B.2 are shown in Figure B.13.

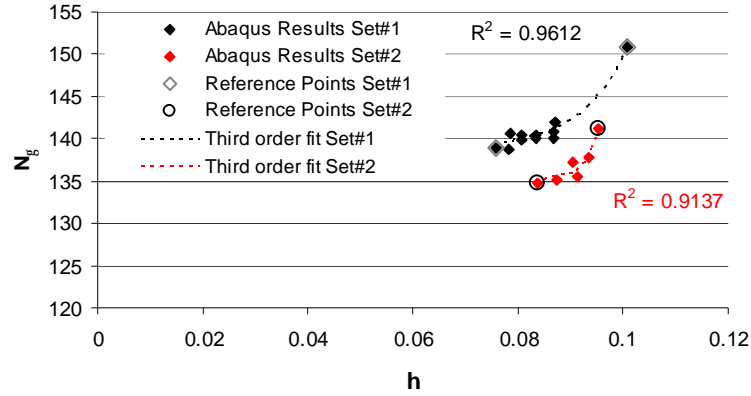


Figure B.13 Results from axis-symmetric calculations

From Figure B.13 it can be seen that the convergence is best fitted with a third order polynomial, i.e. $e=O(h^3)$, which means that $p=3$ and $n=3$, since the problem actually is a special case of a three dimensional problem. The results are seen to be grouped around two lines, denoted Set no.1 and Set no.2. The described method is used to extrapolate the calculated values of the two set of results, giving two fully converged values of N_γ . The values are estimated to 130 and 121, using the reference point shown in Figure B.12. The true fully converged value is assumed to lie in between these values. Assuming that this value is the mean value of the extrapolated values a converged value of N_g is estimated to 125.5. The value according to Martin (2004) should be 123.7 which is close to this mean value and lies within the range of the converged values estimated.

C. Appendix Elastic displacements of bucket foundations.

The elastic displacements of a bucket foundation subjected to combined loading can be calculated based on an elastic stiffness matrix. This appendix contains a description of the elastic stiffness matrix and constants associated with this, according to the macro model approach described in chapter 4. The constants are presented graphically and relations are presented that fits the conditions of the experiments performed within this thesis.

Within the macro model approach described in chapter 5 the complete elastic displacements of a bucket foundation can be determined from the general stiffness matrix:

Equation C.1

$$\begin{bmatrix} V / GR^2 \\ H_1 / GR^2 \\ H_2 / GR^2 \\ T / GR^3 \\ M_1 / GR^3 \\ M_2 / GR^3 \end{bmatrix} = \begin{bmatrix} K_{VV}^0 & 0 & 0 & 0 & 0 & 0 \\ 0 & K_{HH}^0 & 0 & 0 & 0 & -K_{HM}^0 \\ 0 & 0 & K_{HH}^0 & 0 & K_{HM}^0 & 0 \\ 0 & 0 & 0 & K_{TT}^0 & 0 & 0 \\ 0 & 0 & K_{HM}^0 & 0 & K_{MM}^0 & 0 \\ 0 & -K_{HM}^0 & 0 & 0 & 0 & K_{MM}^0 \end{bmatrix} \begin{bmatrix} w / R \\ u_1 / R \\ u_2 / R \\ q_T \\ q_{M1} \\ q_{M2} \end{bmatrix}$$

where R is the radius of the foundation, G is the shear modulus of the soil and K^0 is non-dimensional static stiffness components. The dimension of rotations is in radians. Loads and displacements are according to the sign convention presented in chapter 1.

Within the domain examined in this thesis Equation C.1 can be reduced according to the sign convention used:

$$\text{Equation C.2} \quad \begin{bmatrix} V / GR^2 \\ H / GR^2 \\ M / GR^3 \end{bmatrix} = \begin{bmatrix} K_{VV}^0 & 0 & 0 \\ 0 & K_{HH}^0 & K_{HM}^0 \\ 0 & K_{HM}^0 & K_{MM}^0 \end{bmatrix} \begin{bmatrix} w / R \\ u / R \\ q_M \end{bmatrix}$$

where $H=H_2$, $u = u_2$, $M=M_1$ and $q_M = q_{M1}$.

The vertical load is from Equation C.2 seen to be uncoupled with the remaining displacements. The values of K^0 is by use of the FE-code ABAQUS investigated for bucket foundations by Liingaard (2006) for chosen values of Poissons ratio, shear stiffness and embedment ratio, d/D . The stiffness coefficients are dependent of the ratio E_{steel}/E_{soil} as well as the thickness of the bucket skirt, t/D . The ratio t/D used in the evaluations by Liingaard (2006) is similar to the one present in the laboratory for $D=300\text{mm}$.

From the general stiffness matrix the following relation between the vertical load and displacement is obtained.

$$\text{Equation C.3} \quad \frac{V}{GR^2} = K_{vv}^0 \frac{w}{R}$$

where K_{vv}^0 is the vertical stiffness of the bucket foundation under pure vertical load.

The relation between the shear modulus, the elastic stiffness, E and Poissons ratio, n determined in chapter 3 are given as follows.

$$\text{Equation C.4} \quad G = \frac{E}{2(1+n)}$$

From the elastic stiffness matrix the rotation is found to be a function of both the horizontal force and moment due to the coupling term. From Equation C.2 the elastic rotation can be calculated as follows.

$$\text{Equation C.5} \quad q = \frac{\frac{M}{GR^3} - \frac{H \cdot K_{HM}}{GR^2 K_{HH}}}{K_{MM} - \frac{K_{HM}^2}{K_{HH}}}$$

When the elastic rotation is known the horizontal displacement can be determined by the elastic stiffness matrix:

$$\text{Equation C.6} \quad u = \frac{\frac{H}{GR^2} - K_{HM}^0 \cdot q}{K_{HH}^0}$$

C.1. Vertical stiffness component

The vertical static stiffness can for a circular rigid surface foundation with rough base be determined by the following equation, Spence (1968)

$$\text{Equation C.7} \quad K_{vv}^0 = \frac{4 \ln(3-4n)}{1-2n}$$

In case of smooth base the stiffness component can be determined by Equation C.8, Poulos and Davies (1974).

$$\text{Equation C.8} \quad K_{vv}^0 = \frac{4}{1-n}$$

The value of K_{vv}^0 is by use of the FE-code ABAQUS investigated for bucket foundations by Liingaard (2006) for chosen values of poissons ratio, shear stiffness and embedment ratio, d/D . The results are presented in Figure C.1 to Figure C.3.

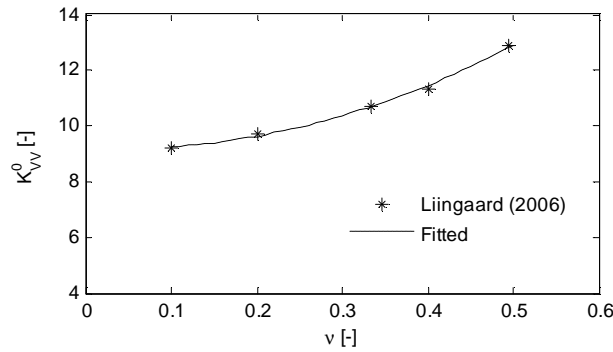


Figure C.1 Variation of K_{vv}^0 with change in poissons ratio. $G = 1 \text{ MPa}$ and $d/D = 1$.

The variation of the vertical stiffness with v is from Figure C.1 seen to follow a second order polynomial. Using linear interpolation between the known values is though seen only to introduce small errors.

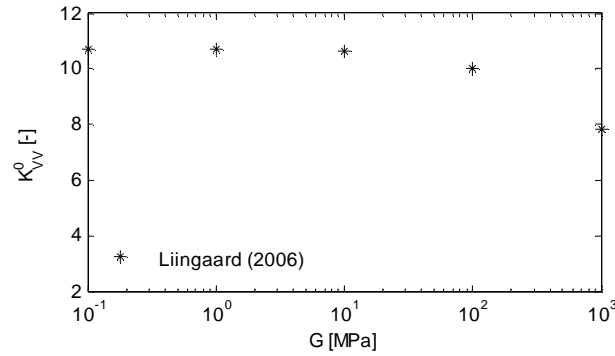


Figure C.2 Variation of K_{vv}^0 with change in G . $n=0.33$ and $d/D=1$.

From Figure C.2 it is seen that the vertical stiffness is almost constant for a shear modulus of the soil less than 100MPa.

The vertical stiffness of bucket foundations with various embedment ratios are shown in Figure C.3. The relation is seen to be linear going toward the stiffness of a rough surface footing by Spence (1968).

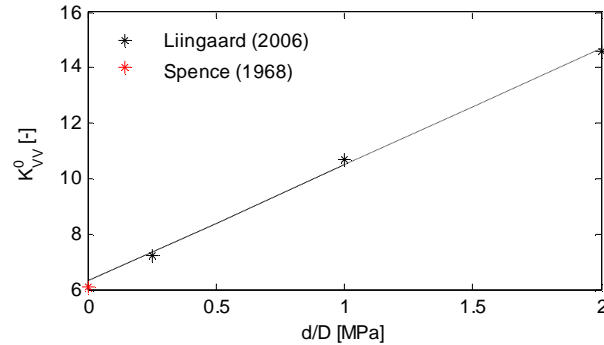


Figure C.3 Variation of K_{vv}^0 with change in embedment ratio. $n=0.33$ and $G=1\text{MPa}$.

The value of ν is determined to 0.25 for the soil tested in the laboratory. The presented results are in the following used to predict the vertical stiffness of bucket foundations with a poissons ratio equal 0.25. The shear modulus of the soil samples tested is significantly lower than 100MPa, hence the stiffness is independent of any variation in the shear modulus. The vertical stiffness of the bucket foundations tested in the laboratory is assumed throughout the thesis to be given as shown in Figure C.4 which is given by Equation C.9

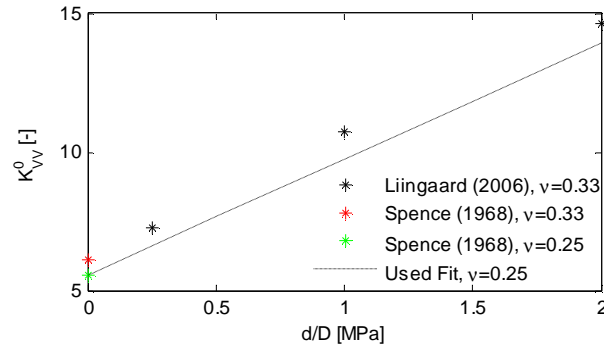


Figure C.4 Proposed values of the vertical stiffness for $n=0,25$.

Equation C.9
$$K_{VV}^0 = 5.55 + d / D * 4.19$$

Equation C.9 is valid for sands with $n=0,25$ and $G < 100$ MPa

C.2. Rotational stiffness component

The rotational stiffness of bucket foundations from a pure moment load K_{MM}^0 by Liingaard (2006) is presented in Figure C.5 and Figure C.6.

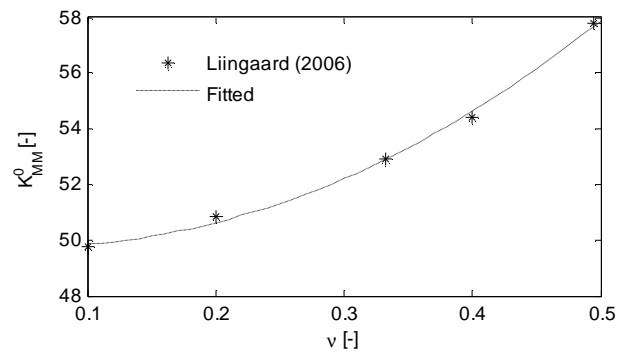


Figure C.5 Variation of K_{MM}^0 with change in Poisson's ratio. $d/D = 1$ and $G = 1$ MPa

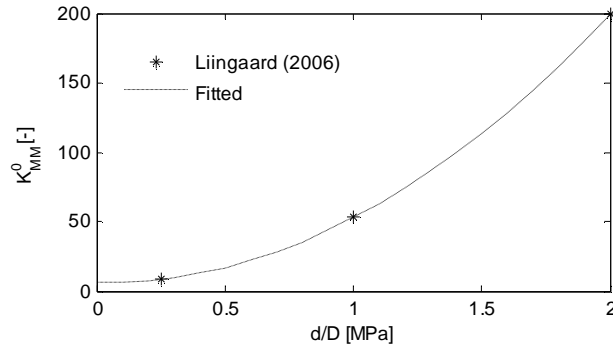


Figure C.6 Variation of K_{MM}^0 with change in embedment ratio. $G = 1\text{MPa}$ and $n = 0,33$

From Figure C.5 the error introduced by using a value of the moment stiffness corresponding to a poissons ratio equal 0.33 instead of 0.25 can be determined to only 3-4 percent. The rotational stiffness in Figure C.6 is therefore used throughout the thesis ignoring the influence of ν . The variation in Figure C.6 can be described by the following second order polynomial

Equation C.10
$$K_{MM}^0 = 49,6\left(\frac{d}{D}\right)^2 - 2,8\frac{d}{D} + 6,1$$

C.3. Horizontal stiffness component

The horizontal stiffness of bucket foundations from a pure horizontal load K_{HH}^0 by Liingaard (2006) is presented in Figure C.7 and Figure C.8.

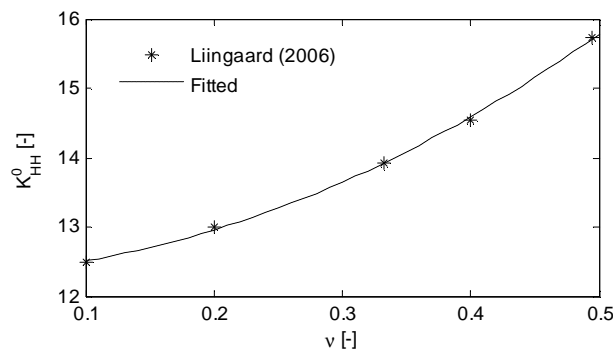


Figure C.7 Variation of K_{HH}^0 with change in poissons ratio. $d/D = 1$ and $G = 1\text{MPa}$

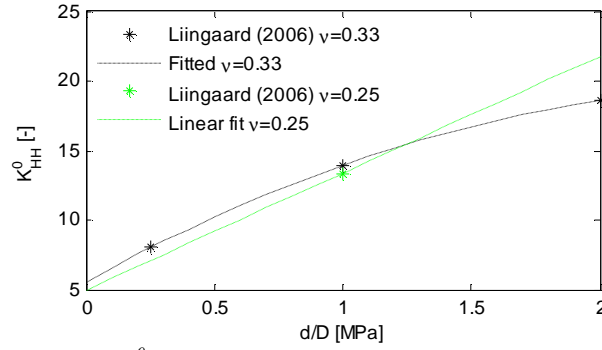


Figure C.8 Variation of K_{HH}^0 with change in embedment ratio. $G = 1\text{MPa}$

The variation of the horizontal stiffness with ν is from Figure C.7 seen to follow a second order polynomial. Using linear interpolation between the known values though only introduces small errors. In Figure C.8 this is used to determine a value of K_{HH}^0 for $d/D = 1$ corresponding to a Poisson's ratio of 0.25. The variation of K_{HH}^0 is in Figure C.8 fitted to a second order polynomial for $\nu = 0.33$. For $d/D \leq 1$ a linear relation is though assumed accurate enough. A proposed linear fit of the horizontal stiffness with a Poisson's ratio equal 0.25 is shown in the figure by the following equation:

Equation C.11
$$K_{HH}^0 = 5,0 + 8,38 \frac{d}{D} \text{ for } d/D \leq 1$$

C.4. Coupled stiffness components

A coupling between horizontal sliding and rocking of the bucket foundation is seen from the stiffness matrix in Equation C.2 to exist. The value of this stiffness component K_{HM}^0 is shown in Figure C.9 and Figure C.10, Liingaard (2006).

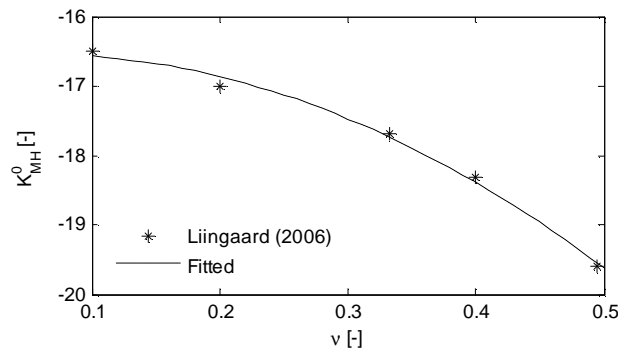


Figure C.9 Variation of K_{HM}^0 with change in Poisson's ratio. $d/D = 1$ and $G = 1\text{MPa}$

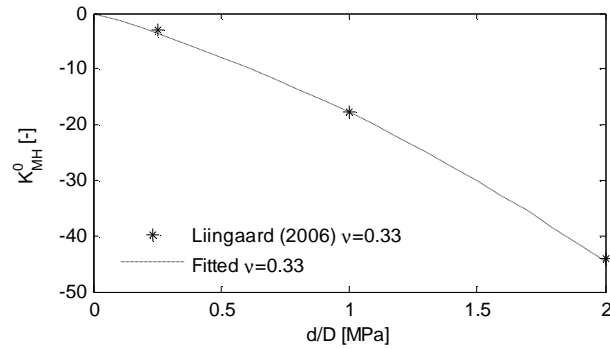


Figure C.10 Variation of K_{HM}^0 with change in d/D . $G = 1 \text{ MPa}$ and $n = 0.33$

The influence of Poissons ratio can be seen not to affect the coupled stiffness significantly. Ignoring the influence of Poissons ratio the coupled stiffness can be fitted by the following expression, as shown in Figure C.10.

Equation C.12
$$K_{MH}^0 = -4.5 \left(\frac{d}{D} \right)^2 - 13.3 \frac{d}{D}$$

C.5. Stiffness components for embedded foundations.

The stiffness components in Equation C.2 can as alternative be estimated for an embedded rigid and solid foundation according to DNV (2004). Though no information on the coupling term, K_{HM}^0 is given here.

D. Appendix FE- calculations

The commercial FE-code ABAQUS is used to simulate the behaviour of the tested bucket foundations subjected to combined loading. Several simulations of the combined loading of the bucket foundation are performed in order to investigate the influence of the choices made within the model. Some of these results are presented in this appendix. The use of ABAQUS has resulted in a useful experience about the program. This experience is found to be important in order to complete the simulations and is summarized at the end of this appendix.

D.1. Small scale simulations

D.1.1. Convergence study

In this section the results from a convergence study with the FE-models of the laboratory tests is presented. The simulations are performed as described in chapter 7. It has been found that linear (i.e. first order) solid elements with reduced gauss integration are the best choice of element type for this problem. Second order elements have been found not to have a convergence rate that is different from the first order reduced elements. Generally numerical problems are seen with the mesh coarseness necessary when second order elements are used.

Using first order elements with full gauss integrations have shown to give a response that is too stiff and over predicts the capacity, which is the result of shear locking. Second order elements can suffer from volume locking when the material is close to incompressible if full gauss integration is used. This is however not registered in calculations as poissons ratio is significantly different from 0.5.

The convergence study is performed with bucket foundations with a diameter of 300 mm and embedment ratios equal 0.25 and 1. The bucket foundations are loaded vertically with 1884N and with a horizontal load acting at height of 2610mm above the bucket lid. The material properties of the soil used in the

convergence study are given in Table D.1. Only the results from simulations with first order elements and full gauss integration is presented. These are denoted C3D8R in ABAQUS. The results from the simulations are presented in Figure D.1 as the moment applied relative to the rotation of the bucket. The convergence study has been performed by a systematic refinement of the mesh. The number of elements in all three directions are increased as uniform as possible between the simulations.

Table D.1 Soil parameters used through out the convergence study

γ' [kN/m ³]	ϕ [°]	ψ [°]	c [kPa]	ν [-]	E [MPa]	$\tan(\delta)$ [-]
10	45	15	1	0.26	20	0.6

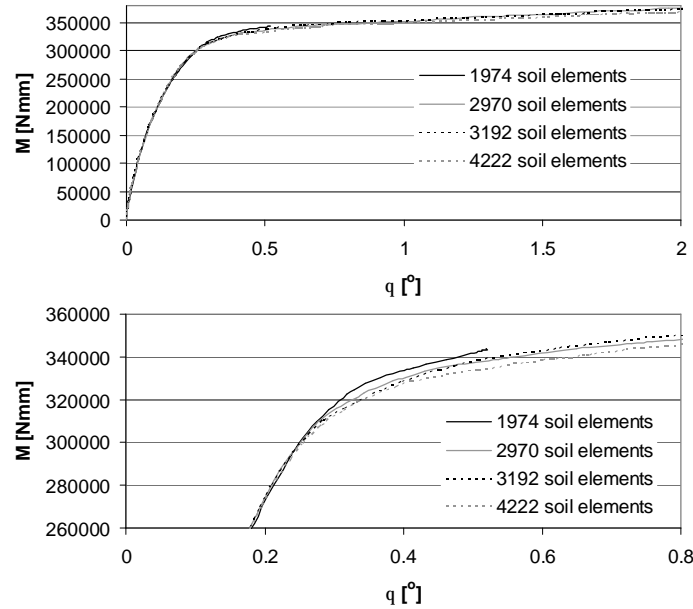


Figure D.1 Results from convergence study of bucket foundation with $d/D=1$.

From the convergence study with a full bucket (i.e. $d/D=1$) it can be seen from Figure D.1 that the mesh containing 2970 elements gives a result that is converged with good accuracy. This mesh is used throughout the thesis for simulations on full bucket foundations and is shown in Figure D.2.

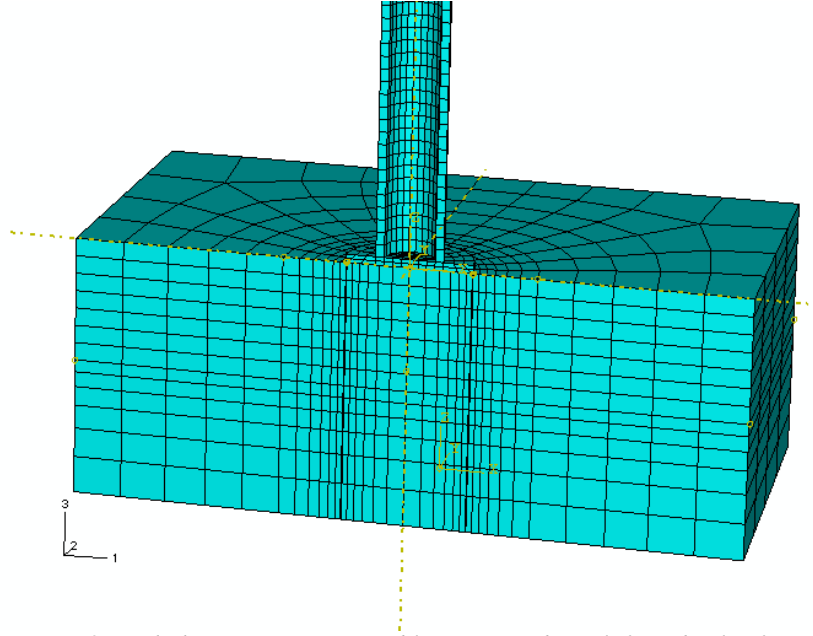


Figure D.2 Mesh that gives an acceptable converged result for a bucket foundation with $d/D=1$. The mesh contains 2970 soil elements.

The simulations are found not to be sensitive with respect to the number of elements used to model the bucket foundation. An element length of approximately 25 and 50 mm for bucket and tower respectively is found to work well.

The results from a similar convergence study of a bucket foundation with an embedment ratio equal 0.25 are shown in Figure D.3. It is found that a reduction of the element length along and below the skirt is necessary in order to obtain full convergence. The rest of the mesh is identical to the one in Figure D.2 in the simulations. The height of these elements (down to 300mm below soil surface) is determined to $d/3$. The mesh containing 3276 elements corresponds to the mesh in Figure D.2. The difference in the number of elements is caused by the mesh generator in Abaqus.

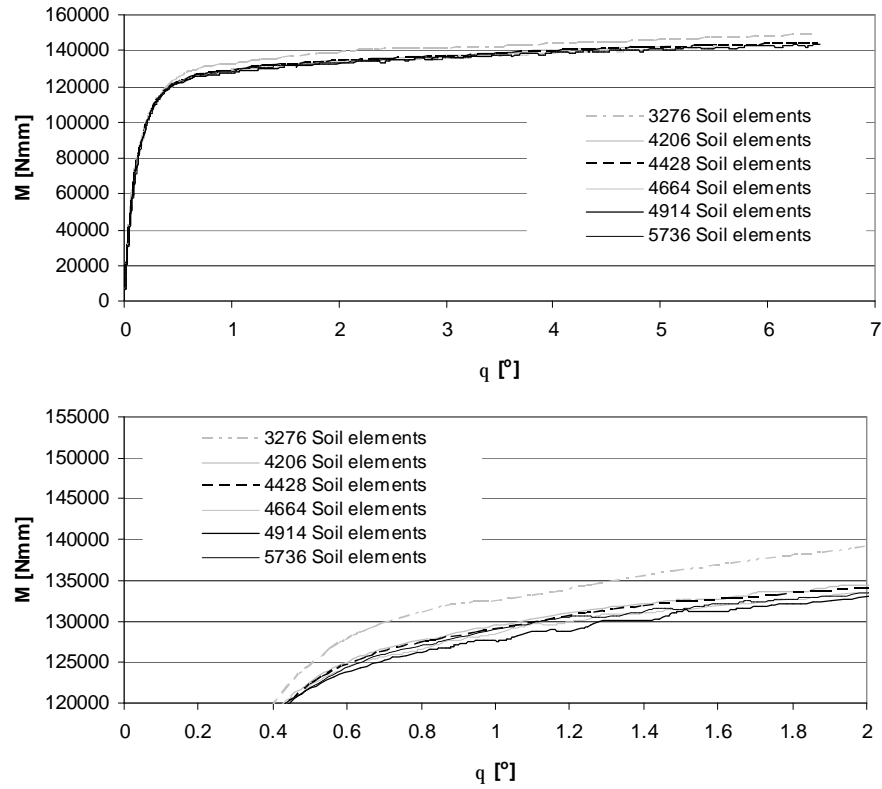


Figure D.3 Results from convergence study of bucket foundation with $d/D=0.25$

From figure Figure D.3 it is concluded that the mesh containing 4206 elements is sufficient to get an acceptable accuracy of the calculations. This mesh is presented in Figure D.4.

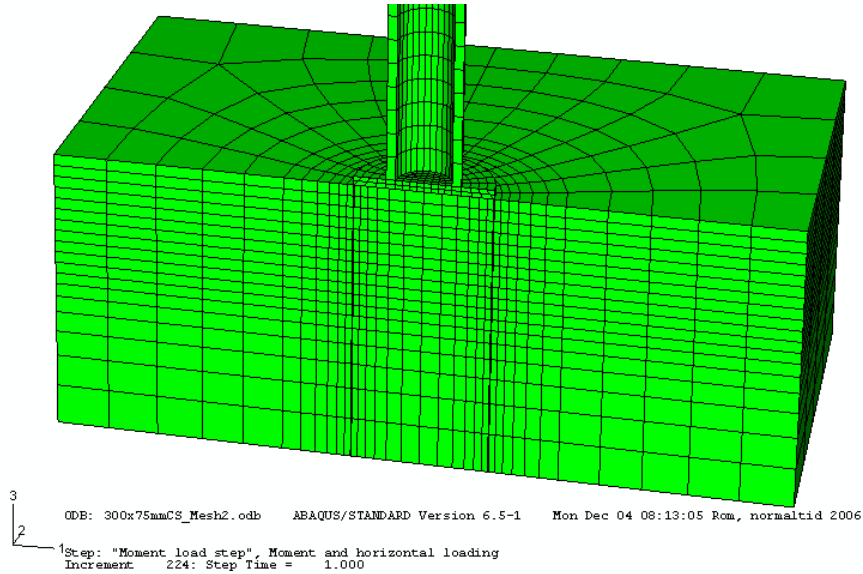


Figure D.4 Mesh that gives an acceptable converged result for a bucket foundation with $d/D=0.25$. The mesh contains 4206 soil elements.

D.1.2. Initial Clearance of interfaces

The interaction between the soil and steel is modelled using the contact pair option in ABAQUS. Due to the linear elements used a small gap between the soil and bucket foundation can occur in some cases. This gap can be removed by the Clearance command. This however must manually be added to the input file after the model is created in ABAQUS CAE. The influence of the initial clearance present is investigated from simulations corresponding to the ones performed in the convergence study with a full bucket foundation. The results are shown in Figure D.5.

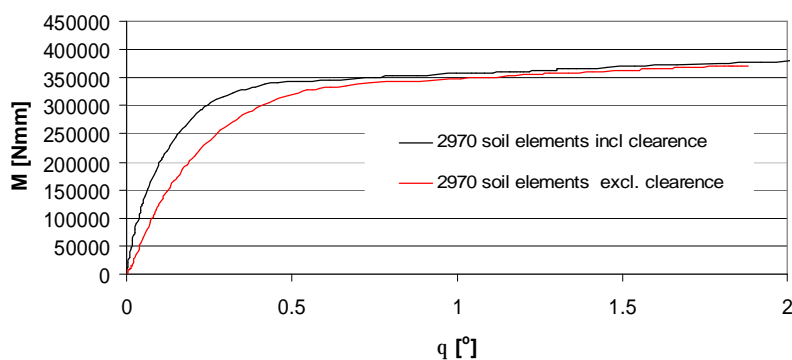


Figure D.5 Influence of clearance command on the calculated result. Parameters and model corresponds to the calculations in the convergence analysis with $d/D=1$.

It is clear from Figure D.5 that the clearance command has a great effect on the simulated behaviour prior to failure. The response is seen to be much softer if the clearance command is not used. In this case larger deformations are needed before the earth pressure is mobilized. The clearance command is used with no initial clearance throughout the thesis.

The clearance command is applied to the input file in the following way, corresponding to initial coincidence of the surfaces:

```
-----
** INTERACTIONS
**
** Interaction: BucketPlate
*Contact Pair, interaction=Fric06, small sliding, type=SURFACE TO SURFACE,
adjust=0.0
_PickedSurf68, _PickedSurf67
*Clearance, slave=_PickedSurf68, master=_PickedSurf67, value=0
-----
```

D.1.3. Influence of soft elements at skirt tip

The FE-modelling of the bucket foundations with the finite element program ABAQUS can in some cases induce large stress concentrations in the soil below the skirt tip. This is of course a phenomenon that only occurs in the models as the soil in nature will rearrange when the skirt tip is penetrated into the soil. Feld (2001) suggests that soft elements are modelled below the skirt tip to avoid this. Simulations introducing these soft elements have shown to give problems in obtaining equilibrium in the model during loading. Instead it is proposed to model the lower part of the skirt tip as soft elements as described in the following. The geometry and load specifications of the problem as well as the soil and interface properties used are given in Table D.2 and Table D.3

Table D.2 Soil and interface parameters

γ' [kN/m ³]	ϕ [°]	ψ [°]	c [kPa]	ν [-]	E [MPa]	$\tan(\delta)$ [-]
10	35	5	10	0.21	20	0.6

Table D.3 Geometry of problem

D [mm]	d [mm]	h [mm]	V [N]
300	300	2610	184

Definition of orthotropic elastic skirt tips.

The lower part of the skirts is modelled as a linear elastic orthotropic material with the following definition of the engineering elastic constants:

Equation D.1

$$\begin{Bmatrix} e_{11} \\ e_{22} \\ e_{33} \\ g_{12} \\ g_{13} \\ g_{23} \end{Bmatrix} = \begin{bmatrix} 1/E_1 & -n_{21}/E_2 & -n_{31}/E_3 & 0 & 0 & 0 \\ -n_{12}/E_1 & 1/E_2 & -n_{32}/E_3 & 0 & 0 & 0 \\ -n_{13}/E_1 & -n_{23}/E_2 & 1/E_3 & 0 & 0 & 0 \\ 0 & 0 & 0 & 1/G_{12} & 0 & 0 \\ 0 & 0 & 0 & 0 & 1/G_{13} & 0 \\ 0 & 0 & 0 & 0 & 0 & 1/G_{23} \end{bmatrix} \begin{Bmatrix} s_{11} \\ s_{22} \\ s_{33} \\ s_{12} \\ s_{13} \\ s_{23} \end{Bmatrix}$$

where index refers to the orientation of the coordinate system in the FE-model and v_{ij} has the physical interpretation of the poisson's ratio characterizing the transverse strain in the j-direction, when the material is stressed in the i-direction. In order to get a symmetric stiffness matrix the following relation is necessary:

Equation D.2
$$n_{ij} / E_i = n_{ji} / E_j$$

Equation D.2 is satisfied when the soil parameters are entered in the input file as merely $E_1, E_2, E_3, v_{12}, v_{13}, v_{23}, G_1, G_2, G_3$.

The soft elements are modelled as described above because only the vertical stiffness of the skirts must be soft. If the stiffness in the transverse direction is also small the elements will not be capable of mobilizing the earth pressure between the side of the skirt and the soil. Furthermore problems in the soil next to these elements can occur, due to a reduction in the minor principal stress in this area because of the low transverse stiffness.

The direction of the gravity in the 3D models in Abaqus must by definition be the 3-direction. This means that the stiffness E_3 is reduced and that E_1 and E_2 is equal to the stiffness of steel as the rest of the bucket. Simulations is carried out with a value of the reduced vertical stiffness equal to 50, 20 and 2 MPa i.e. 2.5, 1 and 0.1 times the soil stiffness. The value of Poisson's ratio for the steel is set to 0.3 in the part of the bucket foundation where an isotropic material is used. In the material the value of the poissons ratios v_{12} and v_{13} must be small to avoid an increase in the lateral pressure due to the compression in the vertical direction. A value of 0.01 is used in the

calculations. The value of ν_{23} must however be identical to the general Poisson's ratio with a value of 0.3. The shear modulus G_i is calculated based on the elasticity E_3 by the following relation:

Equation D.3
$$G_i = \frac{E_{steel}}{2(1+\nu_{steel})}$$

The properties of the lower skirt part are given in the input file in the following way:

```
-----
*Elastic, type=ENGINEERING CONSTANTS
**E1, E2, E3,  $\nu_{12}$ ,  $\nu_{13}$ ,  $\nu_{23}$ , G1, G2, G3
2e+07, 2e+07, 20., 0.01, 0.01, 0.3, 1e+07, 1e+07
1e+07
-----
```

The results from the simulations are compared in Figure D.6 where the influence of the soft elements at the skirt tip is seen to be negligible. The vertical stresses and strains at failure in the bucket foundation is shown in Figure D.7 Figure D.8. From these it can be seen that the orthotropic elements applied to the lower part of the skirt, transmits only small load to the soil skeleton as the elements are deformed vertically. The influence of soft elements is only performed corresponding to the loading conditions relevant to this thesis. No conclusion of the effect can be drawn from these simulations if the bucket foundation is subjected to large vertical load.

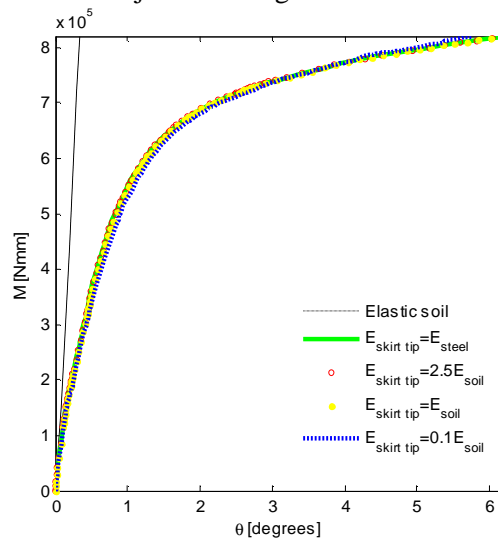


Figure D.6 Comparison of results from Abaqus calculations with different orthotropic stiffness of the skirt tip.

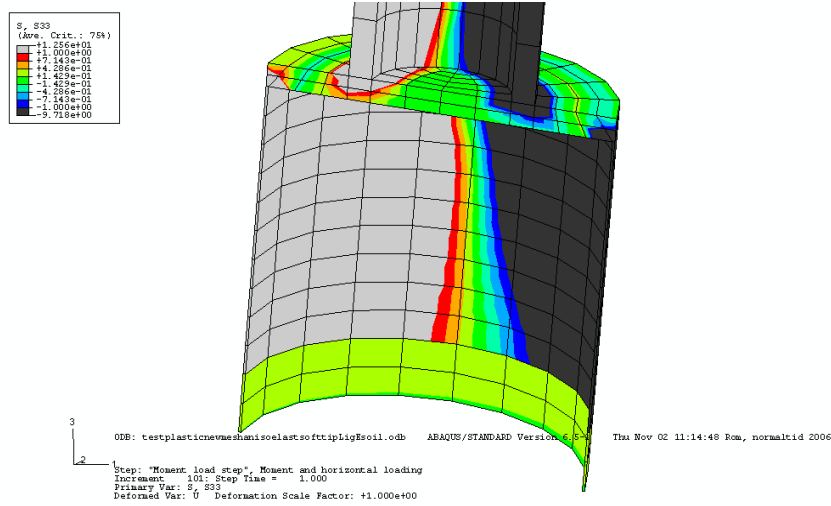


Figure D.7 Vertical stresses in the bucket foundation at failure. $E_{skirt\ tip}=E_{soil}$

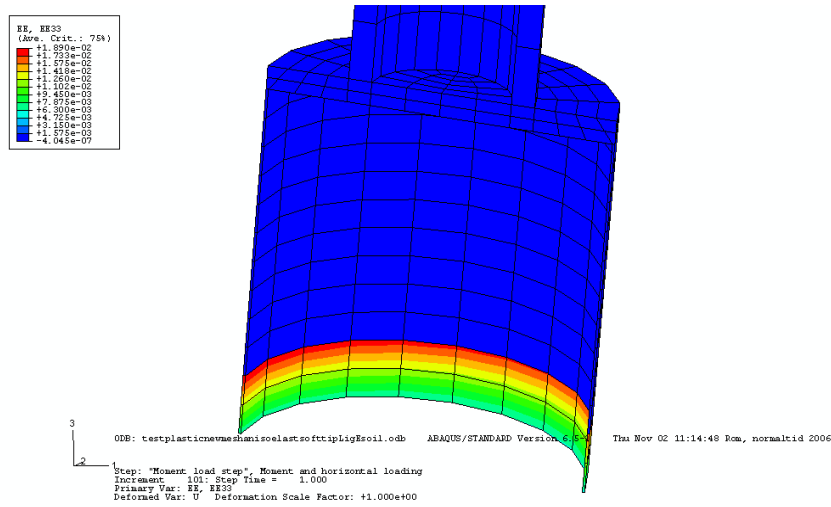


Figure D.8 Vertical strains in the bucket foundation at failure. $E_{skirt\ tip}=E_{soil}$

Jostad (2004) suggests the use of elongated interfaces when simulating the pull out capacity of suction caissons in clay, which also in the 3D model gives modelling difficulties. Using soft elements at the lower part of the skirt gives a model that is similar to the use of elongated interfaces.

D.1.4. Pressure load contra traction load

The vertical load of the bucket foundation is in ABAQUS applied using the load type “pressure” on the bucket lid. This subjects the bucket lid to a uniform distributed load in direction perpendicular to the bucket lid. A small error is introduced with this approach since the direction of the pressure rotates with the bucket whereas the true load on the bucket foundation is vertically through out the test. The error introduced due to the rotation of the load direction is investigated in abaqus by loading the bucket vertically with a load of the type “traction”. With this load type it is possible to constraining the direction of the load on the lid throughout the moment loading of the foundation.

A simulation with a full bucket foundation identical to the one used in the convergence analysis is performed, though applying the vertical load with the type “traction load”. The influence from the load type used is shown in Figure D.9.

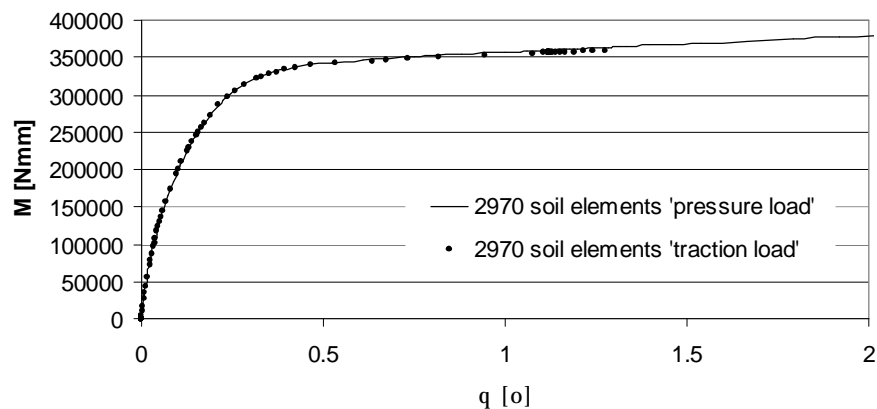


Figure D.9 Investigation of error introduced from method used to apply the vertical load. Parameters and geometry similar to convergence study of full bucket is used.

Since the model is less stable using the “traction” load compared to the pressure load and no significant influence of the rotated pressure on the response is found, the “pressure” load is used throughout the calculations.

The use of “pressure” and “traction” load in the input file is shown below:

```
-----
** LOADS
**
** Name: VerticalLoad  Type: Pressure
*Dload
_PickedSurf151, P, 0.0305
-----
```

```
-----
** LOADS
**
** Name: Vertical load  Type: Surface traction
*Dload, op=NEW, follower=NO, constant resultant=YES
_PickedSurf196, TRVEC, 0.0305, 0., 0., -1.
-----
```

The traction load is applied to the bucket lid in the vertical direction by not rotating the traction with the rotation of the bucket.

The error induced by using the pressure load distribution can alternatively by a simple geometric consideration be determined to only 0.4% at a rotation equal 5 degrees.

D.2. Large scale simulations

The simulations performed in this section are performed with dimensions corresponding to the large scale test presented in chapter 2. The soil parameters, interface behaviour is unless specified identical to the simulation of the large scale test performed in chapter 7.

D.2.1. Influence of the stiffness of steel

It has been observed that changing the elastic stiffness of the bucket foundation in some situations can result in more stable calculations. The influence of the elastic stiffness of the bucket on the behaviour is investigated in the following. In Figure D.10 the results from a set of simulations with the ABAQUS model of the 2-meter bucket foundation presented in chapter 7 is shown using varying steel stiffness. The true stiffness of soil is approximately $2.1 \cdot 10^5$ MPa.

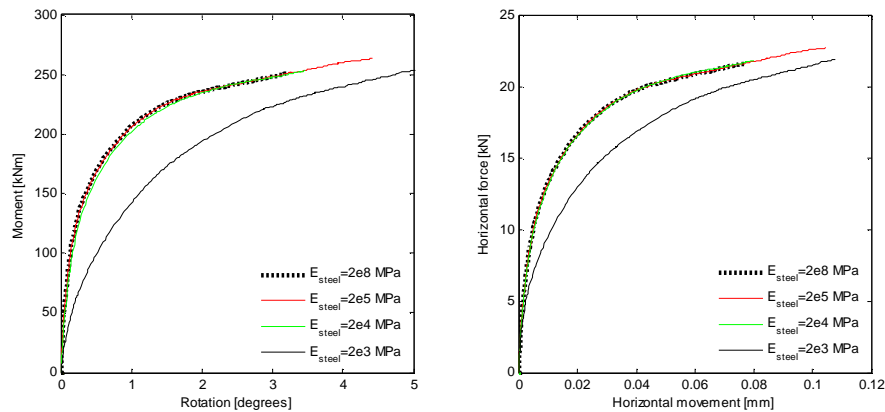


Figure D.10 Influence of the elastic stiffness of the bucket foundation on the behaviour.

From Figure D.10 it can be seen that neither an increase nor decrease in the elastic stiffness of the steel affects the response of the bucket foundation. A lower limit is though seen with a decrease of a factor 10.

D.2.2. Influence of interface properties and vertical boundary conditions

The influence of interface properties between the soil and steel and the boundary conditions at the vertical boundaries of the modelled soil is investigated in the following. The interaction between the soil and the bucket foundation is modelled with the contact pair option as described in chapter 7.

The following simulations are carried out:

- *Basic calculation:* Vertical boundary conditions are smooth. Separation of the soil and steel is allowed after contact.
- *Tied Tip calculation:* The interface between the soil and skirt tip is replaced as a tied connection (i.e. completely rough interface)
- *No Separation calculation:* The soil and bucket is forced to be in contact during the entire calculation.
- *Rough vertical BC calculation:* The vertical boundaries of the soil are modelled as rough, i.e. only vertical movement is allowed.

The results from the simulations are compared in Figure D.11 from which it can be concluded that neither of the changes affects the behaviour of the bucket foundation significantly. The basic simulation is found to be the most time consuming of the simulations in Figure D.11. By changing the properties investigated the calculation time can be reduced without significant changes in the simulated behaviour.

The changes to the model can further more be used to complete calculations that for some reason gives numerical problems with the basic calculation.

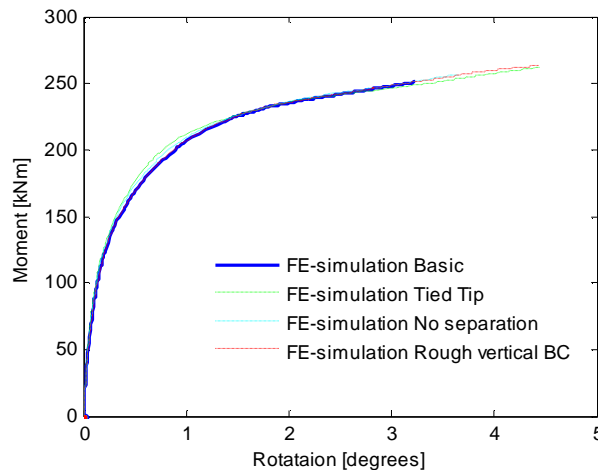


Figure D.11 Results from simulations with different interface properties and boundary conditions.

D.3. Working with abaqus (changes to the inp.-file)

Using Abaqus to simulate the behaviour of the bucket foundations have shown not to be straight forward. Numerical problems are found to occur in some calculations. Working with Abaqus has given a great experience in overcoming some of these problems. Changes to the model and standard settings that have shown to overcome these are listed in the following. Only non-previously presented actions are given here. Some of these actions must be done manually in the input file of the model. The extension of this file is denoted .inp and can be changed by any text editor.

From the start of this thesis several updates of Abaqus have become available. The solver routine in the newer versions seems the most stable.

The criterion of the error on the residual force, defining equilibrium in the model, can be changed by the user. This is generally necessary since the standard setting is too strict for nonlinear problems. If the criterion is increased severely, a too stiff and strong response however might be the case. A criterion of 0.01 is used throughout the simulations.

The criterion on displacement corrections can be changed without any overall difference in the response. Increasing this criterion is found to be necessary in many cases and a value of 0.1 is used.

The criteria for residual force and displacement correction must be done manually in the input file with the “controls” command. This command is also useful in strongly nonlinear problems with the “discontinuous” command. The “discontinuous” command increases the maximum equilibrium iterations allowed, which is found to be necessary in most of the simulations performed. In Abaqus the standard settings is often incapable of finding equilibrium in the model when the response is non linear.

The use of the “controls” command in the input file is illustrated below:

```
-----
*controls, analysis=discontinuous
*controls,parameter=field
**Criterion on residual force, Criterion on displacement correction
1e-2, 0.1
** LOADS
**
-----
```

The load or boundary conditions applied in a given step are applied linearly over the step time. The step time is by default 1. The load or boundary condition is automatically divided into a number of increments from the settings given by the “static” command:

```
-----
** STEP: Vertical Load Step
**
*Step, name="Vertical Load Step", nlgeom, unsymm=YES, inc=1000
*Static
**Initial inc. size, maximum inc. size, minimum inc. size, total step time.
0.001, 1, 1e-05, 1
-----
```

The size of the start increment is important for obtaining equilibrium. Too large an increment and a too small increment can both lead to equilibrium problems. The maximum and minimum increment must be chosen to match the problem. The number of increments used to apply any given load or boundary condition are determined by the problem and the maximum number of increments allowed by the user:

```
-----
** STEP: Vertical Load Step
**
*Step, inc=500
-----
```

Abaqus uses by default the Newton integration scheme to obtain equilibrium in the model. This method uses a linear extrapolation of the stresses in the following increment. Alternatively no extrapolation or a parabolic extrapolation technique can be used. The method of extrapolation technique is given by the user in the input file by the following command:

```
-----
** STEP: Vertical Load Step

*step, Extrapolation=parabolic      **Parabolic extrapolation technique
*step, Extrapolation=no            **No extrapolation technique
*step,                             **Linear extrapolation technique
-----
```

The change in extrapolation technique is found to be very effective to achieve equilibrium in the nonlinear problem investigated. The technique can advantageously be changed continuously during the simulation.

If the settings in the input-file are changed during simulation the restart command can be used. A new input-file must be created with the given changes.

Note that the restart command can only be used if the model is prepared by the following command:

```
-----
** OUTPUT REQUESTS
**
*Restart, write, frequency=1
-----
```

The restart frequency defines the frequency of which the information's necessary for any restart are updated in the output file.

When the restart command is used the information's saved can be limited to the information's from the last increment per step that is completed:

```
-----
** OUTPUT REQUESTS
**
*Restart, write, overlay
-----
```

The output file from a model where the degrees of freedom is large the size of the output file can if the default settings are used be extremely large, i.e. several GB. The variables saved in the output file can be selected by the user

in the CAE or in the input file with the following command shown for the Field Outputs.

```
-----  
** OUTPUT REQUESTS  
**  
** FIELD OUTPUT: Field-Output-Name  
**  
*Output, field,  
*Node Output  
**Reaction forces, Displacements  
RF,U  
*Element Output, directions=Yes  
**Strains, Plastic strains. Stresses  
E,PE,S  
-----
```

In the abaqus command window, the following command is used to submit the input-file if this is changed by user:

```
-----  
Abaqus job=fil_navn.inp  
-----
```

E. Appendix. Survey of measured capacities

Loads and displacements at failure from experiments performed in the geotechnical laboratory at Aalborg University are summarized in this appendix. The relative density of the tested soil, the geometry of the tested foundations and the load path (M/HD) are given for each experiment as well.

Test No.	Dr [%]	d [mm]	D [mm]	d/D [-]	M/H/D [-]	V [N]	M [Nmm]	H [N]	u [mm]	w [mm]	θ [°]
0104_701	80	300	300	1	6.85	1000	302628	147.37	11	-1.44	2.79
0104_702		300	300	1	6.99	1000	262134	124.93	6.92	-1.59	1.24
0104_703		300	300	1	6.93	1000	302226	145.31	5.77	-0.86	1.45
0104_704		300	300	1	6.96	1000	316070	151.4	5.18	-1.31	1.49
0104_801	85	300	300	1	5.81	30	150777	86.53	2.24	-0.97	0.65
0104_802	86	225	300	0.75	5.73	30	66911	38.9	1.72	-1.16	0.68
0104_803	88	150	300	0.5	5.77	30	24035	13.88	0.77	-0.91	0.48
0104_901	89	300	300	1	8.69	0	188698	72.34	3.93	-1.85	1.3
0104_902	88	300	300	1	8.72	100	209508	80.08	3.9	-1.63	1.2
0104_903	86	300	300	1	8.69	100	189734	72.78	2.76	-1.12	0.79
0104_1001	86	225	300	0.75	8.79	100	114641	43.49	3.51	-1.85	1.32
0104_1002	88	150	300	0.5	8.83	100	48021	18.13	2.99	-1.72	1.41
0104_1003	88	75	300	0.25	8.72	100	15148	5.79	0.32	0.1	0.28
0104_1101	87	75	300	0.25	8.68	100	14825	5.69	0.55	-0.68	0.49
0104_1102	89	225	300	0.75	8.68	100	112616	43.26	3.69	-1.71	1.4
0104_1103	89	150	300	0.5	8.84	100	47883	18.06	3.76	-2.22	1.9
0104_1104		75	300	0.25	8.71	100	14503	5.55	0.32	-0.7	0.49
0104_1202	88	200	400	0.5	6.49	85	128614	49.51	5.23	-4.44	2.12
0104_1203	87	100	400	0.25	6.54	100	31584	12.07	1.59	-1.44	1.18
0104_1301	87	400	400	1	6.53	100	688056	263.22	5	-2.23	1.32
0104_1302	87	0	400	0	6.48	100	17035	6.57	0.76	-0.91	0.41
0104_1401	88	400	400	1	6.53	100	667570	255.57	6.21	-2.81	1.5
0104_1501	87	400	400	1	6.52	280	667845	255.93	4.82	-2	1.2
0104_1601	87	400	400	1	6.53	200	620721	237.6	3.02	-1.53	0.81
0104_1701	86	300	300	1	8.70	0	195512	74.92	3.43	-1.79	1.09
0104_1702	88	225	300	0.75	8.63	0	92128	35.6	4.33	-2.98	1.62
0104_1801	86	225	300	0.75	8.73	0	97354	37.18	3.55	-2.2	1.31
0104_1802	89	150	300	0.5	8.65	0	33034	12.73		-4.54	1.69
0104_1901	86	300	300	1	8.68	0	195514	75.05	3.5	-1.7	1.12
0104_1902	86	150	300	0.5	8.69	0	40615	15.58		-4.95	2.19
0104_2002	89	150	300	0.5	5.79	1000	150521	86.65	9.36	-2.07	3.89
0104_2201	87	150	300	0.5	5.84	190	60950	34.76	6.13	-2.88	2.88
0302_2501	83	300	300	1	3.17	65	114720	120.63	2.31	-1.05	0.63
0302_2502	83	300	300	1	5.80	184	190813	109.64	6.31	-2.32	1.66

Test No.	Dr [%]	d [mm]	D [mm]	d/D [-]	M/HD [-]	V [N]	M [Nmm]	H [N]	u [mm]	w [mm]	θ [°]
0302_2601	82	300	300	1	5.80	184	197869	113.72	4.75	-1.79	1.38
0302_2602	84	300	300	1	3.17	65	131849	138.76	3.4	-1.39	0.98
0302_2701	85	300	300	1	5.80	184	205089.4	117.91	4.56	-2.01	1.25
0302_2802	86	300	300	1	0.38	184	89471	777.61	10.91	-4.02	2.69
0302_2901	86	300	300	1	0.37	184	90903	826.79	8.43	-2.79	2.08
0302_2902	88	300	300	1	0.37	184	79784	725	10.16	-5.65	1.92
0104_3001	79	300	300	1	5.83	100	148076	84.63	4.84	-1.72	1.32
0104_3002	81	300	300	1	8.70	100	171755	65.81	4.4	-1.64	1.17
0104_3201	82	0	200	0		4550			7.5	-1	
0104_3301	84	0	200	0		4500			9	0.4	
0104_3501	81	0	100	0		380			6	-1.2	
0104_3502	85	0	100	0							
0104_3503	83	0	100	0		170			4.6	-0.05	
0104_3504	85	0	100	0							
0104_3505	84	0	100	0							
0104_3601	84	0	50	0		72			1.6	0	
0104_3602	84	0	50	0		51			1.5	0.01	
0104_3603	84	0	50	0		49			1.75	0.02	
0104_3604	83	0	50	0		111			1.9	0	
0104_3605	84	0	50	0		60			1.65	-0.02	
0104_3606	85	0	50	0		115			2.4	-0.02	
0104_3607	84	0	50	0		69			1.9	-0.03	
0104_3608	84	0	50	0		109			2.4	-0.03	
0104_3701		0	200	0		4600			4.6	0.07	
0104_3801	86	0	200	0		5400			8.4		
0104_3901	87	0	200	0		6600			9	-0.1	
0104_4001	86	0	200	0		7000			9.5	0.2	
0104_4101	86	0	200	0		6900			9.5		
0104_4201	86	0	200	0		7200			10	0.07	
0104_4301		0	200	0		7200			11.2		
0104_4401	86	50	200	0.25		12600			17	-0.6	
0104_4501	85	50	50	1		640			5	-0.2	
0104_4502	84	50	50	1		400			4	0.3	
0104_4503	84	25	50	0.5		290			3.5	0.24	

Test No.	Dr [%]	d [mm]	D [mm]	d/D [-]	M/HD [-]	V [N]	M [Nmm]	H [N]	u [mm]	w [mm]	θ [°]
0104_4504	86	50	50	1		420				3.5	-0.03
0104_4505	85	25	100	0.25		1120				5	0.3
0104_4601	86	100	100	1		3200				10	0.6
0104_4602	86	75	100	0.75		2200				8	-0.7
0104_4603	86	50	100	0.5		1400				7.4	0.3
0104_4604	86	25	100	0.25		1400				5	-0.04
0104_4605	86	0	100	0		1040				3.6	
0104_4701	89	225	300	0.75	5.83	184	123622	70.68	5.57	-2.04	1.85
0104_4801	90	75	300	0.25	5.77	184	27878	16.1	2.22	-1.87	1.56
0104_4901	89	150	300	0.5	8.79	184	62063	23.54	6.41	-2.55	2.86
0104_5001	89	225	300	0.75	8.73	184	125208	47.79	3.66	-1.42	1.21
0104_5101		300	300	1	8.72	184	245029	93.63	5.2	-2.1	1.51
0104_5201	88	75	300	0.25	8.70	184	28338	10.86	2.57	-2.24	1.85
0104_5301	86	150	300	0.5	0.37	184	30751	279.97	5.37	-2.02	2.08
0104_5401	84	225	300	0.75	0.37	184	57291	520.56	7.6	-3.36	2.2
0104_5501	85	75	300	0.25	0.37	184	18593	168.91	2.08	-0.92	1.12
0104_5601	82	150	300	0.5	8.69	1000	153384	58.81	5.49	-0.81	2.41
0104_5701	88	150	300	0.5	5.79	0	31604	18.21	2.16	-1.96	0.96
0104_5801	86	150	300	0.5	0.37	0	22414	203.5	9.08	-8.81	3.91
0104_5901	86	150	300	0.5	0.37	1000	66958	608.44	7.67	-1.24	2.51
0104_6001	86	225	300	0.75	0.37	1000	84515	768	7.41	-0.97	1.84
0104_6101	88	300	300	1	0.37	1000	133332	1212	11.79	-2.26	2.38
0104_6201	87	75	300	0.25	0.37	1000	56970	518	6.41	-0.17	1.7
0104_6301	86	225	300	0.75	0.37	1000	90089	819	13.09	-2.12	3.41
0104_6401	86	225	300	0.75	5.81	1000	228099	130.82	7.12	-0.7	2.3
0104_6501	85	75	300	0.25	5.81	1000	122969	70.57	3.42	-0.48	1.76
0104_6601	85	300	300	1	5.79	1000	350696	202	7.38	-1.7	2
0104_6701	88	225	300	0.75	8.74	1000	237087	90.47	9.25	-1.36	2.76
0104_6801	89	75	300	0.25	8.62	1000	125484	48.52	5.86	-1.09	2.94
0104_6901	91	300	300	1	8.67	1000	361535	138.92	4.99	-1.3	1.44
0104_7101	90	225	300	0.75	0.37	0	47715	434.12	7.23	-4.49	2.12
0104_7301		300	300	1	0.37	0	79706	724.12	6.99	-3.52	1.65
0104_7401	90	300	300	1	5.82	0	186458	106.8	2.77	-1.41	0.82
0104_7501	90	225	300	0.75	5.78	0	83098	47.89	4.56	-2.98	1.72

Test No.	Dr [%]	d [mm]	D [mm]	d/D [-]	M/HD [-]	V [N]	M [Nmm]	H [N]	u [mm]	w [mm]	θ [°]
0104_7601	90	75	300	0.25	5.81	0	4076	2.34	0.22	-0.36	0.18
0008_E2	60	0	100	0		300				9.8	
0008_E3	86	0	100	0		743				9.5	
0008_E4	93	0	100	0		836				6.8	
0008-F2	60	0	100	0		191				10.5	
0008-F3	80	0	100	0		572				5.6	
0008-F4	85	0	100	0		462				5.8	
0008-301	89	0	200	0	-5.74	3638	81692	-71.1	0.26	0.92	1.04
0008-302	88	0	200	0	-0.96	3638	86000	-449	-0.59	4.22	3.2
0008-401	87	200	200	1	-0.97	12388	1328458	-6833	-0.42	3.24	2.11
0008-501	87	200	200	1	-0.84	12388	1180075	-7005	-9.48	8.18	2
0008-701	89	100	200	0.5	-6.96	8199	398081	-286	6.07	1.55	3.19
0008-702	87	100	200	0.5	-0.76	8199	498572	-3278	-0.42	7.42	4.78
0008-703	90	200	200	1	-5.41	12388	827041	-764	12.2	1.99	3.84
0008-901	90	0	50	0		101				2.38	
0008-902	87	25	50	0.5		271				2.08	
0008-903	85	37.5	50	0.75		315				3.2	
0008-904	89	37.5	50	0.75		389				3.16	
0008-1001	89	0	50	0		111				2.64	
0008-1002	89	12.5	50	0.25		159				1.84	
0008-1003	88	0	100	0		608				3	
0008-1004	85	25	100	0.25		900				5.06	
0008-1005	84	50	100	0.5		1723				0	
0008-1101	91	0	50	0		106				2.32	
0008-1102	90	12.5	50	0.25		200				1.81	
0008-1103	91	12.5	50	0.25		218				2.51	
0008-1104	89	100	100	1		3691				7.36	
0008-1201	92	0	200	0		6823				8.32	
0008-1301	89	50	200	0.25		13300				14	
0008-1401	90	0	100	0		922				3.32	
0008-1402	89	75	100	0.75		2544				5.47	
0008-1501	90	100	200	0.5		17707				18.88	
0008-1601	90	0	100	0		1300				4.5	
0008-1602	90	0	100	0		1089				4.18	

Test No.	Dr [%]	d [mm]	D [mm]	d/D [-]	M/H/D [-]	V [N]	M [Nmm]	H [N]	u [mm]	w [mm]	θ [°]
0008-1603	90	0	100	0		821				3.27	
0008-1604	90	0	100	0		1011				4.52	
0008-1701	95	0	300	0		17732				15.07	
0008-1801	92	0	300	0		21308				17.23	
0008-1901	94	0	200	0		3638	67713	-242	0.74	3.8	3.42
0008-2001	91	0	200	0		3638	66395	-899	-4.29	3.21	2.03
0008-2002	91	0	200	0		3638	38400	-855	-4.16	2.54	0.97
0008-2003	91	100	200	0.5		8199	614066	-2629	3.45	4.1	5.09
0008-2101	89	200	200	1		12388	849031	-1086	13.37	1.72	4.31
0008-2201	89	200	200	1		12388	443428	-5047	18.29	4.13	2.58
0008-2202	91	200	200	1		12388	1433239	-6957	1.2	4.76	3.18
0008-2301	92	100	200	0.5		8199	329633	-3366	2.04	11.92	1.23
0008-2302	91	100	200	0.5		8199	145000	-3082			
0008-2401	89	0	200	0		3638	58025	806	4.09	2.37	0.73
0005-0101		0	200	0		8087				19.71	0.61
0005-0202	80	0	200	0		7149				12.87	0.1
0005-0503	85	0	200	0		7279				21.66	0.53
0005-1604	89	0	200	0		9158				14.37	-0.53
0005-1605	89	0	200	0		7366				24	0.6
0005-1606	89	0	200	0		7759				14.72	-0.05
0005-1207	91	0	200	0		3638	16519	1180	6.44	2.77	0.02
0005-1108	91	0	200	0		3638	133843	-1.11	1.09	1.44	2.09
0005-1509	93	0	200	0		3638	85412	610	2.99	1.67	1.11
0005-1510	93	0	200	0		3638	116636	530	3.43	1.91	1.65
0005-1111	91	0	200	0		3638	120855	353	2.33	2.09	1.84
0005-1212	90	0	200	0		3638	138450	202	2.13	2.21	2.59
0005-1113	91	0	200	0		3638	111438	92	2.34	2.51	2.2
0005-1114	91	0	200	0		3638	120932	198	2.9	1.94	2.11
0005-0115		50	200	0.25		14398				25.21	0.05
0005-0216	78	50	200	0.25		12676				21.73	0.15
0005-0517	85	50	200	0.25		12926				16.87	-0.2
0005-1018	95	50	200	0.25		6463	20188	2019	11.94	5.52	1.44
0005-1019	94	50	200	0.25		6463	256382	-0.39	9.02	3.74	3.91
0005-1520	93	50	200	0.25		6463	194080	882	10.63	4.72	4.02

Test No.	Dr [%]	d [mm]	D [mm]	d/D [-]	M/H/D [-]	V [N]	M [Nmm]	H [N]	u [mm]	w [mm]	θ [°]
0005-1521	93	50	200	0.25	0.70	6463	175521	1254	10.41	3.92	2.99
0005-1122	91	50	200	0.25	5.92	6463	267661	226	9.81	3.96	4.38
0005-1123	91	50	200	0.25	3.06	6463	273885	448	5.72	1.56	2.72
0005-1024	94	50	200	0.25	3.51	6463	206374	294	3.95	2.06	2.59
0005-1025	94	50	200	0.25	1.84	6463	207803	565	12.72	-0.72	1.52
0005-0126		100	200	0.5		14612				20.14	0.25
0005-0227	78	100	200	0.5		15535				10.28	-0.12
0005-0528	85	100	200	0.5		16588				27.75	0.37
0005-0729	93	100	200	0.5		8205	37667	2690	14.88	7.3	3.38
0005-0830	93	100	200	0.5	0.07	8205	43661	2911	8.81	4.76	2.96
0005-0731	93	100	200	0.5	0.07	8205	393024	-16.8	5.71	1.88	3.88
0005-0832	94	100	200	0.5	-116.97	8205	324418	954	10.99	5.37	5.48
0005-0833	94	100	200	0.5	2.26	8205	373897	829	14.06	3.88	6.12
0005-0734	93	100	200	0.5	12.33	8205	359912	146	6.3	2.47	3.31
0005-0735	93	100	200	0.5	30.38	8205	419229	69	7.14	1.95	3.08
0005-0636	89	100	200	0.5	3.76	8205	366485	487	14.42	-1.32	0.9
0005-0637	89	100	200	0.5	1.83	8205	292717	798	8.9	2.82	3.05
0005-0638	89	100	200	0.5	2.45	8205	330475	674	8.58	3.37	4.29
0005-1539	93	100	200	0.5	0.70	8205	238384	1702	12.84	2.19	4.36
0005-1540	93	100	200	0.5	1.10	8205	272195	1237	14.21	2.75	4.72
0005-0142		150	200	0.75		20932				15.87	0.16
0005-0243	78	150	200	0.75		18537				33.97	-0.26
0005-0544	85	150	200	0.75		20805				13.67	0.43
0005-1245	91	150	200	0.75	0.07	10403	42509	3036	23.84	8.32	6.35
0005-1246	90	150	200	0.75	-299.42	10403	520998	-8.7	8.62	3.28	3.73
0005-1447	88	150	200	0.75	1.10	10403	313400	1425	15.89	2.91	5.42
0005-1448	88	150	200	0.75	0.70	10403	269047	1922	16.6	2.71	3.86
0005-1449	88	150	200	0.75	5.91	10403	498699	422	9.19	2.44	3.55
0005-1450	88	150	200	0.75	3.37	10403	530391	787	13.85	2.06	4.76
0005-1351	91	150	200	0.75	1.70	10403	374823	1102	14.33	3.29	4.67
0005-1352	91	150	200	0.75	3.02	10403	420170	696	12.3	2.58	4.5
0005-0353	89	200	200	1		19475				32.39	-0.02
0005-0555	85	200	200	1		24766				20	0.25
0005-0856	93	200	200	1	0.08	12386	37601	2350	5.22	1.26	1.29

Test No.	Dr [%]	d [mm]	D [mm]	d/D [-]	M/HD [-]	V [N]	M [Nmm]	H [N]	u [mm]	w [mm]	θ [°]
0005-0957	88	200	200	1	0.08	12386	56909	3557	16.85	5.1	4.1
0005-1058	95	200	200	1	0.05	12386	33741	3749	8.96	4.86	7.06
0005-0859	94	200	200	1	-745.20	12386	596157	-4	12.23	2.15	2.94
0005-1460	88	200	200	1	0.70	12386	307995	2200	15.15	2.42	4.29
0005-1461	88	200	200	1	1.13	12386	361760	1598	16.68	2.62	4.05
0005-1062	94	200	200	1	3.38	12386	536170	792	11.15	1.73	3.41
0005-0963	88	200	200	1	2.59	12386	473782	914	14.11	2.94	3.89
0005-0964	88	200	200	1	1.72	12386	416469	1214	20.11	5.28	5.52
0005-0965	88	200	200	1	6.00	12386	629312	524	10.79	2.33	3.37
0005-0966	88	200	200	1	2.92	12386	526109	901	13.5	2.69	3.48